NASA [redacted]
TRW Document No. 2291-6011-RU-00

CR 137510

CR 137510

Systems Design Study of the Pioneer Venus Spacecraft

Final Study Report

Appendices to Volume I
Sections 8-11 (Part 3 of 3)

29 July 1973

Contract No. NAS2-7249

Prepared for

AMES RESEARCH CENTER
NATIONAL AERONAUTICS AND SPACE ADMINISTRATION

TRW
SYSTEMS GROUP

MARTIN MARIETTA

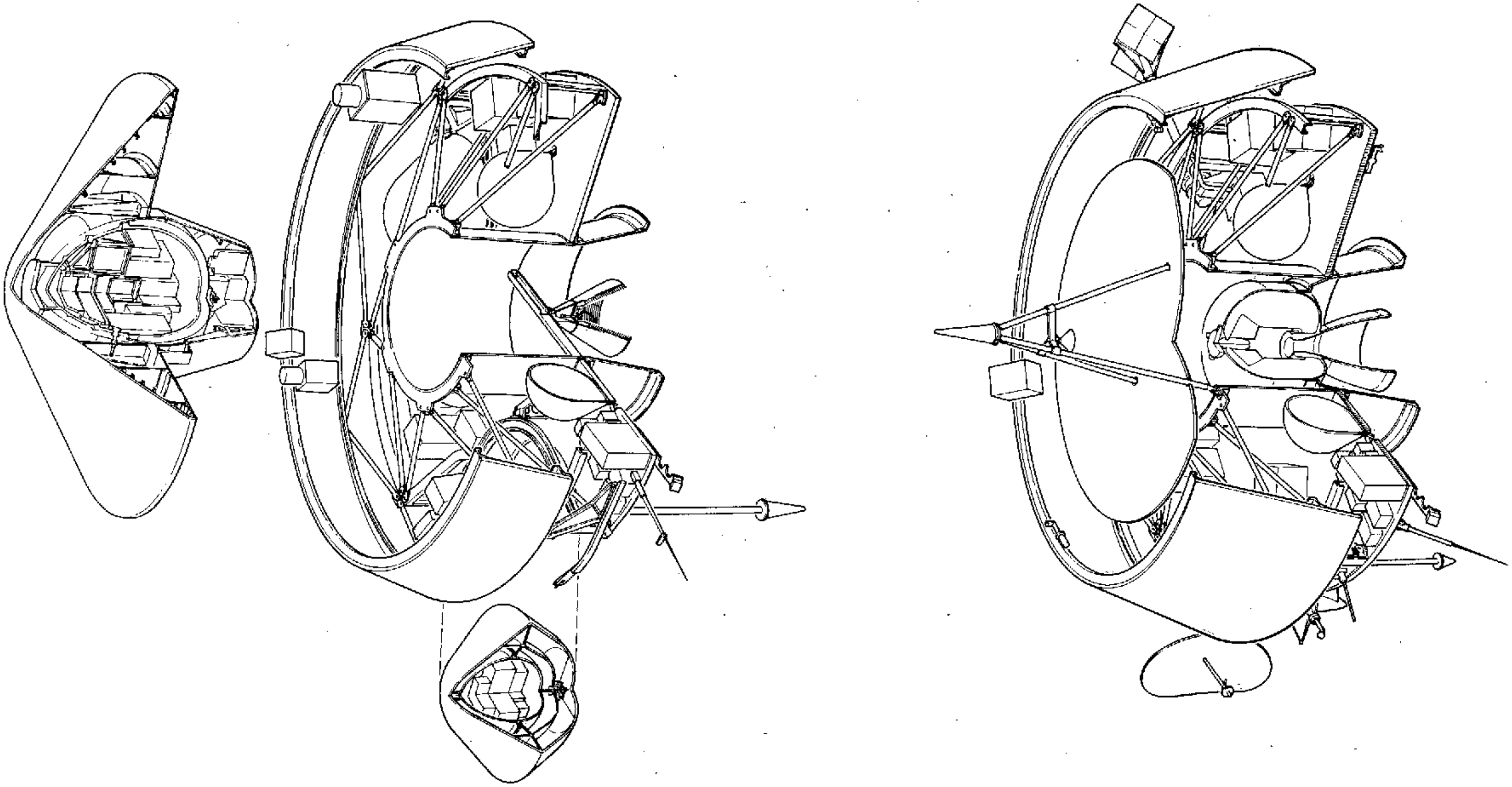

LIST OF VOLUMES

CR 137510

NASA[redacted]
TRW Document No. 2291-6011-RU-00

Systems Design Study of the Pioneer Venus Spacecraft

Final Study Report

Appendices to Volume I
Sections 8-11 (Part 3 of 3)

29 July 1973

Contract No. NAS2-7249

Prepared for

AMES RESEARCH CENTER
NATIONAL AERONAUTICS AND SPACE ADMINISTRATION

TRW
SYSTEMS GROUP

MARTIN MARIETTA

CONTENTS

SECTION 8 APPENDICES

CONTENTS (CONTINUED)

SECTION 10 APPENDICES

SECTION 11 APPENDICES

ACRONYMS AND ABBREVIATIONS

A	ampere analog
abA	abampere
AC	alternating current
A/C	Atlas/Centaur
ADA	avalanche diode amplifier
ADCS	attitude determination and control subsystem
ADPE	automatic data processing equipment
AEHS	advanced entry heating simulator
AEO	aureole/extinction detector
AEDC	Arnold Engineering Development Corporation
AF	audio frequency
AGC	automatic gain control
AgCd	silver-cadmium
AgO	silver oxide
AgZn	silver zinc
ALU	authorized limited usage
AM	amplitude modulation
a.m.	ante meridian
AMP	amplifier
APM	assistant project manager
ARC	Ames Research Center
ARO	after receipt of order
ASK	amplitude shift key
at. wt	atomic weight
ATM	atmosphere
ATRS	attenuated total refractance spectrometer
AU	astronomical unit
AWG	American wire gauge
AWGN	additive white gaussian noise
B	bilevel
B	bus (probe bus)
BED	bus entry degradation

BER	bit error rate
BLIMP	boundary layer integral matrix procedure
BPIS	bus-probe interface simulator
BPL	bandpass limiter
BPN	boron potassium nitrate
bps	bits per second
BTU	British thermal unit
C	Canberra tracking station — NASA DSN
CADM	configuration administration and data management
C&CO	calibration and checkout
CCU	central control unit
CDU	command distribution unit
CEA	control electronics assembly
CFA	crossed field amplifier
cg	centigram
c.g.	center of gravity
CIA	counting/integration assembly
CKAFS	Cape Kennedy Air Force Station
cm	centimeter
c.m.	center of mass
C/M	current monitor
CMD	command
CMO	configuration management office
C-MOS	complementary metal oxide silicon
CMS	configuration management system
const	constant construction
COSMOS	complementary metal oxide silicon
c.p.	center of pressure
CPSA	cloud particle size analyzer
CPSS	cloud particle size spectrometer

ACRONYMS AND ABBREVIATIONS (CONTINUED)

CPU	central processing unit
CRT	cathode ray tube
CSU	Colorado State University
CTRF	central transformer rectifier filter
D	digital
DACS	data and command subsystem
DCE	despin control electronics
DDA	despin drive assembly
DDE	despin drive electronics
DDU	digital decoder unit
DDULBI	doubly differenced very long baseline interferometry
DEA	despin electronics assembly
DEHP	di-2-ethylhexyl phthalate
DFG	data format generator
DGB	disk gap band
DHC	data handling and command
DIO	direct input/output
DIOC	direct input/output channel
DIP	dual in-line package
DISS REG	dissipative regulator
DLA	declination of the launch azimuth
DLBI	doubly differenced very long baseline interferometry
DMA	despin mechanical assembly
DOF	degree of freedom
DR	design review
DSCS II	Defense System Communications Satellite II
DSIF	Deep Space Instrumentation Facility
DSL	duration and steering logic
DSN	NASA Deep Space Network
DSP	Defense Support Program
DSU	digital storage unit
DTC	design to cost
DTM	decelerator test model

DTP	descent timer/programmer
DTU	digital telemetry unit
DVU	design verification unit
E	encounter entry
EDA	electronically despun antenna
EGSE	electrical ground support equipment
EIRP	effective isotropic radiated power
EMC	electromagnetic compatibility
EMI	electromagnetic interference
EO	engineering order
EOF	end of frame
EOM	end of mission
EP	earth pointer
ESA	elastomeric silicone ablator
ESLE	equivalent station error level
ESRO	European Space Research Organization
ETM	electrical test model
ETR	Eastern Test Range
EXP	experiment
FFT	fast Fourier transform
FIPP	fabrication/inspection process procedure
FMEA	failure mode and effects analysis
FOV	field of view
FP	fixed price frame pulse (telemetry)
FS	federal stock
FSK	frequency shift keying
FTA	fixed time of arrival

ACRONYMS AND ABBREVIATIONS (CONTINUED)

G	Goldstone Tracking Station - NASA DSN gravitational acceleration
g	gravity
G&A	general and administrative
GCC	ground control console
GFE	government furnished equipment
GHE	ground handling equipment
GMT	Greenwich mean time
GSE	ground support equipment
GSFC	Goddard Space Flight Center
H	Haystack Tracking Station - NASA DSN
HFFB	Ames Hypersonic Free Flight Ballistic Range
HPBW	half-power beamwidth
htr	heater
HTT	heat transfer tunnel
I	current
IA	inverter assembly
IC	integrated circuit
ICD	interface control document
IEEE	Institute of Electrical and Electronics Engineering
IFC	interface control document
IFJ	in-flight jumper
IMP	interplanetary monitoring platform
I/O	input/output
IOP	input/output processor
IR	infrared
IRAD	independent research and development
IRIS	infrared interferometer spectrometer
IST	integrated system test
I&T	integration and test
I-V	current-voltage

ACRONYMS AND ABBREVIATIONS (CONTINUED)

JPL	Jet Propulsion Laboratory
KSC	Kennedy Space Center
L	launch
LD/AD	launch date/arrival date
LP	large probe
LPM	lines per minute
LPTTL MSI	low power transistor-transistor logic medium scale integration
LRC	Langley Research Center
M	Madrid tracking station - NASA DSN
MAG	magnetometer
max	maximum
MEOP	maximum expected operating pressure
MFSK	M'ary frequency shift keying
MGSE	mechanical ground support equipment
MH	mechanical handling
MIC	microwave integrated circuit
min	minimum
MJS	Mariner Jupiter-Saturn
MMBPS	multimission bipropellant propulsion subsystem
MMC	Martin Marietta Corporation
MN	Mach number
mod	modulation
MOI	moment of inertia
MOS LSI	metal over silicone large scale integration
MP	maximum power
MSFC	Marshall Space Flight Center
MPSK	M'ary phase shift keying
MSI	medium scale integration
MUX	multiplexer
MVM	Mariner Venus-Mars

ACRONYMS AND ABBREVIATIONS (CONTINUED)

NAD	Naval Ammunition Depot, Crane, Indiana
N/A	not available
NiCd	nickel cadmium
NM/IM	neutral mass spectrometer and ion mass spectrometer
NRZ	non-return to zero
NVOP	normal to Venus orbital plane
OEM	other equipment manufacturers
OGO	Orbiting Geophysical Observatory
OIM	orbit insertion motor
P	power
PAM	pulse amplitude modulation
PC	printed circuit
PCM	pulse code modulation
PCM-PSK-PM	pulse code modulation-phase shift keying-phase modulation
PCU	power control unit
PDA	platform drive assembly
PDM	pulse duration modulation
PI	principal investigator proposed instrument
PJU	Pioneer Jupiter-Uranus
PLL	phase-locked loop
PM	phase modulation
p.m.	post meridian
P-MOS	positive channel metal oxide silicon
PMP	parts, materials, processes
PMS	probe mission spacecraft
PMT	photomultiplier tube
PPM	parts per million pulse position modulation
PR	process requirements
PROM	programmable read-only memory
PSE	program storage and execution assembly

ACRONYMS AND ABBREVIATIONS (CONTINUED)

PSIA	pounds per square inch absolute
PSK	phase shift key
PSU	Pioneer Saturn-Uranus
PTE	probe test equipment
QOI	quality operation instructions
QTM	qualification test model
RCS	reaction control subsystem
REF	reference
RF	radio frequency
RHCP	right hand circularly polarized
RHS	reflecting heat shield
RMP-B	Reentry Measurements Program, Phase B
RMS	root mean square
RMU	remote multiplexer unit
ROM	read only memory rough order of magnitude
RSS	root sum square
RT	retargeting
RTU	remote terminal unit
S	separation
SBASI	single bridgewire Apollo standard initiator
SCP	stored command programmer
SCR	silicon controlled rectifier
SCT	spin control thrusters
SEA	shunt electronics assembly
SFOF	Space Flight Operations Facility
SGLS	space ground link subsystem
SHIV	shock induced vorticity
SLR	shock layer radiometer
SLRC	shock layer radiometer calibration

ACRONYMS AND ABBREVIATIONS (CONTINUED)

SMAA	semimajor axis
SMIA	semiminor axis
SNR	signal to noise ratio
SP	small probe
SPC	sensor and power control
SPSG	spin sector generator
SR	shunt radiator
SRM	solid rocket motor
SSG	Science Steering Group
SSI	small scale integration
STM	structural test model
STM/TTM	structural test model/thermal test model
STS	system test set
sync	synchronous
TBD	to be determined
TCC	test conductor's console
T/D	Thor/Delta
TDC	telemetry data console
TEMP	temperature
TS	test set
TTL MSI	transistor-transistor logic medium scale integration
TLM	telemetry
TOF	time of flight
TRF	tuned radio frequency
TTM	thermal test model
T/V	thermo vacuum
TWT	travelling wave tube
TWTA	travelling wave tube amplifier
UHF	ultrahigh frequency
UV	ultraviolet

ACRONYMS AND ABBREVIATIONS (CONTINUED)

VAC	volts alternating current
VCM	vacuum condensable matter
VCO	voltage controlled oscillator
VDC	volts direct current
VLBI	very long baseline interferometry
VOI	Venus orbit insertion
VOP	Venus orbital plane
VSI	Viking standard initiator
VTA	variable time of arrival
XDS	Xerox Data Systems

SECTION 8 APPENDICES

APPENDIX 8. 1A

POWER SUBSYSTEM COST/WEIGHT TRADEOFFS

APPENDIX 8.1A

POWER SUBSYSTEM COST/WEIGHT TRADEOFFS

1. COST

The cost estimations of power subsystem units were based upon DSCS-II, DSP, and Pioneer 10 and 11 hardware design and development and manufacturing experience. Parts count and degree of modification of existing hardware were factored into the estimate of manufacturing and design and development costs. Cost data includes sufficient quantities of units to equip probe bus and orbiter versions. It was based on the orbiter complement of equipment, but the savings in fewer slices for the probe bus balance the cost of the different probe bus battery. The preferred systems are 6 for Thor/Delta and 15 for Atlas/Centaur (see Table 8.1A-1).

2. WEIGHTS

The weights of the candidate designs were based upon slice or tray weights for functionally equivalent circuitry measured on existing hardware such as Pioneers 10 and 11, Intelsat III, DSCS-II, or DSP programs. Battery weights were based on measured cell weight data adjusted for case weight or off-the-shelf battery weights. The solar array weight estimate was based upon recent hardware experience on DSCS-II and DSP arrays.

Table 8.1A-1. Orbiter Power Subsystem Cost/Weight Tradeoffs

	CONFIGURATION		POWER CONTROL UNIT	REGULATOR	POWER CONDITIONING	SOLAR ARRAY	BATTERY	TOTAL WEIGHT (KG)	$K TOTAL
1.	22 TO 33 VDC BUS, Ni-Cd BATTERY BUCKING ARRAY REGULATOR CONFIGURATION 3 POWER CONDITIONING	KG	2.14	4.82	6.6	17.0	17.3*	47.86	2619.0
		$	370	646	941	542	120**		
2.	28 VDC ±2% BUS, Ni-Cd BATTERY BUCKING ARRAY REGULATOR CONFIGURATION 3 POWER CONDITIONING	KG	5.02	4.82	2.4	17.0	17.5	46.74	2970.0
		$	1037	646	420	542	325		
3.	22 TO 33 VDC BUS, Ni-Cd BATTERY BUCK-BOOST ARRAY REGULATOR CONFIGURATION 3 POWER CONDITIONING	KG	2.14	4.82	6.6	18.4	17.3	49.26	2652.0
		$	370	646	941	575	120		
4.	28 VDC ±2% Ni-Cd BATTERY BUCK-BOOST ARRAY REGULATOR CONFIGURATION 3 POWER CONDITIONING	KG	4.32	4.82	2.4	18.4	17.5	47.44	3003
		$	1037	646	420	575	325		
5.	INTELSAT III TYPE SYSTEM 22 TO 33 VDC SHUNT LIMITED BUS, Ni-Cd BATTERY CONFIGURATION 3 POWER CONDITIONING	KG	4.32	----	6.6	15.6	17.3*	43.82	2079
		$	508	----	941	510	120		
6	PIONEER 10 AND 11 TYPE SYSTEM 28 VDC ±2%, Ni-Cd BATTERY CONFIGURATION 3 POWER CONDITIONING PREFERRED THOR/DELTA	KG	6.35	----	2.4	15.6	17.5	41.85	2115
		$	860	----	420	510	325		
7.	PIONEER 10 AND 11 TYPE SYSTEM 28 VDC ±2% BUS, Ag-Cd BATTERY CONFIGURATION 2 POWER CONDITIONING	KG	6.8	----	2.4	15.6	14.0***	38.8	2415
		$	864	----	420	510	621		
8.	SHUNT BOOST SYSTEM 22 TO 33 VDC BUS, Ni-Cd BATTERY CONFIGURATION 3 POWER CONDITIONING	KG	3.9	4.82	6.6	17.0	17.3*	49.62	3128
		$	876	646	941	545	120		
9.	UNREGULATED SYSTEM 22 TO 70 VDC BUS, Ni-Cd BATTERY CONFIGURATION 3 POWER CONDITIONING	KG	2.82		6.6	15.6	17.3*	42.32	1986
		$	415		941	510	120		
10.	UNREGULATED SYSTEM 22 TO 70 VDC BUS, Ag-Cd BATTERY CONFIGURATION 3 POWER CONDITIONING	KG	3.28	----	6.6	15.6	11.9*	37.38	2781
		$	523	----	941	510	807		
11.	PIONEER 10 AND 11 TYPE SYSTEM 28 VDC ±2% BUS, Ni-Cd BATTERY CONFIGURATION 1 POWER CONDITIONING	KG	6.35	----	2.3	15.6	17.5	41.75	2305
		$	860	----	610	510	325		
12.	PIONEER 10 AND 11 TYPE SYSTEM 28 VDC ±2% BUS, Ag-Cd BATTERY CONFIGURATION 1 POWER CONDITIONING	KG	6.8	----	2.3	15.6	14.0	38.7	2605
		$	864	----	610	510	621		
13.	SHUNT BOOST SYSTEM 28 VDC ±2% BUS, Ni-Cd BATTERY CONFIGURATION 3 POWER CONDITIONING	KG	6.8	4.82	2.9	17.0	17.5	49.02	3180
		$	1247	646	420	542	325		
14.	BASELINE SYSTEM PIONEER 10 AND 11 TYPE SYSTEM 28 VDC ±2% BUS, Ag-Cd BATTERY CONFIGURATION 2A POWER CONDITIONING (INVERTER AND CTRF)	KG	6.8	----	7.4	16.1	14.0	44.3	2210
		$	864	----	188	537	621		
15.	PIONEER 10 AND 11 TYPE SYSTEM 28 VDC ±2% BUS, Ni-Cd BATTERY CONFIGURATION 2A POWER CONDITIONING (INVERTER AND CTRF) PREFERRED ATLAS/CENTAUR	KG	6.35	----	7.4	15.6	17.5	46.85	1883
		$	860	----	188	510	325		

*REDUCED BATTERY WEIGHT DUE TO DIRECT DISCHARGE TO BUS.

**OFF-THE-SHELF DSP (30K EACH).

***14 KG BASED ON 24 A-HR SCALEUP TO 30 A-HR CELL

APPENDIX 8. 1B

BATTERIES

APPENDIX 8.1B

BATTERIES

1. NICKEL CADMIUM BATTERY CYCLE LIFE

Nickel cadmium batteries have the best cycle life and are more rugged than any other type of secondary battery for space purposes. However, nickel cadmium batteries are heavier and have high residual magnetic fields. Data in Section 3.3.2 shows that the magnetometer boom length must be increased slightly to accommodate this low risk battery.

The depth of discharge will be 31 percent during the first eclipse season, 66 percent during the 1.4-hour maximum eclipse season, and approximately 10 percent during launch. Figure 8.1B-1 shows the battery is conservatively sized, with a cycle life capability considerably in excess of Pioneer Venus requirements. Future growth could be accommodated with increased depth of discharge to 80 percent. Cell bypass circuitry is not required for the nickel cadmium battery because of the high cycle life capability and conservative usage.

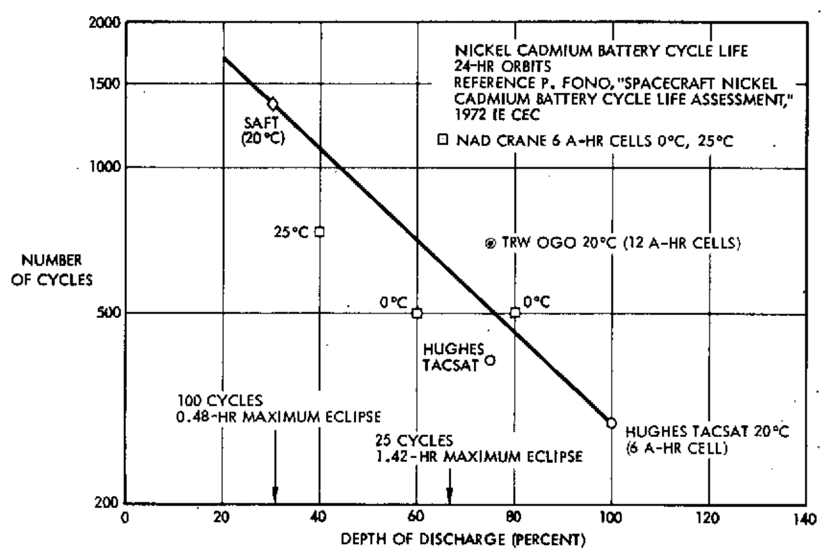

Figure 8.1B-1. Nickel-Cadmium Battery Cycle Life

2. SILVER CADMIUM BATTERY CYCLE LIFE

Table 8.1B-1 shows the NAD Crane 24-hour orbit silver cadmium cell cycle life data. Note the wide variations in cycle life for tests under identical conditions. Other sources of data for silver cadmium cycle life are summarized in Table 8.1B-2.

Table 8.1B-1. Silver Cadmium Battery Cycle Life Tests (NAD Crane)

DEPTH OF DISCHARGE	TEMPERATURE	CYCLES	YEAR	VOLTAGE LIMIT
50	40	210	1964	1.50
43	40	310	1968	1.51
20	40	61	1965	1.50
20	40	269	1967	1.50
18	40	447	1969	1.51
40	25	69	1967	1.51
18	25	507	1969	1.51
20	25	34	1965	1.97
20	25	98	1965	1.50
20	25	720	1967	1.49
20	25	610	1967	1.50
20	25	77	1967	1.50
20	25	661	1968	1.50
18	0	1548	(IN PROGRESS)	1.51 6/20/72
50	0	168	1964	1.50
43	0	61	1967	1.51
40	0	121	1967	1.51
20	0	267	1966	1.50
20	0	2542	1971	1.50

Table 1.1B-2. Data on Silver Cadmium Cycle Life from Other Programs

PROGRAM OR SOURCE	DEPTH OF DISCHARGE (5%)	CYCLES
FR-1 SATELLITE	15	10 000
P/F SUBSATELLITE	8	5 000
JPL 20 A-HR CELLS 1.5-VOLT CHARGE LIMIT [23.89°C (75°F)] 24-HOUR ORBIT (7 MONTHS STORAGE)	60	56 TO 90
JPL 20 A-HR CELLS 1.5-VOLT CHARGE LIMIT (-20°C) 24-HOUR ORBIT (7 MONTHS STORAGE)	60	144 TO 261
NAD CRANE 10 CELL PACKS 24-HOUR ORBIT (14 MAY 1965)	50	166

2. 1 Need for Individual Cell Bypassing

Because 1) overcharge current is highly sensitive to applied voltage limit in Ag-Cd cells, 2) the I-V characteristic of each cell is different, and 3) the voltage dispersion of those cells tends to become large as time passes, individual voltage limiting on charge is used for this application.

2. 2 Silver Cadmium Battery Wet Storage

Figure 8. 1B-2 shows data for silver cadmium battery wet stand storage based on Goddard Space Flight Center IMP and JPL test experience.

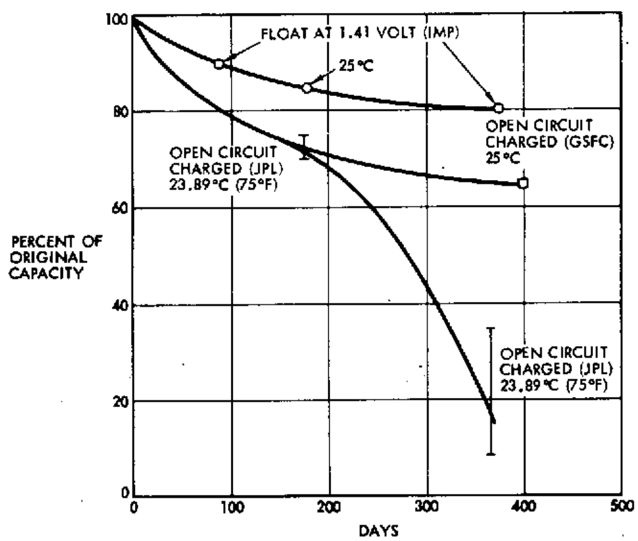

Figure 8. 1B-2. Silver-Cadmium Battery Wet Storage Capacity Loss

Silver cadmium cells lose capacity throughout their life, starting as soon as they are activated with electrolyte. The rate of capacity loss largely depends on temperature and less strongly on whether the cells are cycled or stored inactive, except that very high depths of discharge accelerate the rate. Also, the rate of capacity loss is about the same for charged open-circuit storage as for discharged open-circuit storage. "Floating" the battery decreases capacity loss, at least for the first 6 months. Figure 8. 1B-2 shows capacity versus storage data for Ag-Cd cells at 25°C. Note that the results for charged open-circuit storage at 1-year are quite different for Goddard SFC and JPL, an example of the wide variations typical of state-of-the-art Ag-Cd cells.

3. SILVER ZINC SECONDARY BATTERY CYCLE LIFE

Silver zinc secondary cell cycle life data (NAD crane) shows wide variation similar to that of the silver cadmium cell (see Table 8.1B-3). The cycle life capability at high depths of discharge is questionable. Other silver zinc data is presented in Table 8.1B-4. Because of the extreme data scatter for silver zinc cells in cycling tests, they were eliminated as candidates for the orbiter mission.

Table 8.1B-3. Secondary Silver Zinc Tests (24 Hour Orbits) (NAD Crane)

DEPTH OF DISCHARGE	TEMPERATURE (°C)	DATE	CYCLES
40	25	1967	90
40	25	1964	32
40	25	1964	80
31	25	1967	281
42	25	1965	58
25	25	1965	139
40	25	1966	121

Table 8.1B-4. Data on Silver Zinc Cycle Life from Other Programs

PROGRAM/SOURCE	TEMPERATURE (°C)	DEPTH OF DISCHARGE (%)	CYCLE LIFE
25TH POWER SOURCES CONFERENCE T.J. HENNIGAN (GSFC) 24-HOUR ORBIT	24	25	230
25TH POWER SOURCES CONFERENCE T.J. HENNIGAN (GSFC) 6 CYCLES PER DAY	20	25	800
19TH POWER SOURCES CONFERENCE G.M. WYLIE (ESB) 3.5-DAY CYCLE	--	APPROXIMATELY 70 PERCENT DISCHARGE TO 1.25 V/CELL	50
JPL SPACE PROGRAM SUMMARY 37-60 VOL. III, 1969	25	60	90, 120, 230

APPENDIX 8.1C

PIONEER VENUS BUS VOLTAGE REGULATION SCHEME

APPENDIX 8.1C

PIONEER VENUS BUS VOLTAGE REGULATION SCHEME

The Pioneer Venus power subsystem employs a full shunt regulator connected across the array terminals, together with a discharge regulator. Figure 8.1C-1 shows a simplified block diagram of the system. The central control unit is the heart of the system. It controls the shunt driver and the battery charge and discharge regulators to maintain the bus voltage within the regulation limits of 28 VDC ±1 percent (excluding long-term drift effects). This regulation band is divided into nonoverlapping regions of control as shown.

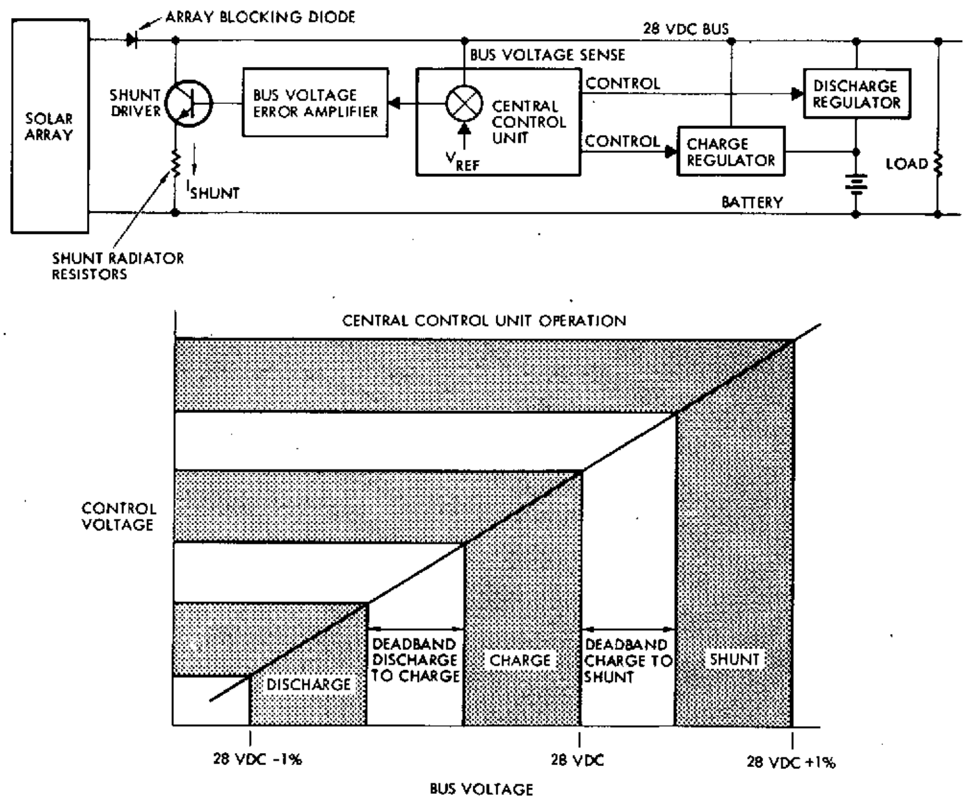

Figure 8.1C-1. Pioneer Venus Power Subsystem Simplified Block Diagram

The shunt, charger, and discharger may be thought of as transconductance amplifiers where the output current is linearly varied as controlled by an error signal proportional to the bus voltage. Below 28 VDC -1 percent, the discharger is supplying all the current it can (up to its built-in current limit) to the bus. At the lower end of the deadband between discharge and charge, it is turned off and the array completely supports the bus. The deadband assures that discharge and charge do not occur simultaneously. Once the bus voltage rises to the upper limit of the discharge-to-charge deadband, the charger is enabled and provides current to the battery in proportion to the bus's ability to provide it up to 28 VDC. At this point, the charger is at its current limit of (about 2 A) and thereafter the internal charge control will control battery current as a function of voltage. If the solar array capability exceeds charging and load requirements, the bus voltage will rise above the charge-to-shunt deadband and the shunt will be enabled. The shunt current capability is sized such that the bus voltage never exceeds 28 VDC +1 percent.

Figure 8.1C-2 shows the case where the array power at 28 volts exceeds load requirements and the battery is fully charged (trickle mode). The shunt current is the difference between the intersection of the constant power load line and the array I-V curve at 28 VDC. The array operating point is shown at the intersection of the 28-volt vertical line and the I-V curve. As the load changes, the shunt current adjusts to keep the operating point below 28 volts +1 percent.

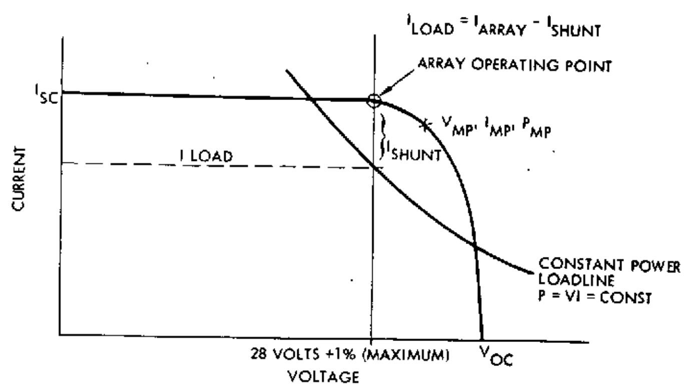

Figure 8.1C-2. Array Power Exceeds Load Power

Figure 8.1C-3 shows the end-of-life situation where load power just equals array power capability. Shunt current is zero and battery discharge is not required. At this point, the shunt control method is most efficient since losses are virtually zero. For Pioneer Venus, this theoretical design point will be achieved after 225 days in orbit (orbiter mission).

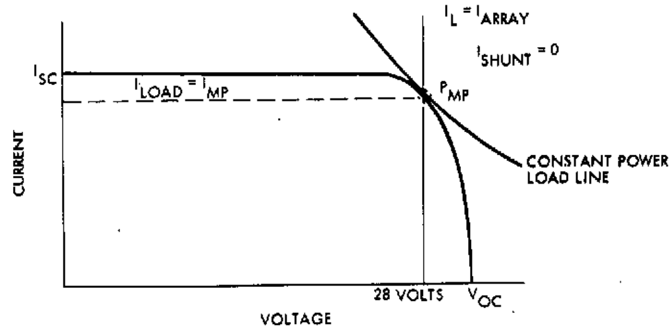

Figure 8.1C-3. Array Power Equals Load Power
$I_{Shunt} = 0$ (End of Life Operating Point)

Figure 8.1C-4 shows the case where load power exceeds the array capability but the open circuit voltage of the array is greater than 28 volts. The CCU senses that the bus voltage has dropped slightly and enables the discharger to maintain the bus above 28 volts -1 percent. The array operating point is at the intersection of the 28-volt vertical line and the I-V curve. The discharger supplies the difference in current between array capability and load demand. Shunt current is zero. For this case the battery and array operate in a sharing mode.

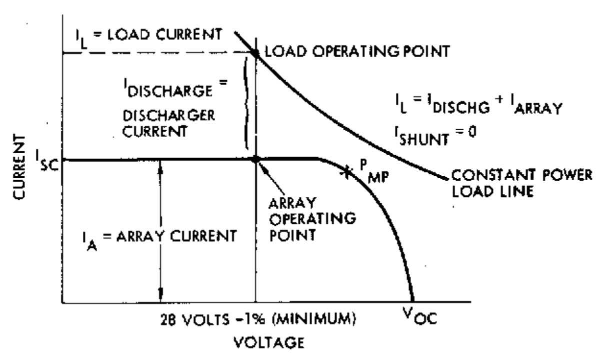

Figure 8.1C-4. Array Power Less Than Load Power

Figure 8.1C-5 shows what happens if the array voltage falls below 28 volts -1 percent. Since there is no intersection of the 28-volt vertical line and the I-V curve, no power is supplied by the array (blocking diodes back biased). The shunt is disabled and the discharger carries the full load, which, of course, is an abnormal operating mode.

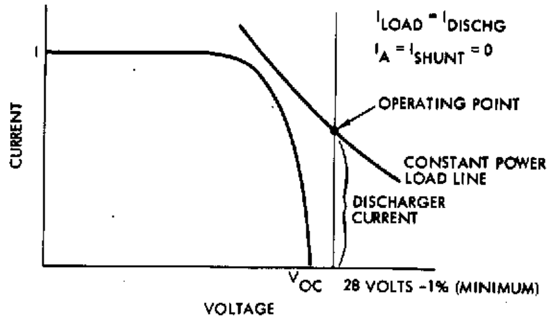

Figure 8.1C-5. Array Open Circuit Voltage Less Than 28 Volts

APPENDIX 8.1D

PIONEER VENUS SHUNT DATA

APPENDIX 8.1D

PIONEER VENUS SHUNT DATA

1. SHUNT SIZING ANALYSIS

The Pioneers 10 and 11 shunt regulator simplified block diagram is shown in Figure 8.1D-1. The shunt consists of a 2 of 3 majority voting error amplifier that feeds six shunt driver power transistors. The power transistors are arranged in a 2 x 3 array to preclude catastrophic single-part failures. Figure 8.1D-2 gives the detailed schematic diagram and Figure 8.1D-3, the simplified schematic diagram.

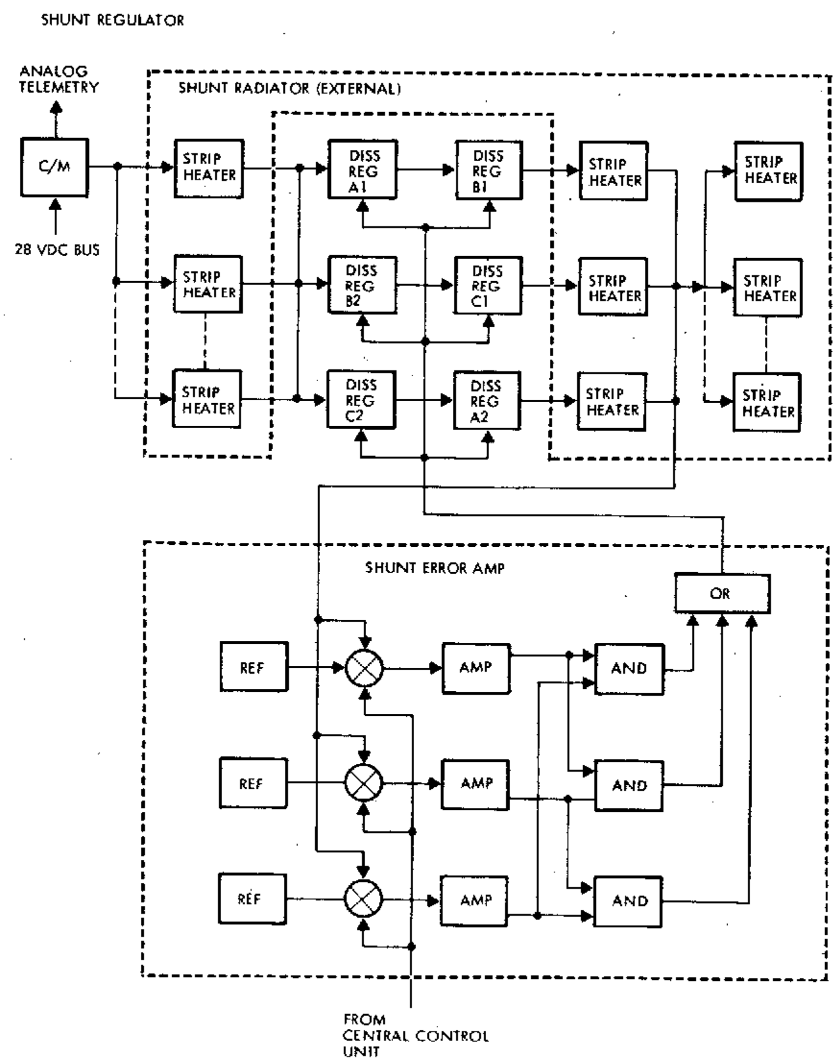

Figure 8.1D-1. Shunt Block Diagram

The maximum shunt current is given by:

$$\frac{(28-2.5)}{5.88} = 4.5 \text{ amperes}$$

and the maximum resistor dissipation is:

$$(4.5)^2 \times 5.88 = 119 \text{ watts.}$$

The transistor dissipation is:

$$2.5 \times 4.5 = 11.25 \text{ watts.}$$

Therefore, the total shunt dissipation capability is

$$119 + 11.25 = 130.25 \text{ watts.}$$

2. THOR/DELTA ORBITER SHUNT POWER REQUIREMENTS

31 W T/D III

Figure 8.1D-4 shows the array I-V characteristics for degraded (7×10^{14}/meV equivalent electrons) and undegraded conditions at Venus. Constant power load lines have been drawn for the 225.7-watt load at periapsis, for undervoltage with battery charging and for undervoltage without battery charging. Table 8.1D-1 summarizes the shunt power requirements for these loads.

The shunt current capability can adequately handle all conditions except for the undegraded array with the undervoltage load (neglecting trickle charging current). If the battery trickle charge current of 0.3 ampere is considered, then the shunt capability required is 4.5 amperes, which the Pioneers 10 and 11 shunt can handle without modification. It is important to note that an undervoltage condition occurring simultaneously with an undegraded array is highly unlikely since the undegraded array provides excess power above battery and load requirements. Also, the undegraded array maximum power is 21 percent above the degraded array maximum power due to the conservative radiation environment used in array sizing. A less conservative environment would reduce shunt current requirements. The Thor/Delta probe bus power requirements are virtually identical to those of the Atlas/Centaur version of Section 4. The probe bus shunt sizing in Section 4 applies also to the Thor/Delta bus.

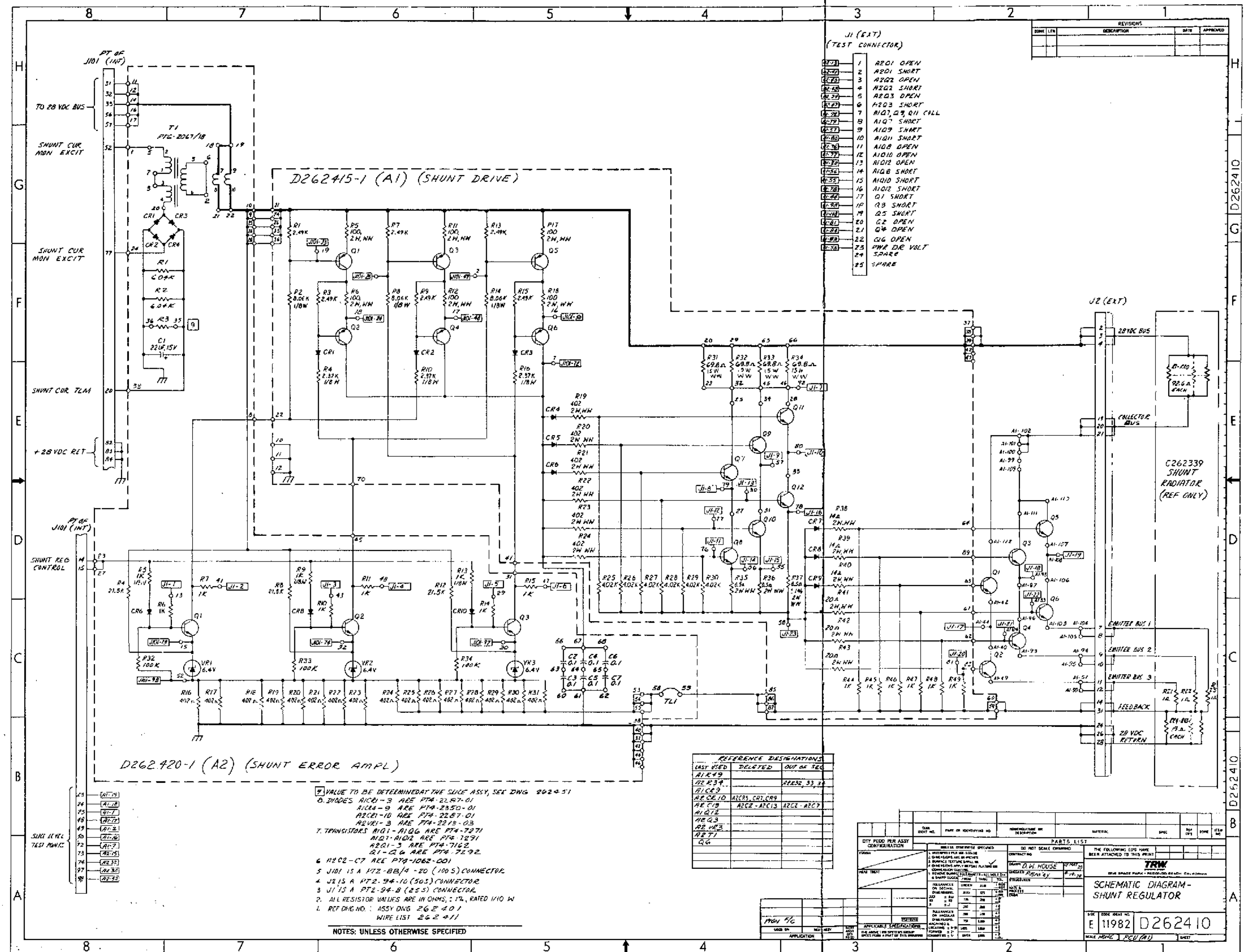

Figure 8.1D-2, Shunt Regulator Schematic Diagram

FOLDOUT FRAME 1

FOLDOUT FRAME 2

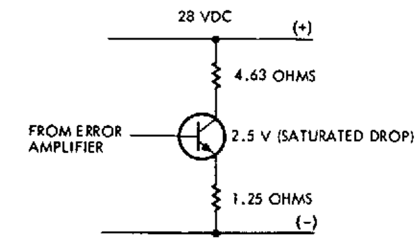

Figure 8.1D-3. Simplified Shunt Schematic

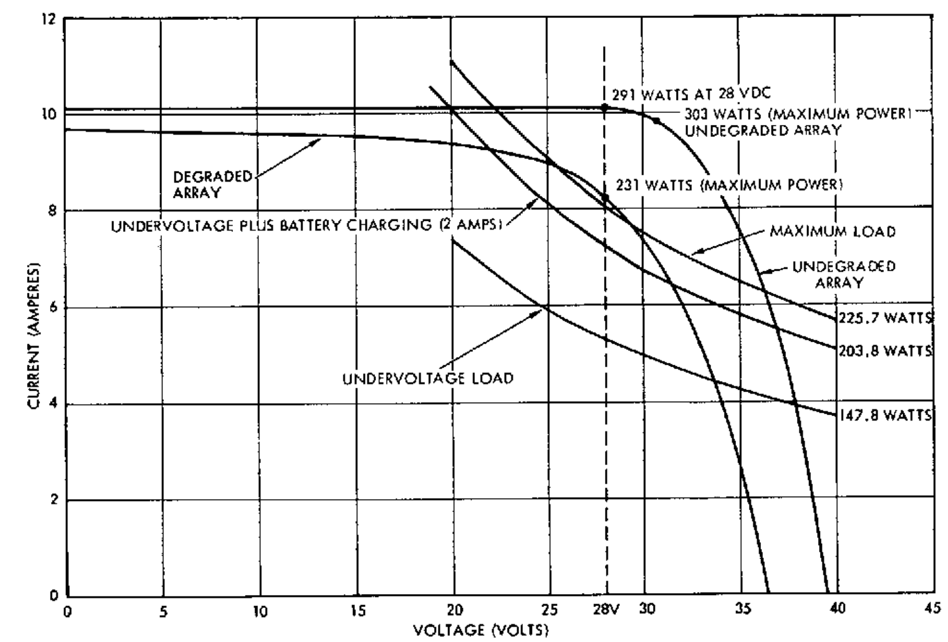

Figure 8.1D-4. Thor/Delta Orbiter Array Characteristics 106.96 Gigameters (0.715 AU), 150 Parallel x 77 Series Cells 2 X 2 CM, 0.015 CM (0.006 IN.) Thick μ Sheet Covers

Table 8.1D-1. Shunt Current as a Function of Operating Mode

CONDITION (AT VENUS)	I_{SHUNT} (AMPERES)
UNDEGRADED ARRAY, 225.7-WATT LOAD	2.0
UNDEGRADED ARRAY, 203.8-WATT LOAD (BATTERY CHARGING 2 AMPERES)	2.9
UNDEGRADED ARRAY, 147.8-WATT LOAD	4.8 (4.5 AMPERES LOAD WITH 0.3-AMPERE TRICKLE CHARGE)
DEGRADED ARRAY, 225.7-WATT LOAD	0.22
DEGRADED ARRAY, 203.8-WATT LOAD	1.1
DEGRADED ARRAY, 147.8-WATT LOAD	3.0

3. SHUNT POWER GROWTH

The shunt power capability may be increased appreciably by employing various techniques as listed below:

- Supplement shunt resistance or array switching
- Add power transistor strings to the three strings presently used on Pioneers 10 and 11
- Use Vela V shunt string configuration
- Use a Defense Support Program (DSP) or Intelsat III shunt element assembly to drive a shunt radiator.

3.1 Supplemental Resistor or Array Switching

The simplest method of increasing shunt capability is to add a commandable resistive load across the array or switch off a portion of the array (see Figure 8.1D-5). The resistor shunts off a portion of the array current and reduces the PCU shunt current requirement. The resistor is commandable through a fail-safe circuit as shown. If K1 or K2 fails in either contact position, the other relay commands the resistor on or off. Thus, single-failure modes are precluded. In practice, the resistor would be commanded on only if the increased shunt current on telemetry indicated that the capability of the shunt would be exceeded. Since the array capability increases slowly as the spacecraft approaches Venus, the timing of the command to switch in the resistor is not critical.

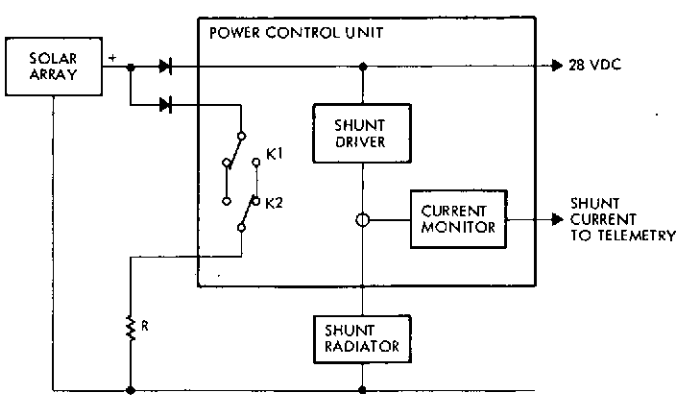

Figure 8.1D-5. Shunt Growth Version with Supplemental Resistor

The resistor would be mounted on a flat plate similar to the shunt radiator design. Since the resistor has a wide allowable temperature range of approximately -160 to +125°C, its placement on the spacecraft can minimize the impact on the compartment dissipation and can ease the thermal control problem. The resistor is sized to dissipate the power in excess of shunt capability.

Switching off a portion of the array also would decrease shunt requirements. The advantage is that no resistor would be required since the power is not removed from the array. Hence, the switched array has a simpler thermal interface than the resistive load. A disadvantage is the difficult timing interface with the undervoltage/overload circuit during load turnoff.

3.2 Add Power Transistor Strings

The Pioneers 10 and 11 shunt slice package is shown in Figure 8.1D-6. Six power transistors are shown mounted on three external surfaces of the slice. Two additional transistors can be mounted on the remaining surface. Each string has the capability to handle 2.25 amperes of shunt current (4.5 amperes with one string failed). The addition of two more transistors to the shunt slice would raise the current capability to 6.75 amperes, corresponding to 185 watts (one string failed). However, the peak shunt slice dissipation would be 60 watts. Increasing the baseplate area of the shunt slice with a doubler plate would provide increased dissipation capability. If the full 6.75-ampere shunt capability is not required, the PCU dissipation can be reduced by employing a higher resistance in the shunt radiator to reduce the current in the shunt transistors at peak dissipation (equal power in transistors and shunt radiator).

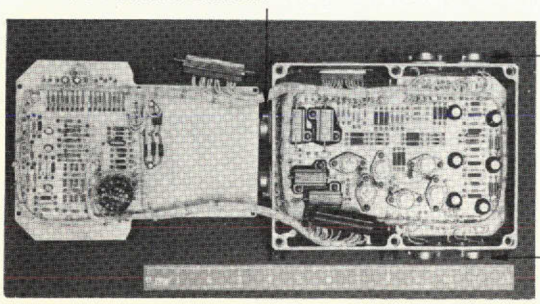

Figure 8.1D-6. Pioneer 10 and 11 Shunt Slice Package

3.3 Vela V Shunt String

The preferred shunt regulator configuration to provide higher power dissipation capability is shown in Figure 8.1D-7. Electrically, it is identical to the Pioneer 10 and 11 circuit; however, the supplemental shunt transistor strings are mounted external to the slice in individual housings. In this way, the power in these transistors can be dissipated at some other more thermally convenient location and thus increase power dissipation capability without overheating the PCU or other adjoining equipment. Table 8.1D-2 summarizes the Vela V shunt string characteristics.

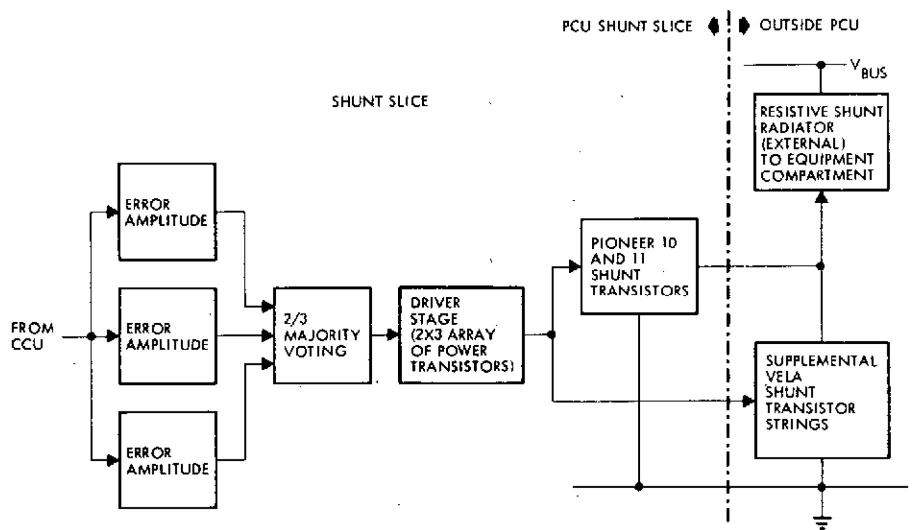

Figure 8.1D-7. Preferred Shunt Regulator Configuration

Table 8.1D-2. Shunt String Characteristics

	DSP	INTELSAT III	VELA V
NUMBER OF STRINGS PER ASSEMBLY	3	2	1
WEIGHT PER ASSEMBLY [KG (LB)]	1.77 (3.9)	0.68 (1.5)	0.36 (0.8)
TYPE OF HEAT REJECTION	RADIATION	CONDUCTION	CONDUCTION
DRIVERS INCLUDED (NOT REQUIRED)	YES	YES	NO
POWER DISSIPATION/ STRING (T_{BP} = 85°C) (WATTS)	25	25	25

3.4 DSP or Intelsat III Shunt Element Assembly

Candidate shunt element assemblies (SEA's) which are available and could be used are the DSP SEA and the Intelsat III SEA. Their characteristics are compared in Table 8.1D-2. These assemblies would be substituted for the Pioneer 10 and 11 power transistors mounted on the sides of the shunt slice housing. Then, the driver stage would be driving the external shunt transistors as shown in Figure 8.1D-8.

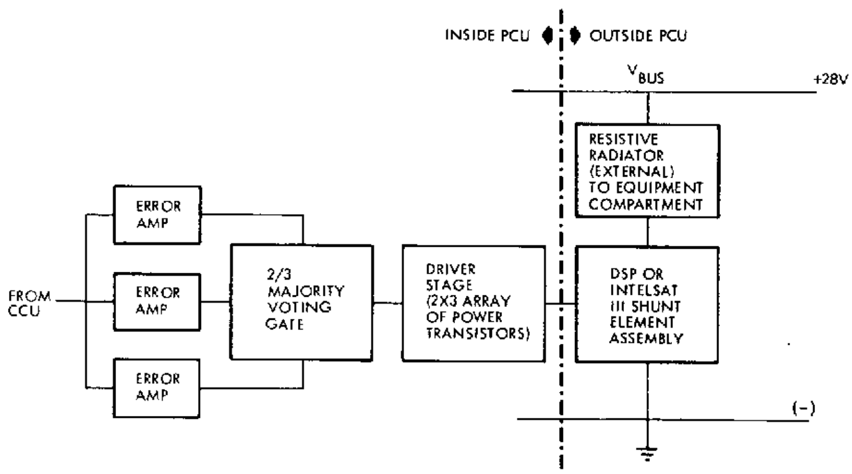

Figure 8.1D-8. DSP or Intelsat III Sea with Pioneer 10 and 11 Shunt Driver

4. CONCLUSIONS

For comparison, two cases are considered in Table 8.1D-3 based on the following assumptions:

Maximum dissipation required	200 watts (power transistors plus external radiator)
Redundancy	2/3

Based on this comparison, the Vela V option appears to be the most attractive. However, the convenience of heat rejection would most likely be the determining factor.

All these designs (Pioneer, Vela V, DSP, and Intelsat III) use the same basic shunt transistor string. A convenient relationship between baseplate temperature and power dissipated in the string is

$$T_{BP} = 125 - 1.5\, P_D$$

where

P_D = string power in watts (neglecting lower transistor)

T_{BP} = baseplate temperature in ^oC.

From this, a tradeoff can be made between the number of strings, power per string, and baseplate temperature. However, P_D should be limited to 50 watts, maximum.

Table 8.1D-3. Shunt String Comparison

	DSP	VELA V
NUMBER OF ASSEMBLIES REQUIRED	1	3
WEIGHT [KG (LB)]	1.54 (3.4)*	1.09 (2.4)
DEVELOPMENT COST ($K)	SOME	NONE
MANUFACTURING COST PER SPACECRAFT ($K)	7	6
MAXIMUM POWER PER STRING (ONE FAILED OPEN) (WATTS)	25	25

*ASSUMES 0.23 KG (0.5 LB) DECREASE FOR DELETION OF DRIVER STAGES

5. PREFERRED ATLAS/CENTAUR PROBE BUS SHUNT SIZING A/C IV

The probe bus degraded and undegraded array I-V characteristics are shown in Figure 8.1D-9. Superimposed are constant power load

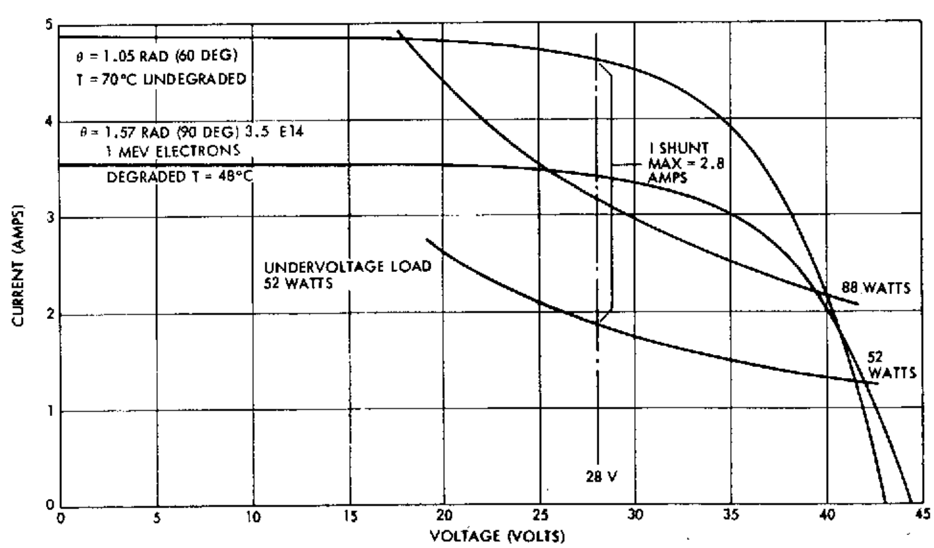

Figure 8.1D-9. Preferred Atlas/Centaur Probe Bus Solar Array Characteristics 106.96 Gigameters (0.715 AU), N_P = 54 N_S = 88, 0.39 RAD (22.5 DEG) Cone, Version IV Science

A/C IV lines for 88- and 52-watt loads. The worst case shunt current is 2.8 amperes. The Pioneers 10 and 11 shunt driver slice in the PCU can be used as is. The shunt radiator resistance is increased to 9.1 ohms to decrease the peak shunt driver slice dissipation to 24 watts, as shown in Figure 8.1D-10 (on Pioneers 10 and 11 the peak shunt slice dissipation was 40 watts).

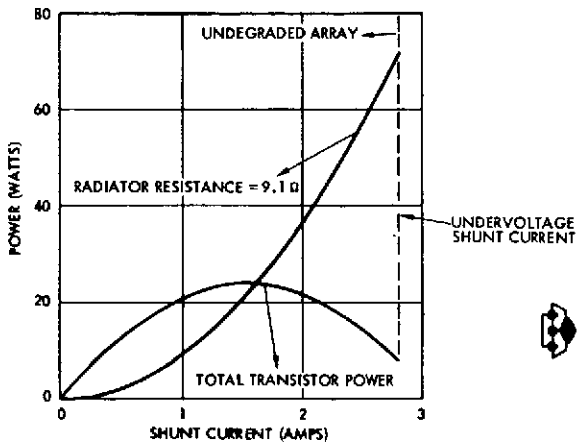

A/C IV

Figure 8.1D-10. Version IV Science Atlas/Centaur Probe Bus Shunt Dissipation Uses Pioneer 10 and 11 Shunt Driver As-Is; Change Shunt Radiator Resistance to 9.1 Ω

6. PREFERRED ATLAS/CENTAUR ORBITER SHUNT SIZING A/C IV

Figure 8.1D-11 shows the degraded and undegraded solar array I-V current-voltage characteristics at Venus. The load lines show that the difference between the full load (182 watts) and undervoltage load is quite large. When the undegraded array characteristic is used, the maximum shunt current is 7.2 amperes. This exceeds the Pioneers 10 and 11 shunt driver capability.

In Section 3.3 it was shown that the Vela V type shunt string can be added to the present Pioneers 10 and 11 power transistor strings to increase the shunt current capability. Figure 8.1D-12 shows the design for the orbiter shunt. Two Vela V supplemental shunt strings provide the required shunt capability. Note that the PCU shunt driver power dissipation is only 46.5 watts (6.5 watts higher than Pioneers 10 and 11). The supplemental shunt string dissipation is 15.5 watts with one of five strings failed. The shunt radiator resistance is reduced to 3.5 ohms to handle the higher shunt current.

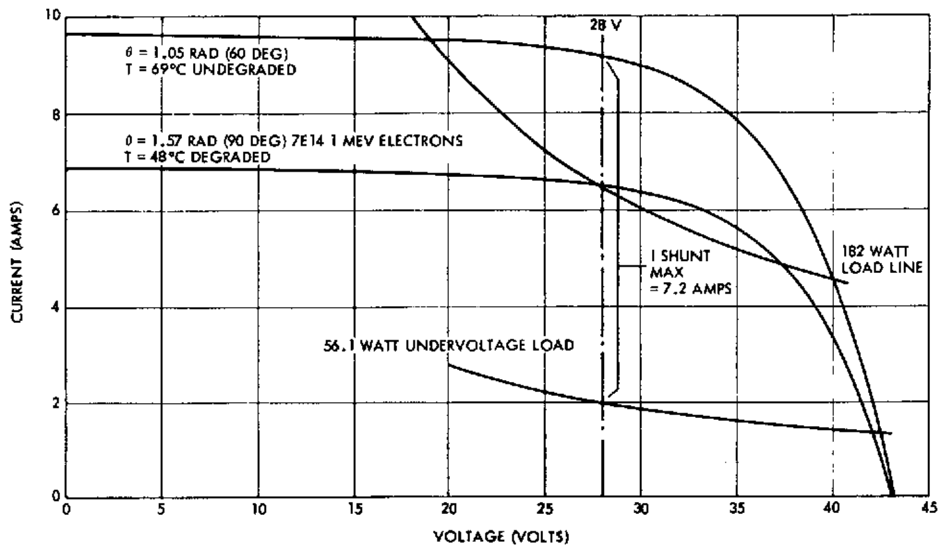

Figure 8.1D-11. Preferred Atlas/Centaur Orbiter Solar Array Characteristics 106.96 Gigameters (0.715 AU), N_P = 108 N_S = 88, 0.39 RAD (22.5 DEG) Cone, Version IV Science

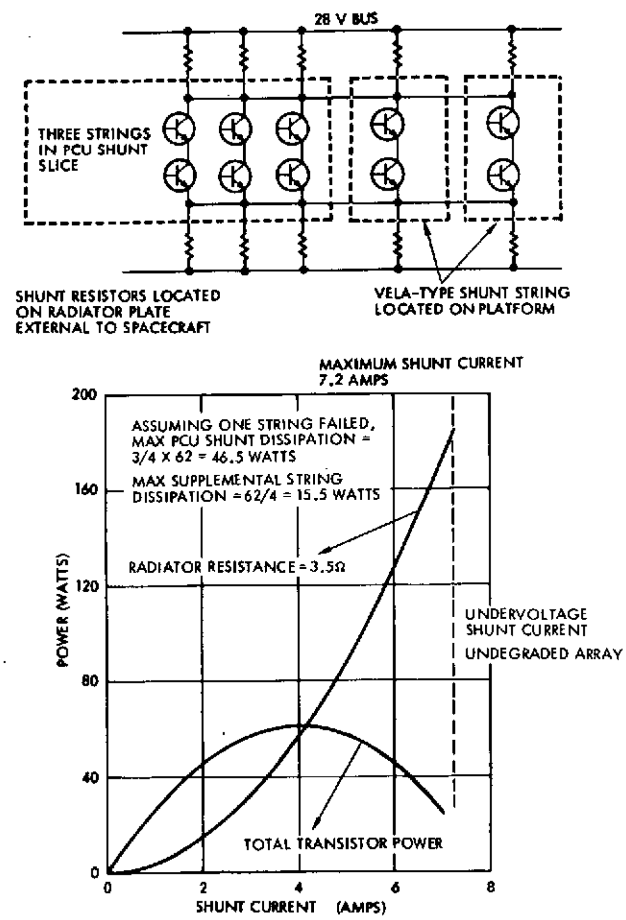

Figure 8.1D-12. Version IV Science Atlas/Centaur Orbiter Shunt Dissipation (Three Transistor Strings Inside PCU Plus Two Supplemental Vela Shunt Strings on Platform)

APPENDIX 8. 1E

SOLAR ARRAY DETAILED DESIGN INFORMATION

APPENDIX 8.1E

SOLAR ARRAY DETAILED DESIGN INFORMATION

This appendix contains raw data used as inputs to the solar array computer program (AM-142), including sun angle as a function of time, temperature versus astronomical units (AU)* and sun angle, albedo heat inputs, and temperature as a function of time near periapsis. The output data provides array I-V characteristics as a function of sun angle and AU* for degraded and undegraded cases. Included is the Atlas/Centaur preferred version with the Version IV science complement and Thor/Delta versions with pre-Version IV science. The array data presented compares cylinders and cones.

1. CONICAL ARRAY PROJECTED AREA ALL CONFIGURATIONS

Figure 8.1E-1 shows the ratio of the projected area (effective) to the total array area (actual) as a function of sun angle for cones of various half angles and a cylinder. The curves show that the conical array projected area is nearly constant as a function of sun angle for half cone angles near 0.35 radian (20 degrees).

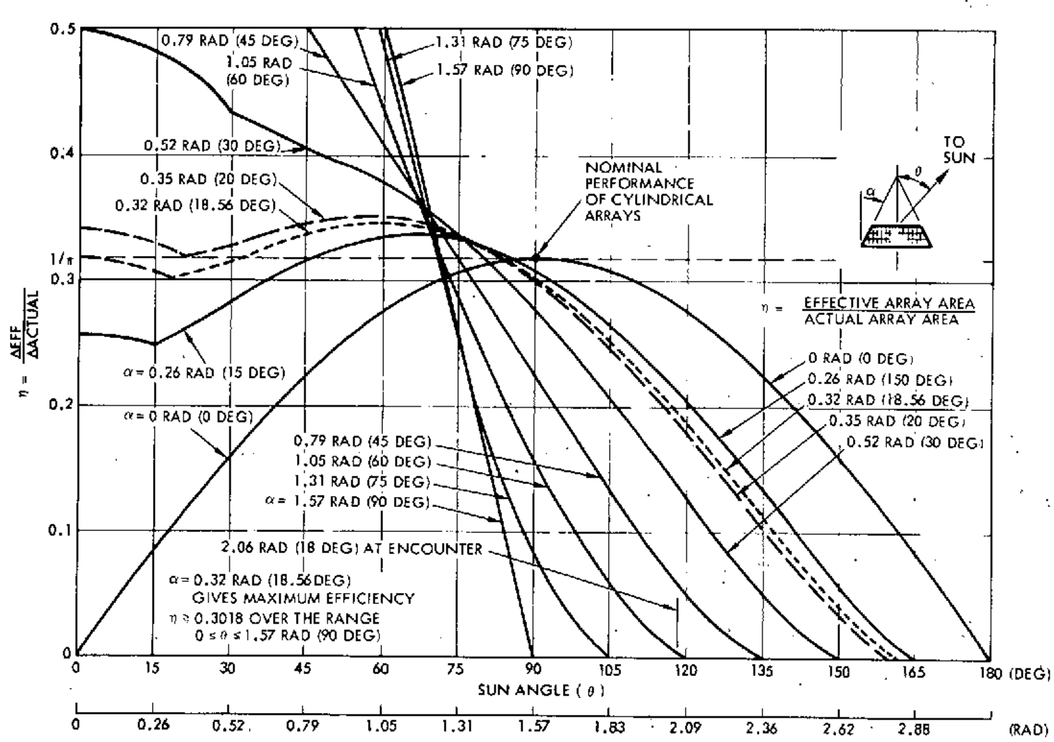

Figure 8.1E-1. Areal Efficiency of Conical Solar Arrays on Spinning Spacecraft

*1 AU = 1.5×10^{11} meter.

2. EARTH POINTING 1978 MISSIONS

2.1 Sun Angle History

Figure 8.1E-2 shows the probe bus sun angle variation as a function of mission time. The sun angle changes from 0.35 radian (20 degrees) at launch to approximately 1.08 radians (62 degrees) at bus entry into the Venus atmosphere. Calculations of array power as a function of time include this sun angle variation.

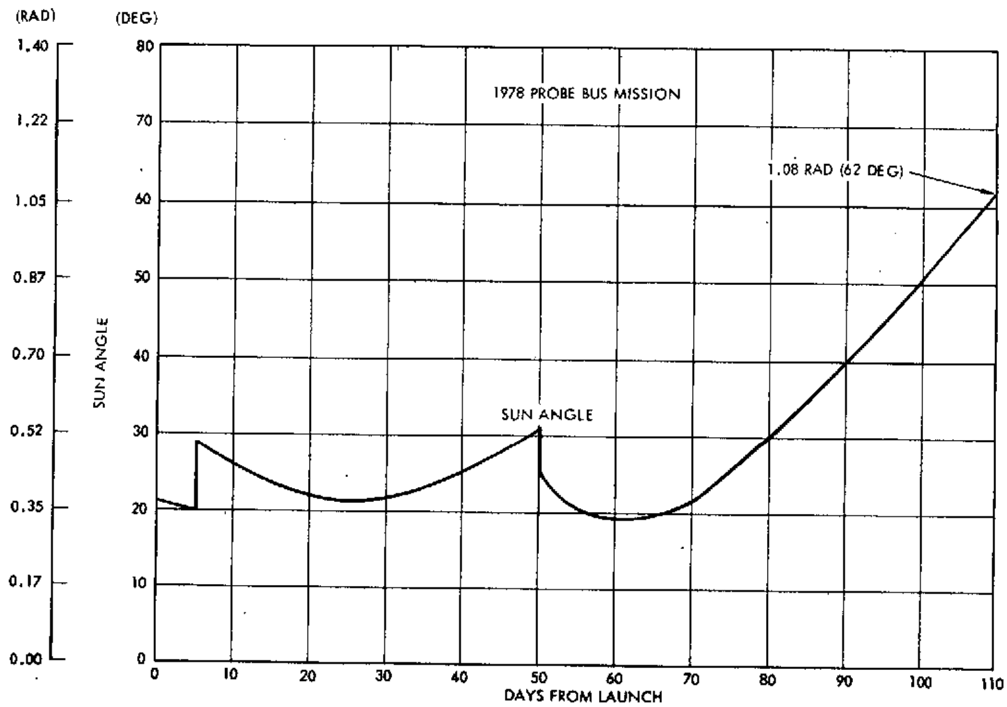

Figure 8.1E-2. Probe Bus Sun Angle as a Function of Mission Time

The earth-pointing orbiter sun angle is shown in Figure 8.1E-3. The sun angle ranges from 0.09 to 1.57 radians (5 to 90 degrees) over the 425-day nominal mission. "Flipping" the spacecraft precludes sun angles of greater than 1.57 radians (90 degrees).

2.2 Array Temperature

The Atlas/Centaur probe bus solar array temperature as a function of AU and sun angle is shown in Figure 8.1E-4. The array temperature at 134.64 gigameters (0.9 AU) considers the effect of the probes while the temperature at 106.96 gigameters (0.715 AU) is calculated for after probe release. Array temperature for the orbiter is shown in Figure 8.1E-5.

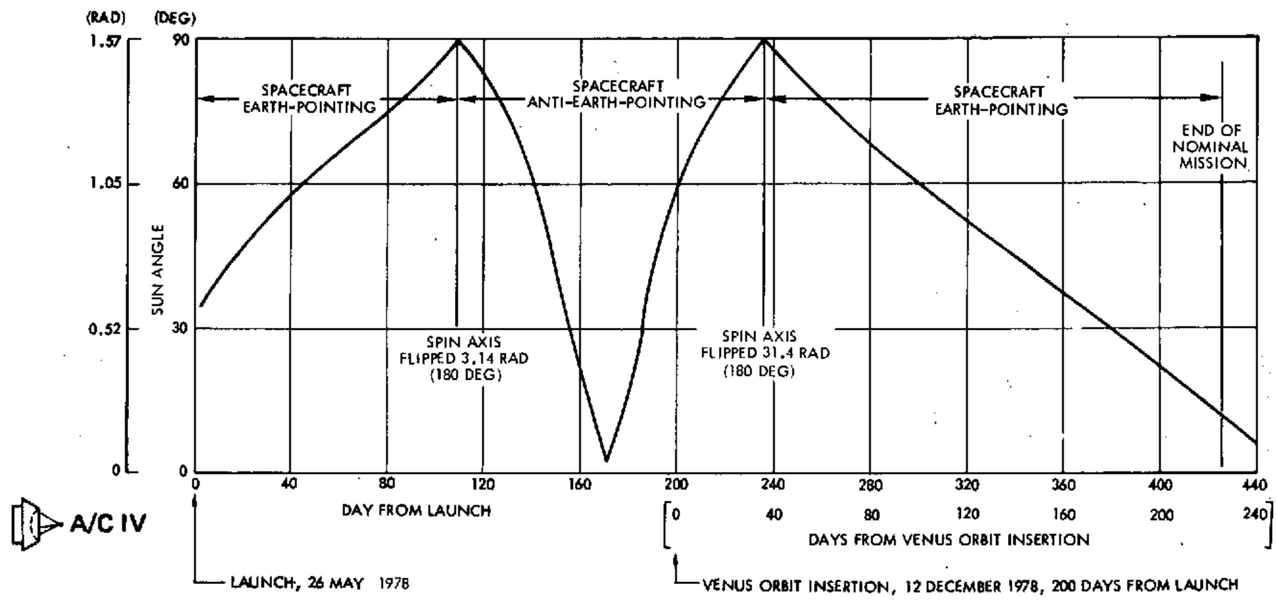

Figure 8.1E-3. Pioneer Venus Orbiter Mission Spacecraft Sun Aspect Profile

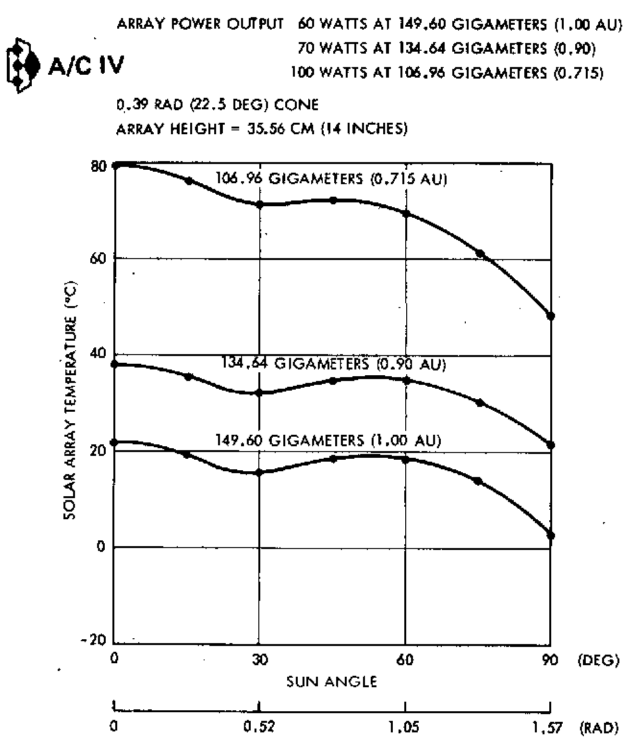

Figure 8.1E-4. Probe Bus Solar Array Temperature, Version IV Science Atlas/Centaur

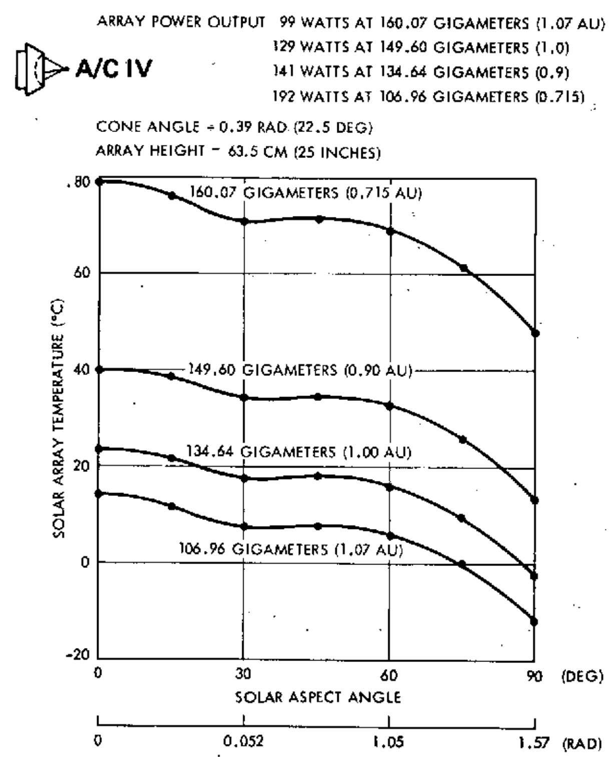

Figure 8.1E-5. Orbiter Solar Array Temperature Version IV Science Atlas/Centaur

2.3 Array Characteristics

Tables 8.1E-1 and 8.1E-2 contain probe bus and orbiter array I-V characteristic data for various sun angles and solar distances (undegraded

Table 8.1E-1. Atlas/Centaur Probe Bus Version IV Science Array Data

SUN ANGLE [RAD (DEG)]	TEMPERATURE (°C)	POWER AT 28 VOLTS (W)	MAXIMUM POWER (W)	VOLTAGE AT MAXIMUM POWER (V)	OPEN CIRCUIT VOLTAGE (V)	SHORT CIRCUIT CURRENT (A)
0.39 RADIAN (22.5-DEGREE) CONE, 106.96 GIGAMETERS (0.715 AU), 54 PARALLEL BY 88 SERIES DEGRADED (3.5E14-1 MEV)						
0 (0)	79	104	105	27	35	4.53
0.26 (15)	76	103	103	28	37	4.38
0.52 (30)	71	107	107	30	39	4.30
0.79 (45)	72	111	113	30	40	4.45
1.05 (60)	70	111	113	30	40	4.40
1.31 (75)	60	107	113	32	42	4.10
1.57 (90)	48	95.5	106	34	44	3.56
1.83 (105)	2	77.0	96.5	39	49	2.79
0.39 RADIAN (22.5-DEGREE) CONE, 106.96 GIGAMETERS (0.715 AU), 54 PARALLEL BY 88 SERIES, UNDEGRADED						
0 (0)	79	127	129	30	38	4.97
0.26 (15)	76	124	127	30	40	4.81
0.52 (30)	71	125	133	32	42	4.73
0.79 (45)	72	129	139	33	42	4.88
1.05 (60)	70	129	140	33	43	4.82
1.31 (75)	60	122	139	35	45	4.50
1.57 (90)	48	107	131	38	47	3.90
1.83 (105)	2	85	119	43	52	3.06
0.39 RADIAN (22.5-DEGREE) CONE, 149.60 GIGAMETERS (1.0 AU), 54 PARALLEL BY 88 SERIES, UNDEGRADED						
0.38 (22)	16	64.6	86	41	51	2.33
0.39 RADIAN (22.5-DEGREE) CONE, 149.60 GIGAMETERS (1.0 AU), 54 PARALLEL BY 88 SERIES, DEGRADED (1.7E14-1MEV)						
0.38 (22)	16	60.4	74.7	38	49	2.21

Table 8.1E-2. Atlas/Centaur Orbiter/Version IV Science Array Data

SUN ANGLE [RAD (DEG)]	TEMPERATURE (°C)	POWER AT 28 VOLTS (W)	MAXIMUM POWER (W)	VOLTAGE AT MAXIMUM POWER (V)	OPEN CIRCUIT VOLTAGE (V)	SHORT CIRCUIT CURRENT (A)
0.39 RADIAN (22.5-DEGREE) CONE, 106.96 GIGAMETERS (0.715 AU), 108 PARALLEL BY 88 SERIES, 182 WATTS, DEGRADED (7E14-1 MEV)						
0 (0)	79	194.4	196	27	35	8.70
0.26 (15)	76	193	193	28	37	8.41
0.52 (30)	71	201	202	29	39	8.26
0.79 (45)	72	211	211	29	39	8.54
1.05 (60)	69	211	214	30	40	8.43
1.31 (75)	62	202	210	31	41	7.87
1.57 (90)	48	182	198	34	43	6.83
1.83 (105)	2	147	181	38	48	5.36
0.39 RADIAN (22.5-DEGREE) CONE, 106.96 GIGAMETERS (0.715 AU), 108 PARALLEL BY 88 SERIES, 182 WATTS, UNDEGRADED						
0 (0)	79	253	257	30	38	9.91
0.26 (15)	76	247	253	30	40	9.58
0.52 (30)	71	249	265	32	42	9.42
0.79 (45)	72	258	277	33	42	9.73
1.05 (60)	69	257	280	34	43	9.61
1.31 (75)	62	243	275	35	44	8.79
1.57 (90)	48	214	260	38	47	7.79
1.83 (105)	2	170	237	43	52	6.10
0.39 RADIAN (22.5-DEGREE) CONE, 160.07 GIGAMETERS (1.07 AU), 108 PARALLEL BY 88 SERIES, 182 WATTS, UNDEGRADED						
1.17 (67)	4	111	159	44	53	3.99
0.48 RADIAN (27.5-DEGREE) CONE, 160.07 GIGAMETERS (1.07 AU), 108 PARALLEL BY 88 SERIES, 182 WATTS, DEGRADED (3.5E14-1 MEV)						
1.17 (67)	4	100	130	40	50	3.64

and degraded). Cell performance is based upon data from JPL technical memorandum 33-473, "Measured Performance of Silicon Solar Cell Assemblies Designed for use at High Solar Intensities," 15 March 1971. The raw data was smoothed for input to the AM-142 computer program.

2.4 Orbiter Earth Pointer Sunlit Periapsis Pass A/C IV

The thermal data for the sunlit periapsis pass is shown in Figures 8.1E-6 and 8.1E-7. The sun angle of 0.59 radian (34 degrees) is taken from Figure 8.1E-3 (165 days after orbital insertion). Table 8.1E-3 contains the computer sunlit periapsis pass array characteristics.

A/C IV

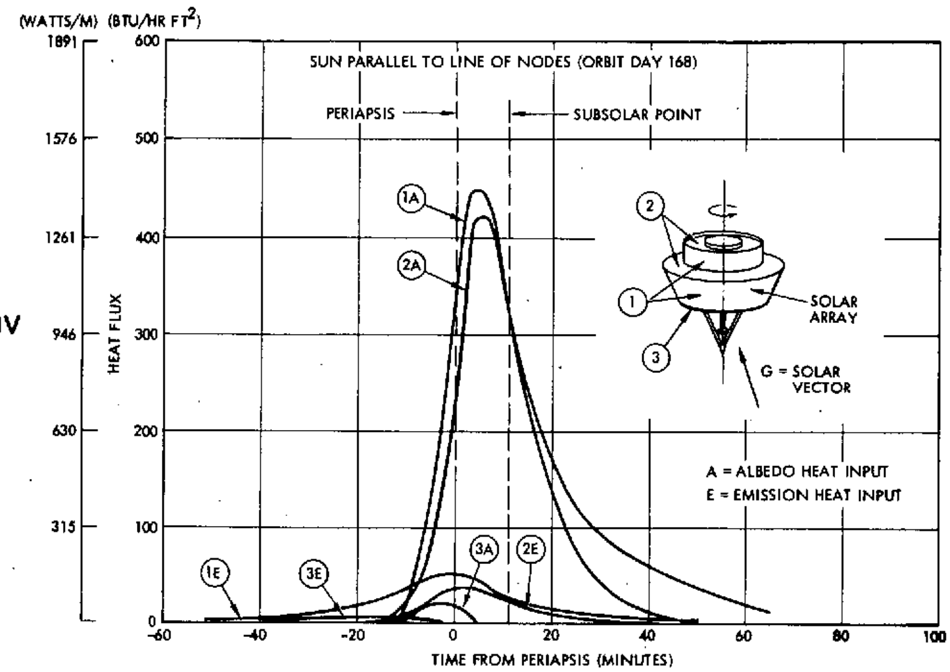

Figure 8.1E-6. Venus Input During Orbit, Atlas/Centaur Earth-Pointer, θ = 0.59 rad (34 deg)

3. PRE-VERSION IV SCIENCE

ALL VERSION III SCIENCE PAYLOAD

3.1 Sun Angle History 31 W A/C III 31 W T/D III

The Option 2 fanbeam/fanscan orbiter spin axis orientation is normally perpendicular to the sun line [0.05 radian (±3 degrees)] except during periapsis maintenance, ΔV, and orbit insertion maneuvers.

3.2 Array Temperature 31 W A/C III 31 W T/D III

Solar array temperature for conical and cylindrical arrays is shown in Figure 8.1E-8 as a function of sun angle and solar distance. The data is for a 1.02-meter (40-inch) high array.

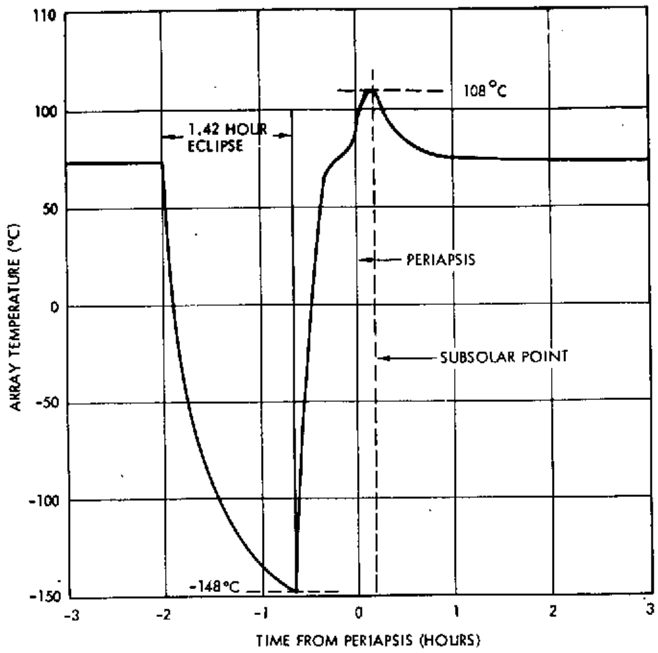

Figure 8. 1E-7. Solar Array Temperature Near Periapsis, Atlas/Centaur Earth-Pointer, = 0.59 RAD (34 DEG)

Table 8. 1E-3. Preferred Atlas/Centaur Orbiter (Earth Pointer) Sunlit Periapsis Pass, θ = 0.59 rad (34 deg) 7E14-1 MeV Electrons (Albedo Contribution to Array Power Output Not Included)

TIME FROM PERIAPSIS (MIN)	ARRAY TEMPERATURE (°C)	POWER AT 28 VOLTS (W)	POWER AT MAXIMUM POWER (W)	VOLTAGE AT MAXIMUM POWER (V)	OPEN CIRCUIT VOLTAGE (V)	SHORT CIRCUIT CURRENT (A)
-30	-12	215	306	44	54	7.74
-24	49	218	234	33	43	8.23
-18	69	206	208	30	39	8.34
-12	75	200	200	28	38	8.37
-6	81	192	192	27	37	8.40
0 (PERIAPSIS)	94	163	174	25	34	8.46
+6	108	112	155	23	32	8.51
+12	104	129	160	23	33	8.5
+18	96	157	171	25	34	8.47
+24	89	176	181	26	35	8.44
+30	84	187	188	27	36	8.42
+36	82	190	191	27	37	8.41
+60	76	199	199	28	38	8.38
+108	74	201	202	29	38	8.37

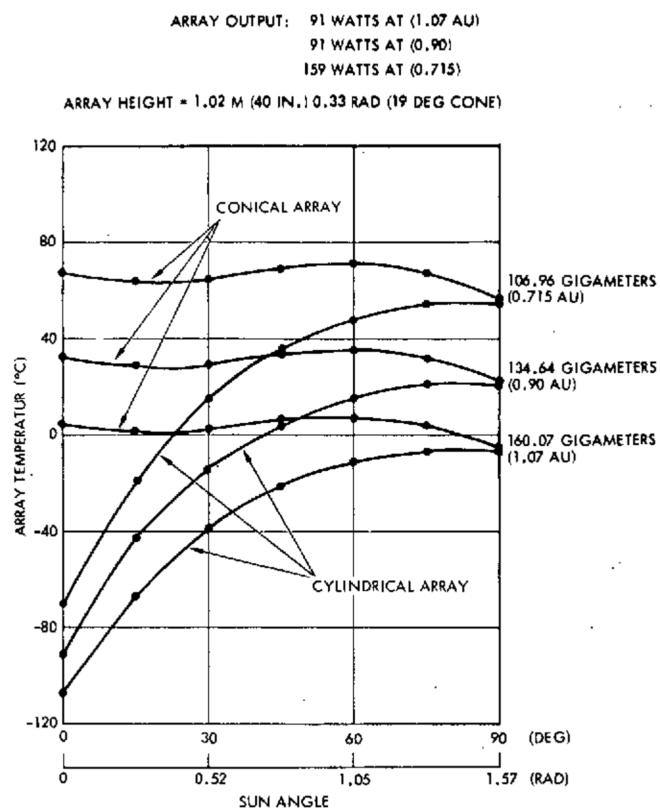

Figure 8. 1E-8. Solar Array Temperature

3. 3 Array Characteristics

Table 8. 1E-4 contains array I-V current-voltage data as a function of sun angle and solar distance for the fanbeam/fanscan, Thor/Delta and Atlas/Centaur versions. Data are shown for 0. 33-radian (19-degree) conical and cylindrical arrays. The Atlas/Centaur 276-watt conical array data is for 180 parallel by 77 series cells. Figure 8. 1E-9 shows that this configuration falls slightly below the 276-watt requirement at 1. 66 radians (95 degrees). If 186 parallel by 77 series cells are used, then the 276-watt requirement is exceeded. Hence, the data for the Atlas/Centaur 276-watt configuration in Table 8. 1E-4 should be scaled up by the ratio 186/180.

3.4 Sunlit Periapsis Pass Data

The solar array temperature for the hot periapsis pass is shown in Figure 8. 1E-10 for conical and cylindrical arrays. Table 8. 1E-5 contains array I-V characteristic data as a function of time from periapsis.

Table 8.1E-4. Orbiter Solar Array Characteristics, Conical Array

SUN ANGLE [RAD (DEG)]	TEMPERATURE (°C)	POWER AT 28 VOLTS (W)	MAXIMUM POWER (W)	VOLTAGE AT MAXIMUM POWER (V)	OPEN CIRCUIT VOLTAGE (V)	SHORT CIRCUIT CURRENT (A)
THOR/DELTA 0.33 RADIAN (19-DEGREE) CONE 160.07 GIGAMETERS (1.07 AU), 150 PARALLEL BY 77 SERIES, 225.7 WATTS, UNDEGRADED						
0 (0)	4	131.0	154.0	36	43	4.78
0.26 (15)	2	127.6	149.4	36	45	4.65
0.54 (30)	4	136.3	165.5	37	46	4.94
0.79 (45)	6	147.6	180.5	37	46	5.34
1.05 (60)	7	150.8	185.4	38	46	5.46
1.31 (75)	4	145.2	181.1	38	46	5.25
1.59 (90)	-4	129.7	167.1	39	48	4.67
1.83 (105)	-22	105.5	143.3	42	50	3.79
THOR/DELTA 0.33 RADIAN (19-DEGREE) CONE 160.07 GIGAMETERS (1.07 AU), 150 PARALLEL BY 77 SERIES, 225.7 WATTS, DEGRADED (5.8E 13-1 MEV)						
0 (0)	4	126.8	144.3	35	42	4.64
0.26 (15)	2	123.5	140.5	35	44	4.53
0.54 (30)	4	132.1	155.5	36	45	4.82
0.79 (45)	6	143.2	169.6	36	45	5.21
1.05 (60)	7	146.4	174.0	36	45	5.33
1.31 (75)	4	141.0	170.0	37	45	5.11
1.57 (90)	-4	126.1	156.9	38	47	4.55
1.83 (105)	-22	102.6	134.8	40	49	3.69
ATLAS/CENTAUR 0.33 RADIAN (19-DEGREE) CONE 160.07 GIGAMETERS (1.07 AU), 180 PARALLEL BY 77 SERIES, 276 WATTS, DEGRADED (5.8E 13-1 MEV)						
0 (0)	4	152.2	173.2	35	42	5.57
0.26 (15)	2	148.3	168.7	35	44	5.44
0.54 (30)	4	158.5	186.6	36	45	5.79
0.79 (45)	6	171.9	203.5	36	45	6.25
1.05 (60)	7	175.6	208.9	36	45	6.39
1.31 (75)	4	169.2	204.0	37	45	6.14
1.57 (90)	-4	151.3	188.3	38	47	5.47
1.83 (105)	-22	123.1	161.8	40	49	4.43
THOR/DELTA 0.33 RADIAN (19-DEGREE) CONE 106.96 GIGAMETERS (0.715 AU), 150 PARALLEL BY 77 SERIES, 225.7 WATTS, UNDEGRADED						
0 (0)	67	265	265	28	35	11.0
0.26 (15)	64	265	265	28	37	10.8
0.54 (30)	64	294	297	29	37	11.5
0.79 (45)	69	313	314	29	37	12.5
1.05 (60)	71	318	318	29	37	12.7
1.31 (75)	67	311	314	30	38	12.2
1.57 (90)	57	291	303	31	39	11.0
1.83 (105)	40	247	274	34	42	9.07
THOR/DELTA 0.33 RADIAN (19-DEGREE) CONE 106.96 GIGAMETERS (0.715 AU), 150 PARALLEL BY 77 SERIES, 225.7 WATTS, DEGRADED (7E 14-1 MEV)						
0 (0)	67	177	201	25	31	9.66
0.26 (15)	64	188	203	25	34	9.51
0.54 (30)	64	220	226	26	34	10.1
0.79 (45)	69	229	239	26	34	10.9
1.05 (60)	71	231	242	26	34	11.1
1.31 (75)	67	234	239	26	35	10.1
1.57 (90)	57	231	231	28	36	9.66
1.83 (105)	40	205	209	30	39	7.16
ATLAS/CENTAUR 0.33 RADIAN (19-DEGREE) CONE 106.96 GIGAMETERS (0.715 AU), 180 PARALLEL BY 77 SERIES, 276 WATTS, DEGRADED (7E 14-1 MEV)						
0 (0)	67	212	242	25	31	11.5
0.26 (15)	64	226	244	25	34	11.4
0.54 (30)	64	264	271	26	34	12.1
0.79 (45)	69	276	287	26	34	13.1
1.05 (60)	71	278	296	26	35	13.4
1.31 (75)	67	281	287	26	35	12.9
1.57 (90)	57	277	277	28	36	15.9
1.83 (105)	40	246	250	30	39	9.55

Table 8.1E-4. Orbiter Solar Array Characteristics, Conical Array (Continued)

SUN ANGLE [RAD (DEG)]	TEMPERATURE (°C)	POWER AT 28 VOLTS (W)	MAXIMUM POWER (W)	VOLTAGE AT MAXIMUM POWER (V)	OPEN CIRCUIT VOLTAGE (V)	SHORT CIRCUIT CURRENT (A)
THOR/DELTA CYLINDER, 160.07 GIGAMETERS (1.07 AU), 138 PARALLEL BY 77 SERIES, 227 WATTS, DEGRADED (5.8E 13-1 MEV)						
0 (0)	-107	0	0	0	0	0
0.26 (15)	-67	23.4	31.1	42	53	0.85
0.54 (30)	-39	55.1	73.6	41	51	1.98
0.79 (45)	-22	83.9	109.2	40	49	3.02
1.05 (60)	-11	105.3	133.7	39	47	3.8
1.31 (75)	-7	118.2	149.0	39	47	4.27
1.58 (90)	-7	122.0	154.4	38	47	4.42
1.83 (105)	-7	118.2	149.0	39	47	4.27
THOR/DELTA CYLINDER, 160.07 GIGAMETERS (1.07 AU), 138 PARALLEL BY 77 SERIES, 227 WATTS, UNDEGRADED						
0 (0)	-107	0	0	0	0	0
0.26 (15)	-67	24.1	33.1	44	54	0.87
0.54 (30)	-39	56.6	78.2	42	52	2.03
0.79 (45)	-22	86.2	116.1	41	50	3.10
1.05 (60)	-11	108.0	142.2	40	48	3.89
1.31 (75)	-7	121.6	158.7	40	48	4.37
1.57 (90)	-7	125.9	164.8	40	48	4.53
1.83 (105)	-7	121.0	158.7	40	48	4.37
ATLAS/CENTAUR CYLINDER, 160.07 GIGAMETERS (1.07 AU), 168 PARALLEL BY 77 SERIES, 276 WATTS, DEGRADED (5.8E 13-1 MEV)						
0 (0)	-107	0	0	0	0	0
0.26 (15)	-67	28.5	37.9	42.0	53	1.03
0.52 (30)	-39	67.1	89.6	41.0	51	2.41
0.79 (45)	-22	102.0	133.0	40.0	49	3.68
1.05 (60)	-11	128.2	162.7	39.0	47	4.62
1.31 (75)	-7	143.9	181.4	39.0	47	5.19
1.57 (90)	-7	149.0	188.4	39.0	47	5.38
1.83 (105)	-7	143.9	181.4	39.0	47	5.19
ATLAS/CENTAUR CYLINDER, 106.96 GIGAMETERS (0.715 AU), 168 PARALLEL BY 77 SERIES, 276 WATTS, DEGRADED (7E 14-1 MEV)						
0 (0)	-70	0	0	0	0	0
0.26 (15)	-19	62.5	71.9	35	45	2.29
0.52 (30)	15	140	150	33	41	5.23
0.79 (45)	35	206	212	31	39	7.9
1.05 (60)	48	247	248	29	37	9.86
1.31 (75)	54	269	269	28	37	11.0
1.57 (90)	54	278	278	28	37	11.4
1.83 (105)	54	269	269	28	37	11.0
THOR/DELTA CYLINDER, 106.96 GIGAMETERS (0.715 AU), 138 PARALLEL BY 77 SERIES, 227 WATTS, DEGRADED (7E 14-1 MEV)						
0 (0)	-70	0	0	0	0	0
0.26 (15)	-19	51	59	35	45	1.88
0.52 (30)	15	115	123	33	41	4.30
0.79 (45)	35	169	174	31	39	6.49
1.05 (60)	48	203	204	29	37	8.10
1.31 (75)	54	221	221	28	37	9.06
1.57 (90)	54	228	228	28	39	9.36
1.83 (105)	54	221	221	28	37	9.06
THOR/DELTA CYLINDER, 106.96 GIGAMETERS (0.715 AU), 138 PARALLEL BY 77 SERIES, 227 WATTS, UNDEGRADED						
0 (0)	-70	0	0	0	0	0
0.26 (15)	-19	60	77	40	48	2.15
0.52 (30)	15	135	161	36	45	4.9
0.79 (45)	35	202	228	34	42	7.39
1.05 (60)	48	249	267	33	41	9.23
1.31 (75)	54	275	290	32	40	10.3
1.57 (90)	54	284	300	31	40	10.6
1.83 (105)	54	275	290	32	40	10.3

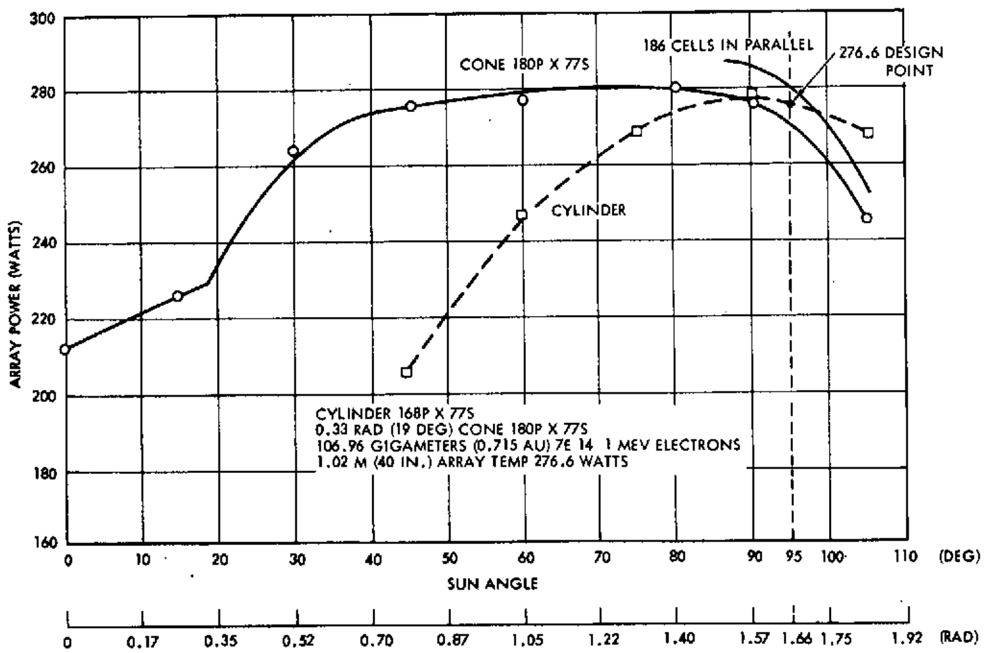

Figure 8.1E-9. Orbiter Array Power Versus Sun Angle 276.6 Watt Atlas/Centaur

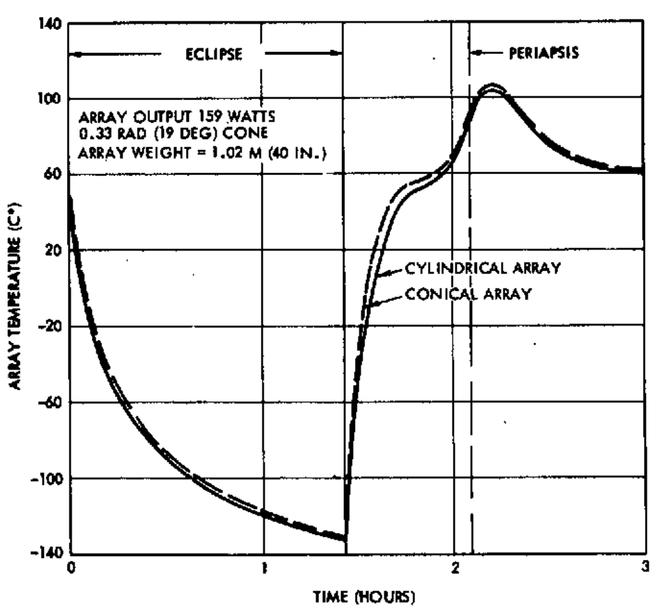

Figure 8.1E-10. Solar Array Temperature History Near Periapsis

4. CONE ANGLE SELECTION

Figure 8.1E-11 shows array power output as a function of cone angle for the spin-axis-perpendicular and earth-pointing configurations. At the study midterm briefing, a 0.33-radian (19-degree) cone angle was selected as the best compromise for the orbiter (spin-axis-perpendicular)

Table 8.1-5. Thor/Delta Orbiter (225.7 Watts), Hot Periapsis Pass Data, Sun Angle = 1.57 rad (90 deg)

TIME FROM PERIAPSIS (MIN)	ARRAY TEMPERATURE (°C)	POWER AT 28 VOLTS (W)	POWER AT MAXIMUM POWER (W)	VOLTAGE AT MAXIMUM POWER (V)	OPEN CIRCUIT VOLTAGE (V)	SHORT CIRCUIT CURRENT (A)
0.33 RADIAN (19-DEGREE) CONE, 150 PARALLEL BY 77 SERIES						
-12	59	227.4	227.6	27	36	9.67
-8	64	217.9	220.4	27	35	10.13
-4	74	191.4	218.7	24	32	10.85
0	91	153.2	281.4	22	31	15.43
4	105	25.7	276.8	20	28	16.9
8	108	9.54	252.7	19	28	15.9
12	98	70.6	239.5	21	30	14.1
20	85	148.7	222.4	23	32	11.9
30	71	202.9	232.2	25	34	10.8
40	65	215.0	220.0	26	35	10.3
80	60	225.7	226.3	27	36	9.67
CYLINDER, 138 PARALLEL BY 77 SERIES						
-12	55	227.2	227.2	28	37	9.36
-8	60	220.0	220.6	27	36	9.91
-4	71	202.3	222.3	25	34	10.72
0	89	186.7	291.7	23	31	15.62
4	102	66.4	286.2	21	29	16.89
8	104	38.6	270.7	20	29	16.29
12	103	41.9	235.2	20	29	14.32
20	82	170.9	230.0	23	32	11.96
30	69	209.0	225.6	25	34	10.72
40	63	214.5	218.7	26	35	10.04
80	62	216.4	217.5	27	36	9.39

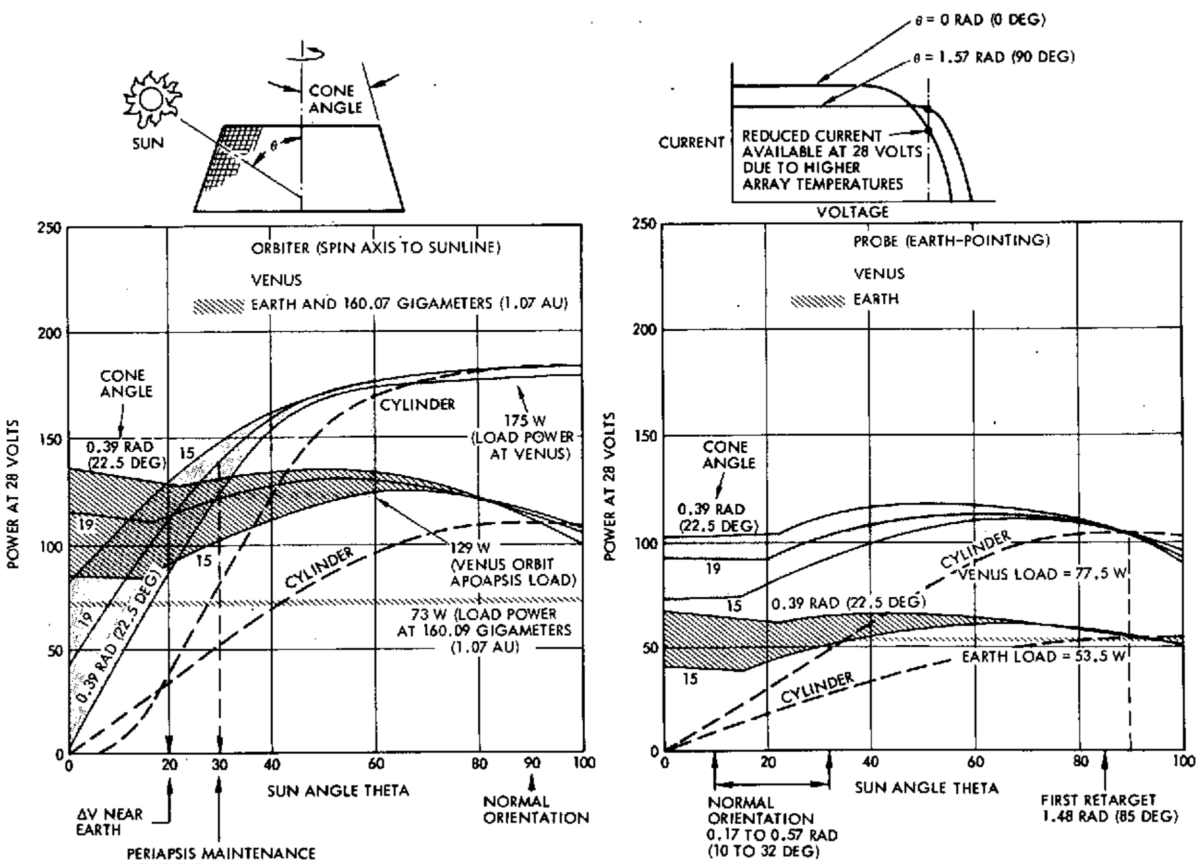

Figure 8.1E-11. Solar Array Cone Angle Trade

and probe bus (earth-pointing) missions. The preferred Atlas/Centaur spacecraft configuration is two earth pointers. The right-hand graph in Figure 8.1E-11 shows that a cone angle of 0.39 radian (22.5 degrees) provides nearly equal power at 0 and 1.57 radians (0 and 90 degrees). Therefore, 0.39 radian (22.5 degrees) was selected as the cone angle for the orbiter/probe bus earth-pointing missions. (The power levels shown in the figure are for the design as it existed during the mid-term presentation at NASA Ames).

APPENDIX 8.1F

ELECTRICAL POWER REQUIREMENTS

APPENDIX 8.1F

ELECTRICAL POWER REQUIREMENTS

The electrical power requirements for the various probe bus and orbiter configurations considered during the study are listed in the following tables. Estimated power consumption at the unit equipment level for several critical phases of the mission is also given. The following configurations are included.

Table	Configuration
8.1F-1	Probe Bus With Version IV Science (Preferred Atlas/Centaur Configuration)
8.1F-2	Orbiter With Version IV Science (Preferred Atlas/Centaur Configuration)
8.1F-3	Probe Bus With Version III Science (Preferred Thor/Delta Configuration)
8.1F-4	Orbiter With Version III Science, 31-Watt Transmitter, and Fanbeam/Fanscan Antennas (Preferred Thor/Delta Configuration)
8.1F-5	Probe Bus With Version III Science (Atlas/Centaur)
8.1F-6	Orbiter With Version III Science, 12-Watt Transmitter, and Fanbeam/Fanscan Antennas (Thor/Delta)
8.1F-7	Orbiter With Version III Science and Despun Reflector Antenna (Thor/Delta)
8.1F-8	Orbiter With Version III Science, 31-Watt Transmitter, and Fanbeam/Fanscan Antennas (Atlas/Centaur)
8.1F-9	Orbiter With Version III Science, 12-Watt Transmitter, and Fanbeam/Fanscan Antennas (Atlas/Centaur)
8.1F-10	Orbiter With Version IV Science, and Despun Reflector Antenna (Atlas/Centaur)

Table 8.1F-1. Probe Bus With Version IV Science (Preferred Atlas/Centaur Configuration)

PROBE BUS - 6W PA, A/C 11.16.28. 05/18/73.
ELECTRICAL POWER REQUIREMENTS

	1	2	3	4	5	6
SCIENCE						
NEUTRAL MASS SPECTROMETER	0.0	0.0	0.0	0.0	14.4	0.0
ION MASS SPECTROMETER	0.0	0.0	0.0	0.0	3.0	0.0
ELECTRON TEMP PROBE	0.0	0.0	0.0	0.0	3.6	0.0
UV SPECTROMETER	0.0	0.0	0.0	0.0	1.8	0.0
RETARDING POTENTIAL ANAL	0.0	0.0	0.0	0.0	3.0	0.0
SUBTOTAL	0.0	0.0	0.0	0.0	25.8	0.0
DATA HANDLING						
DIGITAL TELEMETRY UNIT	3.6	3.6	3.6	3.6	3.6	3.6
DIGITAL DECODER UNIT	.3	.3	.3	.3	.3	.3
SUBTOTAL	3.9	3.9	3.9	3.9	3.9	3.9
COMMUNICATIONS						
S-BAND RECEIVERS (2 ON)	3.4	3.4	3.4	3.4	3.4	3.4
S-BAND XMTR DRIVER	1.3	1.3	1.3	1.3	1.3	1.3
S-BAND PWR AMPL	22.0	22.0	22.0	22.0	22.0	22.0
SUBTOTAL	26.7	26.7	26.7	26.7	26.7	26.7
ACS/PROPULSION						
CONTROL ELECTR ASSY/SS	1.7	1.7	1.7	1.7	1.7	1.7
PRESSURE TRANSDUCER	.4	.4	.4	.4	.4	.4
SUBTOTAL	2.1	2.1	2.1	2.1	2.1	2.1
ELECTRICAL PWR/CONTROL						
PCU	4.0	4.0	4.0	4.0	4.0	4.0
COMMAND DISTRIBUTION UNIT	2.1	2.1	2.1	2.1	2.1	2.1
CONVERTER LOSSES (60 PCT)	8.1	8.1	8.1	8.1	8.1	8.1
SUBTOTAL	14.2	14.2	14.2	14.2	14.2	14.2
THERMAL						

Table 8.1F-1. Probe Bus With Version IV Science (Preferred Atlas/Centaur Configuration)(Continued)

PROPELLANT HEATERS	0.0	0.0	6.0	6.0	6.0	0.0
SUBTOTAL	0.0	0.0	6.0	6.0	6.0	0.0
SPACECRAFT SUBTOTAL 1	46.9	46.9	52.9	52.9	78.7	46.9
CABLE LOSSES (SPACECRAFT)	.9	.9	1.1	1.1	1.6	.9
BATTERY CHARGING	0.0	0.0	0.0	0.0	0.0	0.0
SPACECRAFT SUBTOTAL 2	47.8	47.8	53.9	53.9	80.2	47.8
SUBTOTAL 3 (LESS SCI)	47.8	47.8	53.9	53.9	54.4	47.8
CONTINGENCY (10 PCT)	4.8	4.8	5.4	5.4	5.4	4.8
TOTAL PRIMARY BUS LOAD	52.6	52.6	59.3	59.3	85.7	52.6
	1	2	3	4	5	6

1. LAUNCH,6W,NO SCI,NO HTR
2. TRANSIT,6W,CRUISE SCI ON,NO HTR
3. TRANSIT,6W,CRUISE SCI,HTR ON
4. TRANSIT,6W,CRUISE SCI,HTR
5. ENCOUNTER,6W,ALL SCI ON
6. UNDERVOLTAGE — NON-ESSENTIAL LOADS OFF

TAPE2=VBJXPP,TAPE4=CONV6AA,VENBJ1

Table 8.1F-2. Orbiter With Version IV Science (Preferred Atlas/Centaur Configuration)

ORBITER-6W PA EARTH PTR,A/C   11.16.39.   05/18/73.
ELECTRICAL POWER REQUIREMENTS

	1	2	3	4	5	6	7	8	9	10	11	12
SCIENCE												
MAGNETOMETER	0.0	4.8	4.8	4.8	4.8	4.8	4.8	4.8	4.8	0.0	0.0	0.0
SOLAR WIND ANALYZER	0.0	0.0	0.0	0.0	0.0	6.0	6.0	6.0	6.0	0.0	0.0	0.0
ELECTRON TEMPERATURE PROBE	0.0	0.0	0.0	0.0	0.0	3.0	3.0	3.0	3.0	0.0	0.0	0.0
NEUTRAL MASS SPECTROMETER	0.0	0.0	0.0	0.0	0.0	14.4	14.4	14.4	14.4	0.0	0.0	0.0
ION MASS SPECTROMETER	0.0	0.0	0.0	0.0	0.0	2.4	2.4	2.4	2.4	0.0	0.0	0.0
UV SPECTROMETER	0.0	0.0	0.0	0.0	0.0	7.2	7.2	7.2	7.2	0.0	0.0	0.0
IR RADIOMETER	0.0	0.0	0.0	0.0	0.0	7.2	7.2	7.2	7.2	0.0	0.0	0.0
X-BAND OCCULTATION	0.0	0.0	0.0	0.0	0.0	14.4	14.4	14.4	14.4	0.0	0.0	0.0
RADAR ALTIMETER	0.0	0.0	0.0	0.0	0.0	48.0	0.0	0.0	0.0	0.0	0.0	0.0
SUBTOTAL	0.0	4.8	4.8	4.8	4.8	107.4	59.4	59.4	59.4	0.0	0.0	0.0
DATA HANDLING												
DIGITAL TELEMETRY UNIT	3.9	3.9	3.9	3.9	3.9	3.9	3.9	3.9	3.9	3.9	0.0	0.0
DATA STORAGE UNIT	0.0	0.0	0.0	0.0	0.0	4.5	4.5	0.0	0.0	0.0	0.0	0.0
DIGITAL DECODER UNIT	.3	.3	.3	.3	.3	.3	.3	.3	.3	.3	0.0	0.0
SUBTOTAL	4.2	4.2	4.2	4.2	4.2	8.7	8.7	4.2	4.2	4.2	0.0	0.0
COMMUNICATIONS												
S-BAND RECEIVERS (2 ON)	7.0	7.0	7.0	7.0	7.0	7.0	7.0	7.0	7.0	7.0	0.0	0.0
S-BAND XMTR DRIVER	3.5	3.5	3.5	3.5	3.5	3.5	3.5	3.5	3.5	3.5	0.0	0.0
S-BAND PWR AMPL	22.0	22.0	22.0	22.0	22.0	22.0	22.0	22.0	22.0	22.0	0.0	0.0
SUBTOTAL	32.5	32.5	32.5	32.5	32.5	32.5	32.5	32.5	32.5	32.5	0.0	0.0
ACS/PROPULSION												
CONTROL ELECTR ASSY/SS	1.7	1.7	1.7	1.7	1.7	1.7	1.7	1.7	1.7	1.7	0.0	0.0
PRESSURE XDUCER	.4	.4	.4	.4	.4	.4	.4	.4	.4	.4	0.0	0.0
CONSCAN PROCESSOR	0.0	0.0	0.0	0.0	0.0	0.0	0.0	0.0	0.0	0.0	0.0	0.0
SUBTOTAL	2.1	2.1	2.1	2.1	2.1	2.1	2.1	2.1	2.1	2.1	0.0	0.0
ELECTRICAL PWR/CONTROL												
PCU	4.0	4.0	4.0	4.0	4.0	4.0	4.0	4.0	4.0	4.0	0.0	0.0

Table 8.1F-2. Orbiter With Version IV Science (Preferred Atlas/Centaur Configuration)(Continued)

COMMAND DISTR UNIT	2.1	2.1	2.1	2.1	2.1	2.1	2.1	2.1	2.1	2.1	0.0	0.0
CONVERTER LOSSES (60 PCT)	5.1	5.1	5.1	5.1	5.1	8.1	5.1	5.1	5.1	5.1	0.0	0.0
SUBTOTAL	11.2	11.2	11.2	11.2	11.2	14.2	11.2	11.2	11.2	11.2	0.0	0.0
THERMAL												
PROPELLANT HTRS	0.0	0.0	6.0	6.0	6.0	6.0	6.0	6.0	6.0	0.0	0.0	0.0
SUBTOTAL	0.0	0.0	6.0	6.0	6.0	6.0	6.0	6.0	6.0	0.0	0.0	0.0
SPACECRAFT SUBTOTAL 1	50.0	54.8	60.8	60.8	60.8	170.9	119.9	115.4	115.4	50.0	0.0	0.0
CABLE LOSSES (SPACECRAFT)	1.0	1.1	1.2	1.2	1.2	3.4	2.4	2.3	2.3	1.0	0.0	0.0
BATTERY CHARGING	0.0	0.0	0.0	0.0	0.0	0.0	0.0	0.0	25.0	0.0	0.0	0.0
SPACECRAFT SUBTOTAL 2	51.0	55.9	62.0	62.0	62.0	174.4	122.3	117.7	142.7	51.0	0.0	0.0
SUBTOTAL 3 (LESS SCI)	51.0	51.1	57.2	57.2	57.2	67.0	62.9	58.3	83.3	51.0	0.0	0.0
CONTINGENCY (10 PCT)	5.1	5.1	5.7	5.7	5.7	6.7	6.3	5.8	8.3	5.1	0.0	0.0
TOTAL PRIMARY BUS LOAD	56.1	61.0	67.8	67.8	67.8	181.0	128.6	123.6	151.1	56.1	0.0	0.0
	1	2	3	4	5	6	7	8	9	10	11	12

1. LAUNCH,6W,NO SCI,NO HTR
2. TRANSIT,6W,CRUISE SCI ON,NO HTR
3. TRANSIT,6W,CRUISE SCI,HTR ON
4. TRANSIT,6W,CRUISE SCI,HTR
5. TRANSIT,6W,CRUISE SCI
6. SHORT ECLIPSE,6W,ALL SCI,DSU ON (PERIAPSIS)
7. POST ELLIPSE,6W,ALL SCI,RADAR OFF
8. LONG ECLIPSE,6W,DUTY SCI OFF
9. POST ELCIPSE,6W,DUTY SCI OFF,BATT CHARGING ON
10. UNDERVOLTAGE -- NON-ESSENTIAL LOADS OFF

Table 8.1F-3. Probe Bus With Version III Science (Preferred Thor/Delta Configuration)

PROBE BUS - 6W PA, T/D 09.34.49. 04/10/73.
ELECTRICAL POWER REQUIREMENTS

	1	2	3	4	5	6
SCIENCE						
MAGNETOMETER	0.0	3.5	3.5	3.5	3.5	0.0
UV FLUORESCENT	0.0	0.0	0.0	0.0	2.5	0.0
ION MASS SPECTROMETER	0.0	0.0	0.0	0.0	2.0	0.0
NEUTRAL MASS SPECTROMETER	0.0	0.0	0.0	0.0	5.9	0.0
ELECTRON TEMP PROBE	0.0	0.0	0.0	0.0	2.0	0.0
SUBTOTAL	0.0	3.5	3.5	3.5	15.9	0.0
DATA HANDLING						
DIGITAL TELEMETRY UNIT	3.6	3.6	3.6	3.6	3.6	3.6
DIGITAL DECODER UNIT	.3	.3	.3	.3	.3	.3
SUBTOTAL	3.9	3.9	3.9	3.9	3.9	3.9
COMMUNICATIONS						
S-BAND RECEIVERS (2 ON)	7.0	7.0	7.0	7.0	7.0	7.0
S-BAND XMTR DRIVER	3.5	3.5	3.5	3.5	3.5	3.5
S-BAND PWR AMPL	15.0	15.0	15.0	22.0	22.0	22.0
SUBTOTAL	25.5	25.5	25.5	32.5	32.5	32.5
ACS/PROPULSION						
CONTROL ELECTR ASSY/SS	1.7	1.7	1.7	1.7	1.7	1.7
PRESSURE TRANSDUCER	.4	.4	.4	.4	.4	.4
SUBTOTAL	2.1	2.1	2.1	2.1	2.1	2.1
ELECTRICAL PWR/CONTROL						
PCU	4.0	4.0	4.0	4.0	4.0	4.0
COMMAND DISTRIBUTION UNIT	2.1	2.1	2.1	2.1	2.1	2.1
CONVERTER LOSSES (70 PCT)	3.2	3.2	3.2	3.2	3.2	3.2
SUBTOTAL	9.3	9.3	9.3	9.3	9.3	9.3
THERMAL						

Table 8.1F-3. Probe Bus With Version III Science (Preferred Thor/Delta Configuration)(Continued)

	1	2	3	4	5	6
PRCPELLANT HEATERS	0.C	C.0	6.C	6.0	6.C	0.0
SLBTCTAL	0.0	C.0	6.C	6.0	6.C	0.0
SPACECRAFT SUETCTAL 1	4C.8	44.3	5C.3	57.3	69.7	47.8
CAELE LCSSES (SPACECRAFT)	.8	.9	1.C	1.1	1.4	1.0
EATTERY CHARGING	0.C	C.C	C.C	C.0	0.C	0.0
SPACECRAFT SLBTCTAL 2	41.6	45.2	51.3	58.4	71.1	48.7
CCNTINGENCY (1C PCT)	4.2	4.5	5.1	5.8	7.1	4.9
TCTAL PRIMARY ELS LCAC	45.7	49.7	56.4	64.3	78.2	53.6

1. LAUNCH,3W,NC SCI,NC HTR
2. TRANSIT,3W,CRLISE SCI CN,NC HTR
3. TRANSIT,3W,CRLISE SCI,HTR CN
4. TRANSIT,6W,CRLISE SCI,HTR
5. ENCCLNTER,6W,ALL SCI CN
6. LNCERVCLTAGE -- NCN-ESSENTIAL LCADS CFF

TAPE2=VBJXP,TAPE4=CCNV6

Table 8.1F-4. Orbiter With Version III Science, 31-Watt Transmitter, and Fanbeam/Fanscan Antennas (Preferred Thor/Delta Configuration)

ORBITER-35W TWTA FANBEAM,T/D 09.34.56. 04/10/73.
ELECTRICAL POWER REQUIREMENTS

	1	2	3	4	5	6	7	8	9	10	11	12
SCIENCE												
MAGNETOMETER	0.0	3.0	3.0	3.0	3.0	3.0	3.0	3.0	3.0	0.0	0.0	0.0
UV SPECTROMETER	0.0	0.0	0.0	0.0	0.0	8.0	8.0	8.0	8.0	0.0	0.0	0.0
ION MASS SPECTROMETER	0.0	0.0	0.0	0.0	0.0	1.0	1.0	1.0	1.0	0.0	0.0	0.0
IR RADIOMETER	0.0	0.0	0.0	0.0	0.0	6.0	6.0	0.0	6.0	0.0	0.0	0.0
NEUTRAL MASS SPECTROMETER	0.0	0.0	0.0	0.0	0.0	12.0	12.0	12.0	12.0	0.0	0.0	0.0
ELECTRON TEMP PROBE	0.0	0.0	0.0	0.0	0.0	2.0	2.0	0.0	2.0	0.0	0.0	0.0
RADAR ALTIMETER	0.0	0.0	0.0	0.0	0.0	25.0	0.0	0.0	0.0	0.0	0.0	0.0
SUBTOTAL	0.0	3.0	3.0	3.0	3.0	57.0	32.0	24.0	32.0	0.0	0.0	0.0
DATA HANDLING												
DIGITAL TELEMETRY UNIT	3.6	3.6	3.6	3.6	3.6	3.6	3.6	3.6	3.6	3.6	0.0	0.0
DATA STORAGE UNIT	0.0	0.0	0.0	0.0	0.0	4.5	4.5	0.0	4.5	0.0	0.0	0.0
DIGITAL DECODER UNIT	.3	.3	.3	.3	.3	.3	.3	.3	.3	.3	0.0	0.0
SUBTOTAL	3.9	3.9	3.9	3.9	3.9	8.4	8.4	3.9	8.4	3.9	0.0	0.0
COMMUNICATIONS												
S-BAND RECEIVERS (2 ON)	7.0	7.0	7.0	7.0	7.0	7.0	7.0	7.0	7.0	7.0	0.0	0.0
S-BAND XMTR DRIVER	3.5	3.5	3.5	3.5	3.5	3.5	3.5	3.5	3.5	3.5	0.0	0.0
S-BAND TWTA	55.0	55.0	55.0	55.0	106.0	106.0	106.0	106.0	106.0	106.0	0.0	0.0
SUBTOTAL	65.5	65.5	65.5	65.5	116.5	116.5	116.5	116.5	116.5	116.5	0.0	0.0
ACS/PROPULSION												
CONTROL ELECTR ASSY/SS	1.7	1.7	1.7	1.7	1.7	1.7	1.7	1.7	1.7	1.7	0.0	0.0
PRESSURE XDUCER	.4	.4	.4	.4	.4	.4	.4	.4	.4	.4	0.0	0.0
SUBTOTAL	2.1	2.1	2.1	2.1	2.1	2.1	2.1	2.1	2.1	2.1	0.0	0.0
ELECTRICAL PWR/CONTROL												
PCU	4.0	4.0	4.0	4.0	4.0	4.0	4.0	4.0	4.0	4.0	0.0	0.0
COMMAND DISTR UNIT	2.1	2.1	2.1	2.1	2.1	2.1	2.1	2.1	2.1	2.1	0.0	0.0
CONVERTER LOSSES (70 PCT)	3.2	3.2	3.2	3.2	3.2	5.1	3.2	3.2	3.2	3.2	0.0	0.0

Table 8. 1F-4. Orbiter With Version III Science, 31-Watt Transmitter, and Fanbeam/Fanscan Antennas (Preferred Thor/Delta Configuration)(Continued)

	1	2	3	4	5	6	7	8	9	10	11	12
SUBTOTAL	9.3	9.3	9.3	9.3	9.3	11.2	9.3	9.3	9.3	9.3	0.0	0.0
THERMAL												
PROPELLANT HTRS	0.0	0.0	6.0	6.0	6.0	6.0	6.0	6.0	6.0	0.0	0.0	0.0
SUBTOTAL	0.0	0.0	6.0	6.0	6.0	6.0	6.0	6.0	6.0	0.0	0.0	0.0
SPACECRAFT SUBTOTAL 1	80.8	83.8	89.8	89.8	140.8	201.2	174.3	161.8	174.3	131.8	0.0	0.0
CABLE LOSSES (SPACECRAFT)	1.6	1.7	1.8	1.8	2.8	4.0	3.5	3.2	3.5	2.6	0.0	0.0
BATTERY CHARGING	0.0	0.0	0.0	0.0	0.0	0.0	0.0	0.0	25.0	0.0	0.0	0.0
SPACECRAFT SUBTOTAL 2	82.4	85.4	91.6	91.6	143.6	205.2	177.8	165.0	202.8	134.4	0.0	0.0
CONTINGENCY (10 PCT)	8.2	8.5	9.2	9.2	14.4	20.5	17.8	16.5	20.3	13.4	0.0	0.0
TOTAL PRIMARY EPS LOAD	90.6	94.0	100.7	100.7	157.9	225.7	195.5	181.5	223.0	147.8	0.0	0.0

1. LAUNCH,16W,NO SCI,NO HTR
2. TRANSIT,16W,CRUISE SCI ON,NO HTR
3. TRANSIT,16W,CRUISE SCI,HTR ON
4. TRANSIT,16W,CRUISE SCI,HTR
5. TRANSIT,35W,CRUISE SCI
6. SHORT ECLIPSE,35W,ALL SCI,DSL ON (PERIAPSIS)
7. POST ECLIPSE,35W,ALL SCI,RADAR OFF
8. LONG ECLIPSE,35W,DUTY SCI OFF
9. POST ECLIPSE,35W,DUTY SCI OFF,BATT CHARGING ON
10. UNDERVOLTAGE -- NON-ESSENTIAL LOADS OFF
11.
12.

TAPE2=VBJXCTW,TAPE4=CCNVEE

Table 8.1F-5. Probe Bus With Version III Science (Atlas/Centaur)

PROBE BUS - 8W TWTA, A/C 09.35.17. 04/10/73.
ELECTRICAL POWER REQUIREMENTS

	1	2	3	4	5	6
SCIENCE						
MAGNETOMETER	0.0	4.0	4.0	4.0	4.0	0.0
UV FLUORESCENT	0.0	0.0	0.0	0.0	4.0	0.0
ION MASS SPECTROMETER	0.0	0.0	0.0	0.0	2.0	0.0
NEUTRAL MASS SPECTROMETER	0.0	0.0	0.0	0.0	12.0	0.0
ELECTRON TEMP PROBE	0.0	0.0	0.0	0.0	2.5	0.0
SUBTOTAL	0.0	4.0	4.0	4.0	24.5	0.0
DATA HANDLING						
DIGITAL TELEMETRY UNIT	3.6	3.6	3.6	3.6	3.6	3.6
DIGITAL DECODER UNIT	.3	.3	.3	.3	.3	.3
SUBTOTAL	3.9	3.9	3.9	3.9	3.9	3.9
COMMUNICATIONS						
S-BAND RECEIVERS (2 ON)	3.4	3.4	3.4	3.4	3.4	3.4
S-BAND XMTR DRIVER	1.3	1.3	1.3	1.3	1.3	1.3
S-BAND TWTA	28.0	28.0	28.0	28.0	28.0	28.0
SUBTOTAL	32.7	32.7	32.7	32.7	32.7	32.7
ACS/PROPULSION						
CONTROL ELECTR ASSY/SS	1.7	1.7	1.7	1.7	1.7	1.7
PRESSURE TRANSDUCER	.4	.4	.4	.4	.4	.4
SUBTOTAL	2.1	2.1	2.1	2.1	2.1	2.1
ELECTRICAL PWR/CONTROL						
PCU	4.0	4.0	4.0	4.0	4.0	4.0
COMMAND DISTRIBUTION UNIT	2.1	2.1	2.1	2.1	2.1	2.1
CONVERTER LOSSES (70 PCT)	8.1	8.1	8.1	8.1	8.1	8.1
SUBTOTAL	14.2	14.2	14.2	14.2	14.2	14.2
THERMAL						

Table 8.1F-5. Probe Bus With Version III Science (Atlas/Centaur)(Continued)

PROPELLANT HEATERS	0.0	0.0	6.0	6.0	6.0	0.0
SUBTOTAL	0.0	0.0	6.0	6.0	6.0	0.0
SPACECRAFT SUBTOTAL 1	52.9	56.9	62.9	62.9	83.4	52.9
CABLE LOSSES (SPACECRAFT)	1.1	1.1	1.3	1.3	1.7	1.1
BATTERY CHARGING	0.0	0.0	0.0	0.0	0.0	0.0
SPACECRAFT SUBTOTAL 2	53.9	58.0	64.1	64.1	85.0	53.9
CONTINGENCY (10 PCT)	5.4	5.8	6.4	6.4	8.5	5.4
TOTAL PRIMARY BUS LOAD	59.3	63.8	70.5	70.5	93.5	59.3
	1	2	3	4	5	6

1. LAUNCH,8W,NO SCI,NO HTR
2. TRANSIT,8W,CRUISE SCI ON,NO HTR
3. TRANSIT,8W,CRUISE SCI,HTR ON
4. TRANSIT,8W,CRUISE SCI,HTR
5. ENCOUNTER,8W,ALL SCI ON
6. UNDERVOLTAGE -- NON-ESSENTIAL LOADS OFF

TAPE2=VBJXPA,TAPE4=CONV6AA

Table 8.1F-6. Orbiter With Version III Science, 12-Watt Transmitter, and Fanbeam/Fanscan Antennas (Thor/Delta)

ORBITER-12W PA FANBEAM, T/D   09.35.11.   04/10/73.
ELECTRICAL POWER REQUIREMENTS

	1	2	3	4	5	6	7	8	9	10	11	12
SCIENCE												
MAGNETOMETER	0.0	3.0	3.0	3.0	3.0	3.0	3.0	3.0	3.0	0.0	0.0	0.0
UV SPECTROMETER	0.0	0.0	0.0	0.0	0.0	8.0	8.0	8.0	8.0	0.0	0.0	0.0
ION MASS SPECTROMETER	0.0	0.0	0.0	0.0	0.0	1.0	1.0	1.0	1.0	0.0	0.0	0.0
IR RADIOMETER	0.0	0.0	0.0	0.0	0.0	6.0	6.0	0.0	6.0	0.0	0.0	0.0
NEUTRAL MASS SPECTROMETER	0.0	0.0	0.0	0.0	0.0	12.0	12.0	12.0	12.0	0.0	0.0	0.0
ELECTRON TEMP PROBE	0.0	0.0	0.0	0.0	0.0	2.0	2.0	0.0	2.0	0.0	0.0	0.0
RADAR ALTIMETER	0.0	0.0	0.0	0.0	0.0	25.0	0.0	0.0	0.0	0.0	0.0	0.0
SUBTOTAL	0.0	3.0	3.0	3.0	3.0	57.0	32.0	24.0	32.0	0.0	0.0	0.0
DATA HANDLING												
DIGITAL TELEMETRY UNIT	3.6	3.6	3.6	3.6	3.6	3.6	3.6	3.6	3.6	3.6	0.0	0.0
DATA STORAGE UNIT	0.0	0.0	0.0	0.0	0.0	4.5	4.5	0.0	4.5	0.0	0.0	0.0
DIGITAL DECODER UNIT	.3	.3	.3	.3	.3	.3	.3	.3	.3	.3	0.0	0.0
SUBTOTAL	3.9	3.9	3.9	3.9	3.9	8.4	8.4	3.9	8.4	3.9	0.0	0.0
COMMUNICATIONS												
S-BAND RECEIVERS (2 ON)	7.0	7.0	7.0	7.0	7.0	7.0	7.0	7.0	7.0	7.0	0.0	0.0
S-BAND XMTR DRIVER	3.5	3.5	3.5	3.5	3.5	3.5	3.5	3.5	3.5	3.5	0.0	0.0
S-BAND PWR AMPL	22.0	22.0	22.0	22.0	44.0	44.0	44.0	44.0	44.0	44.0	0.0	0.0
SUBTOTAL	32.5	32.5	32.5	32.5	54.5	54.5	54.5	54.5	54.5	54.5	0.0	0.0
ACS/PROPULSION												
CONTROL ELECTR ASSY/SS	1.7	1.7	1.7	1.7	1.7	1.7	1.7	1.7	1.7	1.7	0.0	0.0
PRESSURE XDUCER	.4	.4	.4	.4	.4	.4	.4	.4	.4	.4	0.0	0.0
CONSCAN PROCESSOR	0.0	0.0	0.0	0.0	0.0	0.0	0.0	0.0	0.0	0.0	0.0	0.0
SUBTOTAL	2.1	2.1	2.1	2.1	2.1	2.1	2.1	2.1	2.1	2.1	0.0	0.0
ELECTRICAL PWR/CONTROL												
PCU	4.0	4.0	4.0	4.0	4.0	4.0	4.0	4.0	4.0	4.0	0.0	0.0
COMMAND DISTR UNIT	2.1	2.1	2.1	2.1	2.1	2.1	2.1	2.1	2.1	2.1	0.0	0.0
CONVERTER LOSSES (70 PCT)	3.2	3.2	3.2	3.2	3.2	5.1	3.2	3.2	3.2	3.2	0.0	0.0

Table 8.1F-6. Orbiter With Version III Science, 12-Watt Transmitter, and Fanbeam/Fanscan Antennas (Thor/Delta)(Continued)

SUBTOTAL	9.3	9.3	9.3	9.3	9.3	11.2	9.3	9.3	9.3	9.3	0.0	0.0
THERMAL												
PROPELLANT HTRS	0.0	0.0	6.0	6.0	6.0	6.0	6.0	6.0	6.0	0.0	0.0	0.0
SUBTOTAL	0.0	0.0	6.0	6.0	6.0	6.0	6.0	6.0	6.0	0.0	0.0	0.0
SPACECRAFT SUBTOTAL 1	47.8	50.8	56.8	56.8	78.8	139.2	112.3	99.8	112.3	69.8	0.0	0.0
CABLE LOSSES (SPACECRAFT)	1.0	1.0	1.1	1.1	1.6	2.8	2.2	2.0	2.2	1.4	0.0	0.0
BATTERY CHARGING	0.0	0.0	0.0	0.0	0.0	0.0	0.0	0.0	25.0	0.0	0.0	0.0
SPACECRAFT SUBTOTAL 2	48.7	51.8	57.9	57.9	80.3	142.0	114.5	101.8	139.5	71.2	0.0	0.0
CONTINGENCY (10 PCT)	4.9	5.2	5.8	5.8	8.0	14.2	11.5	10.2	14.0	7.1	0.0	0.0
TOTAL PRIMARY BUS LOAD	53.6	57.0	63.7	63.7	88.4	156.2	126.0	111.9	153.5	78.3	0.0	0.0
	1	2	3	4	5	6	7	8	9	10	11	12

1. LAUNCH,3W,NO SCI,NO HTR
2. TRANSIT,3W,CRUISE SCI ON,NO HTR
3. TRANSIT,3W,CRUISE SCI,HTR ON
4. TRANSIT,3W,CRUISE SCI,HTR
5. TRANSIT,12W,CRUISE SCI
6. SHORT ECLIPSE,12W,ALL SCI,DSU ON (PERIAPSIS)
7. POST ELLIPSE,12W,ALL SCI,RADAR OFF
8. LONG ECLIPSE,12W,DUTY SCI OFF
9. POST ELCIPSE,12W,DUTY SCI OFF,BATT CHARGING ON
10. UNDERVOLTAGE -- NON-ESSENTIAL LOADS OFF
11.
12.
TAPE2=VBJXOAF,TAPE4=CONVEE

Table 8.1F-7. Orbiter With Version III Science and Despun Reflector Antenna (Thor/Delta)

ORBITER-12W PA DESPUN, T/D 09.35.14. 04/10/73.
ELECTRICAL POWER REQUIREMENTS

	1	2	3	4	5	6	7	8	9	10	11	12
SCIENCE												
MAGNETOMETER	0.0	3.0	3.0	3.0	3.0	3.0	3.0	3.0	3.0	0.0	0.0	0.0
UV SPECTROMETER	0.0	0.0	0.0	0.0	0.0	8.0	8.0	8.0	8.0	0.0	0.0	0.0
ION MASS SPECTROMETER	0.0	0.0	0.0	0.0	0.0	1.0	1.0	1.0	1.0	0.0	0.0	0.0
IR RADIOMETER	0.0	0.0	0.0	0.0	0.0	6.0	6.0	0.0	6.0	0.0	0.0	0.0
NEUTRAL MASS SPECTROMETER	0.0	0.0	0.0	0.0	0.0	12.0	12.0	12.0	12.0	0.0	0.0	0.0
ELECTRON TEMP PROBE	0.0	0.0	0.0	0.0	0.0	2.0	2.0	0.0	2.0	0.0	0.0	0.0
RADAR ALTIMETER	0.0	0.0	0.0	0.0	0.0	25.0	0.0	0.0	0.0	0.0	0.0	0.0
SUBTOTAL	0.0	3.0	3.0	3.0	3.0	57.0	32.0	24.0	32.0	0.0	0.0	0.0
DATA HANDLING												
DIGITAL TELEMETRY UNIT	3.6	3.6	3.6	3.6	3.6	3.6	3.6	3.6	3.6	3.6	0.0	0.0
DATA STORAGE UNIT	0.0	0.0	0.0	0.0	0.0	4.5	4.5	0.0	4.5	0.0	0.0	0.0
DIGITAL DECODER UNIT	.3	.3	.3	.3	.3	.3	.3	.3	.3	.3	0.0	0.0
SUBTOTAL	3.9	3.9	3.9	3.9	3.9	8.4	8.4	3.9	8.4	3.9	0.0	0.0
COMMUNICATIONS												
S-BAND RECEIVERS (2 ON)	7.0	7.0	7.0	7.0	7.0	7.0	7.0	7.0	7.0	7.0	0.0	0.0
S-BAND XMTR DRIVER	3.5	3.5	3.5	3.5	3.5	3.5	3.5	3.5	3.5	3.5	0.0	0.0
S-BAND PWR AMPL	22.0	22.0	22.0	22.0	44.0	44.0	44.0	44.0	44.0	44.0	0.0	0.0
SUBTOTAL	32.5	32.5	32.5	32.5	54.5	54.5	54.5	54.5	54.5	54.5	0.0	0.0
ACS/PROPULSION												
DESPIN ELECTR ASSY	0.0	0.0	0.0	1.5	1.5	1.5	1.5	1.5	1.5	1.5	0.0	0.0
DESPIN MECH ASSY	0.0	0.0	0.0	6.0	6.0	6.0	6.0	6.0	6.0	6.0	0.0	0.0
CONTROL ELECTR ASSY/SS	1.7	1.7	1.7	1.7	1.7	1.7	1.7	1.7	1.7	1.7	0.0	0.0
PRESSURE XDUCER	.4	.4	.4	.4	.4	.4	.4	.4	.4	.4	0.0	0.0
CONSCAN PROCESSOR	0.0	0.0	0.0	0.0	0.0	0.0	0.0	0.0	0.0	0.0	0.0	0.0
SUBTOTAL	2.1	2.1	2.1	9.6	9.6	9.6	9.6	9.6	9.6	9.6	0.0	0.0
ELECTRICAL PWR/CONTROL												
PCU	4.0	4.0	4.0	4.0	4.0	4.0	4.0	4.0	4.0	4.0	0.0	0.0

Table 8.1F-7. Orbiter With Version III Science and Despun Reflector Antenna (Thor/Delta)(Continued)

COMMAND DISTR UNIT	2.1	2.1	2.1	2.1	2.1	2.1	2.1	2.1	2.1	2.1	0.0	0.0
CONVERTER LOSSES (70 PCT)	3.2	3.2	3.2	4.7	4.7	6.6	4.7	4.7	4.7	4.7	0.0	0.0
SUBTOTAL	9.3	9.3	9.3	10.8	10.8	12.7	10.8	10.8	10.8	10.8	0.0	0.0
THERMAL												
PROPELLANT HTRS	0.0	0.0	6.0	6.0	6.0	6.0	6.0	6.0	6.0	0.0	0.0	0.0
SUBTOTAL	0.0	0.0	6.0	6.0	6.0	6.0	6.0	6.0	6.0	0.0	0.0	0.0
SPACECRAFT SUBTOTAL 1	47.8	50.8	56.8	65.8	87.8	148.2	121.3	108.8	121.3	78.8	0.0	0.0
CABLE LOSSES (SPACECRAFT)	1.0	1.0	1.1	1.3	1.8	3.0	2.4	2.2	2.4	1.6	0.0	0.0
BATTERY CHARGING	0.0	0.0	0.0	0.0	0.0	0.0	0.0	0.0	25.0	0.0	0.0	0.0
SPACECRAFT SUBTOTAL 2	48.7	51.8	57.9	67.1	89.5	151.2	123.7	110.9	148.7	80.3	0.0	0.0
CONTINGENCY (10 PCT)	4.9	5.2	5.8	6.7	9.0	15.1	12.4	11.1	14.9	8.0	0.0	0.0
TOTAL PRIMARY BUS LOAD	53.6	57.0	63.7	73.8	98.5	166.3	136.1	122.0	163.6	88.4	0.0	0.0
	1	2	3	4	5	6	7	8	9	10	11	12

1. LAUNCH,3W,NO SCI,NO HTR,NO DMA,DEA
2. TRANSIT,3W,CRUISE SCI ON,NO HTR,NO DMA,DEA
3. TRANSIT,3W,CRUISE SCI,HTR ON,NO DMA,DEA
4. TRANSIT,3W,CRUISE SCI,HTR,DMA,DEA ON
5. TRANSIT,12W,CRUISE SCI
6. SHORT ECLIPSE,12W,ALL SCI, DSU ON (PERIAPSIS)
7. POST ECLIPSE,12W,RADAR OFF
8. LONG ECLIPSE,12W,DUTY SCI OFF
9. POST ECLIPSE,12W,DUTY SCI OFF,BATT CHARGING ON
10. UNDERVOLTAGE -- NON-ESSENTIAL LOADS OFF
11.
12.

TAPE2=VBJXC1H,TAPE4=CONV8H

Table 8.1F-8. Orbiter With Version III Science, 31-Watt Transmitter, and Fanbeam/Fanscan Antennas (Atlas/Centaur)

ORBITER-35W PA FANBEAM,A/C 09.35.32. 04/10/73.
ELECTRICAL POWER REQUIREMENTS

	1	2	3	4	5	6	7	8	9	10	11	12
SCIENCE												
MAGNETOMETER	0.0	4.0	4.0	4.0	4.0	4.0	4.0	4.0	4.0	0.0	0.0	0.0
UV SPECTROMETER	0.0	0.0	0.0	0.0	0.0	8.0	8.0	8.0	8.0	0.0	0.0	0.0
ION MASS SPECTROMETER	0.0	0.0	0.0	0.0	0.0	2.0	2.0	2.0	2.0	0.0	0.0	0.0
IR RADIOMETER	0.0	0.0	0.0	0.0	0.0	6.0	6.0	0.0	6.0	0.0	0.0	0.0
NEUTRAL MASS SPECTROMETER	0.0	0.0	0.0	0.0	0.0	12.0	12.0	12.0	12.0	0.0	0.0	0.0
ELECTRON TEMP PROBE	0.0	0.0	0.0	0.0	0.0	2.5	2.5	0.0	2.5	0.0	0.0	0.0
RADAR ALTIMETER	0.0	0.0	0.0	0.0	0.0	35.0	0.0	0.0	0.0	0.0	0.0	0.0
SUBTOTAL	0.0	4.0	4.0	4.0	4.0	69.5	34.5	26.0	34.5	0.0	0.0	0.0
DATA HANDLING												
DIGITAL TELEMETRY UNIT	3.6	3.6	3.6	3.6	3.6	3.6	3.6	3.6	3.6	3.6	0.0	0.0
DATA STORAGE UNIT	0.0	0.0	0.0	0.0	0.0	4.5	4.5	0.0	4.5	0.0	0.0	0.0
DIGITAL DECODER UNIT	.3	.3	.3	.3	.3	.3	.3	.3	.3	.3	0.0	0.0
SUBTOTAL	3.9	3.9	3.9	3.9	3.9	8.4	8.4	3.9	8.4	3.9	0.0	0.0
COMMUNICATIONS												
S-BAND RECEIVERS (2 ON)	7.0	7.0	7.0	7.0	7.0	7.0	7.0	7.0	7.0	7.0	0.0	0.0
S-BAND XMTR DRIVER	3.5	3.5	3.5	3.5	3.5	3.5	3.5	3.5	3.5	3.5	0.0	0.0
S-BAND PWR AMPL	68.0	68.0	68.0	68.0	136.0	136.0	136.0	136.0	136.0	136.0	0.0	0.0
SUBTOTAL	78.5	78.5	78.5	78.5	146.5	146.5	146.5	146.5	146.5	146.5	0.0	0.0
ACS/PROPULSION												
CONTROL ELECTR ASSY/SS	1.7	1.7	1.7	1.7	1.7	1.7	1.7	1.7	1.7	1.7	0.0	0.0
PRESSURE XDUCER	.4	.4	.4	.4	.4	.4	.4	.4	.4	.4	0.0	0.0
SUBTOTAL	2.1	2.1	2.1	2.1	2.1	2.1	2.1	2.1	2.1	2.1	0.0	0.0
ELECTRICAL PWR/CONTROL												
PCU	4.0	4.0	4.0	4.0	4.0	4.0	4.0	4.0	4.0	4.0	0.0	0.0
COMMAND DISTR UNIT	2.1	2.1	2.1	2.1	2.1	2.1	2.1	2.1	2.1	2.1	0.0	0.0
CONVERTER LOSSES (70 PCT)	4.9	4.9	4.9	4.9	4.9	7.9	4.9	4.9	4.9	4.9	0.0	0.0

Table 8.1F-8. Orbiter With Version III Science, 31-Watt Transmitter, and Fanbeam/Fanscan Antennas (Atlas/Centaur)(Continued)

SUBTCTAL	11.0	11.0	11.C	11.C	11.C	14.C	11.C	11.0	11.C	11.C	0.0	0.0
THERMAL												
PRCPELLANT HTRS	0.0	0.0	6.0	6.0	6.C	6.C	6.C	6.0	6.C	0.0	0.0	0.0
SUBTCTAL	0.C	0.0	6.0	6.C	6.0	6.0	6.C	6.0	6.C	0.0	0.0	0.0
SPACECRAFT SUBTCTAL 1	95.5	95.5	1C5.5	1C5.5	173.5	246.5	208.5	195.5	208.5	163.5	0.0	0.0
CABLE LCSSES (SPACECRAFT)	1.9	2.0	2.1	2.1	3.5	4.9	4.2	3.9	4.2	3.3	0.0	0.0
BATTERY CHARGING	0.0	0.0	C.0	0.0	C.C	0.0	0.0	0.0	25.0	0.0	0.0	0.0
SPACECRAFT SUBTCTAL 2	97.4	1C1.5	107.6	1C7.6	177.C	251.5	212.7	199.4	237.7	166.8	0.0	0.0
CCNTINGENCY (1C PCT)	9.7	10.2	1C.8	1C.8	17.7	25.1	21.3	19.9	23.8	16.7	0.0	0.0
TCTAL PRIMARY BUS LCAC	1C7.2	111.7	118.4	118.4	194.7	276.6	234.0	219.4	261.5	183.5	0.0	0.0
	1	2	3	4	5	6	7	8	9	1C	11	12

1. LAUNCH,8.8W,NC SCI,NC HTR
2. TRANSIT,8.8W,CRUISE SCI CN,NC HTR
3. TRANSIT,8.8W,CRUISE SCI,HTR CN
4. TRANSIT,8.8W,CRUISE SCI,HTR
5. TRANSIT,35W,CRUISE SCI
6. SHCRT ECLIPSE,35W,ALL SCI,DSU CN (PERIAPSIS)
7. PCST ELLIPSE,35W,ALL SCI,RADAR CFF
8. LCNG ECLIPSE,35W,DUTY SCI CFF
9. PCST ELCIPSE,35W,DUTY SCI CFF,BATT CHARGING CN
10. UNDERVCLTAGE -- NCN-ESSENTIAL LCADS CFF
11.
12.

TAPE2=VBJXLAC,TAPE4=CCNVEEA

Table 8.1F-9. Orbiter With Version III Science, 12-Watt Transmitter, and Fanbeam/Fanscan Antennas (Atlas/Centaur)

ORBITER-12W PA FANBEAM,A/C   09.35.35.   04/10/73.
ELECTRICAL POWER REQUIREMENTS

	1	2	3	4	5	6	7	8	9	10	11	12
SCIENCE												
MAGNETOMETER	0.0	4.0	4.0	4.0	4.0	4.0	4.0	4.0	4.0	0.0	0.0	0.0
UV SPECTROMETER	0.0	0.0	0.0	0.0	0.0	8.0	8.0	8.0	8.0	0.0	0.0	0.0
ION MASS SPECTROMETER	0.0	0.0	0.0	0.0	0.0	2.0	2.0	2.0	2.0	0.0	0.0	0.0
IR RADIOMETER	0.0	0.0	0.0	0.0	0.0	6.0	6.0	0.0	6.0	0.0	0.0	0.0
NEUTRAL MASS SPECTROMETER	0.0	0.0	0.0	0.0	0.0	12.0	12.0	12.0	12.0	0.0	0.0	0.0
ELECTRON TEMP PROBE	0.0	0.0	0.0	0.0	0.0	2.5	2.5	0.0	2.5	0.0	0.0	0.0
RADAR ALTIMETER	0.0	0.0	0.0	0.0	0.0	35.0	0.0	0.0	0.0	0.0	0.0	0.0
SUBTOTAL	0.0	4.0	4.0	4.0	4.0	69.5	34.5	26.0	34.5	0.0	0.0	0.0
DATA HANDLING												
DIGITAL TELEMETRY UNIT	3.6	3.6	3.6	3.6	3.6	3.6	3.6	3.6	3.6	3.6	0.0	0.0
DATA STORAGE UNIT	0.0	0.0	0.0	0.0	0.0	4.5	4.5	0.0	4.5	0.0	0.0	0.0
DIGITAL DECODER UNIT	.3	.3	.3	.3	.3	.3	.3	.3	.3	.3	0.0	0.0
SUBTOTAL	3.9	3.9	3.9	3.9	3.9	8.4	8.4	3.9	8.4	3.9	0.0	0.0
COMMUNICATIONS												
S-BAND RECEIVERS (2 ON)	7.0	7.0	7.0	7.0	7.0	7.0	7.0	7.0	7.0	7.0	0.0	0.0
S-BAND XMTR DRIVER	3.5	3.5	3.5	3.5	3.5	3.5	3.5	3.5	3.5	3.5	0.0	0.0
S-BAND PWR AMPL	22.0	22.0	22.0	22.0	44.0	44.0	44.0	44.0	44.0	44.0	0.0	0.0
SUBTOTAL	32.5	32.5	32.5	32.5	54.5	54.5	54.5	54.5	54.5	54.5	0.0	0.0
ACS/PROPULSION												
CONTROL ELECTR ASSY/SS	1.7	1.7	1.7	1.7	1.7	1.7	1.7	1.7	1.7	1.7	0.0	0.0
PRESSURE XDUCER	.4	.4	.4	.4	.4	.4	.4	.4	.4	.4	0.0	0.0
CONSCAN PROCESSOR	0.0	0.0	0.0	0.0	0.0	0.0	0.0	0.0	0.0	0.0	0.0	0.0
SUBTOTAL	2.1	2.1	2.1	2.1	2.1	2.1	2.1	2.1	2.1	2.1	0.0	0.0
ELECTRICAL PWR/CONTROL												
PCU	4.0	4.0	4.0	4.0	4.0	4.0	4.0	4.0	4.0	4.0	0.0	0.0
COMMAND DISTR UNIT	2.1	2.1	2.1	2.1	2.1	2.1	2.1	2.1	2.1	2.1	0.0	0.0
CONVERTER LOSSES (70 PCT)	4.9	4.9	4.9	4.9	4.9	7.9	4.9	4.9	4.9	4.9	0.0	0.0

Table 8.1F-9. Orbiter With Version III Science, 12-Watt Transmitter, and Fanbeam/Fanscan Antennas (Atlas/Centaur)(Continued)

SLBTCTAL	11.0	11.0	11.0	11.0	11.0	14.0	11.0	11.0	11.0	11.0	0.0	0.0
THERMAL												
PRCPELLANT HTRS	0.0	0.0	6.0	6.0	6.0	6.0	6.0	6.0	6.0	0.0	0.0	0.0
SLBTCTAL	0.0	0.0	6.0	6.0	6.0	6.0	6.0	6.0	6.0	0.0	0.0	0.0
SPACECRAFT SLBTCTAL 1	49.5	53.5	59.5	59.5	81.5	154.5	116.5	103.5	116.5	71.5	0.0	0.0
CABLE LCSSES (SPACECRAFT)	1.0	1.1	1.2	1.2	1.6	3.1	2.3	2.1	2.3	1.4	0.0	0.0
BATTERY CHARGING	0.0	0.0	0.0	0.0	0.0	0.0	0.0	0.0	25.0	0.0	0.0	0.0
SPACECRAFT SUBTOTAL 2	50.5	54.6	60.7	60.7	83.2	157.6	118.9	105.6	143.9	73.0	0.0	0.0
CONTINGENCY (10 PCT)	5.1	5.5	6.1	6.1	8.3	15.8	11.9	10.6	14.4	7.3	0.0	0.0
TOTAL PRIMARY BUS LOAD	55.6	60.1	66.8	66.8	91.5	173.4	130.8	116.2	158.3	80.3	0.0	0.0
	1	2	3	4	5	6	7	8	9	10	11	12

1. LAUNCH,3W,NC SCI,NC HTR
2. TRANSIT,3W,CRUISE SCI CN,NC HTR
3. TRANSIT,3W,CRUISE SCI,HTR CN
4. TRANSIT,3W,CRUISE SCI,HTR
5. TRANSIT,12W,CRUISE SCI
6. SHCRT ECLIPSE,12W,ALL SCI,DSU CN (PERIAPSIS)
7. PCST ELLIPSE,12W,ALL SCI,RADAR CFF
8. LCNG ECLIPSE,12W,DUTY SCI CFF
9. PCST ECLIPSE,12W,DUTY SCI CFF,BATT CHARGING CN
10. UNDERVOLTAGE -- NCN-ESSENTIAL LOADS CFF
11.
12.

TAPE2=VEJXCCC,TAPE4=CCNVEEA

Table 8.1F-10. Orbiter With Version IV Science, and Despun Reflector Antenna (Atlas/Centaur)

ORBITER-12W PA DESPUN, A/C 18.49.35. 04/10/73.
ELECTRICAL POWER REQUIREMENTS

	1	2	3	4	5	6	7	8	9	10	11	12
SCIENCE												
MAGNETOMETER	0.0	4.0	4.0	4.0	4.0	4.0	4.0	4.0	4.0	0.0	0.0	0.0
UV SPECTROMETER	0.0	0.0	0.0	0.0	0.0	8.0	8.0	8.0	8.0	0.0	0.0	0.0
ION MASS SPECTROMETER	0.0	0.0	0.0	0.0	0.0	2.0	2.0	2.0	2.0	0.0	0.0	0.0
IR RADIOMETER	0.0	0.0	0.0	0.0	0.0	6.0	6.0	0.0	6.0	0.0	0.0	0.0
NEUTRAL MASS SPECTROMETER	0.0	0.0	0.0	0.0	0.0	12.0	12.0	12.0	12.0	0.0	0.0	0.0
ELECTRON TEMP PROBE	0.0	0.0	0.0	0.0	0.0	2.5	2.5	0.0	2.5	0.0	0.0	0.0
RADAR ALTIMETER	0.0	0.0	0.0	0.0	0.0	35.0	0.0	0.0	0.0	0.0	0.0	0.0
SUBTOTAL	0.0	4.0	4.0	4.0	4.0	69.5	34.5	26.0	34.5	0.0	0.0	0.0
DATA HANDLING												
DIGITAL TELEMETRY UNIT	3.6	3.6	3.6	3.6	3.6	3.6	3.6	3.6	3.6	3.6	0.0	0.0
DATA STORAGE UNIT	0.0	0.0	0.0	0.0	0.0	4.5	4.5	0.0	4.5	0.0	0.0	0.0
DIGITAL DECODER UNIT	.3	.3	.3	.3	.3	.3	.3	.3	.3	.3	0.0	0.0
SUBTOTAL	3.9	3.9	3.9	3.9	3.9	8.4	8.4	3.9	8.4	3.9	0.0	0.0
COMMUNICATIONS												
S-BAND RECEIVERS (2 ON)	7.0	7.0	7.0	7.0	7.0	7.0	7.0	7.0	7.0	7.0	0.0	0.0
S-BAND XMTR DRIVER	3.5	3.5	3.5	3.5	3.5	3.5	3.5	3.5	3.5	3.5	0.0	0.0
S-BAND PWR AMPL	22.0	22.0	22.0	22.0	44.0	44.0	44.0	44.0	44.0	44.0	0.0	0.0
SUBTOTAL	32.5	32.5	32.5	32.5	54.5	54.5	54.5	54.5	54.5	54.5	0.0	0.0
ACS/PROPULSION												
DESPIN ELECTR ASSY	0.0	0.0	0.0	1.5	1.5	1.5	1.5	1.5	1.5	1.5	0.0	0.0
DESPIN MECH ASSY	0.0	0.0	0.0	6.0	6.0	6.0	6.0	6.0	6.0	6.0	0.0	0.0
CONTROL ELECTR ASSY/SS	1.7	1.7	1.7	1.7	1.7	1.7	1.7	1.7	1.7	1.7	0.0	0.0
PRESSURE XDUCER	.4	.4	.4	.4	.4	.4	.4	.4	.4	.4	0.0	0.0
CONSCAN PROCESSOR	0.0	0.0	0.0	0.0	0.0	0.0	0.0	0.0	0.0	0.0	0.0	0.0
SUBTOTAL	2.1	2.1	2.1	9.6	9.6	9.6	9.6	9.6	9.6	9.6	0.0	0.0
ELECTRICAL PWR/CONTROL												
PCU	4.0	4.0	4.0	4.0	4.0	4.0	4.0	4.0	4.0	4.0	0.0	0.0

Table 8.1F-10. Orbiter With Version IV Science, and Despun Reflector Antenna (Atlas/Centaur)(Continued)

COMMAND DISTR UNIT	2.1	2.1	2.1	2.1	2.1	2.1	2.1	2.1	2.1	2.1	0.0	0.0
CONVERTER LOSSES (70 PCT)	4.9	4.9	4.9	7.3	7.3	10.3	7.3	7.3	7.3	7.3	0.0	0.0
SUBTOTAL	11.0	11.0	11.0	13.4	13.4	16.4	13.4	13.4	13.4	13.4	0.0	0.0
THERMAL												
PROPELLANT HTRS	0.0	0.0	6.0	6.0	6.0	6.0	6.0	6.0	6.0	0.0	0.0	0.0
SUBTOTAL	0.0	0.0	6.0	6.0	6.0	6.0	6.0	6.0	6.0	0.0	0.0	0.0
SPACECRAFT SUBTOTAL 1	49.5	53.5	59.5	69.4	91.4	164.4	126.4	113.4	126.4	81.4	0.0	0.0
CABLE LOSSES (SPACECRAFT)	1.0	1.1	1.2	1.4	1.8	3.3	2.5	2.3	2.5	1.6	0.0	0.0
BATTERY CHARGING	0.0	0.0	0.0	0.0	0.0	0.0	0.0	0.0	25.0	0.0	0.0	0.0
SPACECRAFT SUBTOTAL 2	50.5	54.6	60.7	70.8	93.2	167.7	128.9	115.6	153.9	83.0	0.0	0.0
CONTINGENCY (10 PCT)	5.1	5.5	6.1	7.1	9.3	16.8	12.9	11.6	15.4	8.3	0.0	0.0
TOTAL PRIMARY BUS LOAD	55.6	60.1	66.8	77.8	102.5	184.4	141.8	127.2	169.3	91.3	0.0	0.0
	1	2	3	4	5	6	7	8	9	10	11	12

1. LAUNCH,8.8W,NO SCI,NO HTR
2. TRANSIT,8.8W,CRUISE SCI ON,NO HTR
3. TRANSIT,8.8W,CRUISE SCI,HTR ON
4. TRANSIT,8.8W,CRUISE SCI,HTR
5. TRANSIT,35W,CRUISE SCI
6. SHORT ECLIPSE,35W,ALL SCI,DSU ON (PERIAPSIS)
7. POST ELLIPSE,35W,ALL SCI,RADAR OFF
8. LONG ECLIPSE,35W,DUTY SCI OFF
9. POST ELCIPSE,35W,DUTY SCI OFF,BATT CHARGING ON
10. UNDERVOLTAGE -- NON-ESSENTIAL LOADS OFF
11.
12.

TAPE2=VBJXOCA,TAPE4=CCNVEHA

APPENDIX 8. 2A

GROUND RECEIVER PERFORMANCE

APPENDIX 8.2A

GROUND RECEIVER PERFORMANCE

1. SUMMARY

This appendix presents the data which has been used in the design control tables throughout the report for receiver loss. Receiver loss includes losses due to the noisy carrier reference (from carrier tracking loop, subcarrier demodulator, symbol synchronizer, and all combined effects which degrade decoding performance. For low tracking loop signal-to-noise ratios (less than 10 to 12 dB) loop memory effects cause extra sequential decoding degradation through burst errors. This situation can be improved through the use of interleaving symbols in each frame of data. Interleaving is discussed in this appendix, but is not recommended pending further analysis.

2. SEQUENTIAL DECODER PERFORMANCE

The ideal or theoretical performance of a Fano sequential decoder and the Pioneer 10 and 11 rate 1/2, constraint length 32 convolutional code is shown in Figure 8.2A-1. This data has been extracted from computer simulations done by Dale Lumb of NASA/ARC. Figure 8.2A-2 shows the measured performance of the above coder-decoder combination. The tests were performed by D. Lumb at CTA-21. Modulation was PCM/PSK/PM at an angle of 1.16 radians, and the numbers next to the data points indicate loop SNR's in a $2B_{LO}$ bandwidth of 10.8 Hz.

The required E_b/N_o for a code to achieve a 10^{-2} probability of frame deletion under ideal conditions can be found in Figure 8.2A-1. The required E_b/N_o when the decoder has only partial knowledge of the carrier phase, subcarrier phase, and symbol time is found in Figure 8.2A-2. The difference between these two numbers in decibels is defined as the receiver loss. As an example, for 128 bits/s the ideal requirement is 2.3 dB. Figure 8.2A-2 yields a total E_b/N_o requirement of 6.3 dB. This gives a receiver loss of 3.9 dB at 2 loop SNR of ~9.6 dB.

At a 10^{-3} frame deletion rate for 128 bit/s, the NASA data has been extrapolated; this is open for question since the loop SNR increases as E_b/N_o increases for a fixed modulation index. The receiver losses used

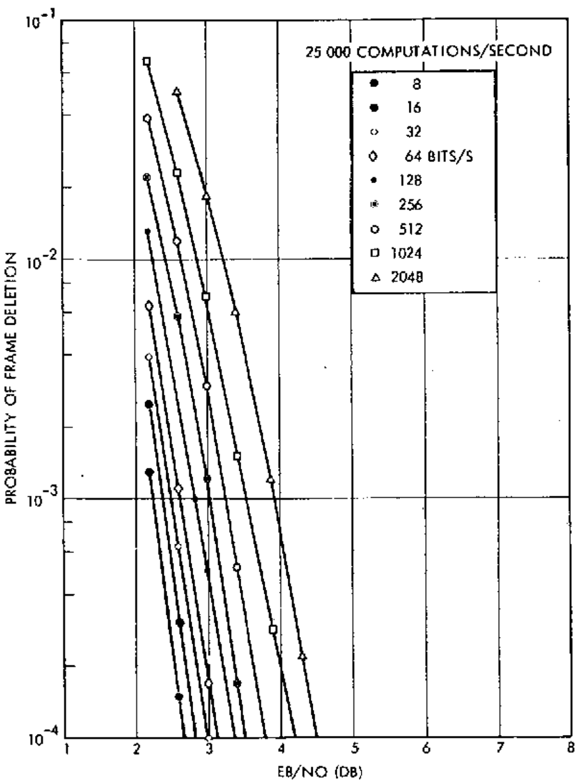

Figure 8.2A-1. Ideal Probability of Frame Deletion Versus E_B/N_0[']

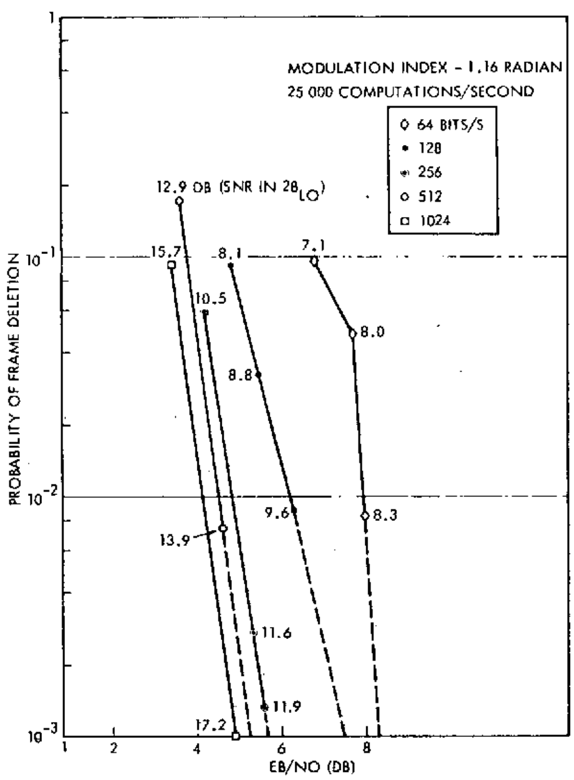

Figure 8.2A-2. Probability of Frame Deletion Versus E_B/N_0 (Receiver Loss Included)[']

[']UNPUBLISHED DATA FROM D. LUMB OF NASA/ARC

in the report, for data rates below 64 bit/s, are estimated to be below the receiver losses shown in Figure 8.2A-2 as long as a loop SNR of ≥10 dB is used. Also, for the lower bit rates at a fixed loop bandwidth (10 Hz) the burst length is not as great as for the higher bit rates and the decoding degradation is less. More simulation data is required to accurately arrive at the receiver losses for bit rates below 64 bits/s.

3. INTERLEAVING

3.1 Summary

Experimental CTA-21 (JPL) performance data by Dale Lumb of NASA/ARC for convolution coding of Pioneers 10 and 11 suggests the possible use of interleaving for further coding improvement. At 128, 64, or 32 bits/s, cycle slipping and memory effects due to the tracking loop bandwidth at less than 10 dB SNR in $2B_{LO}$ (10 Hz) can significantly degrade performance. At 10 dB SNR cycle slipping is probably negligible and coding improvement due to interleaving may be as much as 3 dB (at 5×10^{-3} frame deletion rate). If cycle slipping is assumed for the degradation at

10 dB, two frame interleaving may improve performance by as much as 2 dB. More experimental data at low SNR's and at deletion rates from 10^{-2} to 10^{-4} is required before a decision can be made to interleaving. Costs for including interleaving on the orbiter spacecraft are minimal, estimated at about $15 000. Estimated costs for adding deinterleaving into the DSN are unknown at present, but should be minimal compared to expected performance improvement. Interleaving on the probe bus would not enhance performance significantly since the design point is at 16 bits/s (probe release) where loop memory effects are almost negligible. Also, at bus entry the data rate (512 to 2048 bits/s) and loop SNR is high and memory effects are negligible.

3.2 Interleaving Improves Receiver Memory Loss

Sequential decoding performance is dominated by the frame deletion probability. Frame deletions are caused by the requirement for a large number of computations to decode a frame. Experimental and theoretical investigations have indicated that a frame deletion is most probably caused by a single sequence of high noise. For a memoryless channel, an error sequence of length b symbols has probability of occurrence of $2^{-c_1 b}$ where c_1 is a function of signal-to-noise ratio while the required number of computations to decode the b symbol error sequence is at least[1] $L = (1/2)2^{Rb}$ where R is the code rate. Thus, the pro ability of L computations or more to decode the b symbol error sequence is

$$
\begin{aligned}
P\,(C \quad L) &\simeq 2^{-c_1 b} \\
&= 2^{(-c_1/R)\,\log_2 2L} \\
&= (2L)^{-a}
\end{aligned}
\tag{1}
$$

where $a = c_1/R$. This is the Pareto distribution of computations that is characteristic of sequential decoding over a memoryless channel.

For a channel with memory, the probability of occurrence of an error sequence of length b is not exponentially decreasing with the length of the sequence (i. e., the probability of the error sequence is not some number raised to the b power). Thus, the computations distribution is not Pareto for channels with memory and severe degradation may be observed as the probability of long error sequences increases. To achieve the performance expected for the memoryless channel for channels with memory, an interleaver must be used to decrease the probability of long error sequences.

An example of a channel with memory is a demodulator containing a carrier tracking loop which may have slow variations of the phase error with time. For large signal-to-noise ratio α decreases, the phase error is very small and little of the memory effects are observed. As α decreases, the phase error can reach larger values and the degradation increases. If the loop bandwidth is small compared to the data rate, then the effect of the degradation will be observed over many symbols and significant memory (hence large number of computations) will be encountered by the sequential decoder. As α is decreased still further, loop slips will occur. If the loop reaches the 3.14 radian (180 degree) quasi-stable point, then the number of symbols corresponding to the loop time constant will be complemented. Phase slips have even a greater degradation on soft decision demodulation than hard decision because symbols that normally would be in the most probable quantization level will fall in a very improbable quantization level during phase slips.

To see the effects of the carrier tracking loop, consider Figure 8.2A-3. The curve for no interleaving was observed by Dale Lumb of NASA/ARC. The ideal coherent curve assumes a perfect phase reference, as was obtained from Dale Lumb's simulation results of the computations/second to be perfromed by the sequential decoder. Note that the losses due to the receiver, including the degradation due to phase error in the carrier tracking loop, have been subtracted from the original observations. Thus, the degradation shown in the figure is due to channel memory. As a worst case, assume that the degradation is due to phase slips. Since the probability of frame deletion of the ideal coherent channel is small compared to the observed results, it may be assumed that the probability of phase slip is equal to the frame deletion probability. The loop bandwidth is 10 Hz; hence, assume approximately 26 symbols are complemented for each phase slip. Interleaving is assumed to randomize the 26 complemented symbols throughout the frame. Generally, it is considered adequate randomization if the interleaver period is at least 10 times

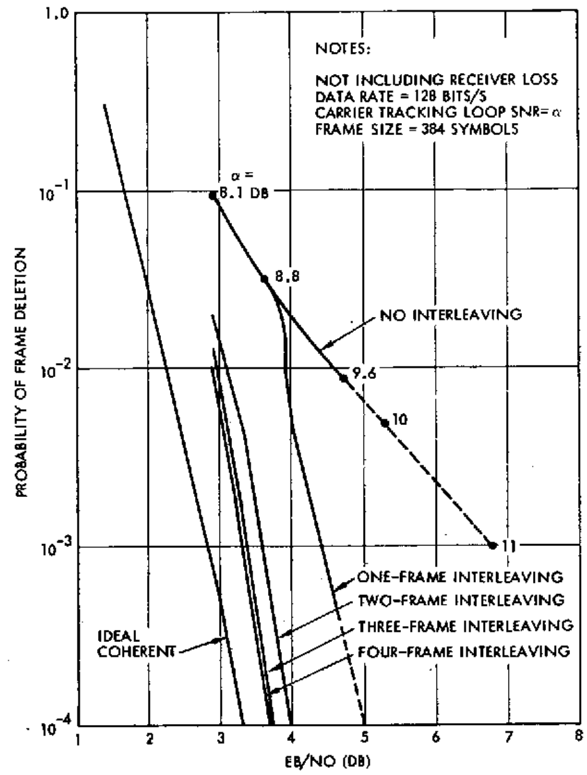

Figure 8.2A-3. Performance of Pioneers 10 and 11 Sequential Decoder with Interleaving

the length of the error burst. Thus, for one-frame interleaving assuming only one phase slip per frame the probability of frame deletion P_{fd} is

$$P_{fd} = (1 - p)\, P_{id} + P_{1b} \tag{2}$$

where p is the probability of a phase slip in a given frame, P_{id} is the probability of frame deletion for the ideal coherent channel, and P_{1b} is the probability of frame deletion for a 384 symbol frame containing 26 + (358) p_c errors, with probability of error p_c for the symbols not in the phase slip. Considering the probability that a phase slip falls in a frame is characterized by a binomial distribution, the probability of frame deletion for the frame interleaving is

$$P_{fd} = (1 - p)^2\, P_{id} + 2p\,(1 - p)\, P_{2b} + p^2\, P_{1b} \tag{3}$$

where P_{2b} is the probability of frame deletion for a frame containing $1/2\ (26 + (358)p_c)$ errors. Similarly, the probability of frame deletion is found for three and four-frame interleaving. Figure 8. 2A-3 indicates that there is only a small improvement by using four-frame interleaving rather than three-frame interleaving. but two-frame interleaving produces significant improvement over no interleaving and one-frame interleaving.

Previous studies[2] have indicated that for high values of α such as 10 dB, there is negligible degradation if the interleaver is 10 times the time constant of the tracking loop. In Figure 8. 2A-3, the results have been extrapolated for α = 10 and 11 dB. Using α = 10 dB and assuming phase slips, the two-frame interleaving reduces the required E_b/N_o by 2. 0 dB. However, if the assumption is made that the degradation observed is due only to channel memory, then there is negligible degradation from the ideal coherent channel by using one-frame interleaving. Therefore, interleaving reduces the required E_b/N_o by 2. 9 dB. Similarly, assuming phase slips for α = 11 dB, two-frame interleaving reduces the required E_b/N_o by 3. 2 dB. Assuming that the degradation is due only to channel memory, then one-frame interleaving reduces the required E_b/N_o by 4. 0 dB.

3. 3 Spacecraft Interleaver Costs

As a result of the potential improvement in telemetry performance due to interleaving, several data interleaver schemes have been investigated. The multiple, variable length, and multiple recirculating register approaches require more power and weight than does the matrix memory scheme. The latter was therefore selected for this costing exercise. See Figure 8. 2A-4 for the interleaver block diagram.

For each interleaver with a spread of 24 symbols over a coded frame of 384 symbols, there are two memories; one fills while the second dumps. The figure depicts a block diagram. There are no new part types used (the CMOS memories are presently planned into the DSU). For each interleaver the statistics are:

Parts - 23 ICs, seven discretes
Power - 0. 310 watts at +5. 3 volts
Weight - 0. 036 kilograms (0. 08 pounds)

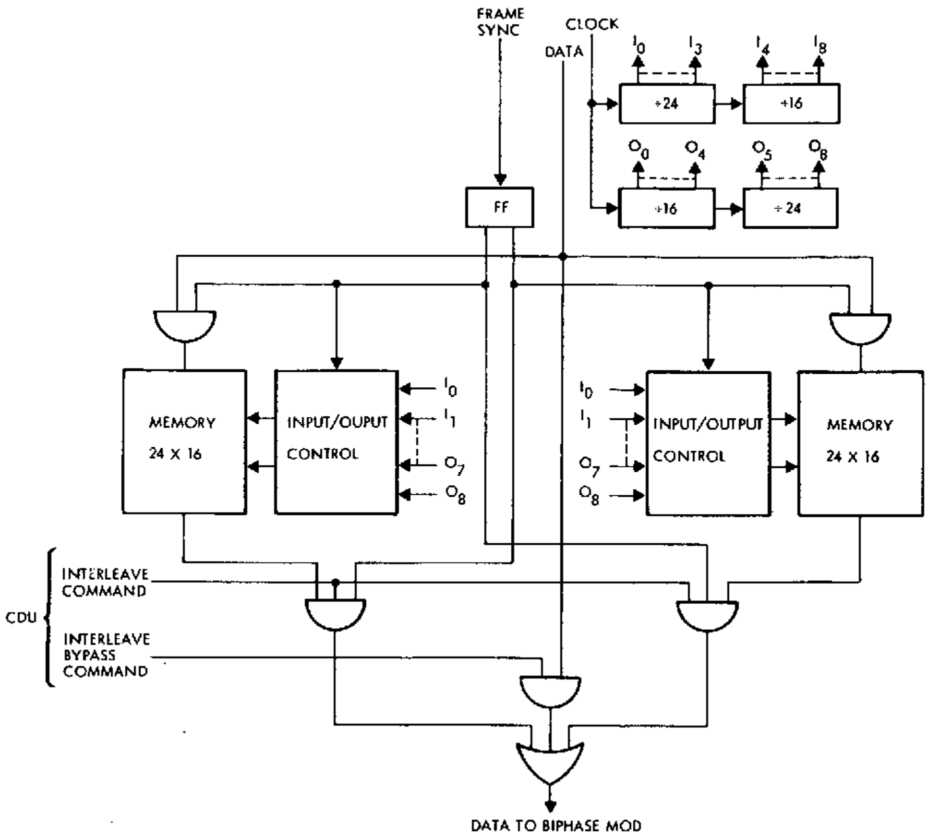

Figure 8.2A-4. Spacecraft Interleaver Implementation

Since modifications are planned for the DTU (with the attendant planning, inspection, retest, etc., already costed with these modifications), the delta costs for interleaving are modest (~$15 000).

For a 24-symbol spread over a coded frame of 768 symbols add approximately 20 percent to cost, power, and weight.

REFERENCES

1. I. M. Jacobs and E. R. Berlekamp, "A Lower Bound to the Distribution of Computations for Sequential Decoding," IEEE Trans. on Info. Theory, Vol. IT-13, No. 2, April 1967, pp 167-174.

2. C. R. Cahn, G. K. Huth, and C. R. Moore, "Simulation of Sequential Decoding with Phase-Locked Demodulation," IEEE Trans. on Comm. Tech.," Vol. COM-21, No. 2, February 1972, pp. 89-97.

APPENDIX 8.2B

DOPPLER CONSIDERATIONS

APPENDIX 8. 2B

DOPPLER CONSIDERATIONS

This appendix deals with the potential one-way and two-way doppler tracking problems that could exist during bus entry and, for a few orbits, during orbiter periapsis. It is shown that for bus entry the 64 meter station with a programmable receiver is required to maintain lock. Also, during worst-case orbits periapsis, doppler may cause loss of ground receiver lock in the 26 meter stations for a few minutes unless careful manual tuning is used.

1. PROBE BUS DOPPLER TRACKING AT ENTRY

1. 1 Summary

Just before entry the probe bus experiences a rapid gravitational acceleration causing a widely varying doppler shift in the uplink and downlink carrier frequencies. Figure 8. 2B-1 shows the doppler shift seen by the probe bus at entry, while Figure 8. 2B-2 shows the doppler seen by the ground station at Goldstone when the communication link is operating in a two-way mode. Figures 8. 2B-3 and 8. 2B-4 show the respective phase-locked loop phase errors resulting from a particular strategy of tuning out the doppler in both links. The analyses that produced these curves are given in the following section.

As shown in Figure 8. 2B-1 the uplink carrier frequency is tuned at 143 kHz above the assigned S-band carrier frequency. This tuning reduces the effective doppler shifts to about ±30 kHz, but does not affect the doppler rates. Nevertheless, assuming a Pioneer 10 and 11 receiver, the phase error remains within ±0. 052 radian (±3 degrees) so that the receiver will stay in phase lock.

The DSN receiver must employ a different tuning strategy, since it must contend with the much larger two-way doppler shifts and rates. The Block IV receiver to be used at the 64 meter stations has the required tuning capability. Its digital control oscillator can store and program four frequency ramps are shown by the dotted lines in Figure 8. 2B-2, and the resulting phase error indicates that the DSN receiver will track the two-way doppler.

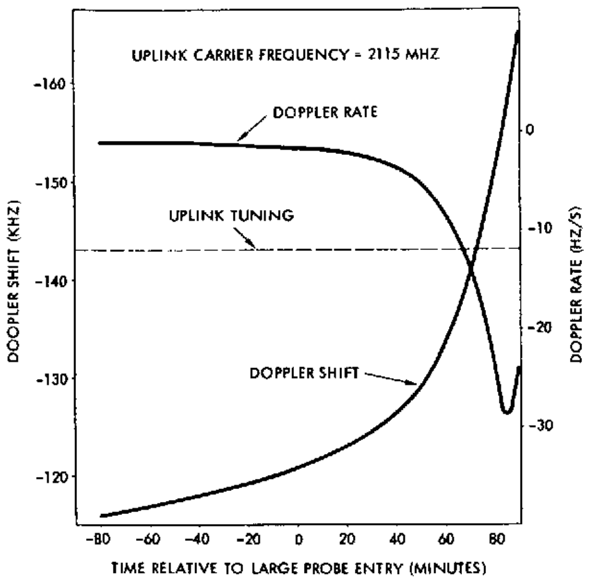

Figure 8.2B-1. Uplink Doppler Profiles Versus Time for Probe Bus at Entry

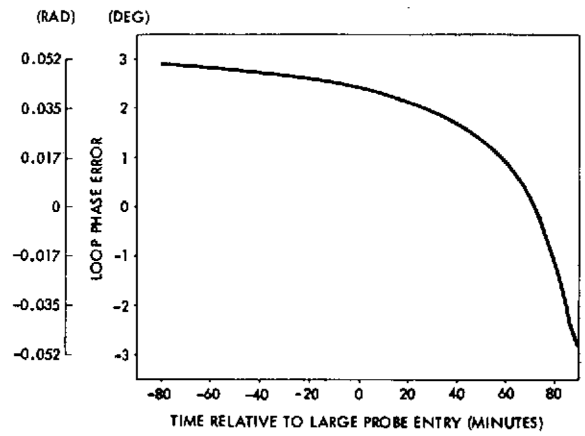

Figure 8.2B-3. Probe Bus Loop Phase Error Versus Time at Entry as Result of Uplink Tuning

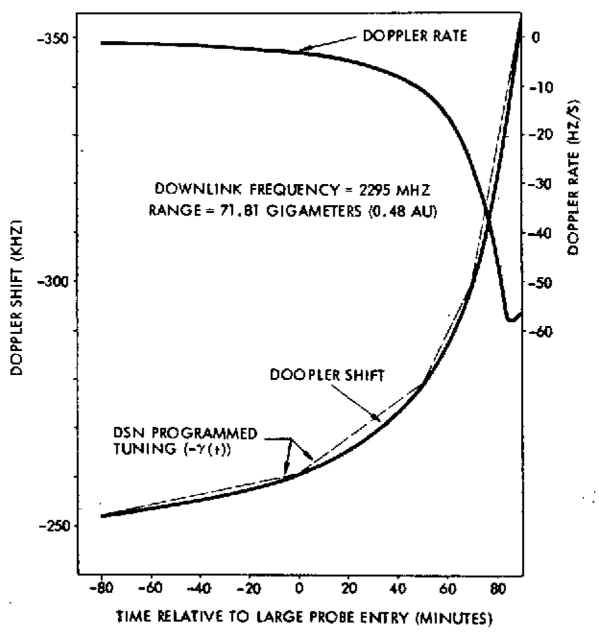

Figure 8.2B-2. Two-Way Doppler Profiles Versus Time for Bus at Entry as Seen at Goldstone

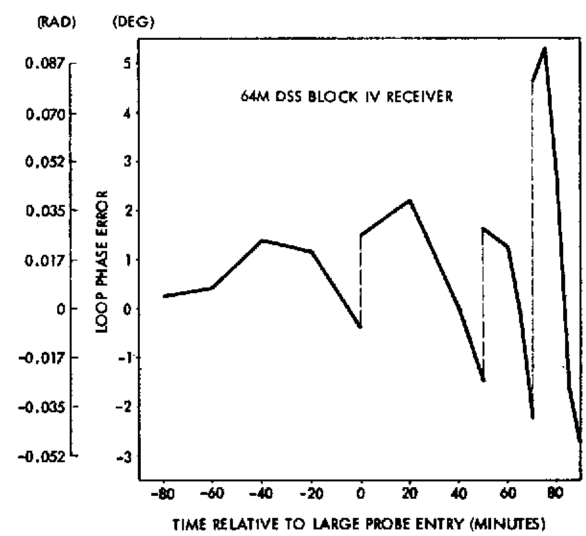

Figure 8.2B-4. Two-Way Loop Phase Error Versus Time for Bus at Entry as Result of DSN Tuning

1.2 Spacecraft Loop Phase Error Analysis (Uplink Only)

Assuming that the uplink signal level is very strong (SNR in $2B_{LO} >$ 25 dB), then the spacecraft's phase-locked loop can be modeled as a noiseless linear system. Let $f(t)$ and $\dot{f}(t)$ denote the doppler shift (radians) and doppler rate (radians/sec) of the incoming signal as a function of time.

Then the loop's steady state phase error (or static phase error) is given by (Reference 1)

$$\phi(t) = \frac{f(t)}{G} + \frac{\dot{f}(t)\ \tau_1}{G} \qquad (1)$$

where G is the loop gain and τ_1 is the larger of the two loop filter time constants.

Figures 8. 2B-5 and 8. 2B-6 show the downlink doppler and the doppler rate profiles for the probe bus during entry as seen at Goldstone.

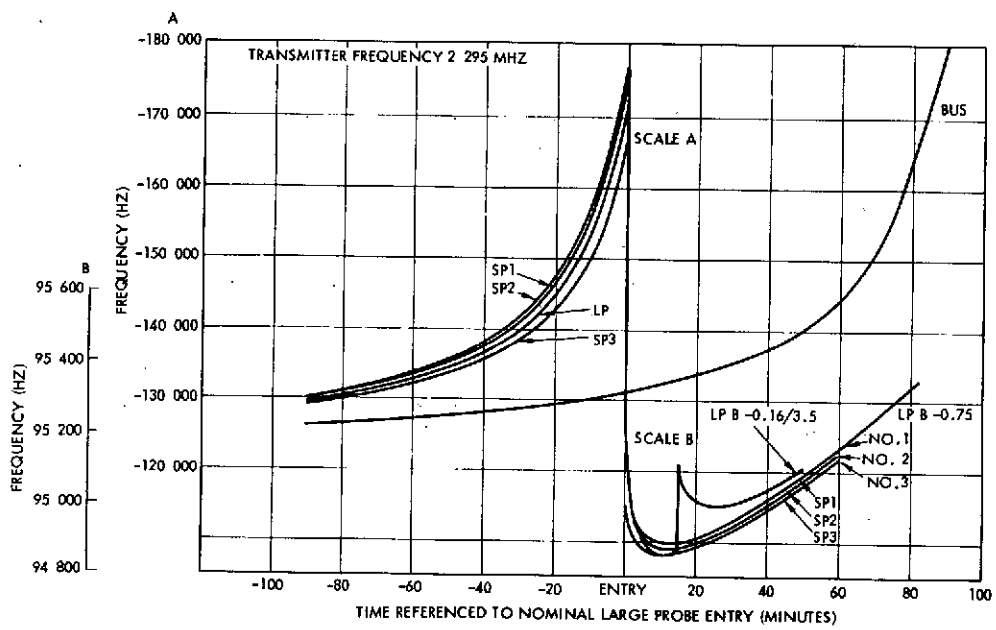

Figure 8. 2B-5. Preferred Probe Mission Doppler Shift for Goldstone Tracking Station

Assuming we are transmitting from Goldstone, then the doppler profiles for the uplink are just 221/240 times the downlink profiles. Reference 2 lists the following values for G and τ_1:

$$G = 3.23 \times 10^6 \text{ sec}^{-1}$$

$$\tau_1 = 100 \text{ sec}$$

Using this data in Equation (1) allows us to compute the phase error in the loop. The results are shown in Table 8. 2B-1 where it was assumed that

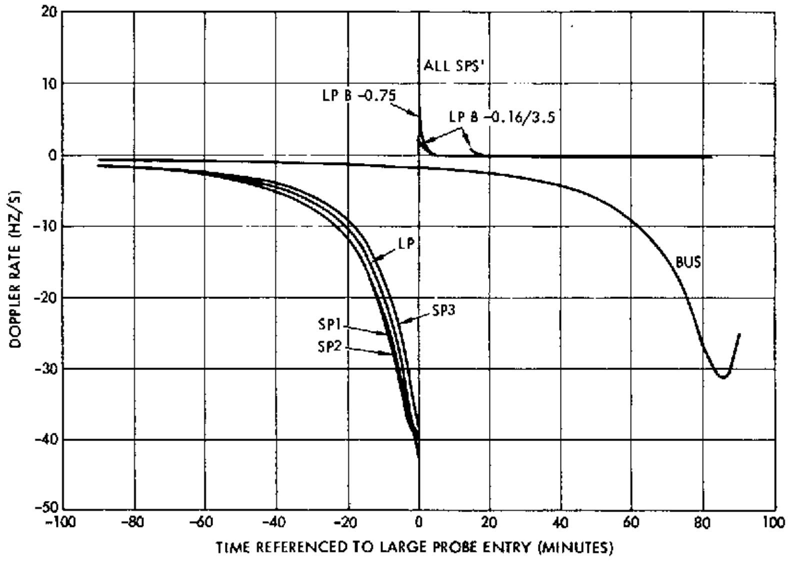

Figure 8.2B-6. Preferred Probe Mission Doppler Rate for Goldstone Tracking Station

Table 8.2B-1. Phase Error in the Probe Bus at Entry

TIME (MIN)	DOPPLER* (kHz)	DOPPLER RATE (Hz/SEC)	PHASE ERROR [RAD (DEG)]
-80	27	-1	0.051 (2.9)
-60	26	-1	0.049 (2.8)
-40	25	-1	0.047 (2.7)
-20	24	-1.5	0.045 (2.6)
0	22	-1.5	0.042 (2.4)
20	20	-2	0.038 (2.2)
40	17	-4	0.030 (1.7)
60	9	-8	0.016 (0.9)
73	0	-16	-0.003 (-0.2)
80	-9	-25	-0.023 (-1.3)
85	-18	-29	-0.038 (-2.2)
90	-23	-23	-0.049 (-2.8)

*NOTES: (1) DOPPLER SHIFT AND RATE DATA FROM FIGURES 8.2B-5 AND 8.2B-6 ARE MULTIPLIED BY 221/240.

(2) DOPPLER SHIFT IS RELATIVE TO -155 kHz.

the uplink transmitter was set at the uplink frequency plus 221/240 times 155 kHz (note that this tuning causes the doppler shift to be zero at t $\cong$ 73 minutes). The results definitely indicate that the receiver will track the incoming signal.

1.3 Coherent Two-Way Loop Phase Error Analysis

Previously it was shown that the spacecraft would remain in phase lock with a small loop phase error if the uplink frequency was tuned to compensate for the one-way doppler. This section considers the coherent two-way link with its associated two-way doppler. By using the capabilities of the dital control oscillator in the DSN's Block IV receiver, the major doppler effects can be tuned out. The result is that the ground station will stay in two-way phase lock during the entire entry sequence.

As in the previous report, strong signal conditions (loop SNR >25 dB) are assumed for both the uplink and the downlink, this being justified by the power budgets. Let $f_u(t)$ and $f_d(t)$ be the one-way doppler profiles for the uplink and downlink, respectively. Let K (= 240/221) be the frequency turnaround ratio in the spacecraft transponder and let T (= 4 minutes) be the one-way light time corresponding to the spacecraft range 71. 81 gigameters (0. 48 AU) at bus entry. Then, the doppler shift on the downlink due to two-way effects is

$$\begin{aligned} f_2(t) &= f_d(t) + K\, f_u(t - T) \\ &= f_d(t) + f_d(t - T) \end{aligned} \tag{2}$$

where $f_d = Kf_u$. Figure 8. 2B-7 shows a plot of $f_2(t)$ and its derivative $f_2(t)$ as seen by Goldstone at bus entry. It can be shown that if a constant frequency tuning method is used for the downlink, the ground loop phase error would be so large as to cause loss of lock. Thus, a different tuning method must be employed.

Let the ground transmitter be tuned at Δ Hz above the assigned S-band uplink frequency, and let the ground receiver be continuously tuned in time by the digital control oscillator. This receiver tuning can be represented mathematically by

$$f_r'(t) = f_r + \delta_0 + \delta_1 t \tag{3}$$

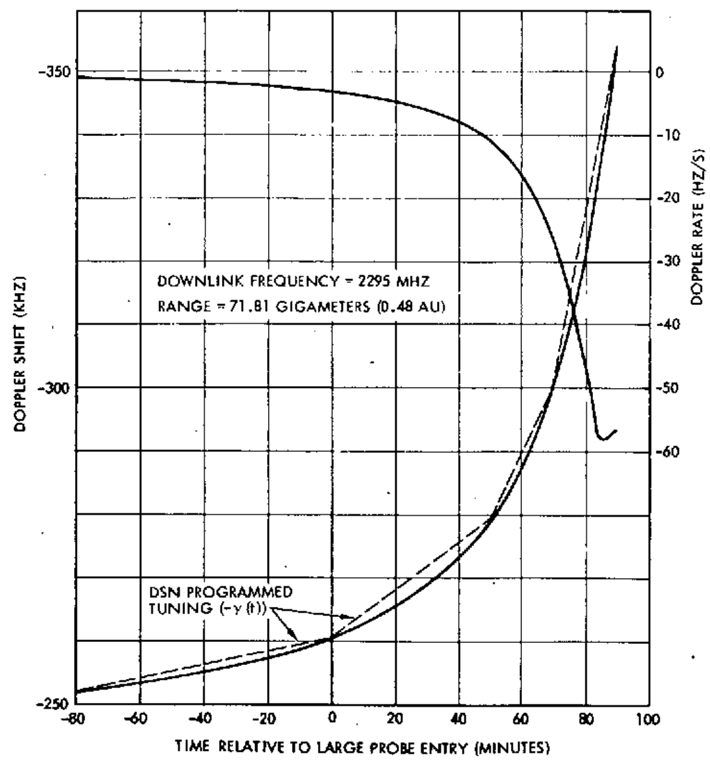

Figure 8.2B-7. Two-Way Doppler Profiles Versus Time for Bus at Entry As Seen at Goldstone

where f_r is the assigned S-band downlink frequency, δ_0 is a constant offset, δ_1 is a frequency rate, and t is time. Then, as shown in the attachment, the ground loop phase error is given approximately by

$$\phi(t) = \frac{1}{G}\left[K\Delta + \delta_0 + \delta_1 t + f_2(t)\right] + \frac{\tau_1}{G}\left[\delta_1 + \dot{f}_2(t)\right] \tag{4}$$

where G is the loop gain constant and τ_1 is the larger of the two filter time constant. Reference 2 lists the following values for G and τ_1:

$$\frac{1}{G} = 0.013 \text{ rad } (0.75 \text{ deg})/\text{kHz}$$

$$\frac{\tau_1}{G} = 0.004 \text{ rad } (0.25 \text{ deg})/\text{Hz/s}$$

It is convenient to rewrite Equation (4) by letting $\gamma(t) = K\Delta + \delta_0 + \delta_1 t$ represent the total tuning caused by the uplink and downlink. Thus Equation (2) becomes

$$\phi(t) = \frac{1}{G}\left[\gamma(t) + f_2(t)\right] + \frac{\tau_1}{G}\left[\dot{\gamma}(t) + \dot{f}_2(t)\right] \tag{5}$$

Figure 8.2B-7 also shows $-\gamma(t)$ for a particular choice of tuning. The four (dotted) straight lines reflect the capability of the digital control oscillator to store and program four frequency ramps. The slopes of these lines are (from left to right) 2, 5.5, 18, and 45.4 Hz/s. The phase error associated with this tuning strategy is shown in Figure 8.2B-8. The jumps in phase error indicated by the dotted lines in Figure 8.2B-8 correspond to the jumps in slope of the straight lines in Figure 8.2B-7. Since the magnitude of the phase error does not exceed 0.105 radian (6 degrees), the ground receiver will stay in phase lock during entry.

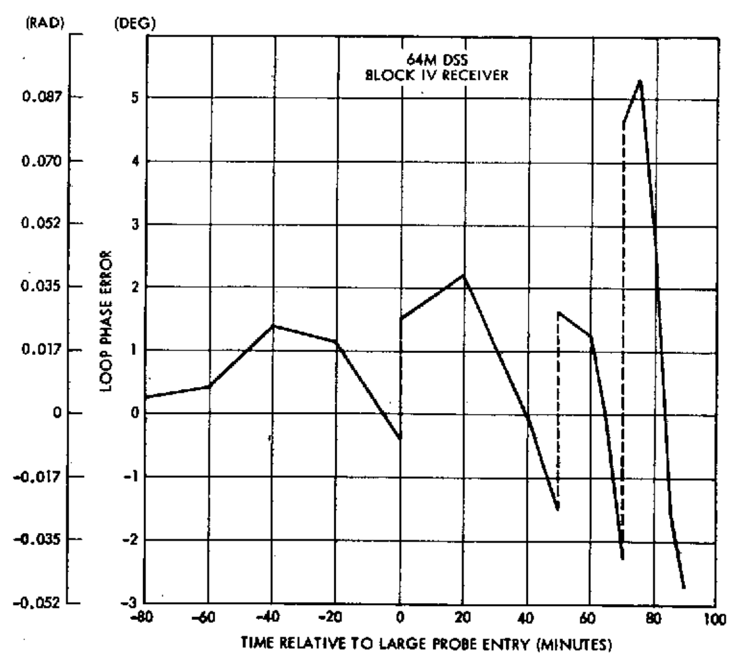

Figure 8.2B-8. Two-Way Loop Phase Error Versus Time for Bus At Entry As Result of DSN Tuning

1.4 Coherent Two-Way Communication System Doppler Effect

The following analysis considers the effects of doppler on a coherent two-way communication system employing an uplink carrier, a coherent "uplink" transponder, and a coherent "downlink" receiver. Specifically, an expression is derived giving the phase error in the downlink receiver phase-locked loop (PLL). Furthermore, it is shown that this phase error can be made arbitrarily small by tuning both the uplink carrier frequency and the downlink receiver frequency to compensate for the doppler shifts.

The coherent two-way link is modeled as the cascade of two PLL's. Assuming that the SNR's in the uplink and downlink loops are very large (>30 dB) allows us to use linear PLL theory. The resultant model is shown in Figure 8.2B-9 where the Θ's represent carrier phases relative to the rest frequencies of the two loops.

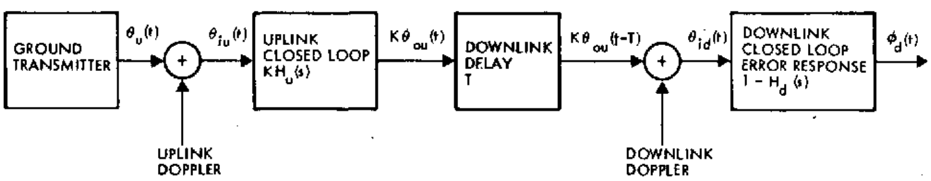

Figure 8.2B-9. Linear Model of Two-Way Coherent Link

The doppler shift is related to the movement of the spacecraft in time. If the range of the spacecraft is denoted by r(t), then the doppler shift is given by

$$f(t) = -\frac{f_c}{c} \dot{r}(t) \tag{6}$$

where f_c is either the uplink or downlink carrier frequency in Hertz, c is the speed of light in meters/second, and $\dot{r}(t)$ is the first derivative of the range (velocity). From Equation (6) we can see that the uplink doppler, $f_u(t)$, is related to the downlink doppler, $f_d(t)$, by the turnaround ration, K; or

$$f_d(t) = K\, f_u(t) \tag{7}$$

The transmitted uplink signal (neglecting command) is

$$\sqrt{2P_u} \cos\,(2\pi\, f_{cu} t + \phi_{0u})$$

where f_{cu} is the carrier frequency (assumed equal to the uplink PLL rest frequency) and ϕ_{0u} is a constant phase offset. The doppler adds the phase factor $\int^t f_u(y)\, dy$ so that the phase input to the uplink PLL is

$$\Theta_{iu}(t) = \phi_o u + \int^t f_u(y)\, dy \tag{8}$$

The output phase of the uplink PLL is linearly related to the input phase by the closed loop transfer function $H_u(s)$. For a second order loop this function is given by (Reference 1)

$$H_u(s) = \frac{1 + \tau_{2u}\, s}{1 + (\tau_{2u} + \frac{1}{G_u})\, s + \frac{\tau_{1u}}{G_u}\, s^2} \tag{9}$$

From Equation (9) it can be shown that the output phase is asymptotically

$$\Theta_{ou}(t) = \Theta_{iu}(t) + \tau_{2u}\, \dot{\Theta}_{iu}(t) \tag{10}$$

where f_{cd} is the downlink carrier frequency. The doppler adds $\int^t f_d\, (y)\, dy$ so that the phase input to the downlink receiver is

$$\Theta_{id}(t) = \phi_{0d} + \int^t f_d\, (y)\, dy + K\, \Theta_{ou}\, (t - T) \tag{11}$$

where ϕ_{0d} is a constant phase offset. Note that the phase factor due to uplink effects is delayed by the one-way light time T.

The downlink loop phase error is linearly related to the input phase by the closed loop transfer function $1 - H_d(s)$. Using an expression for $H_d(s)$ similar to Equation (9) it can be shown that the loop phase error is asymptotically

$$\phi_d(t) = \frac{1}{G_d} \left[\dot{\Theta}_{id}(t) + \tau_{id}\, \ddot{\Theta}_{id}(t)\right] \tag{12}$$

Substituting Equations (7), (8), (10) and (11) into (12) yields

$$\phi_d(t) = \frac{1}{G_d}\left[f_d(t) + f_d(t - T) + \tau_{2u}\,\dot{f}_d(t - T)\right] \tag{13}$$

$$+ \frac{1d}{G_d}\left[f_d(t) + f_d(t - T) + \tau_{2u}\,\ddot{f}_d(t - T)\right]$$

The factors involving τ_{2u} are usually small compared to the rest so they can be neglected. Defining the two-way doppler as

$$f_2(t) = f_d(t) + f_d(t - T) \tag{14}$$

the Equation (13) becomes

$$d(t) = \frac{1}{G_d}\left[f_2(t) + \tau_{1d}\, f_2(t)\right] \tag{15}$$

It is obvious from Figure 8.2B-7 that the two-way doppler and its derivative can be large, resulting in a large phase error and loss of lock. Of course, the loop constants G_{1d} and τ_{1d} can be so large that this would not be the case. Unfortunately, existing DSN receivers do not have loops designed to handle high doppler. One method to overcome this high doppler is to tune the frequency of both the uplink transmitter and the downlink receiver.

Suppose the uplink transmitted frequency is tuned in time by a frequency function $\Delta(t)$. Then the actual uplink frequency would be

$$f_{cu}'(t) = f_{cu} + \Delta(t) \tag{16}$$

Similar, the downlink receiver frequency is tuned by

$$f_{cd}'(t) = f_{cd} + (t) \tag{17}$$

Then the preceding analysis can be redone to yield a ground loop phase error given by

$$\phi_d'(t) = \frac{1}{G_d} \quad K\Delta(t - T) + \delta(t) + f_2(t) \tag{18}$$

$$+ \frac{1d}{G_d} \quad K\Delta(t - T) + \delta(t) + f_2(t)$$

Equation (18) shows that the phase error can be made arbitrarily small by appropriate choices of $\Delta(t)$ and $\delta(t)$.

2. ORBITER DOPPLER TRACKING AT ORBIT PERIAPSIS

The orbiter spacecraft has a doppler problem similar to the probe bus. The large doppler variations shown in Figure 8.2B-10 can occur at periapsis. Since the 26 meter tracking stations will probably be used for most of the orbiter mission, programmable oscillators will not be available to accurately tune out this doppler. Furthermore, since the SNR in

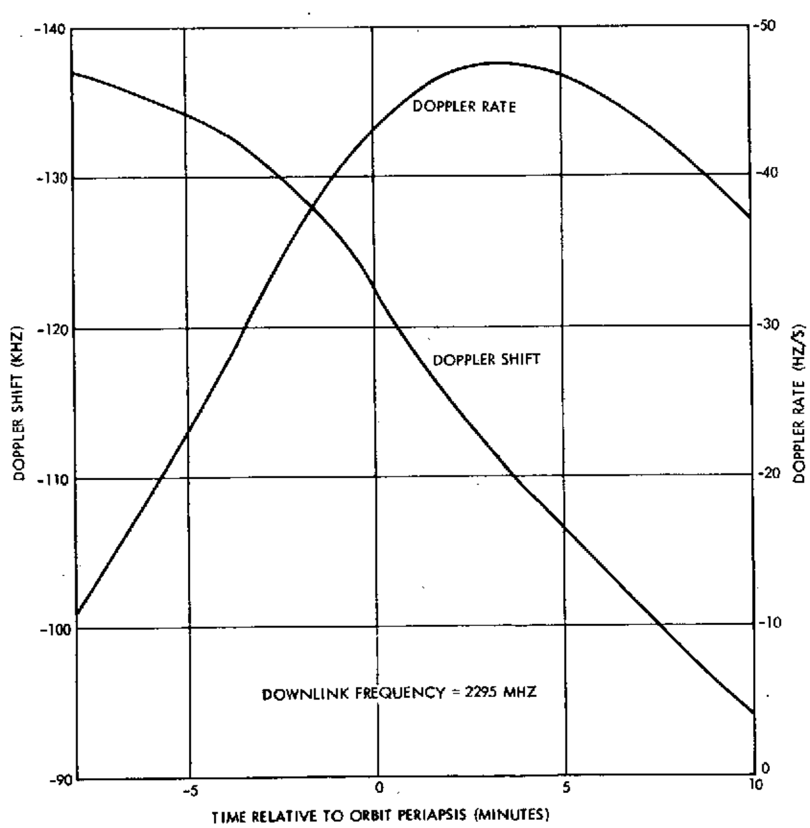

Figure 8.2B-10. Downlink Doppler Profiles Versus Time for Orbiter at Orbit Periapsis as Seen at Goldstone

the ground receiver loop will be about 12 dB at the end of the mission (zero adverse tolerance), data from the DSN Standard Practice document (810-5, Rev. C) indicates that the ground station loop error will be greater than 0.52 radian (30 degrees) for doppler rates of 50 Hz/s. About 0.14 radian (8 degrees) alone is experienced for a 20 kHz doppler shift. Thus, even if an offset doppler tuning strategy is employed, the loop will probably drop lock causing loss of data. Some ways to combat this adverse condition are to rely on experienced DSN operators to manually tune out the doppler, use the 64 meter stations at orbit periapsis, or store the data on board the spacecraft and play it back at a later time.

REFERENCES

1. "Telecommunications Systems Design Handbook," R. E. Edelson, ed., JPL TR33-571.

2. Pioneer F/G Receiver Specification.

3. "Block IV Prototype Receiver Assembly," JPL TRD-335-330).

APPENDIX 8.2C

POWER AMPLIFIER/ANTENNA OPTIMIZATION TRADEOFF

APPENDIX 8.2C

POWER AMPLIFIER/ANTENNA OPTIMIZATION TRADEOFF

The curves in Figure 8.2C-1 were generated to assist in sizing the minimum weight orbiter spacecraft design in terms of transmitter power, antenna size, and solar array weight. The criteria used in the analysis were minimum EIRP of 62 dBm [128 bits/s at 254.30 x 10^6 km (1.7 AU)] conical solar array 0.08 kg (0.10 lb/watt DC), and solid-state power amplifiers (30 percent efficiency). Curves are shown for two antenna configurations: a parabolic cylinder to be used with a configuration despun perpendicular to the earth-line, and a parabolic dish which could either be despun or used in an earth-pointing configuration. The antenna aperture efficiencies used in the analysis were 45 percent for the reflector and 55 percent for the dish. The feed for the reflector is a shortened Pioneer 6 through 9 center-fed Franklin array.

The curves show that as the power amplifier output is increased from 2 watts the weight savings increase to the vicinity of 9 watts before the weight savings begin to decrease. For the lower power outputs, the antenna sizing dominates the weight tradeoff, but for larger amplifier powers the solar array weight dominates as the required antenna size is reduced to a low value. The solid-state power amplifier weight influences the tradeoff curves only slightly as its weight varies from about 0.14 kilogram (0.3 pound) at the low power outpus to only about 1.8 kilogram (4 pounds) at 24 watts output.

A baseline power amplifier output of 10 watts minimum (11 watts nominal) was chosen to be compatible with the Helios reflector of 22.5 dB gain. Commonality with the probe bus transmitter of 6 watts is allowed by coupling two units together as can also be done with the probe transmitters. The 10-watt minimum transmitter also allows about 1 to 2 dB margin for the third midcourse and orbit insertion maneuvers.

A tradeoff was not performed for the fanbeam configuration [8 bit/s minimum at 254.30 x 10^6 km (1.7 AU)], since the Pioneer 6 through 9 11 dB antenna was assumed, requiring a transmitter power of 31 watts minimum.

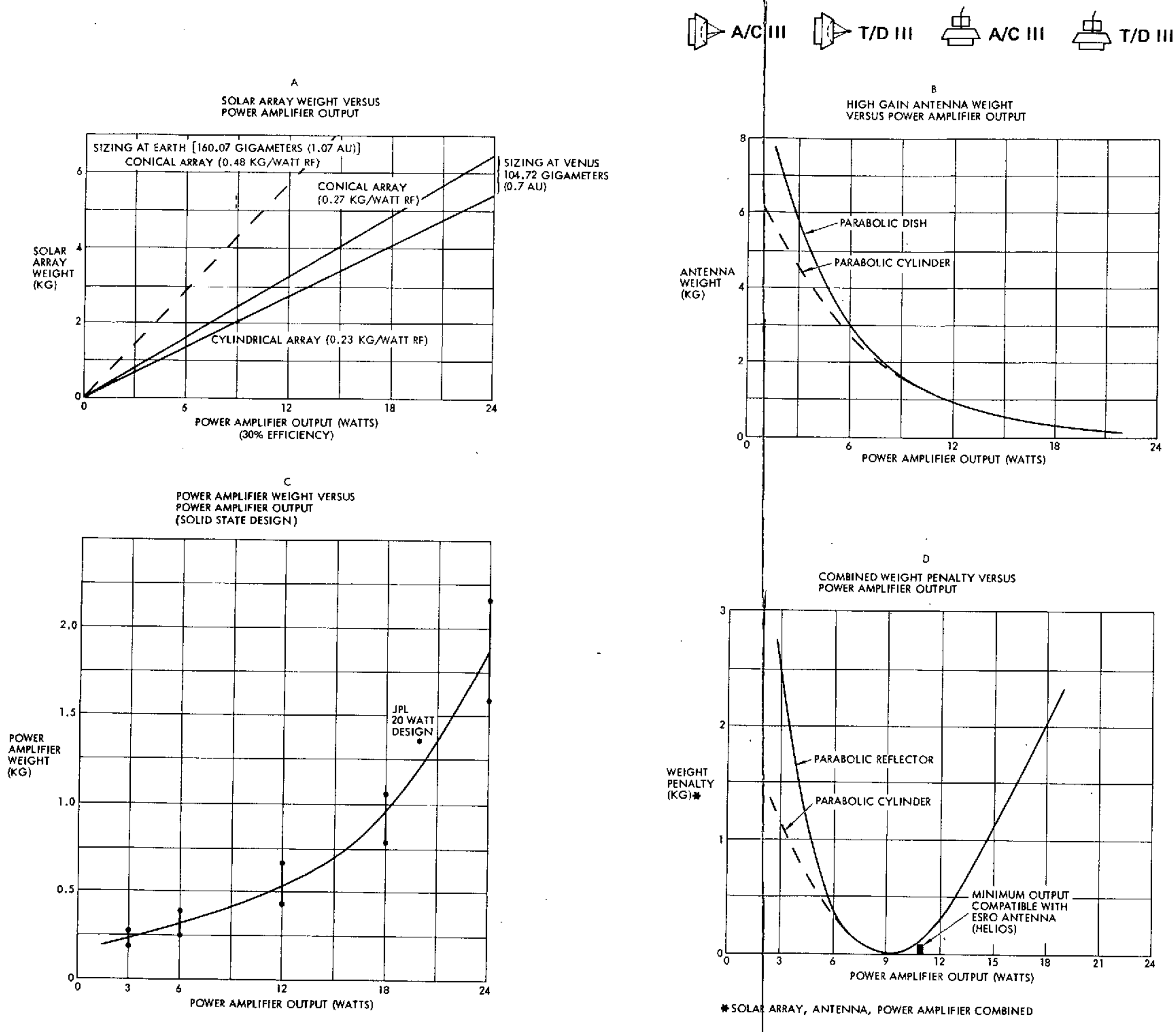

Figure 8.2C-1. Transmitter Power Output Optimization

APPENDIX 8. 3A

TELEMETRY REQUIREMENTS

APPENDIX 8.3A

TELEMETRY REQUIREMENTS

The following is a listing of the Pioneer Venus engineering and scientific instrument housekeeping telemetry measurements for the preferred probe bus and orbiter configurations based on the Atlas/Centaur launch vehicle. Unless otherwise noted, the Version IV science payload requirements have been applied. The telemetry measurements are identified as bilevel (discrete), analog, or digital signals. The bilevel measurements provide an operational status of spacecraft subsystems and scientific instruments, e.g., switching and position functions. Analog signals include voltage, temperature, and current measurements. The digital measurements provide quantitative information from the telemetry sources.

TELEMETRY - BUS

ELECTRICAL DISTRIBUTION

SPACECRAFT SEPARATION STATUS		BILEVEL	
COMMAND EXECUTE STATUS		BILEVEL	
SPACECRAFT ORDNANCE SAFE/ARM RELAY STATUS (PRIME)		BILEVEL	
SPACECRAFT ORDNANCE SAFE/ARM RELAY STATUS (REDNT)		BILEVEL	
UNDERVOLTAGE OVERRIDE STATUS		BILEVEL	
RECEIVER REVERSE STATUS		BILEVEL	
CDU +5 VDC BUS A SELECT STATUS		BILEVEL	
EQUIP CONV FAULT ISOLATOR STATUS	(4)	BILEVEL	(THOR/DELTA)
MAGNETOMETER BOOM RETRACT STATUS		BILEVEL	(THOR/DELTA)
MAGNETOMETER BOOM EXTENSION STATUS		BILEVEL	(THOR/DELTA)
ELECTRON TEMPERATURE PROBE ANT RELEASE STATUS		BILEVEL	
NEUTRAL MASS SPECTROMETER ION CAP EJECT STATUS		BILEVEL	
UV FLUORESCENT PROBE ANT RELEASE STATUS		BILEVEL	(THOR/DELTA)
LARGE PROBE RELEASE STATUS		BILEVEL	
LARGE PROBE CONNECTOR RELEASE STATUS		BILEVEL	
SMALL PROBE THERMAL SHIELD RELEASE STATUS	(3)	BILEVEL	
SMALL PROBE CONNECTOR RELEASE STATUS	(3)	BILEVEL	
SMALL PROBE RELEASE STATUS	(3)	BILEVEL	
RECEIVER REVERSE INHIBIT/ENABLE STATUS		BILEVEL	
CAPACITOR CHARGE STATUS (PRIMARY)	(2)	BILEVEL	
CAPACITOR CHARGE STATUS (REDUNDANT)	(2)	BILEVEL	

ELECTRICAL POWER

BATTERY AUTOMATIC CHARGE MODE STATUS		BILEVEL
BATTERY DISCHARGE ENABLE/DISABLE STATUS		BILEVEL
CHARGE RATE 1 ON/OFF STATUS		BILEVEL
CHARGE RATE 2 ON/OFF STATUS		BILEVEL
CHARGE RATE 3 ON/OFF STATUS		BILEVEL
LARGE PROBE POWER ON/OFF STATUS		BILEVEL
SMALL PROBE 1 POWER ON/OFF STATUS		BILEVEL
SMALL PROBE 2 POWER ON/OFF STATUS		BILEVEL
SMALL PROBE 3 POWER ON/OFF STATUS		BILEVEL
CTRF INVERTER TRANSFER RELAY STATUS		BILEVEL
CTRF INVERTER TEMP		ANALOG
BATTERY CHARGE CURRENT		ANALOG
BATTERY DISCHARGE CURRENT		ANALOG
BATTERY VOLTAGE		ANALOG
BATTERY TEMPERATURE		ANALOG
DC BUS VOLTAGE		ANALOG
DC BUS VOLTAGE, EXPANDED		ANALOG
DC BUS CURRENT		ANALOG
SHUNT BUS CURRENT		ANALOG
TRF +5 VDC CDU OUTPUT CHANNEL A		ANALOG
TRF +5 VDC CDU OUTPUT CHANNEL B		ANALOG

DATA HANDLING

CONVOLUTION CODE GEN STATUS		BILEVEL
ROLL REFERENCE		BILEVEL
SPIN AVERAGING MODE		BILEVEL
ACS OPERATION MODE		BILEVEL
DECODER A STATUS		BILEVEL
DECODER B STATUS		BILEVEL
A/D CALIB VOLTAGE, LOW		ANALOG
A/D CALIB VOLTAGE, MED		ANALOG
A/D CALIB VOLTAGE, HIGH		ANALOG
ROLL ATTITUDE WORD LINES	(2)	DIGITAL
EXTENDED S.C. ID		DIGITAL
SPIN PERIOD WORD LINES	(3)	DIGITAL
PROBE DATA WORD LINES	(4)	DIGITAL

COMMUNICATIONS

RECEIVER A SIGNAL PRESENT STATUS		BILEVEL
RECEIVER B SIGNAL PRESENT STATUS		BILEVEL
RECEIVER A COHERENT MODE STATUS		BILEVEL
RECEIVER B COHERENT MODE STATUS		BILEVEL
RECEIVER A OSC ENABLE/DECODER STATUS		BILEVEL
RECEIVER B OSC ENABLE/DECODER STATUS		BILEVEL
POWER AMP A/B SELECT		BILEVEL
POWER AMP A HIGH/LOW STATUS		BILEVEL (THOR/DELTA)
POWER AMP DRIVER A/B SELECT		BILEVEL
POWER AMP B HIGH/LOW STATUS		BILEVEL (THOR/DELTA)
TRANSFER SWITCH 1 POSITION STATUS		BILEVEL
TRANSFER SWITCH 2 POSITION STATUS		BILEVEL
TRANSFER SWITCH 3 POSITION STATUS		BILEVEL
TRANSFER SWITCH 4 POSITION STATUS		BILEVEL
RECEIVER A LOOP STRESS		ANALOG
RECEIVER B LOOP STRESS		ANALOG
RECEIVER A VCO TEMP		ANALOG
RECEIVER B VCO TEMP		ANALOG
RECEIVER A SIGNAL STRENGTH		ANALOG
RECEIVER B SIGNAL STRENGTH		ANALOG

ATTITUDE CONTROL

AXIAL THRUSTER INITIATION STATUS	(4)	BILEVEL
TRANSVERSE THRUSTER INITIATION STATUS	(4)	BILEVEL
SUN SENSOR TEMP		ANALOG
THRUSTER TEMPERATURES	(8)	ANALOG
PROPELLANT PRESSURE		ANALOG
DATA WORD LINES	(4)	DIGITAL
THRUSTER PULSE COUNTERS	(8)	DIGITAL

THERMAL

PROPELLANT HEATER ENABLE/DISABLE STATUS		BILEVEL
PROPELLANT TEMP		ANALOG
PLATFORM TEMPERATURES	(4)	ANALOG

SCIENCE

MAGNETOMETER	(SCIENCE III)
POWER ON/OFF STATUS	BILEVEL
CALIBRATE MODE STATUS	BILEVEL
DATA RATE HI/LO STATUS	BILEVEL
DATA WORD LINE	DIGITAL
UV FLUORESCENCE	(SCIENCE III)
POWER ON/OFF STATUS	BILEVEL
FURNACE CURRENT MODE 1 ON/OFF STATUS	BILEVEL
FURNACE CURRENT MODE 2 ON/OFF STATUS	BILEVEL
FURNACE CURRENT MODE 3 ON/OFF STATUS	BILEVEL
FURNACE CURRENT MODE 4 ON/OFF STATUS	BILEVEL
CALIBRATE MODE STATUS	BILEVEL
HOUSEKEEPING	ANALOG
DATA WORD	DIGITAL
ION MASS SPECTROMETER	
POWER ON/OFF STATUS	BILEVEL
CALIBRATE MODE STATUS	BILEVEL
DATA WORD LINE	DIGITAL

NEUTRAL PARTICLE MASS SPECTROMETER

POWER ON/OFF STATUS		BILEVEL
DATA WORD LINE		DIGITAL

ELECTRON TEMPERATURE PROBE

POWER ON/OFF STATUS		BILEVEL
DATA WORD LINE		DIGITAL

UV SPECTROMETER

POWER ON/OFF STATUS		BILEVEL
DATA WORD LINE		DIGITAL

RETARDING POTENTIAL ANALYZER (SCIENCE IV)

POWER ON/OFF STATUS		BILEVEL
CALIBRATE MODE STATUS		BILEVEL
DATA RATE HI/LO STATUS		BILEVEL
DATA WORD LINE		DIGITAL

****

TELEMETRY - ORBITER

ELECTRICAL DISTRIBUTION

SPACECRAFT SEPARATION STATUS		BILEVEL
COMMAND EXECUTE STATUS		BILEVEL
SPACECRAFT ORDNANCE SAFE/ARM RELAY STATUS (PRIME)		BILEVEL
SPACECRAFT ORDNANCE SAFE/ARM RELAY STATUS (REDNT)		BILEVEL
SRM ORDNANCE SAFE/ARM MOTOR STATUS		BILEVEL
OVERVOLTAGE OVERRIDE STATUS		BILEVEL
RECEIVER REVERSE STATUS		BILEVEL
EQUIP CONV FAULT ISOLATION RELAY STATUS	(4)	BILEVEL (THOR/DELTA)
MAGNETOMETER BOOM RETRACTED STATUS		BILEVEL
MAGNETOMETER BOOM EXTENSION STATUS		BILEVEL
ELECTRON TEMPERATURE PROBE ANT RELEASE STATUS		BILEVEL
NEUTRAL MASS SPECTROMETER ION CAP EJECT STATUS		BILEVEL
UV SPECTROMETER SUN COVER EJECT STATUS		BILEVEL

RADAR ALTIMETER ANTENNA RELEASE		BILEVEL
CDU +5 V BUS A SELECT STATUS		BILEVEL
CDU +5 V BUS B SELECT STATUS		BILEVEL
RAM PLATFORM RELEASE STATUS		BILEVEL
CAPACITOR CHARGE STATUS (PRIMARY)	(2)	BILEVEL
CAPACITOR CHARGE STATUS (REDUNDANT)	(2)	BILEVEL
COMMAND MEMORY ID TO DTU		BILEVEL
COMMAND MEMORY ENABLE/DISABLE STATUS		BILEVEL
COMMAND MEMORY 1 CONTENTS - CMD 8 BITS	(16)	DIGITAL
COMMAND MEMORY 2 CONTENTS - TIME 8 BITS	(16)	DIGITAL
COMMAND MEMORY 3 CONTENTS - TIME 8 BITS	(16)	DIGITAL
COMMAND MEMORY 4 CONTENTS - ROUTING 3 BITS	(16)	DIGITAL

ELECTRICAL POWER

BATTERY AUTOMATIC CHARGE MODE STATUS		BILEVEL
BATTERY MAX CHARGE MODE STATUS		BILEVEL

BATTERY TRICKLE CHARGE STATUS		BILEVEL
BATTERY DISCHARGE ENABLE/DISABLE STATUS		BILEVEL
BATTERY HIGH TEMP PROTECTION STATUS		BILEVEL
BATTERY RECONDITION/DISCONNECT STATUS		BILEVEL
CTRE INVERTER TRANSFER RELAY STATUS		BILEVEL
BATTERY CHARGE CURRENT		ANALOG
BATTERY DISCHARGE CURRENT		ANALOG
BATTERY VOLTAGE		ANALOG
BATTERY TEMPERATURE		ANALOG
DC BUS VOLTAGE		ANALOG
DC BUS VOLTAGE EXPANDED		ANALOG
DC BUS CURRENT		ANALOG
SHUNT BUS CURRENT		ANALOG
TRE +5 VDC CDU OUTPUT CHANNEL A		ANALOG
TRE +5 VDC CDU OUTPUT CHANNEL B		ANALOG
EQUIPMENT CONVERTER TEMP		ANALOG (THOR/DELTA)
CTRE INVERTER TEMP		ANALOG

DATA HANDLING

CONVOLUTION CODE GEN STATUS		BILEVEL
ROLL REFERENCE		BILEVEL
SPIN AVERAGING MODE		BILEVEL
HIGH/LOW ALTITUDE STORE FORMAT STATUS		BILEVEL

DSU CONFIGURATION SELECT STATUS	(4)	BILEVEL
SCIENCE DATA STORAGE ENABLE	(2)	BILEVEL
ACS OPERATION MODE		BILEVEL
DECODER A STATUS		BILEVEL
DECODER B STATUS		BILEVEL
AD CALIB VOLTAGE, LOW		ANALOG
A/D CALIB VOLTAGE, MED		ANALOG
A/D CALIB VOLTAGE, HIGH		ANALOG
ROLL ALTITUDE WORD LINES	(2)	DIGITAL
EXTENDED S.C. ID		DIGITAL
SPIN PERIOD WORD LINES	(3)	DIGITAL

COMMUNICATIONS

RECEIVER A SIGNAL PRESENT STATUS		BILEVEL
RECEIVER B SIGNAL PRESENT STATUS		BILEVEL
RECEIVER A COHERENT MODE STATUS		BILEVEL
RECEIVER B COHERENT MODE STATUS		BILEVEL
POWER AMP A ON/OFF STATUS		BILEVEL
POWER AMP B ON/OFF STATUS		BILEVEL
POWER AMP C ON/OFF STATUS		BILEVEL (THOR/DELTA)
POWER AMP D ON/OFF STATUS		BILEVEL (THOR/DELTA)
RECEIVER A OSC ENABLE/DISABLE STATUS		BILEVEL
RECEIVER B OSC ENABLE/DISABLE STATUS		BILEVEL
TRANSFER SWITCH 1 POSITION STATUS		BILEVEL
TRANSFER SWITCH 2 POSITION STATUS		BILEVEL
TRANSFER SWITCH 3 POSITION STATUS		BILEVEL
TRANSFER SWITCH 4 POSITION STATUS		BILEVEL
TRANSFER SWITCH 5 POSITION STATUS		BILEVEL

TRANSFER SWITCH 6 POSITION STATUS		BILEVEL
CONSCAN THRESHOLD HIGH/LOW STATUS		BILEVEL
CONSCAN ON/OFF STATUS		BILEVEL
RECEIVER A LOOP STRESS		ANALOG
RECEIVER B LOOP STRESS		ANALOG
RECEIVER A VCO TEMP		ANALOG
RECEIVER B VCO TEMP		ANALOG
RECEIVER A SIGNAL STRENGTH		ANALOG
RECEIVER B SIGNAL STRENGTH		ANALOG
CONSCAN DATA WORD LINE		DIGITAL
ATTITUDE CONTROL		
AXIAL THRUSTER INITIATION STATUS	(4)	BILEVEL
TRANSVERSE THRUSTER INITIATION STATUS	(4)	BILEVEL
SUN SENSOR TEMP		ANALOG
THRUSTER TEMPERATURES	(8)	ANALOG
PROPELLANT PRESSURE		ANALOG
DATA WORD LINES	(4)	DIGITAL
THERMAL		
PROPELLANT HEATERS ENABLE/DISABLE STATUS		BILEVEL
RAM PLATFORM HEATER ENABLE/DISABLE STATUS		BILEVEL
SRM HEATER ENABLE/DISABLE STATUS		BILEVEL
PLATFORM TEMPERATURES	(4)	ANALOG
PROPELLANT TEMPERATURE		ANALOG
SCIENCE		
MAGNETOMETER		
POWER ON/OFF STATUS		BILEVEL
CALIBRATE MODE STATUS		BILEVEL
RANGE HIGH/LOW STATUS		BILEVEL
DATA WORD LINE		DIGITAL
RADAR ALTIMETER		
POWER ON/OFF STATUS		BILEVEL
TRANSMITTER ON/OFF STATUS		BILEVEL
CALIBRATE MODE ON/OFF		BILEVEL
DATA RATE HIGH/LOW STATUS		BILEVEL
MEMORY POWER ON/OFF STATUS		BILEVEL
DATA WORD LINE		DIGITAL
UV SPECTROMETER		
POWER ON/OFF STATUS		BILEVEL
CALIBRATE MODE STATUS		BILEVEL
DATA RATE HIGH/LOW STATUS		BILEVEL
HOUSEKEEPING		ANALOG
DATA WORD LINE		DIGITAL
ION MASS SPECTROMETER		
POWER ON/OFF STATUS		BILEVEL
CALIBRATE MODE STATUS		BILEVEL
DATA WORD LINE		DIGITAL
IR RADIOMETER		
POWER ON/OFF STATUS		BILEVEL
DATA WORD		DIGITAL
NEUTRAL PARTICLE MASS SPECTROMETER		
POWER ON/OFF STATUS		BILEVEL
DATA WORD LINE		DIGITAL

ELECTRON TEMPERATURE PROBE		
POWER ON/OFF STATUS		BILEVEL
DATA WORD LINE		DIGITAL
SOLAR WIND ANALYZER		
POWER ON/OFF		BILEVEL (NEW SCIENCE)
MODE CONTROL STATUS	(3)	BILEVEL (NEW SCIENCE)
DATA WORD LINE		DIGITAL (NEW SCIENCE)
X-BAND OCCULTATION		
POWER ON/OFF STATUS		BILEVEL (NEW SCIENCE)
DATA WORD LINE		DIGITAL (NEW SCIENCE)

APPENDIX 8. 3B

ALTERNATIVE DATA ACQUISITION AND COMMAND SYSTEM

APPENDIX 8. 3B

ALTERNATIVE DATA ACQUISITION AND COMMAND SYSTEM

The alternative data acquisition and command system (DACS) approach is midway between a programmable central processor and the more conventional dedicated telemetry and command system. The advantages of MOS LSI technology coupled with an advanced system architecture achieves high reliability, format efficiency and system flexibility while saving weight and power over the Pioneer 10 design. While the MOS LSI devices are a custom TRW design, they use a standardized, flight-qualified technology which can be readily manufactured by several companies.

Although the DACS for Pioneer Venus requires development, the system architecture and the MOS LSI arrays are fully developed and operational in a breadboard. This work is the result of a 1971 TRW IRAD program.

The basic DACS, Figure 8. 3B-1, consists of a central control unit (CCU) and remote terminal units (RTU's) which respond to CCU instructions. These units provide command distribution, telemetry data sampling and conditioning, and telemetry data formatting using programs stored in solid state read-only memories (ROM's). The DACS accommodates a number of RTU's either as part of the CCU or located within the spacecraft.

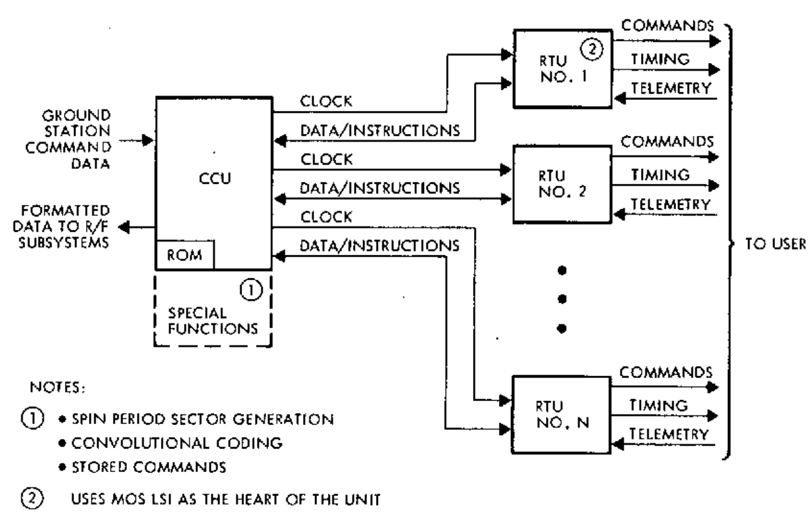

Figure 8. 3B-1. Data Acquisition and Command System

The telemetry format structure is determined by ROM-stored programs. This programmable flexibility optimizes the telemetry format for each mission. Different payload requirements are accommodated by adding RTU's with modular input/output, adaptable to the command and telemetry interface for each mission.

As shown in Figure 8. 3B-1, the CCU contains a special function section to accommodate mission peculiar functions not basic to the DACS All other portions of the DACS use a standard design from mission to mission.

The orbiter data system implementation using the existing Pioneer 10 units, is shown in Figure 8. 3B-2A, and the DACS in Figure 8. 3B-2B. The DACS replaces the DTU and five of eight CDU slices. All but a few Pioneer 10 CDU special functions (ordnance firing, high-level commands, undervoltage monitoring and event sequencing) are performed by the DACS.

The system advantages of the DACS over the Pioneer 10 design for the orbiter mission are:

- Better format flexibility. Formats are ROM programmable both for science and housekeeping telemetry
- More redundancy. Full redundancy is available for all telemetry
- More stored commands available. ROM stores commands
- Modular design to readily accommodate different command and telemetry requirements for each mission.
- More hardware commonality between missions. The same CCU design is used in the orbiter and probe mission and the same RTU design is used in the orbiter, probe bus and the probes.
- Saves weight. 1. 8 kilograms (4 pounds) are saved in the DAC orbiter data system (power is 200 mW less).

Figure 8. 3B-3A illustrates the implementation of the probe mission data system with the Pioneer 10 units, and Figure 8. 3B-3B with the DACS. As in the orbiter mission, the DACS replaces the DTU and all but three CDU slices. Redundant RTU's are used to provide the timing, command and telemetry functions required by the probe bus subsystems and science. One RTU is provided within each probe and forms the heart of each probe data system.

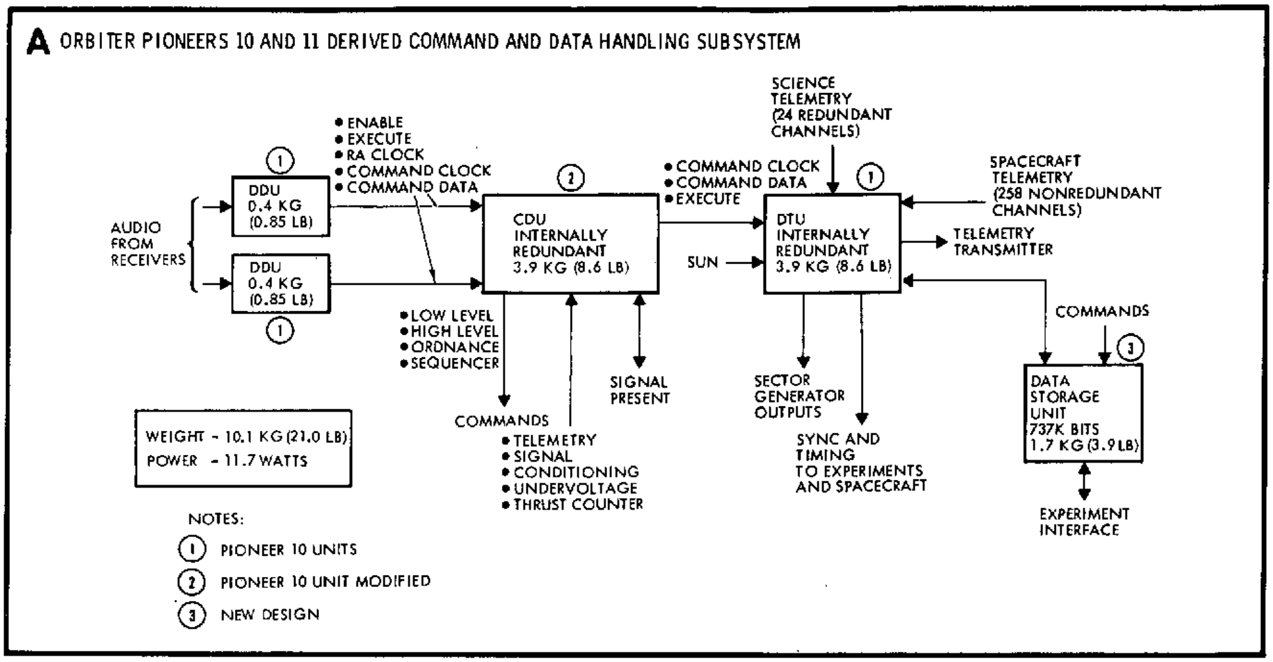

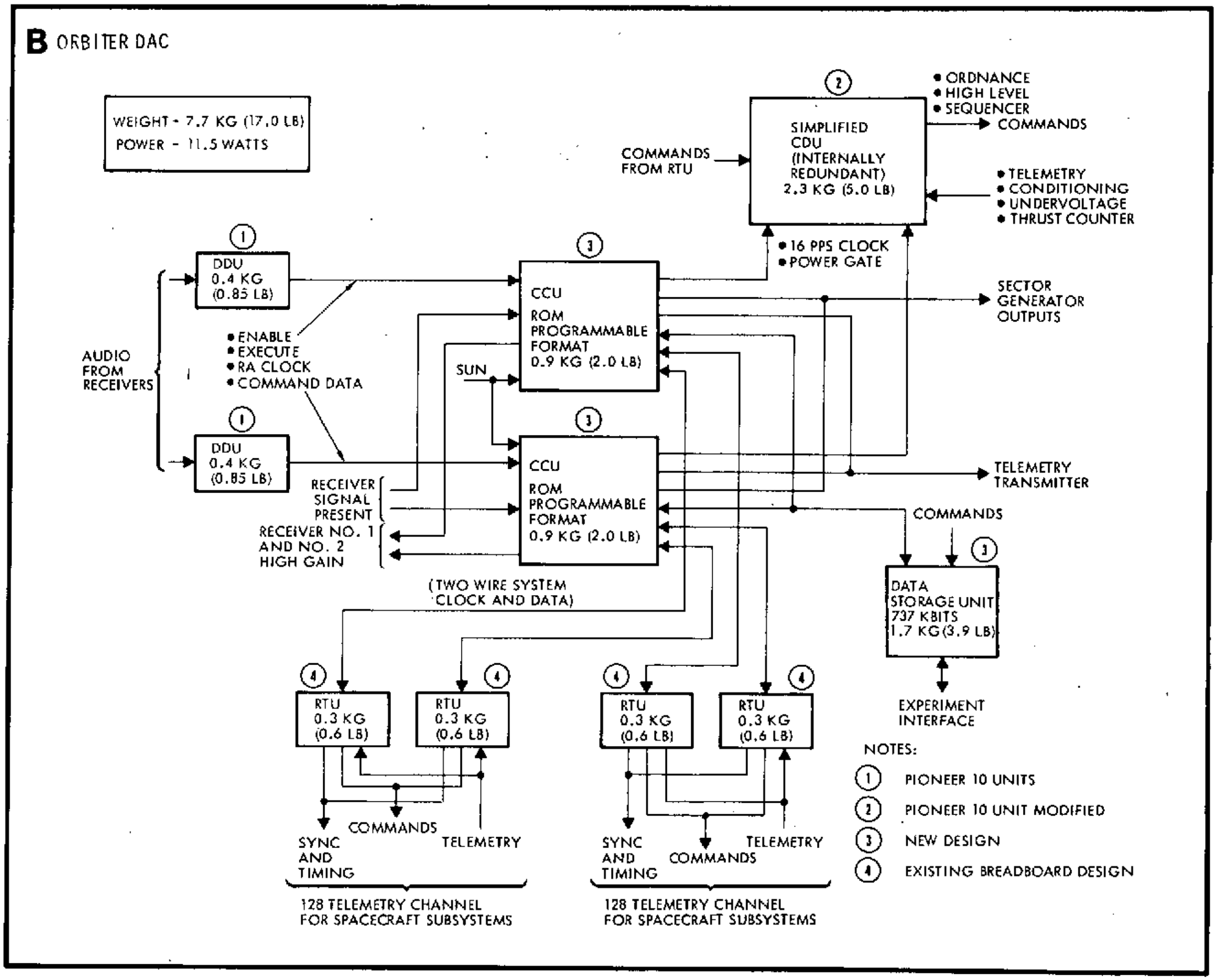

Figure 8.3B-2. Orbiter Configuration

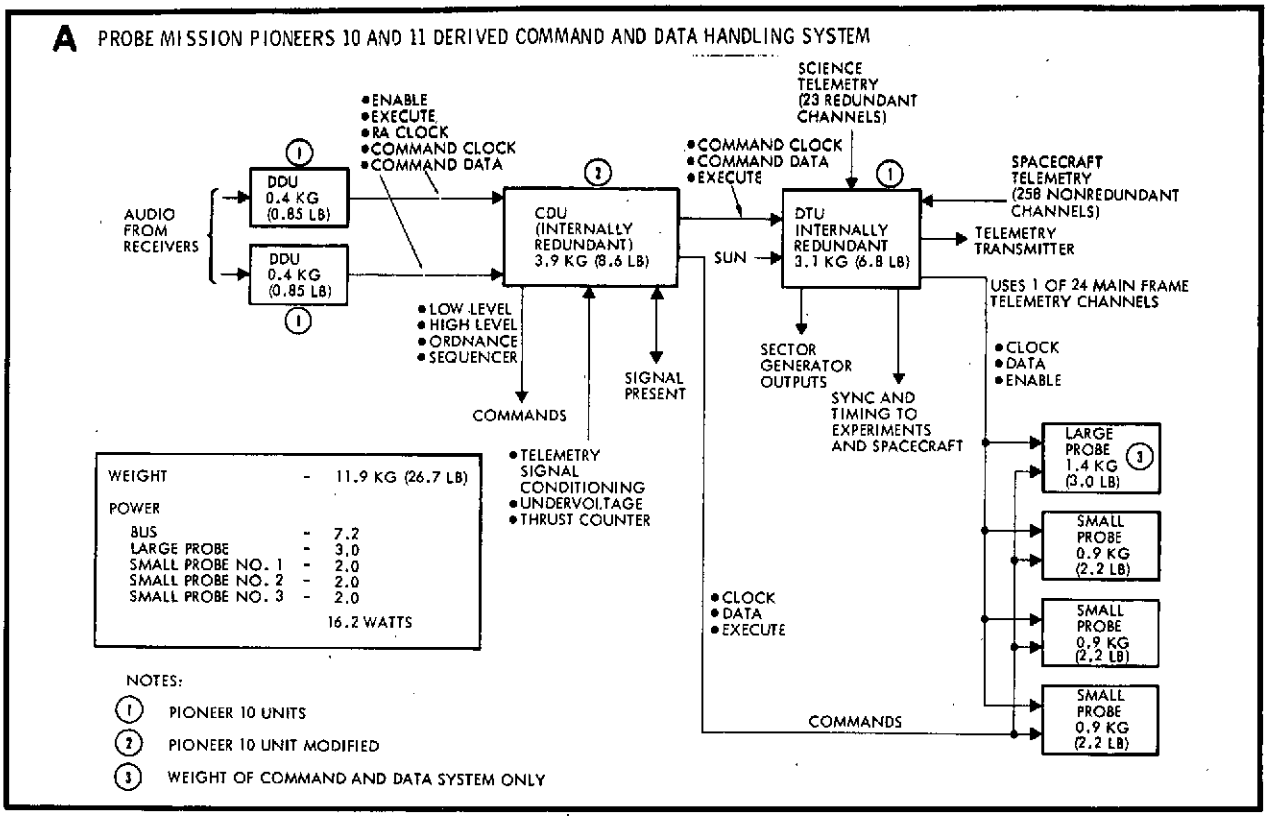

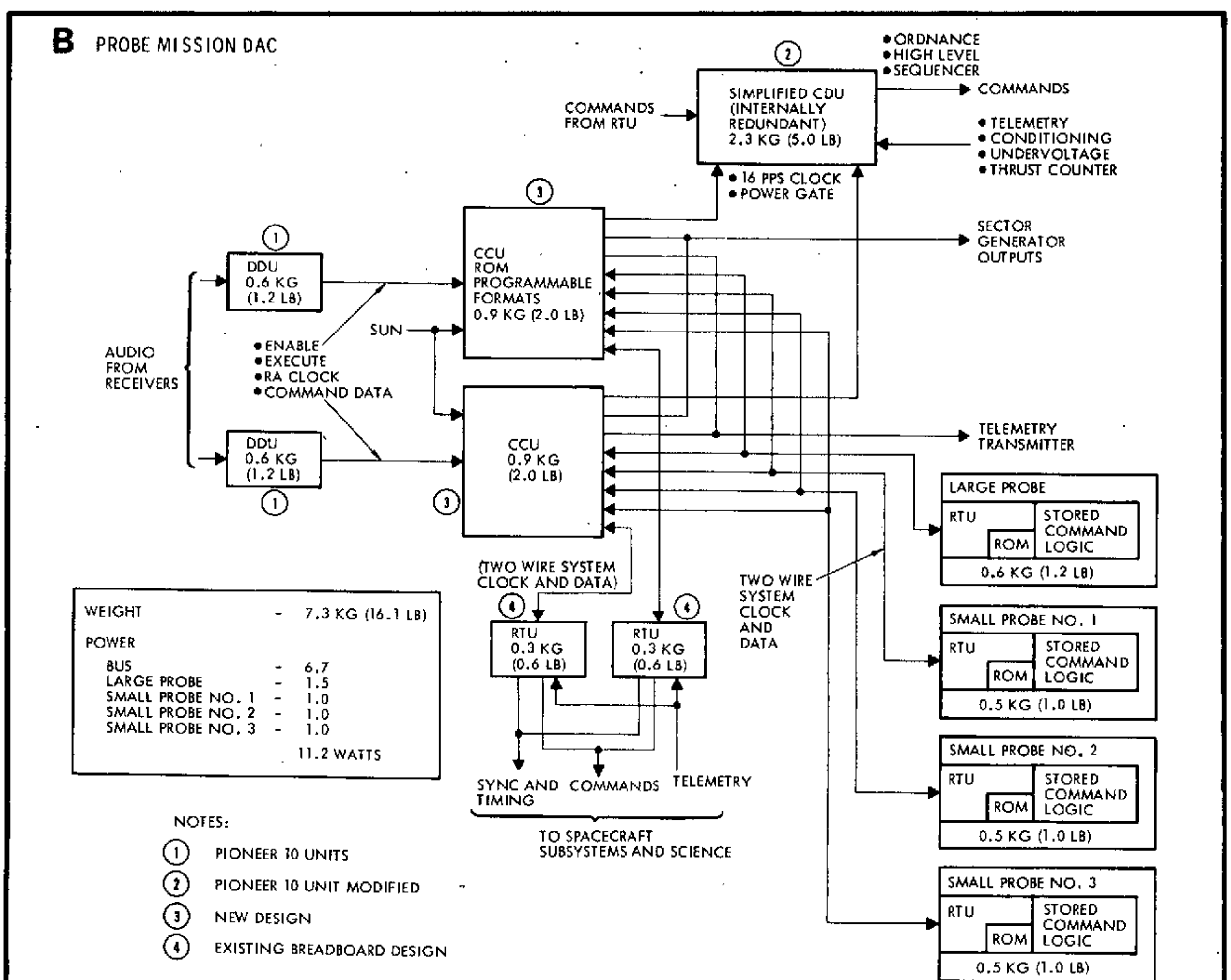

Figure 8.3B-3. Probe Configuration

The RTU operates either under the control of an external controller (CCU) or internally with its own ROM-stored program. This feature is ideally suited for the probe data system where the probe operation can be externally controlled for ground checkout or in-flight probe checkout, then operate autonomously, under its own program, during probe entry phases. This feature saves the addition of test hardware with attendant savings in weight and power. The DACS saves an estimated 4.8 kilograms (10.6 pounds) overall and 0.5 watt in the probe bus, 1.5 watts in the large probe, and 1.0 watt in each small probe.

The CCU, shown in Figure 8.3B-4, sends real-time and stored commands to, and collects telemetry data from, the RTU's. In addition, the CCU provides spacecraft spin sector output signals, convolutional coding and biphase modulation of the formatted data, and the necessary signal present logic to switch receivers.

Real-time commands are received from the Pioneer 10 DDU in groups of three commands (24 bits). The DACS requires 16 bits for address, mode selection, and command steering in addition to the eight actual command bits. Transmitting three commands each time is not necessarily a disadvantage since one DACS command is equivalent to eight Pioneer 10 commands. With the DACS, command decoding is performed by the ground station software, Pioneer 10 decoding is performed by spacecraft hardware. In the DACS, the actual eight command bits follow 16 bits which address a particular 8-bit RTU command output register. The command is routed through the system and ends up in the specified register. The register output is made available to the user as one 8-bit serial command or eight state or pulse commands. Transfer of serial commands can be either under user or RTU control.

Stored commands are programmed into a CCU ROM and are continually compared with a clock. When the stored time matches the clock, the command is processed by the DACS as a real-time command. Provision is made to load the start time in flight which is necessary when selecting redundant units.

Eight essential commands are provided directly from the CCU and are used primarily to select redundant spacecraft units such as CCU's

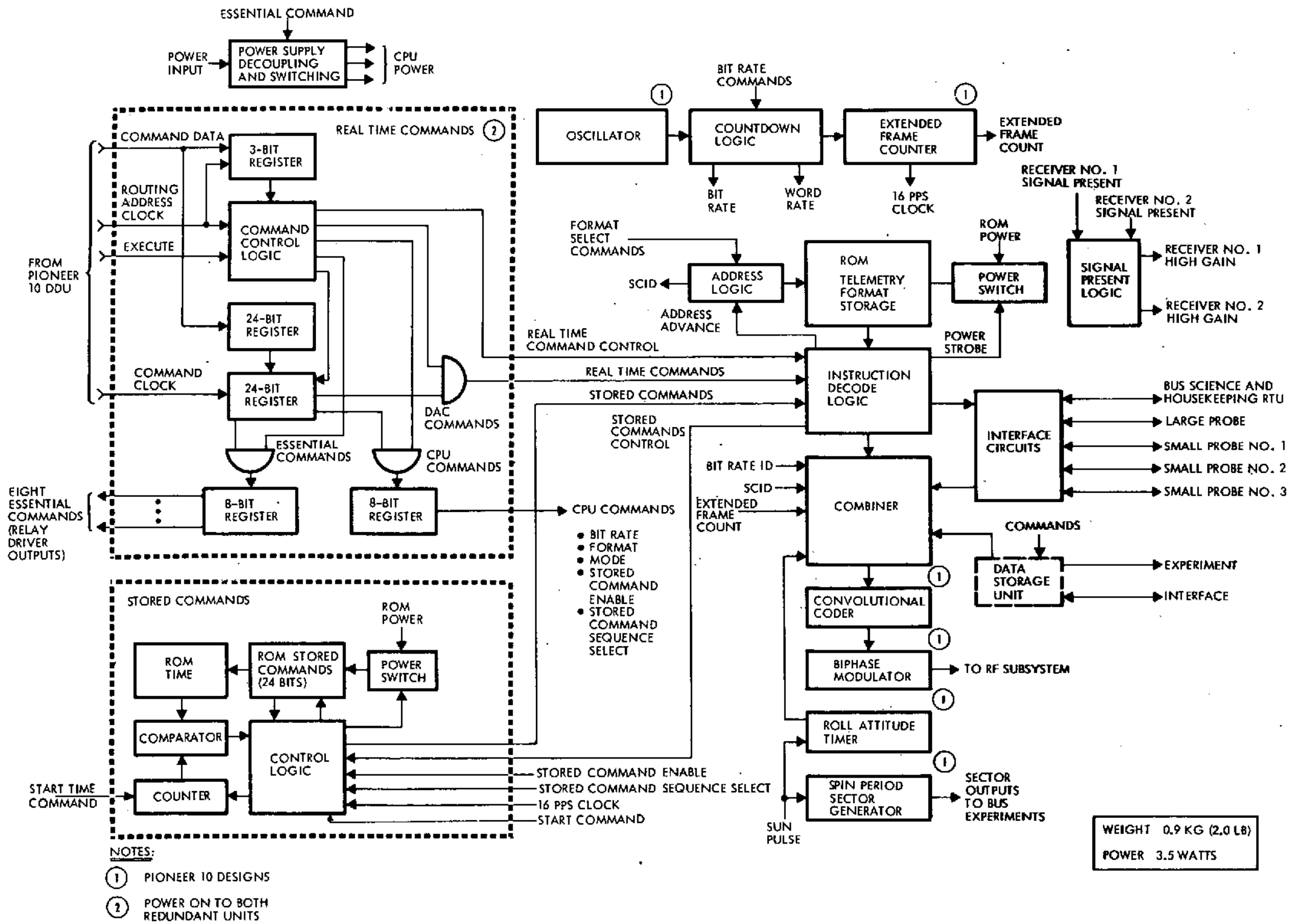

Figure 8.3 B-4. CCU Block Diagram

and RTU's which cannot be commanded through the DACS. The CCU's are used in the power off redundant configuration except for the real-time command logic portion which remains powered on at all times. The real-time command logic must remain on to enable processing of essential commands from either CCU at all times.

The CCU uses the Pioneer 10 designs for the convolutional coder, biphase modulator, roll attitude timer and spin period sector generator. Independent interface circuits are used for communication to each RTU so that a failure of one interface will not disable any other.

The CCU design uses LPTTL MSI and LSI (ROM's) to minimize parts count and power. The estimated weight is 0.9 kilogram (2.0 pounds) and estimated power is 3.5 watts.

Figure 8.3B-5 illustrates the probe bus and orbiter RTU design. The RTU's provide command and timing outputs, and sample and signal condition telemetry from the science instruments and spacecraft subsystems. RTU's are under the control of stored programs within the CCU until the probes separate from the bus at which time the RTU is under the control of its own ROM stored program.

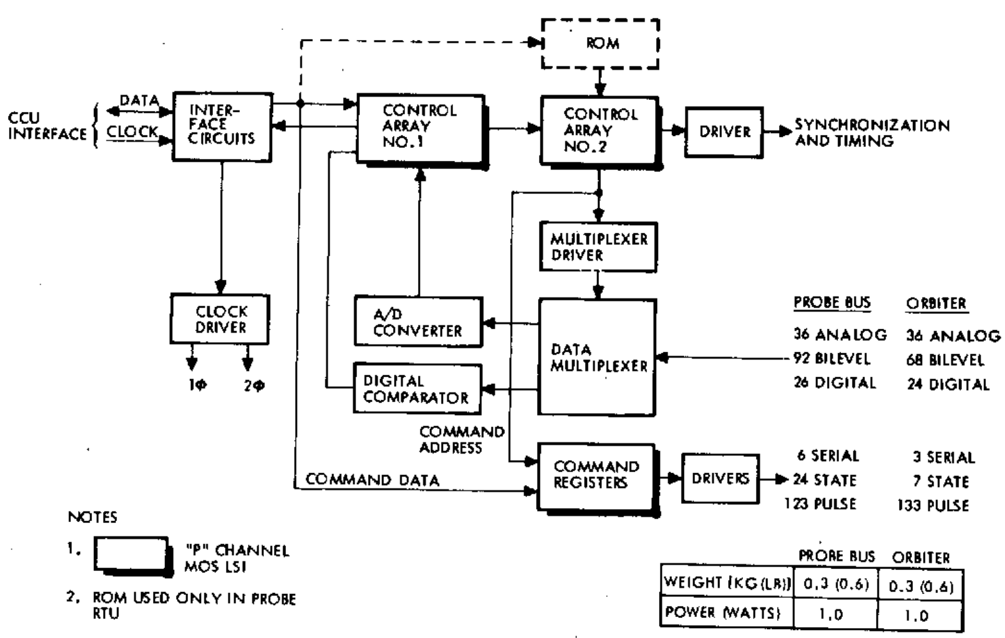

	PROBE BUS	ORBITER
WEIGHT (KG (LB))	0.3 (0.6)	0.3 (0.6)
POWER (WATTS)	1.0	1.0

Figure 8.3B-5. Probe Bus/Orbiter RTU

The advantages of MOS LSI and LPTTL technology are used to provide the command and telemetry functions efficiently. Modular input/output and ROM programs provide system flexibility at low cost.

Figure 8.3B-6 illustrates the probe data system which consists of an RTU, data storage memory, stored command logic, convolution coder and sequencing logic. The data system design is essentially the same for large and small probes except the small probes do not have a coast timer and have a different number of RTU telemetry and command channels.

The data system responds to external instructions during ground testing and in-flight testing. Upon separation from the probe bus, the data system operates under the control of programs stored within the RTU ROM and stored command instructions. Upon separation, the 25-day coast time starts; all other systems are off. At a programmed time, the probe data system is activated for a short time to enable calibration of the magnetometer away from the influences of the probe bus. The calibration data (256 bits) is stored until the entry phase.

During the entry phase, the coast timer or acceleration switch activates the probe and starts the stored command sequence. A telemetry frame pulse (FP), from the stored command countdown circuit, is processed by the telemetry instruction logic and instructs the RTU to collect, format and put into the data memory one frame of data. The time between these frame pulses is determined by stored commands. This technique provides a convenient method for changing the effective data sampling rate to match the science data requirements.

The data system also provides variable length telemetry format words. This is accomplished by storing a word length code for each channel address stored within the RTU ROM. This code programs the length of each telemetry word to eliminate storage and transmission of unnecessary bits.

The data storage unit used within the probes is a scaled-down version of the orbiter memory. The total memory is approximately 10,000 bits. The data storage unit contains a 256-bit section powered by the same special battery which supplies power to the coast timer. This

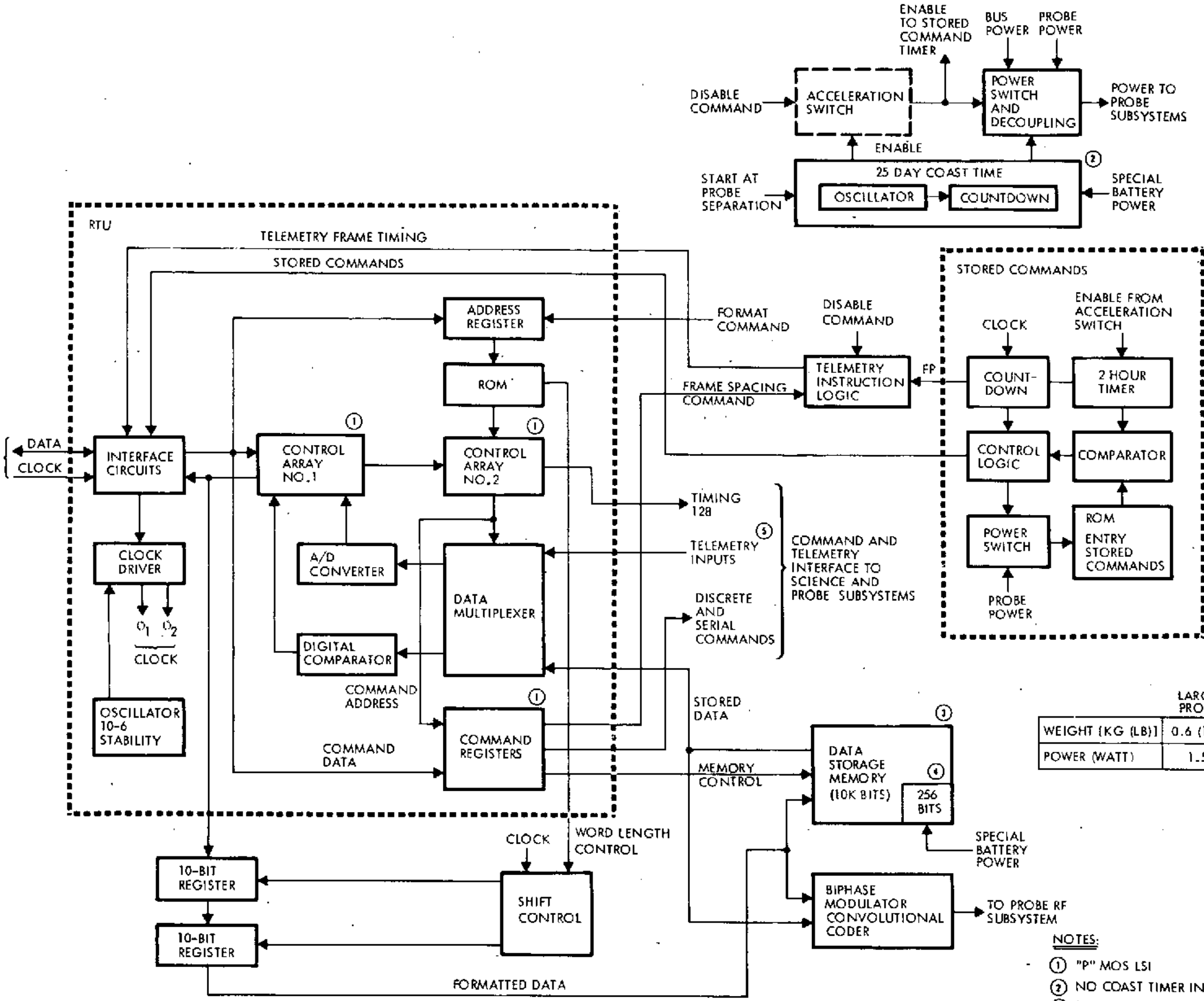

	LARGE PROBE	SMALL PROBE
WEIGHT (KG (LB))	0.6 (1.2)	0.5 (1.0)
POWER (WATT)	1.5	1.0

NOTES:

(1) "P" MOS LSI
(2) NO COAST TIMER IN SMALL PROBES
(3) SCALED DOWN ORBITER MEMORY
(4) 256 BIT STORAGE FOR MAGNITOMETER CALIBRATION DURING COAST PERIOD. POWERED BY SPECIAL BATTERY
(5) 64 CHANNELS FOR SMALL PROBE

Figure 8.3B-6. Large/Small Probe Command and Data Handling Subsystem storage is used to hold the 256-bits of magnetometer calibration data during the coast period. Since available power is extremely limited during the coast period, only the 256-bit portion of the memory is powered on. The power required to preserve this data is approximately 50 microwatts continuous.

Table 8.3B-1 summarizes the parts count, printed circuit boards, slices, weight, and power of each Pioneer Venus command and data system units. The data from this table was used to compute weight, power and reliability for the comparison chart to follow.

Table 8.3B-1. Data Subsystem Parameter Summary

UNIT	PARTS		PRINTED CIRCUIT BOARDS	SLICES	WEIGHT [KG (LB)]	POWER (WATT)
	INTEGRATED CIRCUITS	DISCRETES				
CCU	212	200	4	2	0.9 (2.0)	3.5
DDU	-	-	1	1	0.4 (0.85)	0.14/0.7
DSU	297	129	9	3	1.7 (3.9)	4.5 (ALL 3)
BUS/ORBITER REMOTE TERMINAL UNIT	55	53	1	1	0.3 (0.6)	0.3/1.0
SMALL PROBE DATA SYSTEM	104	95	2	1	0.5 (1.0)	1.0
LARGE PROBE DATA SYSTEM	118	105	2	1	0.6 (1.2)	1.5
LARGE PROBE DATA SYSTEM*	-	-	-	-	1.4 (3.0)	3.0
SMALL PROBE DATA SYSTEM*	-	-	-	-	0.9 (2.2)	2.0
CDU (TOTAL)	-	-	16	8	3.9 (8.6)	2.5
CDU (MODIFIED)	-	-	6	3	2.3 (5.0)	1.4
DTU	-	-	9	1	3.1 (6.8)	3.9

*BASELINE DESIGN

Table 8.3B-2 is a comparison chart listing the most important parameters of the Pioneer 10 versus DACS. The table indicates the DACS can save weight and power within the probes. The disadvantage of the DACS over the Pioneer 10 system is the cost of development. Although the DACS is developed through the operational breadboard stages (including MOS LSI arrays) further system design would be required for the Pioneer Venus mission.

Table 8.3B-2. Comparison Chart

PARAMETER	PIONEERS 10 AND 11		DAC		DELTA	
	ORBITER	PROBE	ORBITER	PROBE	ORBITER	PROBE
WEIGHT [KG(LB)]	10.1 (21.0)	7.7 (17.1) BUS 1.4 (3.0) LP 1.0 (2.2) SP (EACH) 12.1 (26.7)	7.7 (17.0)	5.4 (11.9) BUS 0.2 (1.2) LP 0.5 (1.0) SP (EACH) 7.2 (16.1)	1.8 (4.0)	2.4 (5.2) BUS 0.9 (1.8) LP 0.6 (1.2) SP (EACH) 4.8 (10.6)
POWER (WATTS)	11.7	7.2 BUS 3.0 LP 2.0 SP (EACH)	11.5	6.7 BUS 1.5 LP 1.0 SP (EACH)	0.2	0.5 BUS 1.5 LP 1.0 SP (EACH) 5.0
COST	LOWER	HIGHER	HIGHER	LOWER		
HARDWARE COMMONALITY	PIONEER 10 DTU	PIONEER 10 DTU + NEW DESIGN USED FOR PROBES ONLY	NEW CCU DESIGN	ORBITER CCU + ORBITER RTU AS HEART OF PROBE COMMAND AND DATA SYSTEM		
DESIGN AND HARDWARE STATUS	FLIGHT PROVEN	NEW DESIGN PIONEER 10 TECHNOLOGY	NEW CPU, BREADBOARD RTU	NEW CPU, BREAD-BOARD RTU WITH NEW CONTROL LOGIC		
RELIABILITY	0.889 (SUBMULTIPLEXER INCLUDED)		0.9850		0.0960	
REDUNDANCY	ENGINEERING TELEMETRY NONREDUNDANT		FULL REDUNDANCY			
FORMAT EFFICIENCY	FIT PIONEER VENUS REQUIREMENTS TO PIONEER TO FORMATS	NEW DESIGN TO FIT PIONEER VENUS MISSION	PROGRAMMABLE TO FIT PIONEER VENUS MISSION	PROGRAMMABLE TO FIT PIONEER VENUE MISSION		
SYSTEM FLEXIBILITY	FIXED CAPACITY, FIXED FORMATS	NEW DESIGN TO FIT PIONEER VENUS MISSION	MODULAR CAPACITY, PROGRAMABLE FORMATS	MODULAR CAPACITY, PROGRAMABLE FORMATS		
TECHNICAL RISK	LOWER DUE TO PROVEN HARDWARE	LOWER DUE TO USE OF PIONEER 10 TECHNOLOGY	HIGHER DUE TO NEW SYSTEM DESIGN	HIGHER DUE TO NEW SYSTEM DESIGN		

APPENDIX 8. 3C

CENTRAL PROCESSOR

APPENDIX 8.3C

CENTRAL PROCESSOR

Central processing was examined as an alternative to the conventional approach where each subsystem encompasses its own processing. Certain spacecraft functions can be performed by a central general purpose digital processor, eliminating distributed hardware and minimizing spacecraft weight and cost. Some functions can be performed by software alone, other need small amounts of hardware. In at least one instance, the DEA, a central processor facilitates use of off-the-shelf hardware, by performing rate calculation, a function which does not exist in available units.

1. DIGITAL TELEMETRY UNIT

Most of the functions of this unit can be absorbed by the digital processor. These include:

- The reception of sun pulses from the sun sensor and subsequent issuance of roll attitude and sector pulses (includes three modes: ACS, averaging, and nonaveraging)
- The gathering and formatting of telemetry data
- The implementation of the convolutional encoder
- The implementation of the interleaver (if required by the communications subsystem).

2. COMMAND DISTRIBUTION UNIT

Most of the functions of this unit can be absorbed by the central processor. They include:

- Distribution of discretes (pulse and static)
- Distribution of serial digital data
- Receiver present detection logic (36-hour counter)
- Sequencer logic
- Command storage
- Thruster pulse counting.

. CONTROL ELECTRONICS ASSEMBLY

Since the turn-on/turn-off accuracy for firing thrusters can be met y software, the various multiple event maneuvers can be commanded rom the ground and executed from within the control processor. These nclude:

- Programmed precession/ΔV
- Programmed ΔV/SCT
- Real time processor/ΔV/spin control
- Fixed angle precession
- Programmed precession/spin control
- Programmed precession/probe deployment.

'he capability for auto spin control can exist within the center processor.

. DESPIN ELECTRONICS ASSEMBLY

Despin functions including antenna pointing can be absorbed. Rate alculations, which presently do not exist in any off-the-shelf hardware nits can be performed by the processor. Since "pipper pulses" occur ominally every 24 msec this calculation is trivial. The accuracy of neasurement however is approximately 10 to 20 μsec, thus an 8-bit hard- 'are counter at 100 kbits/s is required.

. SCIENCE PACKAGES

Most experiments require a turn-on/turn-off command and perhaps mode discrete. In addition, both the radar altimeter and UV spectrome- er require:

- Enabling during a 0.52 radian (30-degree) or similar sector of each spacecraft revolution
- Gimballing to facilitate nadir pointing.

'hese functions presently reside within the experiments but can be executed y the central processor.

6. CENTRAL PROGRAMMER SOFTWARE SIZING

Flow diagrams and sample coding was generated in order to obtain the results of Table 8. 3C-1. The candidate processor selected for the exercise was the Comsat processor recently developed (in breadboard form) for the Comsat control system. It's general characteristics are:

- General-purpose digital
- Word length = 16 bits
- Single address instructions
- Serial/parallel organization (4-bit bytes)
- 7.2 μsec ADD; 60 μsec MPY
- Power = 6.0 watts plus memory
- Weight = 0.7 kg (1.5 pound) plus memory.

Table 8. 3C-1. Central Programmer Sizing Requirements

FUNCTION	PROGRAM MEMORY REQUIRED WORDS	DATA MEMORY REQUIRED WORDS	EXECUTION TIME (MS/S)	REMARKS
SPOKE WHEEL GENERATION	50	10	1	EXTERNAL COUNTERS
DEA RATE CALCULATIONS	120	10	10	
CONVOLUTIONAL ENCODER	50	15	250	AT MAXIMUM BIT RATE
ATTITUDE CONTROL	50	15	15	
INTERLEAVER	50	70	100	AT MAXIMUM BIT RATE
TELEMETRY FUNCTION	240	5	6.0	AT MAXIMUM BIT RATE
SCIENCE (RADAR ALTIMETER)	20	5	1.0	SEQUENCING AND GIMBALLING
SCIENCE (UV SPECTROMETER)	20	5	1.0	SEQUENCING AND GIMBALLING
EXECUTIVE ROUTINE	100	35	25	
RX SIGNAL RESET (COUNTING)	20	5	0.100	
THRUSTER PULSE (COUNTING)	20	5	0.100	
COMMAND DISTRIBUTION	40	40	---	
TOTAL	780	220	409.2	

It should be noted that the 2048 bits/s downlink data rate consumes most of the processors effort. A more typical data rate would be 256 bits/s which relates to a telemetry work load of 80 ms/s and a total loading of 123.2 ms/s. Memory requirements are small and entail a 256-word read/write, and a 1024-word read-only memory.

7. HARDWARE SIZING ESTIMATES

Tables 8. 3C-2 and 8. 3C-3 indicate the nature of the hardware tradeoffs. Estimates for the RTU were taken from the parallel study performed on a DACS. The summary of these is included in Table 8. 3C-4.

Table 8.3C-2. Hardware Tradeoffs (Probe Bus)

BASELINE	POWER (WATTS)	WEIGHT KG	WEIGHT (LB)	PROBE BUS (CPU SYSTEM)	POWER (WATTS)	WEIGHT KG	WEIGHT (LB)
DDU	0.15	0.4	(0.9)	DDU	0.15	0.4	(0.9)
DDU	0.68	0.4	(0.9)	DDU	0.68	0.4	(0.9)
CDU	2.5	3.9	(8.6)				
DTU	3.9	3.1	(6.8)				
CEA	4.5	1.8	(4.2)	CEA	3.0	0.9	(2.0)
				CPU_1	6.0	0.7	(1.5)
SMALL PROBE (X3)	6.0	3.0	(6.6)	CPU_2	---	0.7	(1.5)
LARGE PROBE	3.0	1.4	(3.0)	CPU $MEMORY_1$	1.3	0.5	(1.0)
				CPU $MEMORY_2$	---	0.5	(1.0)
				CIA_1	3.4	0.3	(0.7)
				CIA_2	---	0.3	(0.7)
				SPACECRAFT RTU_1	1.0	0.3	(0.6)
				SPACECRAFT RTU_2	---	0.3	(0.6)
				SIGNAL CONDITIONER UNIT	1.0	0.4	(0.8)
				ORDNANCE	.02	1.4	(3.0)
				SMALL PROBE RTU (X3)	3.0	1.4	(3.0)
				LARGE PROBE RTU (X1)	1.2	0.7	(1.5)
TOTAL	20.73	14.1	(31.0)		20.75	8.9	(19.7)

Table 8.3C-3. Hardware Tradeoffs (Orbiter)

BASELINE	POWER (WATTS)	WEIGHT KG	WEIGHT (LB)	ORBITER	POWER (WATTS)	WEIGHT KG	WEIGHT (LB)
DDU	0.15	0.4	(0.9)	DDU	0.15	0.4	(0.9)
DDU	0.68	0.4	(0.9)	DDU	0.68	0.4	(0.9)
CDU	2.5	3.9	(8.6)				
DTU	3.9	3.1	(6.8)				
DSU	0.6	1.8	(3.9)	DSU	0.6	1.8	(3.9)
CEA	4.5	1.9	(4.2)	CEA	3.0	1.4	(3.0)
DEA	1.5	1.8	(4.0)	DEA	1.0	0.9	(2.0)
DEA	---	1.8	(4.0)	DEA	---	0.9	(2.0)
				CPU	6.0	0.7	(1.5)
				CPU	---	0.7	(1.5)
INSTRUMENT PROGRAMMERS	1.5	0.9	(2.0)	CPU MEMORY	1.3	0.5	(1.0)
				CPU MEMORY	---	0.5	(1.0)
				CIA	3.4	0.3	(0.7)
				CIA	---	0.3	(0.7)
				SPACECRAFT RTU	1.0	0.3	(0.6)
				SPACECRAFT RTU	---	0.3	(0.6)
				SCIENCE RTU	1.0	0.3	(0.6)
				SCIENCE RTU	---	0.3	(0.6)
				SIGNAL CONDITIONER UNIT	1.0	0.3	(0.7)
				ORDNANCE	0.02	1.4	(3.0)
TOTAL	15.33	16.0	(35.3)		19.15	11.4	(25.2)

Table 8.3C-4. Data Handling System Tradeoffs

	ORBITER			PROBE BUS		
	DISTRIBUTED PROGRAMMER	CENTRAL PROGRAMMER	DELTA	DISTRIBUTED PROGRAMMER	CENTRAL PROGRAMMER	DELTA
WEIGHT KG(LB)	16.0 (35.3)	11.4 (25.2)	4.7 (10.1)	13.9 (31.0)	9.0 (19.7)	5.1 (11.3)
POWER (WATTS)	15.33	19.15	3.82	20.73	20.75	0

Several items such as the Δweight associated with removing the sequencers from the science packages have been estimated as no information was available at this time.

8. SUMMARY

The control functions of the Pioneer Venus spacecraft can be handled by a centralized programmer. Although the power requirement is approximately equal to the baselines a significant weight savings, 4.5 kilograms (10 pounds) can be achieved. The system is flexible with attendant growth potential, which must be weighed against the risk of developing a centralized spacecraft.

APPENDIX 8.4A

COMMAND REQUIREMENTS

APPENDIX 8.4A

COMMAND REQUIREMENTS

The following list identifies the command requirements for the preferred probe bus and orbiter configurations based on the Atlas/Centaur launch vehicle. The requirements are grouped by subsystem and are categorized as serial, pulse, or state commands.

Those command entries followed by a (Thor/Delta) designator are applicable to spacecraft configurations which are compatible with the Thor/Delta launch vehicle. The (stored) designator identifies functions which would normally be performed via the stored command programmer. Instrument commands annotated with (New Science) are associated with the Version IV science payload.

COMMANDS - BUS

ELECTRICAL DISTRIBUTION

UNDERVOLTAGE OVERRIDE INHIBIT		PULSE	
UNDERVOLTAGE OVERRIDE NORMAL		PULSE	
CDU SELECT 5 VDC BUS A		PULSE	
CDU SELECT 5 VDC BUS B		PULSE	
RECEIVER REVERSE INHIBIT		PULSE	
RECEIVER REVERSE ENABLE		PULSE	
SPACECRAFT ORDNANCE SAFE		PULSE	
SPACECRAFT ORDNANCE ARM		PULSE	
CMD PROC 1 SELECT		PULSE	
CMD PROC 2 SELECT		PULSE	
EQUIPMENT CONVERTER FAULT ISOLATION RELAYS	(8)	PULSE	(THOR/DELTA)
EXTEND MAGNETOMETER BOOM		PULSE	(THOR/DELTA)
RETRACT MAGNETOMETER BOOM		PULSE	(THOR/DELTA)
RELEASE UV FLUORESCENT PROBE ANT		PULSE	(THOR/DELTA)
EJECT NEUTRAL MASS SPECTROMETER ION CAP		PULSE	
RELEASE ELECTRON TEMPERATURE PROBE ANT		PULSE	
LARGE PROBE CONNECTOR RELEASE		PULSE	
LARGE PROBE RELEASE		PULSE	
SMALL PROBE THERMAL SHIELD RELEASE	(3)	PULSE	
SMALL PROBE CONNECTOR RELEASE	(3)	PULSE	
SMALL PROBE RELEASE	(3)	PULSE	
SMALL PROBE SIMULTANEOUS RELEASE		PULSE	

ELECTRICAL POWER

BATTERY AUTOMATIC CHARGE ENABLE		PULSE
BATTERY MAX CHARGE		PULSE
BATTERY DISCHARGE ENABLE		PULSE
BATTERY DISCHARGE DISABLE		PULSE
CHARGE RATE 1 ON		PULSE
CHARGE RATE 1 OFF		PULSE
CHARGE RATE 2 ON		PULSE
CHAEGE RATE 2 OFF		PULSE
CHARGE RATE 3 ON		PULSE
CHARGE RATE 3 OFF		PULSE
LARGE PROBE POWER ON/OFF	(2)	PULSE
SMALL PROBE 1 POWER ON/OFF	(2)	PULSE
SMALL PROBE 2 POWER ON/OFF	(2)	PULSE
SMALL PROBE 3 POWER ON/OFF	(2)	PULSE
CTRF INVERTER TRANSFER RELAY SELECT	(2)	PULSE

DATA HANDLING

DTU A SELECT		PULSE
DTU B SELECT		PULSE
DTU CMD WORDS	(39)	SERIAL
LARGE PROBE CMD WORD		SERIAL *
SMALL PROBE 1 CMD WORD		SERIAL *
SMALL PROBE 2 CMD WORD		SERIAL *
SMALL PROBE 3 CMD WORD		SERIAL *

* ONLY ONE ROUTING ADDRESS IS REQUIRED SINCE ONLY ONE PROBE IS POWERED AT ANY GIVEN TIME.

COMMUNICATIONS

RECEIVER A COHERENT MODE ENABLE	STATE
RECEIVER A COHERENT MODE DISABLE	STATE

RECEIVER B COHERENT MODE ENABLE	STATE	
RECEIVER B COHERENT MODE DISABLE	STATE	
POWER AMP A SELECT (B OFF)	PULSE	
POWER AMP A HIGH POWER	PULSE	(THOR/DELTA)
POWER AMP B SELECT (A OFF)	PULSE	
POWER AMP A LOW POWER	PULSE	(THOR/DELTA)
POWER AMP B HIGH POWER	PULSE	(THOR/DELTA)
POWER AMP DRIVER A SELECT (B OFF)	PULSE	
POWER AMP B LOW POWER	PULSE	(THOR/DELTA)
POWER AMP DRIVER B SELECT (A OFF)	PULSE	
TRANSFER SWITCH 1 TO POSITION 1	PULSE	
TRANSFER SWITCH 1 TO POSITION 2	PULSE	
TRANSFER SWITCH 2 TO POSITION 1	PULSE	
TRANSFER SWITCH 2 TO POSITION 2	PULSE	
TRANSFER SWITCH 3 TO POSITION 1	PULSE	
TRANSFER SWITCH 3 TO POSITION 2	PULSE	
TRANSFER SWITCH 4 TO POSITION 1	PULSE	
TRANSFER SWITCH 4 TO POSITION 2	PULSE	

ATTITUDE CONTROL

SEQUENCE STEP	PULSE
STANDBY POWER ON (PSE ON, DSL OFF)	PULSE
PROGRAM STORAGE AND EXECUTE OFF	PULSE
ARM REGISTER 1 (FOLLOWED BY 4 SERIAL CMDS)	PULSE
ARM REGISTER 2 (FOLLOWED BY 4 SERIAL CMDS)	PULSE
ARM REGISTER 3 (FOLLOWED BY 4 SERIAL CMDS)	PULSE
PULSE LENGTH 1, 31.2 MSEC	PULSE
PULSE LENGTH 2, 62.5 MSEC	PULSE
PULSE LENGTH 3, 125.0 MSEC	PULSE
PULSE LENGTH 4, 1.0 MSEC	PULSE
PULSE LENGTH 5, 2.0 MSEC	PULSE
AXIAL PAIR 1 SELECT	PULSE
AXIAL PAIR 2 SELECT	PULSE
DELTA V PAIR 1 SELECT	PULSE
DELTA V PAIR 2 SELECT	PULSE
TRANSVERSE DIRECTION UP	PULSE
TRANSVERSE DIRECTION DOWN	PULSE
AXIAL PULSE, 0 DEG	PULSE
AXIAL PULSE, 90 DEG	PULSE
AXIAL PULSE 180 DEG	PULSE
AXIAL PULSE, 270 DEG	PULSE
REAL-TIME AXIAL PULSE	PULSE
REAL-TIME TRANSVERSE PULSE	PULSE
REAL-TIME DELTA V PULSE	PULSE
DELTA V/SCT MODE ENABLE	PULSE
CLOCK RESET	PULSE
SELECT SUN SENSOR OUTPUT A	PULSE
SELECT SUN SENSOR OUTPUT B	PULSE
SELECT DTU A CLOCK OUTPUT	PULSE
SELECT DTU B CLOCK OUTPUT	PULSE
DURATION/STEER LOGIC 1 SELECT (DSL 1 ON, 2 OFF)	PULSE
DURATION/STEER LOGIC 2 SELECT (DSL 2 ON, 1 OFF)	PULSE
CEA COMMAND WORDS 1-12	SERIAL

THERMAL

PROPELLANT HEATERS ENABLE	PULSE
PROPELLANT HEATERS DISABLE	PULSE

SCIENCE

MAGNETOMETER		(SCIENCE III)
POWER ON/OFF	(2)	STATE
CALIBRATE MODE ON/OFF	(2)	PULSE
HIGH/LOW RANGE SELECT	(2)	PULSE
UV FLUORESCENCE		(SCIENCE III)
POWER ON/OFF	(2)	STATE
FURNACE CURRENT MODE 1		PULSE
FURNACE CURRENT MODE 2		PULSE
FURNACE CURRENT MODE 3		PULSE
FURNACE CURRENT MODE 4		PULSE
CALIBRATE MODE ON/OFF	(2)	PULSE
ION MASS SPECTROMETER		
POWER ON/OFF	(2)	STATE
CALIBRATE MODE ON/OFF	(2)	PULSE
NEUTRAL PARTICLE MASS SPECTROMETER		
POWER ON/OFF	(2)	STATE
ELECTRON TEMPERATURE PROBE		
POWER ON/OFF	(2)	STATE
UV SPECTROMETER		
POWER ON/OFF	(2)	STATE
RETARDING POTENTIAL ANALYZER		(SCIENCE IV)
POWER ON/OFF	(2)	STATE
CALIBRATE MODE ON/OFF	(2)	PULSE
HIGH/LOW RANGE SELECT	(2)	PULSE

****

COMMANDS - ORBITER

ELECTRICAL DISTRIBUTION

MEMORY ADDRESS COUNTER RESET		PULSE
MEMORY TIME COUNTER RESET		PULSE
CMD MEMORY PROGRAMMER ENABLE		PULSE
CMD MEMORY PROGRAMMER DISABLE		PULSE
MEMORY TIME REGISTER UPDATE		SERIAL
MEMORY ADDRESS PRE-SET		SERIAL
UNDERVOLTAGE OVERRIDE INHIBIT		PULSE
UNDERVOLTAGE OVERRIDE NORMAL		PULSE
CDU SELECT 5 VDC BUS A		PULSE
CDU SELECT 5 VDC BUS B		PULSE
RECEIVER REVERSE INHIBIT		PULSE
RECEIVER REVERSE ENABLE		PULSE
SPACECRAFT ORDNANCE SAFE		PULSE
SPACECRAFT ORDNANCE ARM		PULSE
CMD PROC 1 SELECT		PULSE
CMD PROC 2 SELECT		PULSE
EQUIP CONV FAULT ISOLATION RELAYS	(8)	PULSE (THOR/DELTA)
EXTEND MAGNETOMETER BOOM		PULSE
RETRACT MAGNETOMETER BOOM		PULSE
ARM SRM ORDNANCE (MOTOR DRIVE)		STATE
SAFE SRM ORDNANCE (MOTOR DRIVE)		STATE
FIRE SRM ORDNANCE	(2)	PULSE (STORED)
EJECT NEUTRAL MASS SPECTROMETER ION CAP		PULSE (THOR/DELTA)
EJECT UV SPECTROMETER SUN COVER		PULSE (THOR/DELTA)

RELEASE ELECTRON TEMPERATURE PROBE		PULSE
RELEASE RADAR ALTIMETER ANTENNA		PULSE
RELEASE RAM PLATFORM		PULSE
ELECTRICAL POWER		
BATTERY AUTOMATIC CHARGE ENABLE		PULSE
BATTERY MAX CHARGE		PULSE
TRICKLE CHARGE (0.3A)		PULSE
TRICKLE CHARGE (0.15A)		PULSE
BATTERY DISCHARGE ENABLE		PULSE
BATTERY DISCHARGE DISABLE		PULSE
BATTERY HIGH TEMP PROTECTION ON		PULSE
BATTERY HIGH TEMP PROTECTION OFF		PULSE
BATTERY RECONDITION/DISCONNECT	(2)	PULSE
CTRF INVERTER TRANSFER RELAY SELECT	(2)	PULSE
DATA HANDLING		
DSU CONFIGURATION SELECT	(4)	PULSE
DTU A SELECT		PULSE
DTU B SELECT		PULSE
DTU CMD WORDS 1-39		SERIAL
HIGH/LOW ALTITUDE STORE FORMAT SELECT	(2)	PULSE (STORED)
SCIENCE DATA STORAGE ENABLE	(2)	PULSE (STORED)
COMMUNICATIONS		
RECEIVER A COHERENT MODE ENABLE		STATE
RECEIVER A COHERENT MODE DISABLE		STATE
RECEIVER B COHERENT MODE ENABLE		STATE
RECEIVER B COHERENT MODE DISABLE		STATE
POWER AMP A ON		PULSE
POWER AMP A OFF		PULSE
POWER AMP B ON		PULSE
POWER AMP B OFF		PULSE
POWER AMP C ON		PULSE (THOR/DELTA)
POWER AMP C OFF		PULSE (THOR/DELTA)
POWER AMP D ON		PULSE (THOR/DELTA)
POWER AMP D OFF		PULSE (THOR/DELTA)
POWER AMP DRIVER A SELECT (B OFF)		PULSE
POWER AMP DRIVER B SELECT (A OFF)		PULSE
TRANSFER SWITCH 1 TO POSITION 1		PULSE
TRANSFER SWITCH 1 TO POSITION 2		PULSE
TRANSFER SWITCH 2 TO POSITION 1		PULSE
TRANSFER SWITCH 2 TO POSITION 2		PULSE
TRANSFER SWITCH 3 TO POSITION 1		PULSE
TRANSFER SWITCH 3 TO POSITION 2		PULSE
TRANSFER SWITCH 4 TO POSITION 1		PULSE
TRANSFER SWITCH 4 TO POSITION 2		PULSE
TRANSFER SWITCH 5 TO POSITION 1		PULSE
TRANSFER SWITCH 5 TO POSITION 2		PULSE
TRANSFER SWITCH 6 TO POSITION 1		PULSE
TRANSFER SWITCH 6 TO POSITION 2		PULSE
CONSCAN THRESHOLD HIGH		PULSE
CONSCAN THRESHOLD LOW		PULSE
CONSCAN ON		PULSE
CONSCAN OFF		PULSE
CONSCAN 0 DEGREE PHASE		PULSE
CONSCAN 180 DEGREE PHASE		PULSE
X-BAND XMTR ON/OFF	(2)	STATE

ATTITUDE CONTROL

SEQUENCE STEP		PULSE
STANDBY POWER ON (PSE ON, DSL OFF)		PULSE
PROGRAM STORAGE AND EXECUTE OFF		PULSE
ARM REGISTER 1 (FOLLOWED BY 4 SERIAL CMDS)		PULSE
ARM REGISTER 2 (FOLLOWED BY 4 SERIAL CMDS)		PULSE
ARM REGISTER 3 (FOLLOWED BY 4 SERIAL CMDS)		PULSE
PULSE LENGTH 1, 31.2 MSEC		PULSE
PULSE LENGTH 2, 62.5 MSEC		PULSE
PULSE LENGTH 3, 125.0 MSEC		PULSE
PULSE LENGTH 4, 1.0 SEC		PULSE
PULSE LENGTH 5, 2.0 SEC		PULSE
AXIAL PAIR 1 SELECT		PULSE
AXIAL PAIR 2 SELECT		PULSE
DELTA V PAIR 1 SELECT		PULSE
DELTA V PAIR 2 SELECT		PULSE
TRANSVERSE DIRECTION UP		PULSE
TRANSVERSE DIRECTION DOWN		PULSE
AXIAL PULSE, 0 DET		PULSE
AXIAL PULSE, 90 DEG		PULSE
AXIAL PULSE, 180 DET		PULSE
AXIAL PULSE, 270 DET		PULSE
REAL-TIME AXIAL PULSE		PULSE
REAL-TIME TRANSVERSE PULSE		PULSE
REAL-TIME DELTA V PULSE		PULSE
DELTA V/SCT MODE ENABLE		PULSE
CLOCK RESET		PULSE
SELECT SUN SENSOR OUTPUT A		PULSE
SELECT SUN SENSOR OUTPUT B		PULSE
SELECT DTU A CLOCK OUTPUT		PULSE
SELECT DTU B CLOCK OUTPUT		PULSE
DURATION/STEER LOGIC 1 SELECT (DSL 1 ON, 2 OFF)		PULSE
DURATION/STEER LOGIC 2 SELECT (DSL 2 ON, 1 ON)		PULSE
CEA COMMAND WORDS 1-12		SERIAL
THERMAL		
PROPELLANT HEATERS ENABLE/DISABLE	(2)	PULSE
RAM PLATFORM HEATER ENABLE/DISABLE	(2)	PULSE
SRM HEATER ENABLE/DISABLE	(2)	PULSE
SCIENCE		
MAGNETOMETER		
POWER ON/OFF	(2)	STATE
CALIBRATE MODE ON/OFF	(2)	PULSE
HIGH/LOW RANGE SELECT	(2)	PULSE
UV SPECTROMETER		
POWER ON/OFF	(2)	STATE
CALIBRATE MODE ON/OFF	(2)	PULSE
HIGH DATA RATE ENABLE		PULSE (STORED)
ION MASS SPECTROMETER		
POWER ON/OFF	(2)	STATE
CALIBRATE MODE ON/OFF	(2)	PULSE
MODE 1 ON/OFF	(2)	PULSE
MODE 2 ON/OFF	(2)	PULSE
MODE 3 ON/OFF	(2)	PULSE
MODE 4 ON/OFF	(2)	PULSE

IR RADIOMETER		
POWER ON/OFF	(2)	STATE
NEUTRAL PARTICLE MASS SPECTROMETER		
POWER ON/OFF	(2)	STATE
ELECTRON TEMPERATURE PROBE		
POWER ON/OFF	(2)	STATE
RADAR ALTIMETER		
POWER ON		STATE
POWER OFF		PULSE (STORED)
MEMORY POWER OFF SIGNAL ENABLE/DISABLE	(2)	PULSE
CALIBRATE MODE ON/OFF	(2)	PULSE
XMTR ENABLE, ANT PROGR START		PULSE (STORED)
XMTR DISABLE, ANT PROGR STOP		PULSE (STORED)
SOLAR WIND ANALYZER		(SCIENCE IV)
POWER ON/OFF	(2)	STATE
MODE CONTROL	(6)	PULSE

APPENDIX 8.4B

STORED COMMAND PROGRAMMER

APPENDIX 8.4B
STORED COMMAND PROGRAMMER

The stored command programmer (SCP) is capable of storing 16 ground commands and associated time tags for later execution. The decision for execution is based on equality of the stored time code when compared with a master counter being incremented by the DTU clock. Each stored command is 8 bits and each associated time tag is 16 bits, providing a resolution of 2 seconds within a maximum delay period of 36.4 hours. The SCP characteristics are summarized in Table 8.4B-1.

Table 8.4B-1. Stored Command Programmer Characteristics

16 STORED PROGRAMMABLE COMMANDS PLUS 16 REDUNDANT

1 STORED ARM COMMAND (HARDWIRED) PLUS 1 REDUNDANT

STORED TIME DATA – 16 BITS WITH A RESOLUTION OF 2 SECONDS AND A MAXIMUM TIME TAG OF 36.4 HOURS

STORED COMMAND DATA – 8 BITS

ADDRESS POINTER AND TIME COUNTER ARE PRESETTABLE FOR PROGRAM EXECUTION FLEXIBILITY

FAIL SAFE OPERATION FOR ORDNANCE FIRING

CHARACTERISTICS:

- COMPONENT COUNT: 160 IC, 40 MISCELLANEOUS PARTS
- POWER DISSIPATION: STANDBY – 50 MW
PROCESSING – 750 MW
- REQUIRES ONE BOARD PER PROGRAMMER, TWO FOR REDUNDANCY
- WEIGHT: 0.2 KG (0.45 LB) NONREDUNDANT
0.4 KG (0.9 LB) WITH REDUNDANCY

The SCP operation can be divided into three phases: programmer data load, memory verify, and command processing. Data loading consists of writing or inserting data into a CMOS memory (256 by 2) and normally begins at memory address 0. An option of presetting the address by command is available for loading single commands or blocks of stored commands anywhere in the memory. The memory itself is subdivided into two sectors; one for time codes and one for commands. Each can be controlled individually, which is the case during data load. Sixteen bits of time data are loaded 1 bit at a time into ram-1 in successive addresses, as in 8 bits of command data into ram-2. The SCP schematic is shown in Figure 8.4B-1.

Memory verify is a complete readout or retrieval of the memory contents through telemetry for bit-by-bit comparison on the ground. The readout begins at address 0 and progresses sequentially through the 256 address locations. The verify data will be inserted into a D format requiring 6.0 seconds to dump 512 memory bits at 128 bits/s (includes telemetry inefficiencies).

After data load and verify, command processing will be initiated. Every 2 seconds, each stored command (both time and command data) is read from memory; and the stored time is compared bit-by-bit in parallel with the 16-bit time counter for equality. When equality is detected, the command data in the command register is serially transferred at a rate of 64 bits/s to the CDU processor for further processing and execution. An execute pulse delayed from the data by 50 milliseconds and, generated by the SCP, is routed to the processor for execution of the stored command. Command processing requires that the two address counters operate together with the bit/word counter providing control information for the memory. This complete time comparison is conducted in about 8 milliseconds and permits loading of stored commands in a random fashion. The time counter can be preset by ground command in addition to reset to zero, or the counter can be reset by one of the stored commands. This enhances program flexibility.

Fail-safe stored command operation is necessary for ordnance activation of the retrorocket. This is achieved by using a clock detector which will inhibit the SCP if the DTU 32-kHz clock has failed by increasing (greater than two times) in frequency. The detector samples the 32 kHz with a fixed width pulse, thereby sensing variations in clock pulse width. Premature firing due to fast clocks is thus avoided. All other single-point failures are precluded by using a separately generated arm command. This arm command is isolated from the other 16 commands. Note that there are two arm commands (primary and backup) and two fire

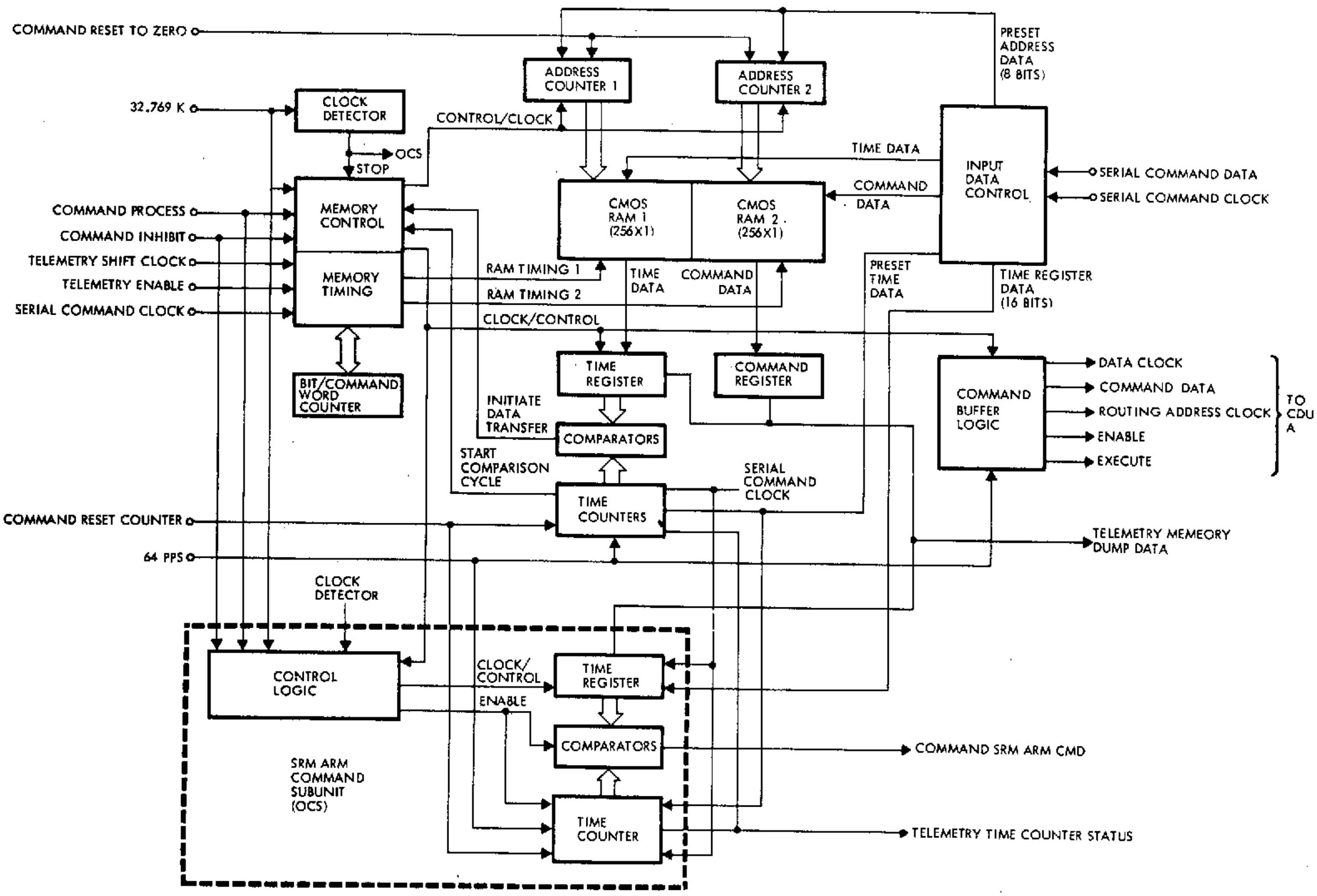

Figure 8.4B-1. Stored Command Programmer Block Diagram (Typical of Two Redundant Boards)

commands (primary and backup) configured so that no single-point failure can cause either an early, late, or no-fire condition.

A maximum of eight ground commands are stored at any one time during the orbiter mission. The stored command programmer, however, was designed to store 16 commands on one board to optimize use of standard 256-bit CMOS chips while providing flexibility in operational use and allowing for potential increase in requirements. In addition, an active redundant capability maximizes reliability of precise firing of the orbit insertion motor.

The 16-command capacity plus the 16 redundant commands are provided at an insignificant increase in cost, based upon only two or three logic components. The net result is a design offering the flexibility of storing 16 redundant commands or 32 nonredundant commands.

APPENDIX 8.5A

CONSCAN/FANSCAN ATTITUDE DETERMINATION

APPENDIX 8.5A

CONSCAN/FANSCAN ATTITUDE DETERMINATION

1. CONSCAN SYSTEM DESCRIPTION

The conscan system, performing successfully on Pioneers 10 and 11, will be used in the Pioneer Venus orbiter to provide the functions described in Figure 8.5A-1.

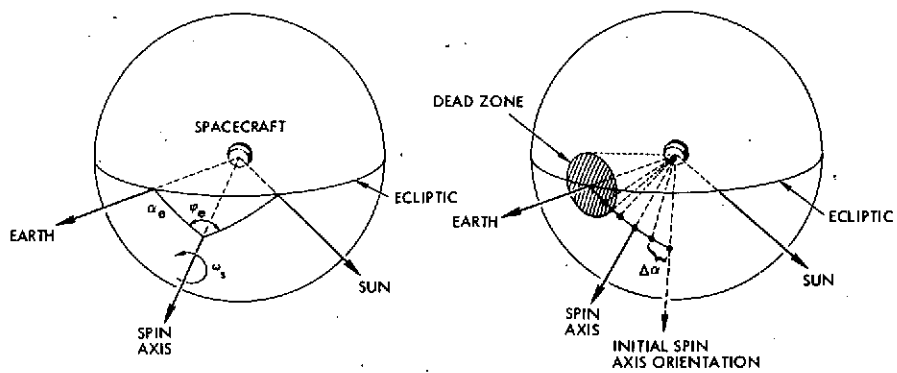

a) ATTITUDE DETERMINATION
THE EARTH ASPECT ANGLE α_e AND THE PHASE ANGLE φ_e (RELATIVE TO THE SUN) ARE DETERMINED ON THE GROUND ON THE BASIS OF TELEMETRY DATA (PROPORTIONAL TO $\alpha_e \cos \varphi_e$ AND $\alpha_e \sin \varphi_e$) PROVIDED BY THE CONSCAN SYSTEM.

b) ATTITUDE CONTROL
THE CONSCAN SYSTEM PROVIDES THRUSTER FIRING PULSES TO PRECESS THE SPACECRAFT TOWARDS THE EARTH UNTIL THE SPIN AXIS FALLS WITHIN A PREDETERMINED ANGULAR DEADZONE. PRECESSION INCREMENTS $\Delta\alpha$ ARE EXECUTED ONCE EVERY TWO SPACECRAFT REVOLUTIONS.

Figure 8.5A-1. Conscan System Functions

THE CONSCAN SYSTEM PROVIDES DATA TO TELEMETRY FROM WHICH THE ATTITUDE OF THE SPACECRAFT CAN BE ESTIMATED ON THE GROUND. ALSO, BY GROUND COMMAND, THE CONSCAN SYSTEM CAN BE ENABLED TO CONTROL THE AXIAL THRUSTERS AUTOMATICALLY FOR PRECESSING THE SPACECRAFT TOWARDS THE EARTH. PRECESSIONS ARE TERMINATED WHEN THE POINTING ERROR BECOMES LESS THAN A PREDETERMINED VALUE.

The principle on which conscan operation is based is shown schematically in Figure 8.5A-2.

A block diagram showing conscan system components and interfaces is presented in Figure 8.5A-3. This system differs from the Pioneer 10 and 11 configurations in antenna size [0.13 meters (44-inch) instead of 2.60 meters (108-inch) diameter], and the feed movement mechanism, which is not required for Pioneer Venus. Also, the antenna configuration is simpler because conscan is required with the high-gain link only.

The amplitude modulated antenna output is coherently detected by the spacecraft PLL receiver AGC. The AGC is required to remove conscan signal amplitude dependence on received carrier power level which

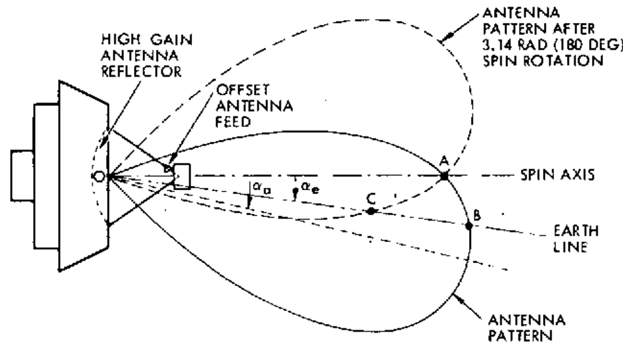

a) CONSCAN GEOMETRY
THE HIGH-GAIN ANTENNA HAS AN OFFSET FEED TO TILT THE RADIATION PATTERN BY AN ANGLE α_a FROM THE SPIN AXIS. IF THE EARTH IS ON THE SPIN AXIS, THE ANTENNA GAIN (OA) WILL BE CONSTANT. WHEN THE EARTH ASPECT ANGLE IS α_e, THE SPIN ROTATION CAUSES THE ANTENNA GAIN TO VARY CYCLICLY (BETWEEN VALUES REPRESENTED BY OC AND OB IN THE FIGURE), THUS CAUSING AN AMPLITUDE MODULATION AS SHOWN IN b)

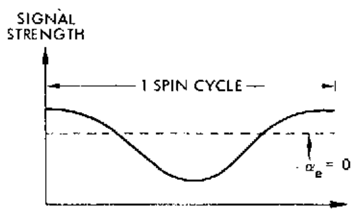

MODULATION INDEX:

$$m = \frac{0.8\sqrt{C}}{\theta_b}\alpha_e$$

WHERE

C = CROSSOVER GAIN IN DB
θ_b = 3 DB BEAMWIDTH IN DEG

b) MODULATION PRODUCED BY CONSCAN
FOR SMALL POINTING ERRORS α_e, THE RECEIVER INPUT IS A CARRIER WITH SINUSOIDAL AMPLITUDE MODULATION.

Figure 8.5A-2. Conscan Principle of Operation

CONSCAN DERIVES ATTITUDE INFORMATION FROM THE AMPLITUDE MODULATION PRODUCED BY POINTING ERRORS AND THE SPACECRAFT SPIN WHEN THE HIGH GAIN ANTENNA PATTERN IS AT AN ANGULAR OFFSET FROM THE SPIN AXIS

varies over a wide range. For weight economy (smaller filter components and IF amplifier design simplicity) wideband AGC is used. The conscan signal (AGC control voltage) is recovered at the output of the AGC amplifier. The main receiver AGC requirement is a 40-dB dynamic range with linearity of ±10 percent.

The digital conscan signal processor determines the amplitude and phase of the conscan signal. It utilizes an internal spacecraft roll reference for optimally processing the conscan signal with minimum transient effects. This unit utilizes the sine-cosine estimating process from which the phase angle and the amplitude of the conscan signal are calculated. Phase information is applied to a countdown circuit and converted to a firing pulse. Amplitude information is compared digitally with fixed threshold values for threshold detection. Digital circuitry is employed in the processor to take advantage of compactness and zero drift characteristics.

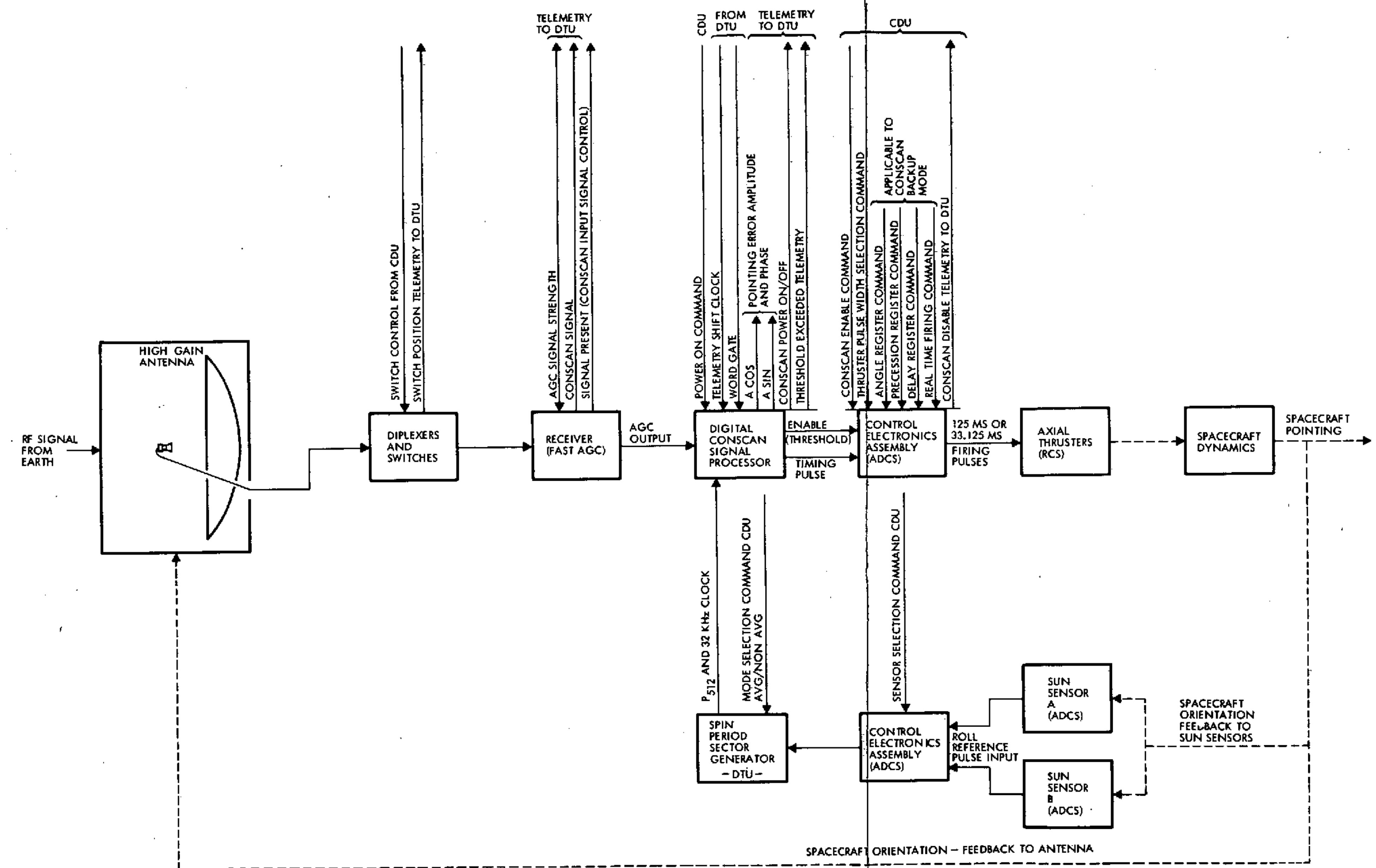

THE HIGH GAIN ANTENNA ASSEMBLY CONSISTS OF A 1.12 METER (44 INCH) DIAMETER PARABOLIC REFLECTOR, A CROSSED DIPOLE FEED, AND THE ASSOCIATED HARDWARE. THIS ASSEMBLY PROVIDES A PENCIL BEAM PATTERN OF ABOUT 0.14 RAD (8.4 DEG) HALF POWER BANDWIDTH. THE FEED IS OFFSET TO TILT THE PATTERN 0.044 RAD (2.5 DEG) FROM THE SPIN AXIS (1 DB CROSSOVER). THE AMPLITUDE MODULATED ANTENNA OUTPUT IS COHERENTLY DETECTED BY THE SPACECRAFT RECEIVER. THE CONSCAN SIGNAL IS RECOVERED AT THE OUTPUT OF THE AGC AMPLIFIER. THE DIGITAL CONSCAN SIGNAL PROCESSOR COMPUTES POINTING ERROR AMPLITUDE AND PHASE AND GENERATES TIMING PULSES FOR THRUSTER FIRING. ALSO, AMPLITUDE INFORMATION IS COMPARED DIGITALLY WITH A FIXED THRESHOLD VALUE FOR PROVIDING A THRUSTER ENABLE SIGNAL. THE CONTROL ELECTRONICS ASSEMBLY HAS LOGICS FOR TURNING CONSCAN PRECESSION ON AND OFF, SELECTING FIRING PULSE DURATIONS, AND IMPLEMENTING A CONTROL DEADZONE. A ROLL REFERENCE IS PROVIDED (TO THE CONSCAN PROCESSOR) BY THE SPIN PERIOD SECTOR GENERATOR ON THE BASIS OF SUN SENSOR PULSES. THE CONTROL ELECTRONICS ASSEMBLY SELECTS SUN SENSORS AND SHAPES THE SUN SENSOR ROLL REFERENCE PULSES.

Figure 8.5A-3. Conscan System Block Diagram

FOLDOUT FRAME /

FOLDOUT FRAME 2

Pulses from the conscan signal processor are applied to the control electronics assembly of the ADCS subsystem for proper timing of precession thruster firings. The threshold signal from the processor is also supplied to the control electronics assembly (CEA) and is used as an enable signal. The CEA utilizes a gated output signal (consisting of the threshold signal, the timing pulse, and a set-reset flip-flop controlled by ground command) to establish the validity of thruster firing. In the event that the conscan signal level should momentarily fall below threshold during closed loop operation, the control electronics assembly turns the conscan function off until receiving a ground command to continue the conscan pointing process.

The control electronics assembly also determines the length of the precession thruster firing pulses. Various step sizes can be used. The 125 millisecond pulse duration (approximately 0.25 degree step) will be used for open-loop precessions. The 33.125 millisecond pulse duration (0.038 degree step size) will be utilized for conscan precession to: 1) minimize the nutation amplitude, which gets amplified by the high-gain antenna, and 2) minimize the possibility of limit cycling at the deadzone boundary. The control electronics assembly requires a ground command to select the proper firing pulse width.

Firing pulses will be issued once every two spacecraft revolutions to minimize the nutation amplitude that occurs during multiple-pulse precessions. Firing once per revolution is desirable, but it is not feasible because the conscan processor needs at least one spin cycle to perform the integrations required for phase and amplitude estimations.

A roll reference signal for the conscan processor is supplied by the spin period sector generator (SPSG). The SPSG receives its reference from the sun sensor assembly. The SPSG counts an internal clock for one spacecraft revolution and digitally divides this interval into a number of sectors for generating evenly spaced timing signals which are harmonically related to the spacecraft spin rate. The digital conscan signal processor utilizes the 512th harmonic of the spin rate (P_{512}) for performing its internal functions. Two operation modes are provided by the spin period sector generator: the spin period averaging mode, and the non-averaging mode. The first updates the spin rate every 64 revolitions of the spacecraft and uses a 64-revolution average for its reference. The second mode utilizes an average based upon the period between the last two roll pulses and has a 1 cycle delay between updating signals. Both modes can be utilized for conscan operation and are selectable by ground command.

2. CONSCAN SYSTEM DESIGN AND PERFORMANCE

The orbiter high-gain antenna consists of the DSCS-II reflector and the Pioneers 10 and 11 feed horn, both without modification. The feed is offset by approximately 0.024 meter (0.9 inch) to provide a radiation pattern tilt angle of about 0.044 radians (2.5 degrees) from the spin axis.

A cross-section of the high-gain antenna radiation pattern is shown in Figure 8.5A-4, which also presents the analytical model used in a digital program (described later) for simulation of the entire conscan system.

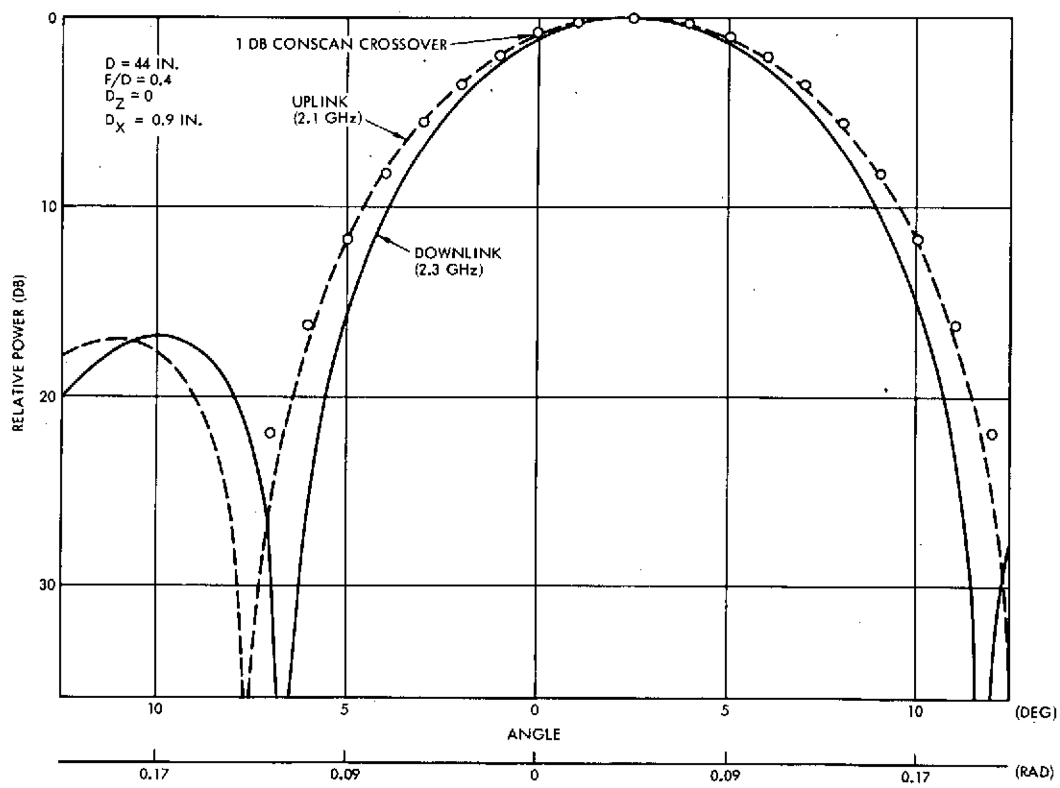

Figure 8.5A-4. High Gain Antenna Pattern

THE RECEIVING ANTENNA PATTERN, SHOWN IN BROKEN LINES, HAS A HALF POWER BEAMWIDTH OF ABOUT 0.14 RAD (8.4 DEG). THE FEED IS OFFSET TO PROVIDE A TILT ANGLE θ OF ABOUT 0.044 RAD (2.5 DEG), WHICH SETS THE -1-DB CROSSOVER POINT ON THE SPIN AXIS. FOR SIMULATION PURPOSES, THE RECEIVING PATTERN HAS BEEN MODELLED BY THE FOLLOWING GAUSSIAN APPROXIMATION

$$R(\alpha) = e^{-[0.0174\alpha^2 + 1.16 \times 10^{-4}\alpha^4]}$$

WHERE α IS THE ANGLE FROM THE BORESIGHT AXIS IN DEGREES. POINTS SHOWN IN THE FIGURE WERE OBTAINED FROM THE PRECEDING ANALYTICAL EXPRESSION.

The Pioneers 10 and 11 receiver, with no modifications, is used in the conscan system. A simplified block diagram and transfer functions of the receiver are given in Figure 8.5A-5, and typical AGC characteristics are shown in Figure 8.5A-6.

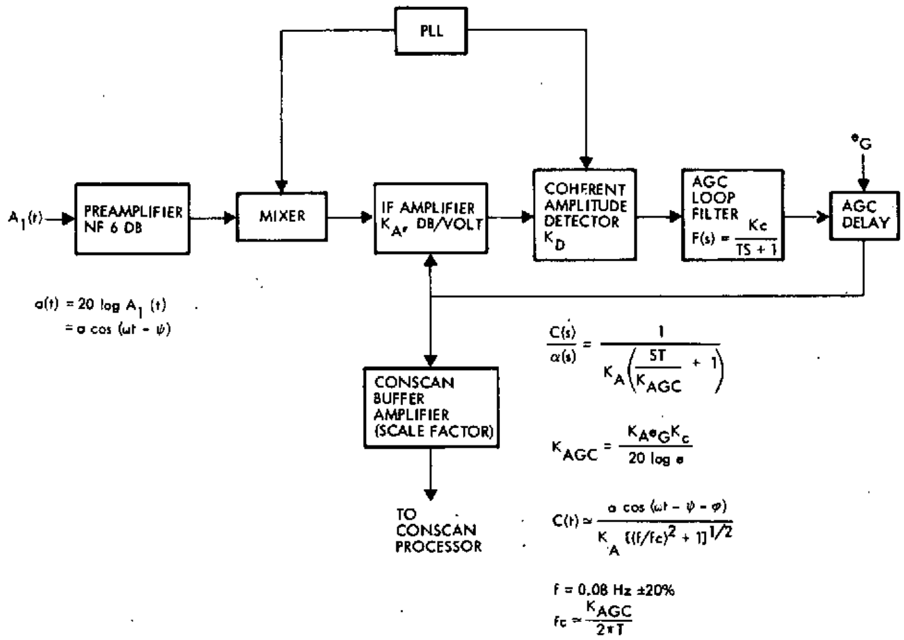

Figure 8.5A-5. Conscan Receiver Simplified Block Diagram

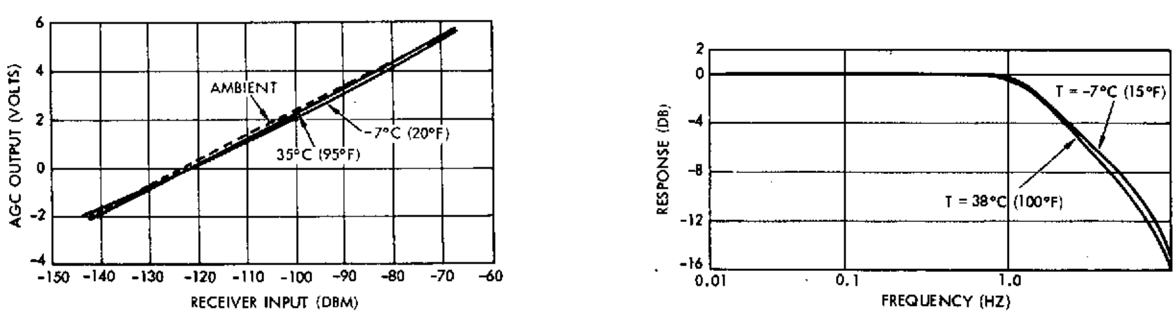

a) RECEIVER AGC CHARACTERISTIC

b) CLOSED LOOP AGC RESPONSE

Figure 8.5A-6. Receiver Characteristics

PART a) SHOWS THE AGC CHARACTERISTIC IS APPROXIMATELY LOGARITHMIC. LINEARITY CAN BE ASSUMED OVER A VARY WIDE RANGE OF INPUT POWERS. PART b) PRESENTS RESULTS OF CLOSED LOOP AGC RESPONSE MEASUREMENTS. THE RESPONSE CAN BE APPROXIMATED BY A SINGLE POLE LOW PASS FILTER.

The S-band preamplifier establishes the receiver noise figure at 6 dB or better and determines conscan noise errors. The S-band signal is heterodyned to a convenient IF for controlled amplification. Since the receiver local oscillator is phase locked to the incoming signal, a coherent amplitude detector is employed and the detected conscan signal is applied to the AGC loop filter. This filter is used to establish the closed loop response and the AGC noise bandwidth. Until an appropriate signal level is attained in the IF amplifier, the action of the AGC is delayed by the comparator and operates when the loop filter signal exceeds the reference voltage e_G. A relatively constant IF signal level is maintained through the application of the comparator output signal to the control terminals of the AGC'd IF amplifier. In order to provide an error signal of sufficient amplitude to drive the conscan processor, an amplifier external to the AGC loop is employed which buffers the control signal and establishes the pointing error voltage sensitivity scale factor.

The closed loop AGC slope is inversely proportional to the IF amplifier attentuation, K_A, in dB/volt. Therefore, the AGC slope linearity as a function of the received carrier strength is mainly established by the linearity of K_A. The variation in the AGC slope also introduces a phase error. However, because of the wide AGC bandwidth, this error is small. Since the processor is basically an integrate-and-dump device, one would expect, ideally, a $\left|\frac{\sin x}{x}\right|$ frequency response about the spin frequency with nulls at multiples of 1/2 the spin frequency. However, the square wave mixer reference signal contains odd harmonics, frequency $= n\omega_s$, of relative magnitude 1/n, which mix with interfering signals near these odd harmonics of the spin frequency and the resulting processor response as shown in the figure. As evident from these data, even harmonics are not significant and odd harmonics (primarily third) may be the dominant interfering signals.

The digital conscan processor is also identical to the Pioneers 10 and 11 unit. A block diagram and a functional description of the processor are given in Figure 8. 5A-7. The conscan signal, from the receiver AGC amplifier, includes the fundamental conscan signal and interference, which consists primarily of higher harmonics, high and low frequency nutation, and thermal noise. The input signal is high-pass filtered to block the DC, and then low-pass filtered to improve the input SNR. These filters will introduce small phase shifts and amplitude variations due to changes in spin frequency. The signal is then sampled (128 samples/cycle) and converted to equivalent binary data with a maximum of ± 7 bits. The data are then multipled by in-phase and quadrature square waveforms. Results are accumulated (integrated) for one conscan revolution. The processor requires an external frequency reference, which is provided by the spin period sector generator. This reference is used to derive the multiplying signals, which can be advanced or delayed (±45 degrees in 3 degree steps) to provide phase compensation for the system components. During the processing cycle, the phase and amplitude of the conscan signal are estimated. In reality, instead of phase, a timing pulse which corresponds to the positive going axis crossing is needed. This is accomplished by first computing tan Φ and generating tan $(360-\theta)$ as shown in the figure. The estimated axis crossing time corresponds to the coincidence between tan Φ and tan $(360-\theta)$. The cot Φ and cot θ are computed in odd octants to conserve processor size. This procedure used in calculating axis crossing time results in peak approximation errors of less than 0.044 radians (±2.5 degrees).

The amplitude estimate is computed approximately by the addition of the larger of the integrator output magnitudes to one half of the smaller. This results in peak errors of ±6 percent with respect to the optimum root sum square method. The resultant estimate is compared to a threshold which is set in 0.39 mV steps. If the threshold is exceeded, the firing pulses are enabled to the attitude determination and control system (ADCS). If the amplitude estimate falls below threshold, the ADCS terminates conscan precession.

Figure 8.5A-8 shows conscan processor frequency responses predicted by analysis and obtained by tests. Superimposed on the graph are points corresponding to frequency response results obtained with the digital simulation program described in Figure 8.5A-9.

Figure 8.5A-9 is a block diagram of the digital simulation program developed for determining attitude determination accuracies provided by conscan telemetry data. As shown in Figure 8.5A-4, a gaussian model of the antenna pattern provides very good fit within ±0.122 radian (±7 degree) from boresight. The model used in the simulation also includes capabilities to introduce ellipticity errors in every cross section of the pattern normal to the boresight axis. A Fourier analysis subroutine

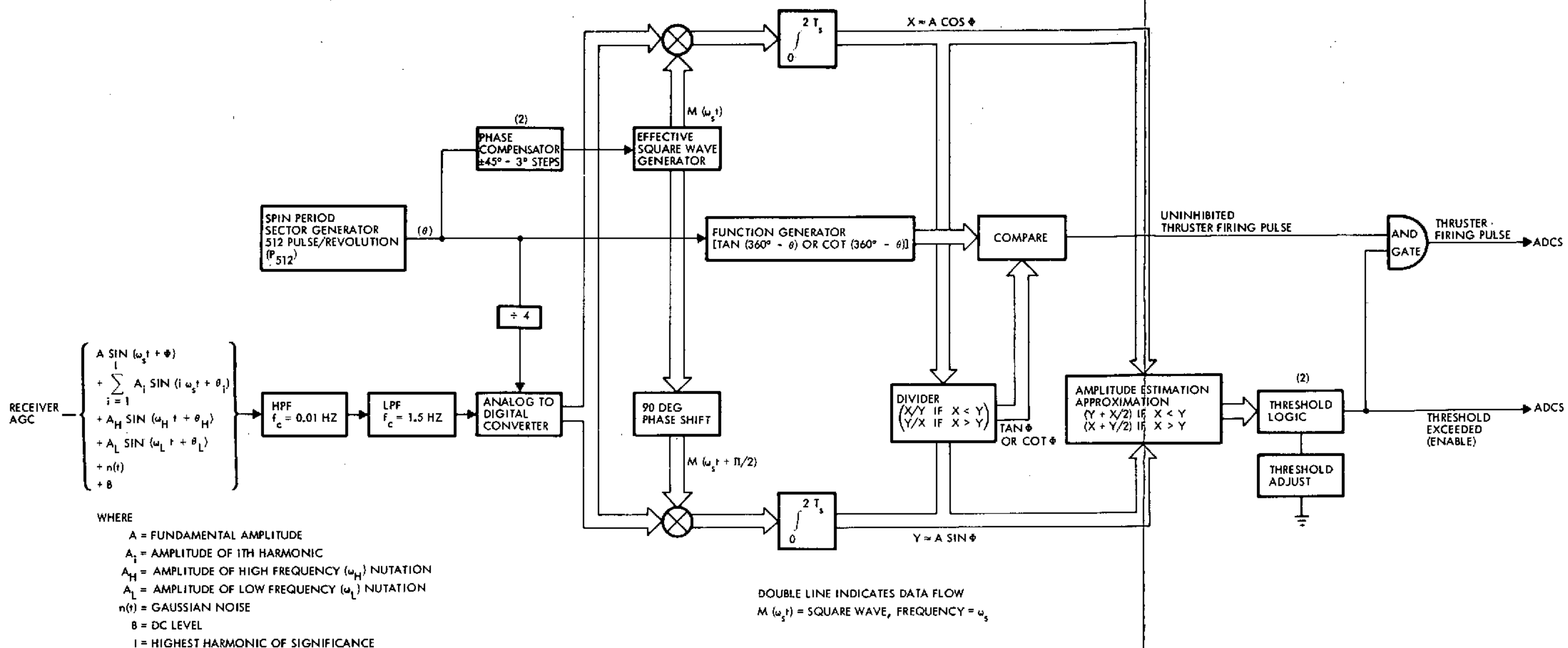

Figure 8.5A-7. Digital Conscan Processor Block Diagram

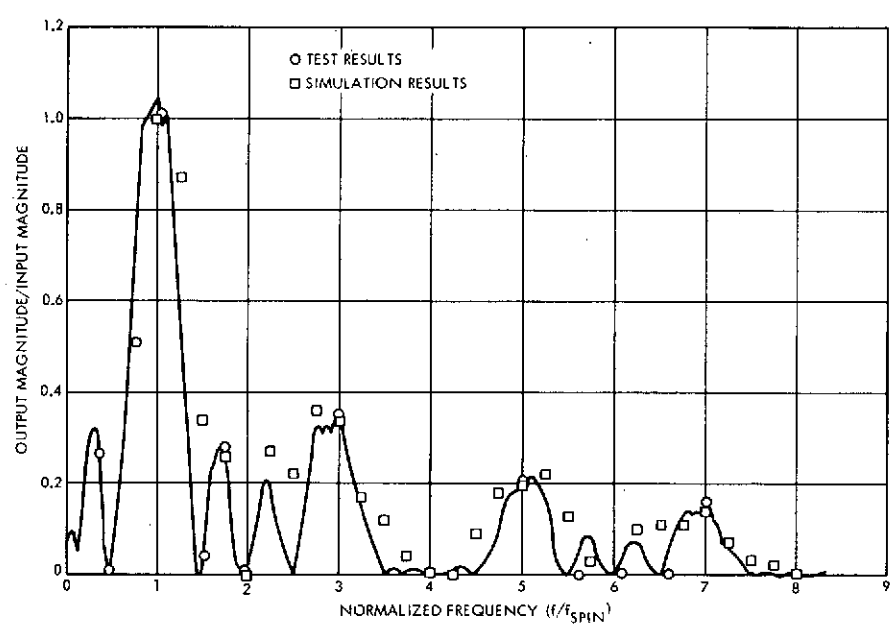

Figure 8.5A-8. Conscan Processor Frequency Response

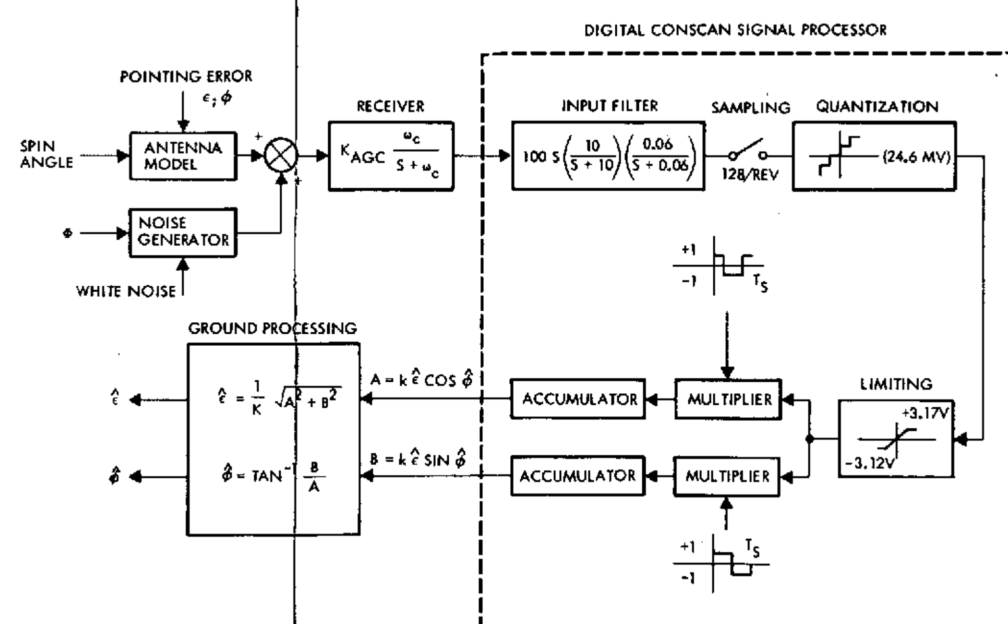

Figure 8.5A-9. Conscan System Simulation Block Diagram

THE ANTENNA IS MODELLED AS GAUSSIAN WITH ELLIPTICITY ERRORS. THE RECEIVER IS ASSUMED LOGARITHMIC AND IS MODELLED AS A FIRST ORDER LAG. THE CONSCAN SIMULATION INCLUDES A MODEL OF THE INPUT FILTER, SAMPLING, QUANTIZATION, LIMITING, AND DIGITAL OPERATIONS PROVIDING ATTITUDE DATA FOR TELEMETRY. LINEARIZED GROUND SIGNAL PROCESSING (K CONSTANT) AND NO TELEMETRY ERRORS ARE ASSUMED.

FOLDOUT FRAME 1

FOLDOUT FRAME 2

is used to compute amplitudes of the DC, and the first five harmonic components of the logarithmic output from the antenna pointing kinematics. The receiver is simulated by a constant gain (K_{agc}) and a first-order lag using values given in Figure 8.5A-6. The digital conscan signal processor is simulated in detail, including input filter, sampling, quantization, limiting, sine and cosine square wave generators (spin synchronous), multipliers, and accumulators. Correlations between the conscan processor simulation and previous analyses and tests are very good, as shown in Figure 8.5A-8. Telemetry errors are neglected and linearized ground processing is assumed (calibration factor K is taken as constant). The program has capabilities for performing Montecarlo sums with random inputs provided by a gaussian subroutine.

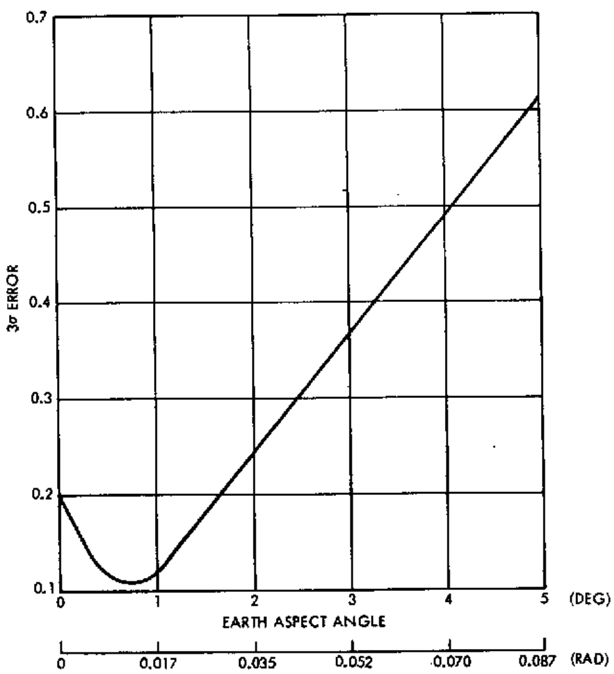

Figure 8.5A-10. Conscan Attitude Determination Errors

THE CURVE SUMMARIZES RESULTS OF A SIMULATION ANALYSIS OF THE CONSCAN SYSTEM OPERATING WITH THE HIGH GAIN ANTENNA SELECTED FOR THE ORBITER. ESTIMATION ERRORS (3σ), BASED ON TELEMETRY DATA, ARE GIVEN AS A FUNCTION OF EARTH ASPECT ANGLE (SPACECRAFT POINTING ERROR, RELATIVE TO EARTH). NOISE EFFECTS ARE NEGLIGIBLE SINCE THE TOTAL RECEIVED POWER WILL BE GREATER THAN -126 DBM. ERROR SOURCES INCLUDE ±3.5 MRAD (±0.2 DEG) MISALIGNMENT, 5 PERCENT SCALE FACTOR UNCERTAINTIES, 6.3 MRAD (0.36 DEG) NUTATION ANGLE, 5 PERCENT AGC NONLINEARITY, AND CONSCAN PROCESSOR QUANTIZATION AND SIGNAL LIMITING

Figure 8.5A-10 shows conscan attitude determination error as a function of earth aspect angle (spacecraft pointing error relative to the earth). These errors are RSS, 3σ, and include contributions due to antenna misalignments, scale factor uncertainties, spacecraft nutation, and receiver and conscan processor nonlinearities.

Figure 8.5A-11 shows effects of calibration curve approximation, and conscan processor nonlinearities, on attitude determination accuracy. Errors due to antenna misalignments are presented in Figure 8.5A-12 as a function of spacecraft pointing errors. Effects of spacecraft nutation on attitude determination accuracy are covered in Figure 8.5A-13.

In the simulation, the conscan calibration curve has been approximated by a constant factor providing good fit for spacecraft pointing

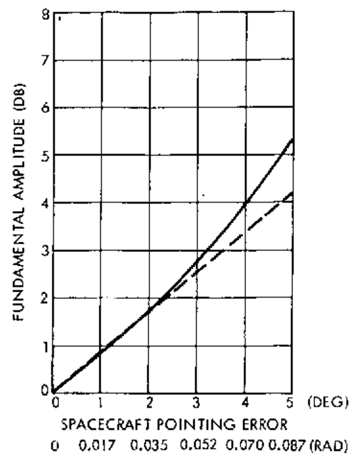

a) CALIBRATION CURVE AND APPROXIMATION USED IN THE SIMULATION

THE SOLID LINE IS A PLOT OF THE AMPLITUDE OF THE FUNDAMENTAL COMPONENT (IN DB) OF THE CONSCAN SIGNAL AS A FUNCTION OF SPACECRAFT POINTING ERROR. THE BROKEN LINE REPRESENTS THE LINEAR APPROXIMATION USED IN THE SIMULATION.

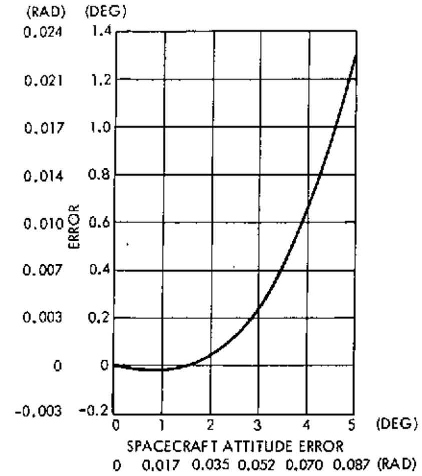

b) EFFECTS OF ANTENNA CALIBRATION AND CONSCAN PROCESSOR NONLINEARITIES ON CONSCAN ACCURACY

THE GRAPH SHOWS ATTITUDE ESTIMATION ERRORS CAUSED BY CONSCAN PROCESSOR NONLINEARITIES (I.E., QUANTIZATION, LIMITING, AND MODULATION PRODUCTS) AND ERRORS IN THE CALIBRATION CURVE MODELING. NOTE THAT IN THE REGION OF GOOD FIT, 0 TO 0.035 RAD (0 TO 2 DEG), THE ESTIMATION ERRORS ARE LESS THAN 0.87 MRAD (0.05 DEG).

Figure 8.5A-11. Conscan Calibration Curve and Attitude Determination Errors due to Antenna Calibration and Conscan Processor Nonlinearities

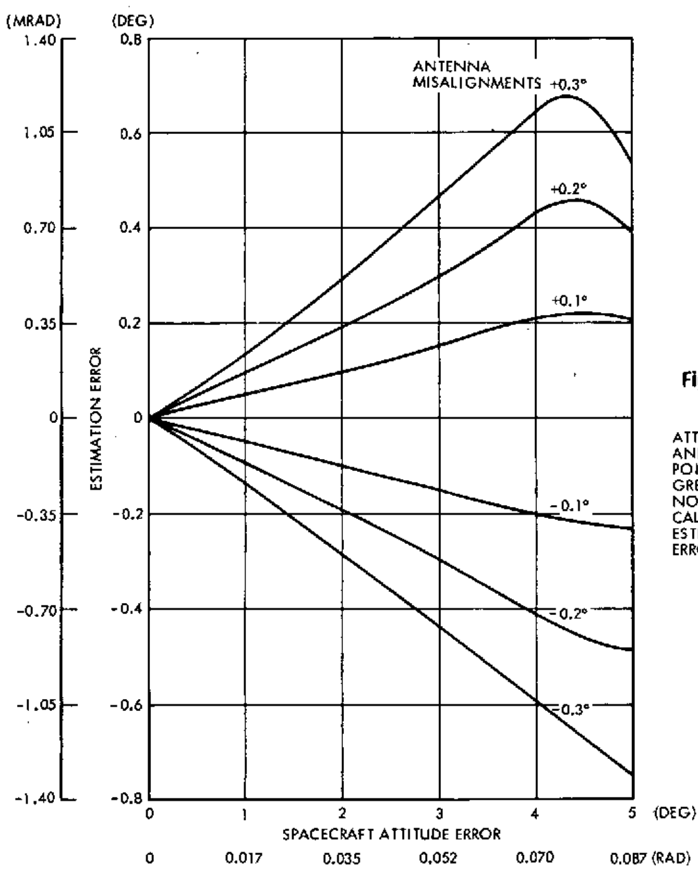

Figure 8.5A-12. Conscan Attitude Determination Errors due to Antenna Misalignments

ATTITUDE DETERMINATION ERRORS PRODUCED BY ANTENNA MECHANICAL AND ELECTRICAL MISALIGNMENTS ARE PROPORTIONAL TO SPACECRAFT POINTING ERRORS. NONLINEARITIES EXHIBITED FOR ATTITUDE ERRORS GREATER THAN 0.070 RADIAN (4 DEGREES) ARE DUE TO LARGE SIGNAL NONLINEAR OPERATION AND ERRORS IN THE MODELLING OF THE ANTENNA CALIBRATION CURVE. FOR ±3.5 MRAD (±0.2 DEG) MISALIGNMENTS, THE ESTIMATION ERRORS ARE ABOUT 10 PERCENT OF THE SPACECRAFT POINTING ERROR.

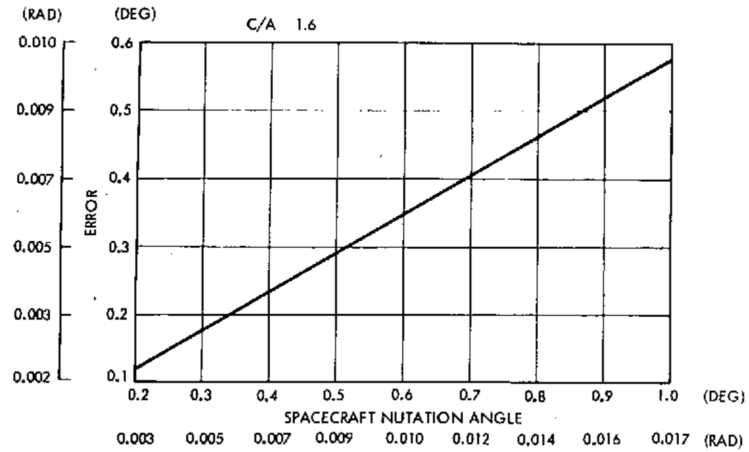

a) CONSCAN ATTITUDE DETERMINATION ERRORS DUE TO SPACECRAFT NUTATION.
ATTITUDE DETERMINATION ERRORS ARE PROPORTIONAL TO SPACECRAFT NUTATION ANGLE. THE GRAPH CORRESPONDS TO A MOMENT OF INERTIA RATIO OF 1.6, WHICH IS TYPICAL FOR THE PIONEER VENUS ORBITER.

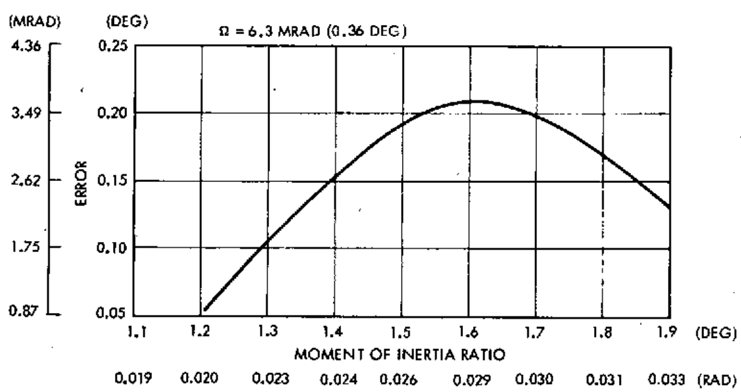

b) EFFECT OF MOMENT OF INERTIA RATIO CHANGES ON ERRORS DUE TO SPACECRAFT NUTATION
ASSUMING A CONSTANT NUTATION AMPLITUDE OF 6.3 MRAD (0.36 DEG) (TYPICAL FOR THE PIONEER VENUS ORBITER AFTER FIRING 125 MSEC PULSES), THE CURVE SHOWS ATTITUDE DETERMINATION ERRORS PRODUCED BY NUTATION AS A FUNCTION OF SPACECRAFT MOMENT OF INERTIA RATIO.

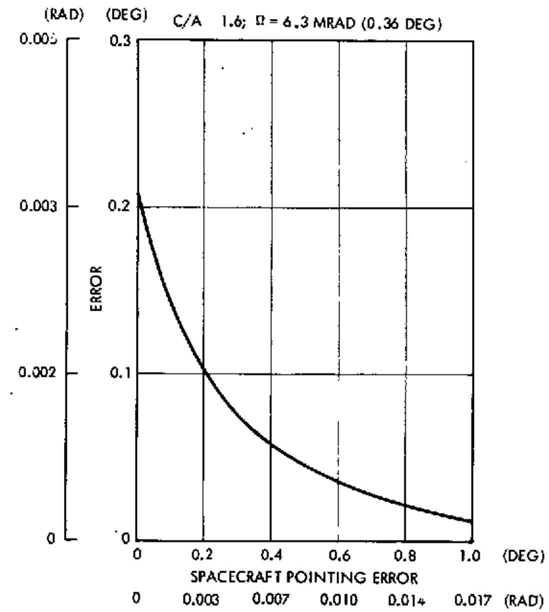

c) CONSCAN ATTITUDE DETERMINATION ERRORS DUE TO NUTATION VERSUS SPACECRAFT POINTING OFFSET.
ATTITUDE DETERMINATION ERRORS DUE TO NUTATION ARE AN INVERSE FUNCTION OF SPACECRAFT POINTING ERROR. THE CURVE ASSUMES A CONSTANT NUTATION ANGLE OF 6.3 MRAD (0.36 DEG) AND A MOMENT OF INERTIA RATIO OF 1.6.

Figure 8.5A-13 Effects of Spacecraft Nutation on Attitude Determination Accuracy errors in the range from 0 to 0.035 radian (0 to 2 degrees). Other scale factor values have been used, and the corresponding effects on attitude determination accuracy are shown in Figure 8.5A-14.

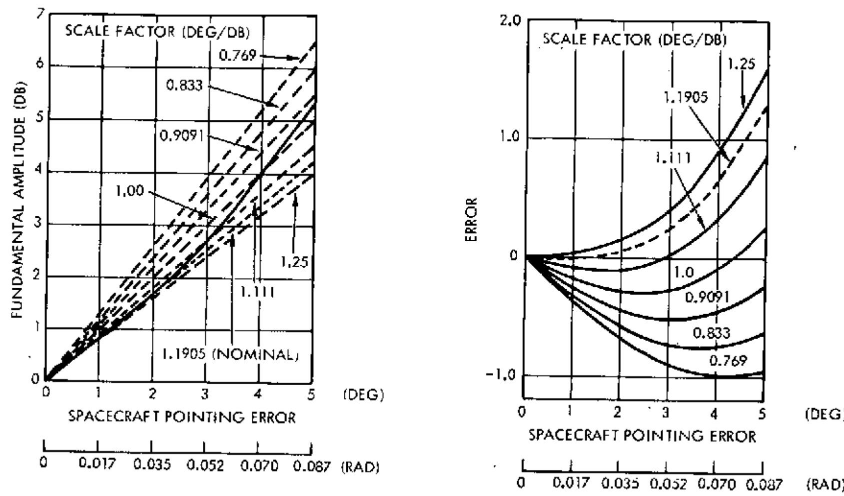

a) NOMINAL AND ALTERNATIVE LINEAR APPROXIMATIONS TO THE ANTENNA CALIBRATION CURVE

b) CONSCAN ATTITUDE DETERMINATION ERRORS VERSUS SCALE FACTOR

Figure 8.5A-14. Effect of Scale Factor Selection on Attitude Determination Accuracy

VARIOUS LINEAR APPROXIMATIONS TO THE CONSCAN CALIBRATION CURVE ASSUMED IN THE SIMULATION ARE SHOWN IN a). THE CORRESPONDING ATTITUDE DETERMINATION ERRORS ARE SHOWN IN b) AS FUNCTIONS OF SPACECRAFT POINTING ERROR.

Figure 8.5A-15 shows results of a series of Montecarlo runs providing estimates of the effects of receiver thermal noise on conscan attitude determination accuracy. Error contributions due to noise are not included in Figure 8.5A-10 because received powers will be greater than -126 dBm, and the small resulting errors can be reduced even further by averaging.

3. FANSCAN SYSTEM DESCRIPTION

Fanscan differs from conscan in the following aspects:

- The antenna pattern is of the fanbeam type (instead of pencil-beam as in Pioneers 10 and 11)
- The spin axis orientation desired is perpendicular to the earth line
- Only error amplitude measurements are significant because phase angles are approximately equal to the sun-spacecraft-earth angle
- Automatic precession capability cannot be implemented without ground intervention (for commanding directions of precession).

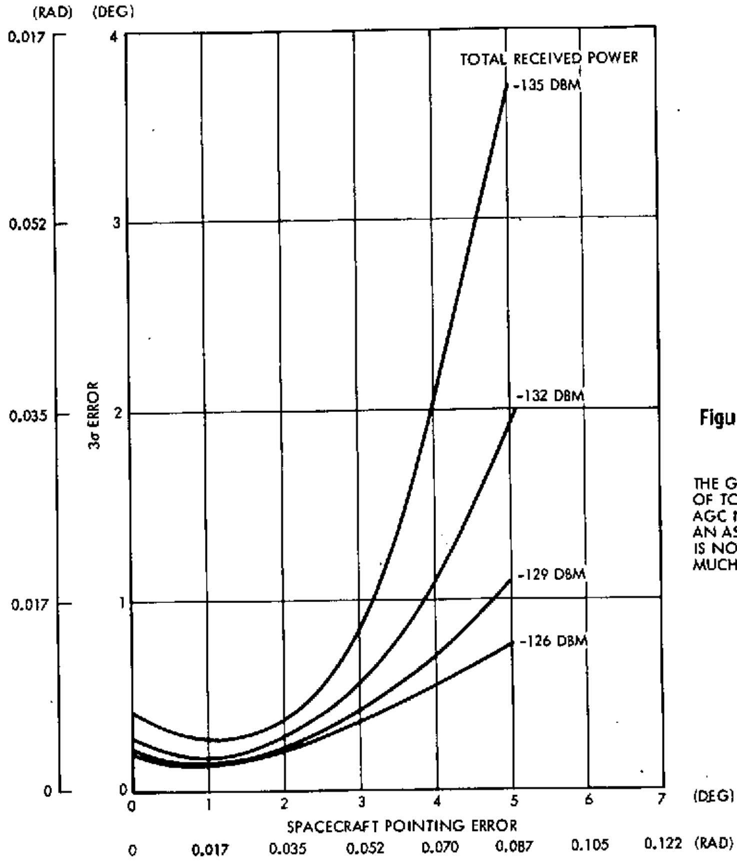

Figure 8.5A-15. Effects of Receiver Thermal Noise on Conscan Attitude Determination Accuracy

THE GRAPH SHOWS 3σ ATTITUDE DETERMINATION ERRORS AS FUNCTIONS OF TOTAL RECEIVED POWER AND SPACECRAFT POINTING ERROR. RECEIVER AGC NOISE HAS BEEN SIMULATED AS A GAUSSIAN RANDOM PROCESS WITH AN ASSSUMED ONE-SIDED NOISE BANDWIDTH OF 1.9 HZ. THERMAL NOISE IS NOT EXPECTED TO BE A PROBLEM BECAUSE RECEIVED POWERS WILL BE MUCH GREATER THAN -126 DBM

An outline of the fanscan principle of operation and its main features is given in Figure 8.5A-16. The digital conscan signal processor can be used to derive attitude data with fanscan because it provides good rejection to even harmonics of the spin frequency.

The fanscan antenna is a shortened Pioneer array consisting of 10 elements. Pattern data are given in Figure 8.5A-17, which also shows points obtained by means of the gaussian approximation used for simulation.

Figure 8.5A-18 shows results of a Fourier analysis of the fanscan signals (as shown in Figure 8.5A-16) corresponding to various values of spacecraft pointing error.

The processor used with fanscan is identical to the Pioneers 10 and 11 conscan processor and, for this reason, it is not described here.

a) ANTENNA CONFIGURATION USED IN FANBEAM/FANSCAN ORBITERS

THE FANSCAN ANTENNA IS A 24 INCH FRANKLIN ARRAY WITH A MAXIMUM GAIN OF 7.5 DB AND A HALF-POWER BEAMWIDTH OF 0.21 RAD (12.3 DEG). ITS AXIS IS AT AN ANGLE OF 0.061 RAD (3.6 DEG) FROM THE SPIN AXIS. THE HIGH GAIN ANTENNA IS A 48-INCH FRANKLIN ARRAY PROVIDING A MAXIMUM GAIN OF 11 DB. THE HALF-POWER BEAMWIDTH IS 0.105 RAD (5.8 DEG).

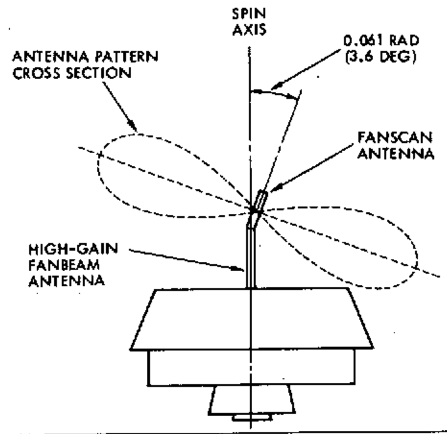

b) FANSCAN GEOMETRY IN FLIGHT

FANSCAN PROVIDES DATA TO TELEMETRY FROM WHICH THE ASPECT ANGLE ERROR CAN BE ESTIMATED. THIS ANGLE IS THE COMPLEMENT OF THE ANGLE BETWEEN THE SPIN AXIS AND EARTH. FANSCAN PROVIDES A PHASE ANGLE MEASUREMENT ANALOGOUS TO CONSCAN, BUT THIS ANGLE IS ONLY AN APPROXIMATE MEASURE OF THE SUN-SPACECRAFT-EARTH ANGLE. AUTOMATIC PRECESSION CAPABILITY CANNOT BE IMPLEMENTED UNLESS ADDITIONAL INFORMATION IS PROVIDED TO DEFINE THE DIRECTION OF PRECESSION REQUIRED.

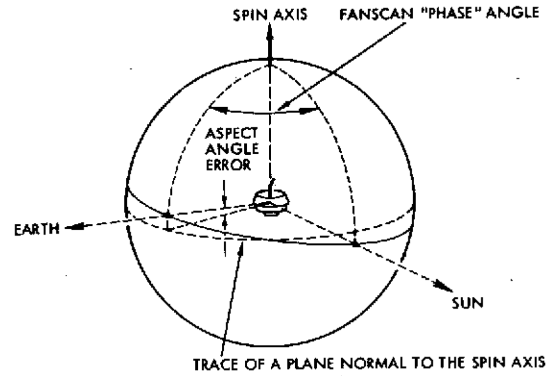

c) FANSCAN WAVEFORMS

WHEN THE SPIN AXIS IS NORMAL TO THE EARTH LINE ($\phi = 0$) THE RECEIVER AGC OUTPUT CONTAINS A SECOND HARMONIC OF THE SPIN FREQUENCY. WITH NONZERO POINTING ERRORS, THE AGC SIGNAL ALSO CONTAINS A FUNDAMENTAL COMPONENT AT THE SPIN FREQUENCY, WHOSE AMPLITUDE IS A FUNCTION OF THE ASPECT ANGLE ERROR. THE CONSCAN PROCESSOR CAN BE USED TO PROCESS FANSCAN DATA ON BOARD THE SPACECRAFT BECAUSE IT REJECTS EVEN HARMONICS OF THE SPIN FREQUENCY.

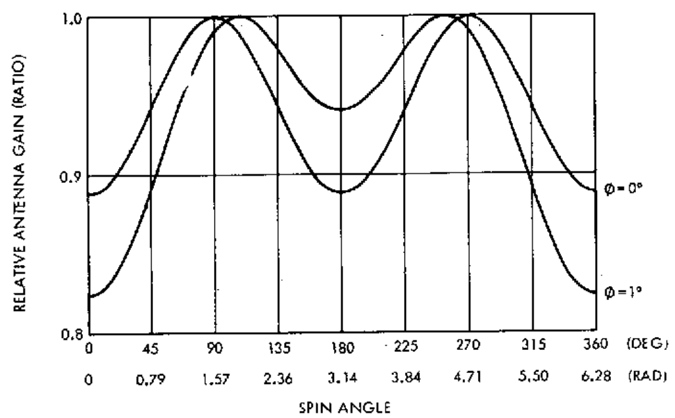

Figure 8.5A-16. Fanscan Principle of Operation

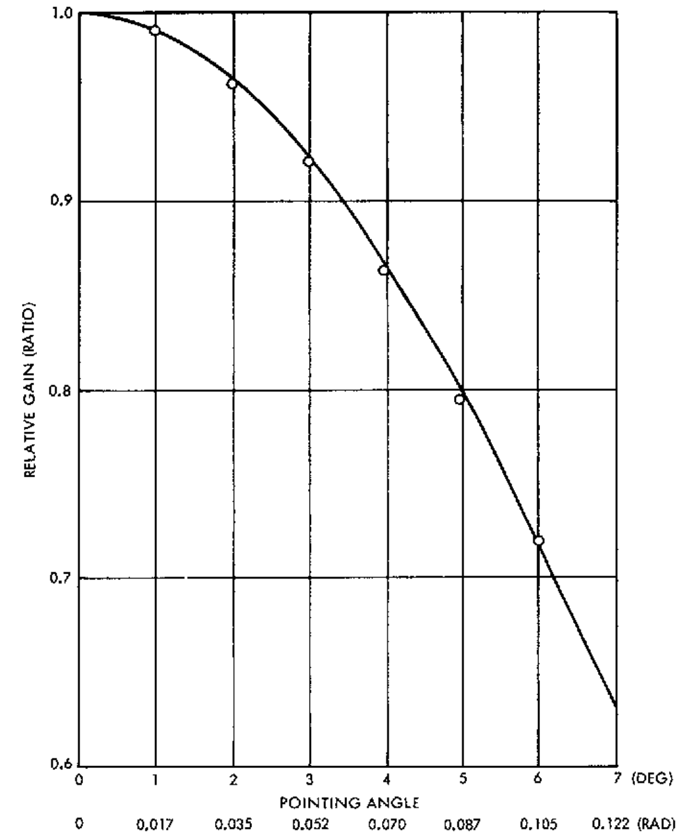

Figure 8.5A-17. Fanscan Antenna Pattern

THE FANSCAN ANTENNA IS A 10 ELEMENT FRANKLIN ARRAY PROVIDING A MAXIMUM GAIN OF 7.5 DB. THE HALF-POWER BEAMWIDTH IS 0.21 RAD (12.3 DEG). FOR SIMULATION PURPOSES, THE ANTENNA GAIN IS GIVEN BY THE THE FOLLOWING EXPRESSION:

$$R(\alpha) = e^{-9.16 \times 10^{-3}\alpha^2}$$

WHERE α IS THE ANGLE IN DEGREES FROM THE PLANE PERPENDICULAR TO THE ANTENNA AXIS

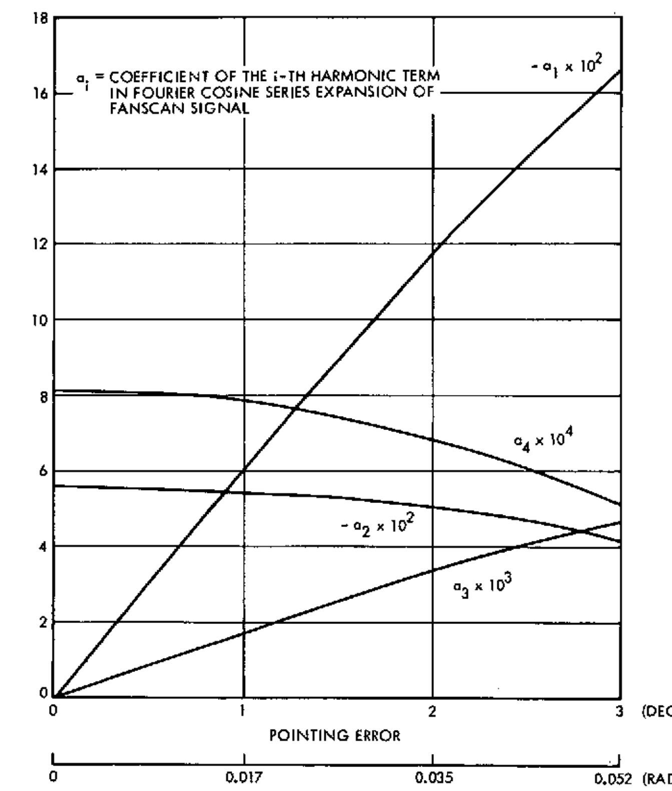

Figure 8.5A-18. Fanscan Signal Harmonics

THE FIGURE GIVES FOURIER COEFFICIENTS OF THE FANSCAN SIGNAL (MODULATION AT THE RECEIVER INPUT, RELATIVE TO CARRIER AMPLITUDE WITH MAXIMUM ANTENNA GAIN) AS FUNCTIONS OF POINTING ERROR. A FANBEAM ANTENNA TILT ANGLE OF 0.061 RAD (3.6 DEG) IS USED.

4. FANSCAN PERFORMANCE

The simulation described in Section 2 of this appendix was modified to include a model of the fanscan antenna kinematics. A limited number of runs were made because the Version IV science payload requirements could not be met by the fanbeam/fanscan configurations and, therefore, fanscan error analysis work was terminated.

Figure 8.5A-19 shows that the effects of sampling, quantization, and fanscan signal harmonics are negligible. Effects of antenna misalignments on fanscan attitude determination accuracy are shown in Figure 8.5A-20.

So far, the antenna radiation pattern has been assumed symmetric about a plane normal to the antenna axis. Distortions invalidating this assumption may occur due to ground plane effects. Figure 8.5A-21 presents estimates of the attitude determination errors caused by ground plane effects, on the assumption that the corresponding distortions are symmetric about the antenna axis.

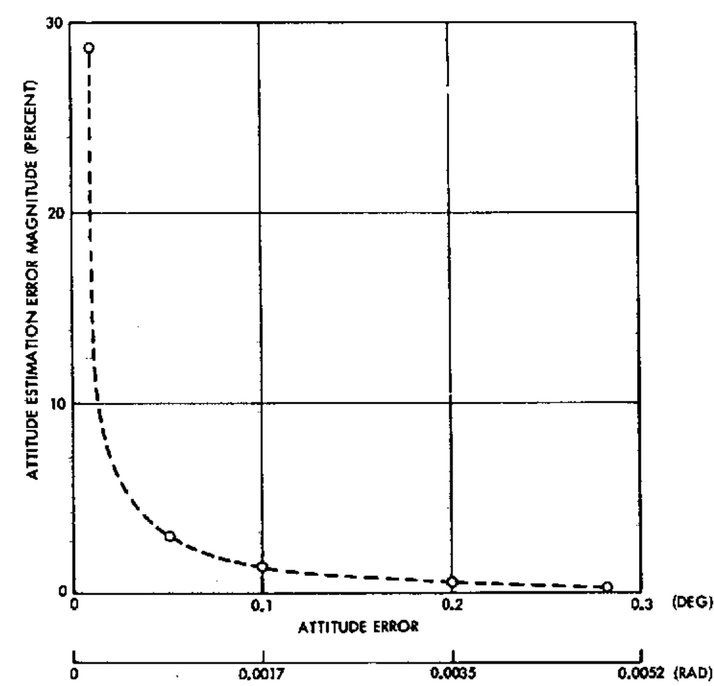

Figure 8.5A-19. Attitude Determination Errors due to Fanscan Signal Harmonics and Fanscan Processor Nonlinearities

RESULTS INCLUDE EFFECTS OF SIGNAL HARMONICS UP TO THE FIFTH AND PROCESSOR SAMPLING AND QUANTIZATION.

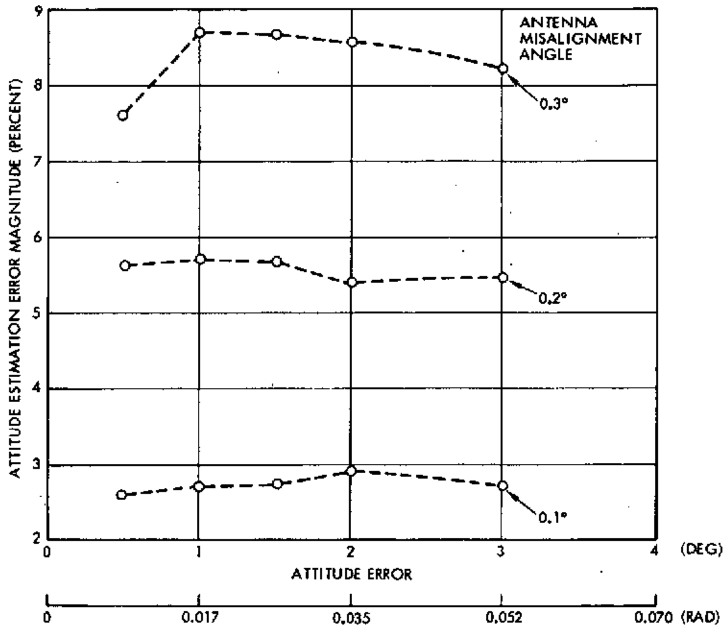

Figure 8.5A-20. Attitude Determination Errors Due to Antenna Misalignments

ATTITUDE DETERMINATION ERRORS ARE GIVEN AS FUNCTIONS OF EARTH ASPECT ERROR WITH ANTENNA MISALIGNMENT ERROR AS A PARAMETER.

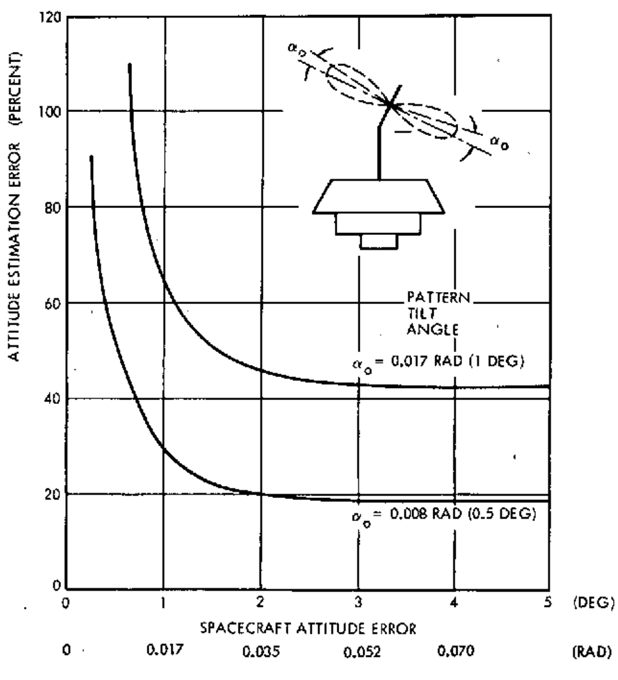

Figure 8.5A-21. Effect of Ground Plane Antenna Pattern Distortions on Fanscan Attitude Determination Accuracy

GROUND PLANE EFFECTS ARE ASSUMED TO PRODUCE SYMMETRIC DISTORTIONS OF THE FANSCAN ANTENNA PATTERN AS SHOWN IN THE FIGURE. ATTITUDE DETERMINATION ERRORS ARE GIVEN AS FUNCTIONS OF EARTH ASPECT ANGLE ERRORS WITH THE TILT ANGLE α_o AS A PARAMETER.

APPENDIX 8.5B

DOPPLER MEASUREMENT OF SPIN AXIS ATTITUDE

APPENDIX 8.5B

DOPPLER MEASUREMENT OF SPIN AXIS ATTITUDE

1. INTRODUCTION

Figures 8.5B-1 and 8.5B-2 describe briefly the doppler measurement techniques proposed for attitude determination on the Pioneer Venus spacecraft. Both methods have been used successfully on Pioneers 10 and 11.

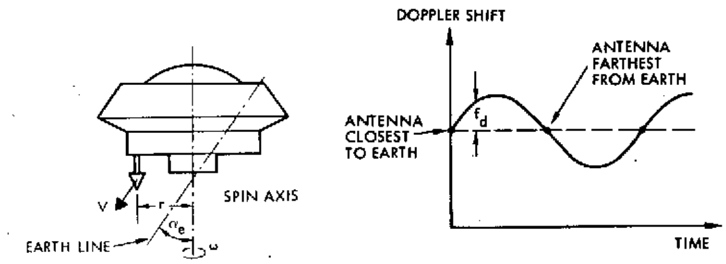

Figure 8.5B-1. Spin Axis Attitude Determination by Doppler Modulation Effects

THE SPIN AXIS ATTITUDE CAN BE DETERMINED FROM CHANGES PRODUCED BY THE SPIN ON THE DOPPLER SHIFT OF RF SIGNALS FROM AN OFFSET ANTENNA. IF THE SPIN AXIS IS AT AN ANGLE α_e FROM THE EARTH LINE, THE DOWNLINK SIGNAL IS FREQUENCY MODULATED AT THE SPIN FREQUENCY. THE PEAK FREQUENCY DEVIATION IS PROPORTIONAL TO THE POINTING ANGLE α_e. DOPPLER MODULATION ALSO PROVIDES PHASE INFORMATION WHICH, WHEN CORRELATED WITH AN ON BOARD SOURCE OF ROLL REFERENCE (i.e. SUN SENSOR), DEFINES THE SPIN AXIS ATTITUDE UNIQUELY. DOPPLER MODULATION SENSITIVITY IS MAXIMUM FOR POINTING ANGLES NEAR ZERO AND DEGRADES RAPIDLY FOR POINTING ERRORS APPROACHING 1.57 RAD (90 DEG).

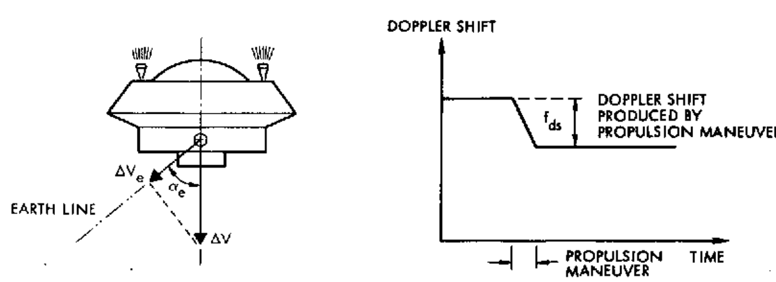

Figure 8.5B-2. Earth Aspect Angle Determination by Doppler Shift Measurement

AFTER A ΔV MANEUVER, THE VELOCITY CHANGE COMPONENT ALONG THE EARTH LINE IS OBTAINED BY DOPPLER MEASUREMENT. THE RATIO OF THIS COMPONENT TO THE PREDICTED VALUE OF THE MANEUVER EXECUTED GIVES THE COSINE OF THE POINTING ANGLE α_e. THIS ATTITUDE DETERMINATION TECHNIQUE PROVIDES ONLY A MEASURE OF THE POINTING ERROR AMPLITUDE AND IT IS MOST SENSITIVE FOR SPIN AXIS ORIENTATIONS NORMAL TO THE EARTH LINE. IT IS PREFERABLE TO USE DOPPLER SHIFT ONLY IN THOSE INSTANCES WHERE A ΔV MANEUVER IS REQUIRED (i.e. MIDCOURSE CORRECTIONS, PERIAPSIS MAINTENANCE, PROBE BUS RETARGETING)

This appendix presents preliminary design considerations and error analyses on which attitude determination performance estimates for the probe bus and orbiter spacecraft are based.

2. DOPPLER TRACKING

Doppler tracking is a technique whereby the radial velocity of a spacecraft is determined by measuring the doppler frequency shift of the received RF signal on the ground. For accurate doppler tracking, the DSIF transmitter must operate at a precisely known frequency. In the majority of spacecraft tracking, the range rates are small enough so that the transmitter can be tuned to a constant frequency (called track synfreq) just after two-way acquisition, which will permit tracking by the spacecraft transponder with acceptable tracking loop phase errors.

The DSIF can acquire tracking data by the use of two types of doppler measurement. One-way doppler is obtained by observing the received frequency and comparing it with the assumed frequency of the spacecraft auxiliary oscillator. Two-way doppler is obtained by tracking the spacecraft in a two-way mode and comparing the uplink transmitted frequency with the received downlink frequency. Because of its much greater accuracy, two-way doppler tracking is the approach used in determining spacecraft trajectories and spin axis attitude.

A block diagram describing the doppler tracking system is presented in Figure 8.5B-3.

The master oscillator provides a stable frequency reference to a frequency synthesizer which establishes the ground transmitter frequency, ω_{GT}. The ground station transmits an RF carrier signal which is received by the PLL receiver in the spacecraft. The received frequency at the input to the spacecraft receiver's first mixer is ω_{SR}. This frequency differs from ω_{GT} by the uplink doppler shift, due to the spacecraft's velocity away from the tracking station. The spacecraft receiver forms an estimate of the phase and frequency of the received signal, coherently multiplies the signal frequency by the transponder turnaround ratio, G, and transmits a downlink RF carrier at a frequency ω_{ST}. The transponder ratio for DSIF-compatible spacecraft is 240/221 for S-band or 880/221 for S-band uplink and X-band downlink. The ground receiver observes a received frequency, ω_{GR}, which differs from the transmitted downlink frequency by the downlink doppler shift. The ground station PLL

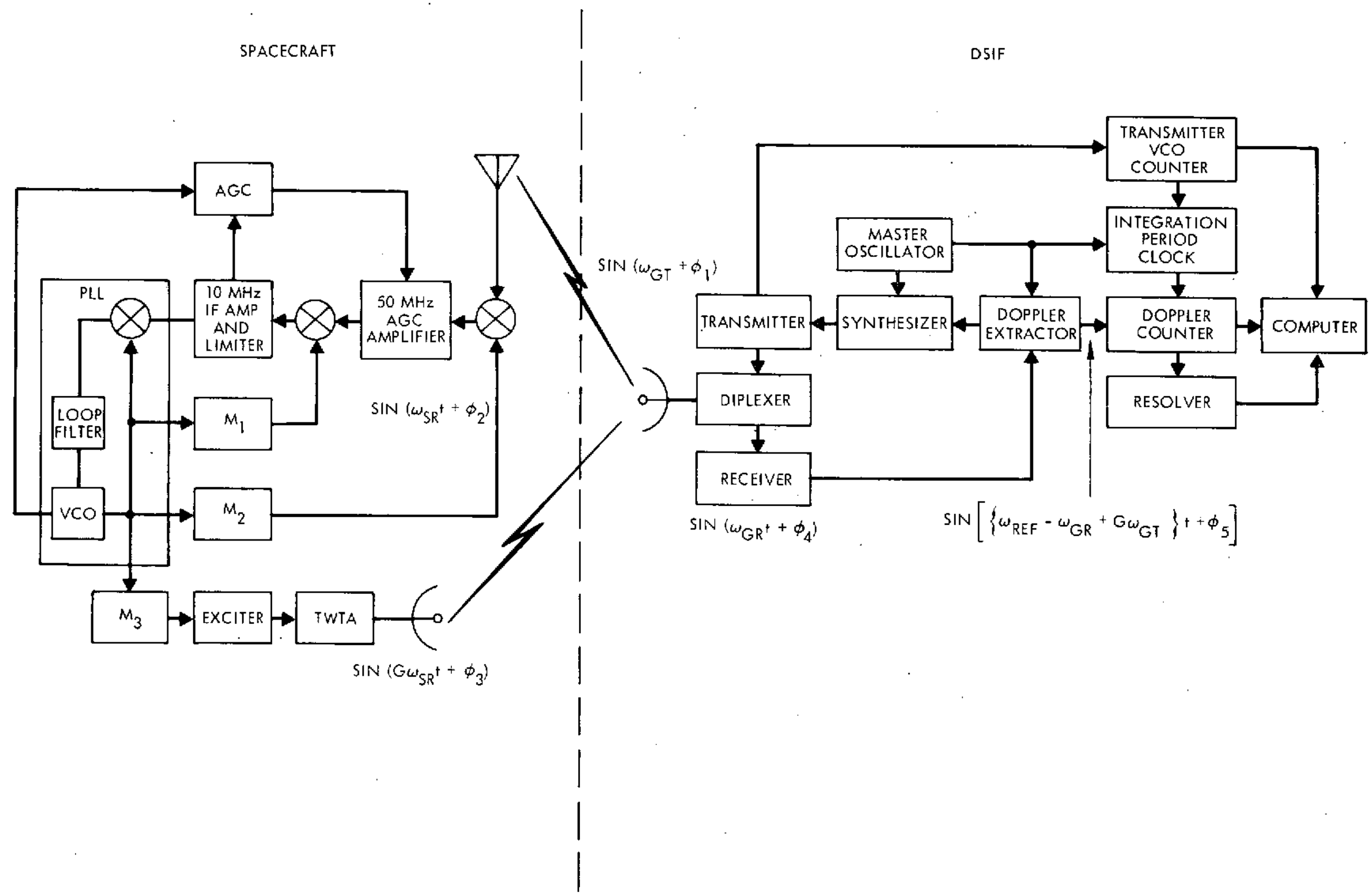

Figure 8.5B-3. Doppler Tracking System Functional Block Diagram

receiver forms an estimate of the phase and frequency of the received signal. This estimate is compared with the frequency of the transmitted signal by the doppler extractor to obtain an estimate of the two-way doppler frequency shift.

Assuming the spacecraft receiver estimate of the received frequency is perfect ($\hat{\omega}_{SR} = \omega_{SR}$), and the range rate $\dot{R} << c \cong 3 \times 10^8$ m/s, the estimate of the frequency received on the ground is given approximately by

$$\hat{\omega}_{GR} = G\,\omega_{GT}\,(1 - \frac{2\dot{R}}{c}) + E_1 + E_2$$

where E_1 and E_2 are the errors due to uplink and downlink phase shifts. The two-way doppler shift is defined as

$$D_2 \triangleq \hat{\omega}_{GR} - G\,\omega_{GT} \cong -\,2\,G\,\frac{\omega_{GT}}{c}\,\dot{R} + E_1 + E_2$$

The primary source of uplink phase errors is the charged particles along the propagation path. Downlink errors include effects due to both charged particles and spacecraft receiver delays. Plasma effects on doppler measurements are frequency dependent and, consequently, can be corrected when S-band and X-band differential doppler measurements are possible. Assuming a ground station transmitter frequency of 2.11×10^9 Hz, the two-way doppler shift is $D_f = 15.3$ Hz/(m/s).

3. DOPPLER MODULATION

Assuming the geometry of Figure 8.5B-1, the instantaneous doppler shift about the average is

$$f_d = D_f\,\omega_s\,r\,\sin\alpha_e\,\cos\omega_s t$$

If F_d is the maximum doppler frequency deviation, the spin axis pointing error is

$$\alpha_e = \sin^{-1}\frac{F_d}{D_f\,\omega_s\,r}$$

Differentiating and averaging, the pointing angle estimation error is

$$\Delta\alpha_e = \tan \alpha_e \left[\left(\frac{\Delta F_d}{F_d}\right)^2 + \left(\frac{\Delta D_f}{D_f}\right)^2 + \left(\frac{\Delta\omega_s}{\omega_s}\right)^2 + \left(\frac{\Delta r}{r}\right)^2 \right]^{\frac{1}{2}}$$

Where $\Delta F_d^{\ 2}$ is the variance of the filter used for estimating the doppler modulation amplitude, ΔD_f is the doppler shift uncertainty, $\Delta\omega_s$ is the spin speed estimation error, and Δr is the radial antenna misalignment (including mechanical misalignments and phase center displacements). For $\alpha_e = 0$ the preceding expression reduces to $\Delta\alpha_e = \Delta F_d/(D_f\, \omega_s\, r)$.

Preliminary estimates of errors in the determination of the spin axis orientation by means of doppler modulation measurements are given in Figure 8.5B-4 for the Version IV science payload spacecraft. The figure also shows effects of estimation parameter variations on attitude determination accuracies for the Thor/Delta Version III science spacecraft spacecraft.

The amplitude of the sinusoidal doppler rate seen by the tracking station is given by

$$\dot{D}_2 = 2\,G\,\frac{\omega_{GT}}{c}\,\omega_s^{\ 2}\; r \sin \alpha_e$$

The tracking loop bandwidth ($2B_L$, in Hz) required is given approximately by

$$(2\,B_L)^2 \cong \dot{D}_2/\Delta\phi$$

where $\Delta\phi$ is the allowed loop static phase error in radians. The maximum allowable spin rate for given $\Delta\phi$ and $2\,B_L$ is

$$N_{max} = \frac{30}{\pi}\left(2\,B_L\right)\left(\frac{c\,\Delta\phi}{2\,G\,\omega_{GT}\; r \sin \alpha_e}\right)^{\frac{1}{2}}$$

Figure 8.5B-5 shows limits on spin speed for two antenna configurations on the assumption of an allowable static error of 0.4 radian, a $2\,B_{LO}$ bandwidth of 10 Hz, and a tracking loop bandwidth $2\,B_L = 25$ Hz.

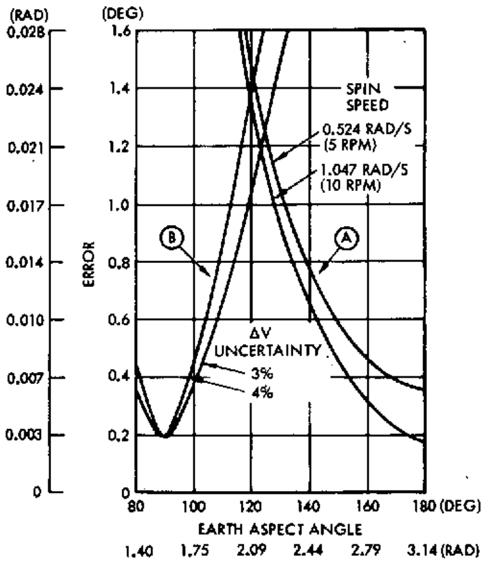

a) DOPPLER ATTITUDE DETERMINATION ACCURACIES VERSION IV SCIENCE SPACECRAFT

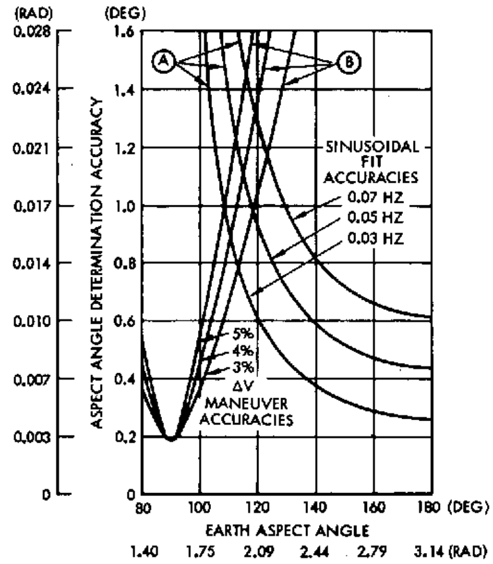

b) EFFECTS OF MODULATION AMPLITUDE ESTIMATION ERRORS AND ΔV MANEUVER UNCERTAINTIES ON DOPPLER ATTITUDE DETERMINATION ACCURACIES

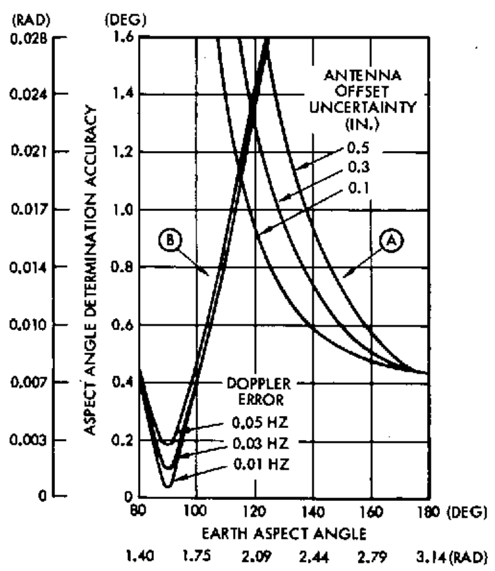

c) EFFECTS OF DOPPLER SHIFT ESTIMATION ERRORS AND ANTENNA OFFSET UNCERTAINTIES ON ATTITUDE DETERMINATION ACCURACY.

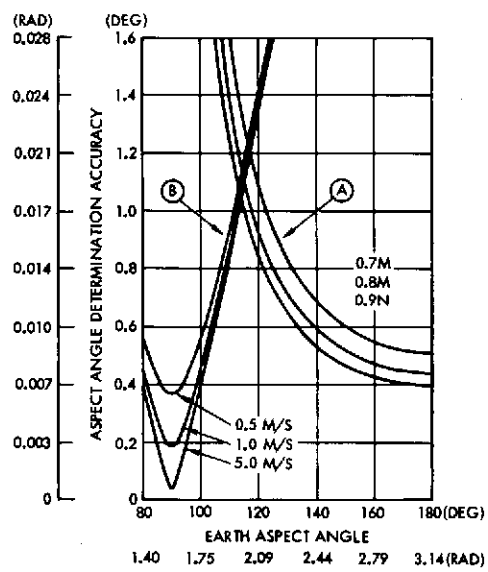

d) EFFECTS OF ΔV MANEUVER AMPLITUDE AND ANTENNA RADIAL DISTANCE FROM SPIN AXIS ON ATTITUDE DETERMINATION ACCURACY

CURVES A CORRESPOND TO SPIN MODULATION EFFECTS. CURVES B ARE FOR DOPPLER SHIFT PRODUCED BY AN AXIAL ΔV MANEUVER.

Figure 8.5B-4. Doppler Attitude Determination Accuracies

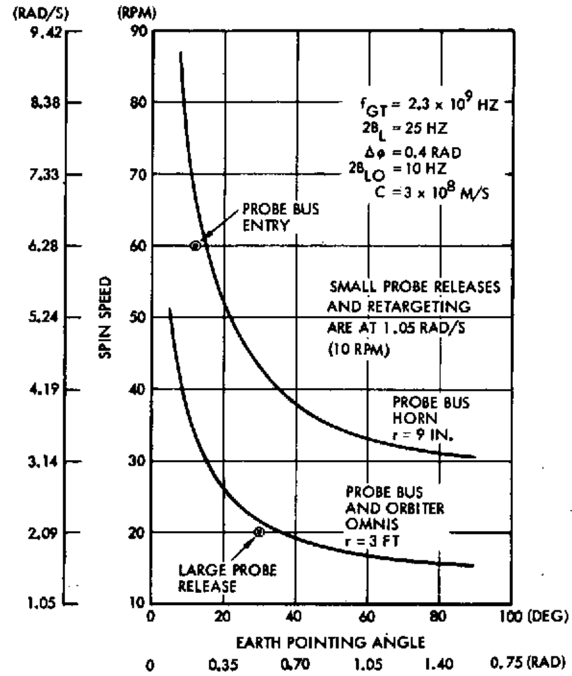

Figure 8.5B-5. Maximum Allowable Spin Speed as a Function of Earth Pointing Angle

MAXIMUM SPIN SPEEDS ARE GIVEN AS FUNCTIONS OF POINTING ANGLE FOR TWO ANTENNA LOCATIONS. THE PROBE BUS AND ORBITER OMNI ANTENNAS ARE OFFSET ABOUT 3 FT FROM THE SPIN AXIS TO MAXIMIZE THE DOPPLER MODULATION SCALE FACTOR. THE PROBE BUS HORN OFFSET IS ONLY 9 INCHES TO ALLOW OPERATION AT 6.28 RAD/S (60 RPM) DURING ENTRY.

4. DOPPLER SHIFT MEASUREMENT

Using the nomenclature of Figure 8.5B-2, the pointing angle α_e is given by

$$\alpha_e = \cos^{-1}\left(\frac{f_{ds}}{D_f\,\Delta V}\right)$$

After differentiation and averaging, the following expression for the pointing angle estimation error is obtained

$$\Delta\,\alpha_e = \cot\,\alpha_e\left[\left(\frac{\Delta f_{ds}}{f_{ds}}\right)^2 + \left(\frac{\Delta D_f}{D_f}\right)^2 + \left(\frac{\Delta\Delta V}{\Delta V}\right)^2\right]^{\frac{1}{2}}$$

For α_e = 1.57 radians (90 degrees) the resulting expression is

$$\Delta\,\alpha_e\Big|_{\alpha_e=90^o} = \frac{\Delta f_{ds}}{D_f\,\Delta V\,\sin\,\alpha_e}$$

Preliminary attitude determination error estimates, based on the preceding expressions, are given in Figure 8.5B-4 for the Version IV science spacecraft. The figure also shows effects of parameter variations on attitude determination accuracies for the Thor/Delta Version III science spacecraft.

5. ANTENNA TESTS

A test program was conducted to determine antenna phase center deviations occurring during rotations about the mechanical axis of symmetry. Relative phase measurements were made on the engineering model conical log spirals in question: the DSP antenna for the probe bus and the Pioneer 10 and 11 antenna for the orbiter. Maximum phase center displacement measured was ±0.122 inch at an aspect angle of 1.05 radian (60 degrees) from the axis. Although the measurements were made on the antenna in "free space," the measured phase center displacements are representative of those achievable with the antennas installed on the spacecraft with proper location and precision alignments. Antenna design requirements could include maximum phase center deviations of ±0.25 inch when installed on the spacecraft.

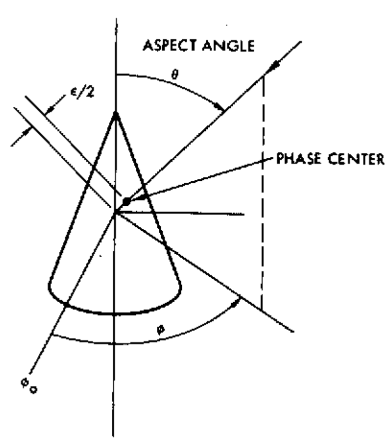

Figure 8.5B-6. Relative Phase Measurement Coordinates

The maximum phase center deviation (ϵ) from the antenna axis of rotation was determined from relative phase measurements as a function of aximuth angle (ϕ) as shown in Figure 8.5B-6. The phase deviation in degrees, convertible to wavelengths, indicates the relative phase center deviation from the axis of rotation as observed from the respective antenna aspect angle. Measurements were made in 0.17-radian (10-degree) increments in aspect angle (θ) from 0 to 1.05 radians (0 to 60 degrees). Test results shown in Figure 8.5B-7 indicate that radial phase center offsets in the 0.12 to 0.21 inch range, occur in the range of aspects from 0.52 to 0.87 radians (30 to 50 degrees). These offsets are included in the error estimates of Figure 8.5B-4a), which are based on a conservative uncertainty allocation of

±0.5 inch for misalignments. The estimated phase error introduced by test alignment and instrumentation drifts is ±0.03 radian (±2 degrees) (±0.03 inch).

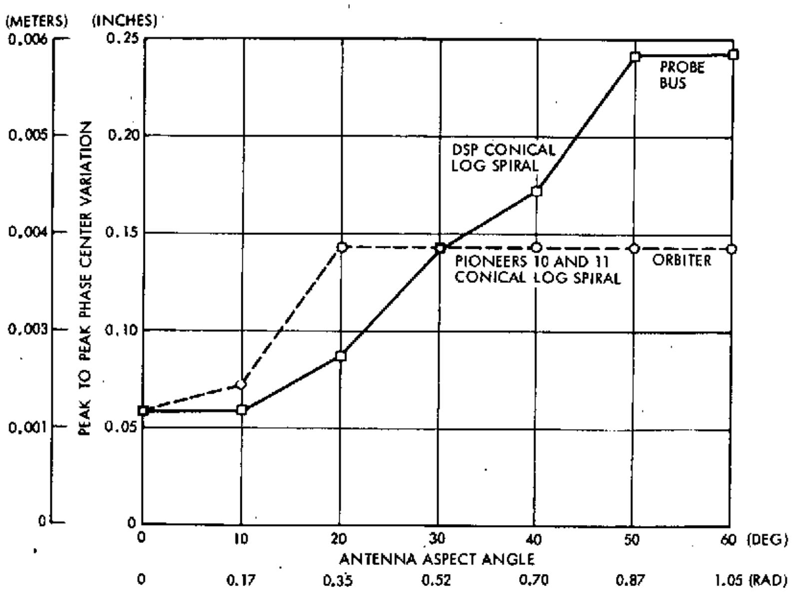

Figure 8.5B-7. Measured Conical Log Spiral Phase Center Deviations

APPENDIX 8.5C

STAR MAPPER SENSOR CONSIDERATIONS

APPENDIX 8.5C

STAR MAPPER SENSOR CONSIDERATIONS

Star mappers have been considered as a potential approach to improving attitude determination accuracy in case the need arises as a consequence of new requirements or changes of design ground rules.

Figure 8.5C-1 summarizes some of the most significant trade-off factors involved in the selection of star mapper design requirements. Consistent with the minimum cost and weight philosophy adopted for the study, the following preliminary requirements were established:

- Accuracy in 0.008 to 0.017 radian (0.5 to 1.0 degree) range (without processing)
- Northern hemisphere view in Venus orbit
- Operation in normal-mode Venus-orbit attitude as baseline
- Some degradation of performance in other orientations (i.e., due to planet interference) is acceptable.

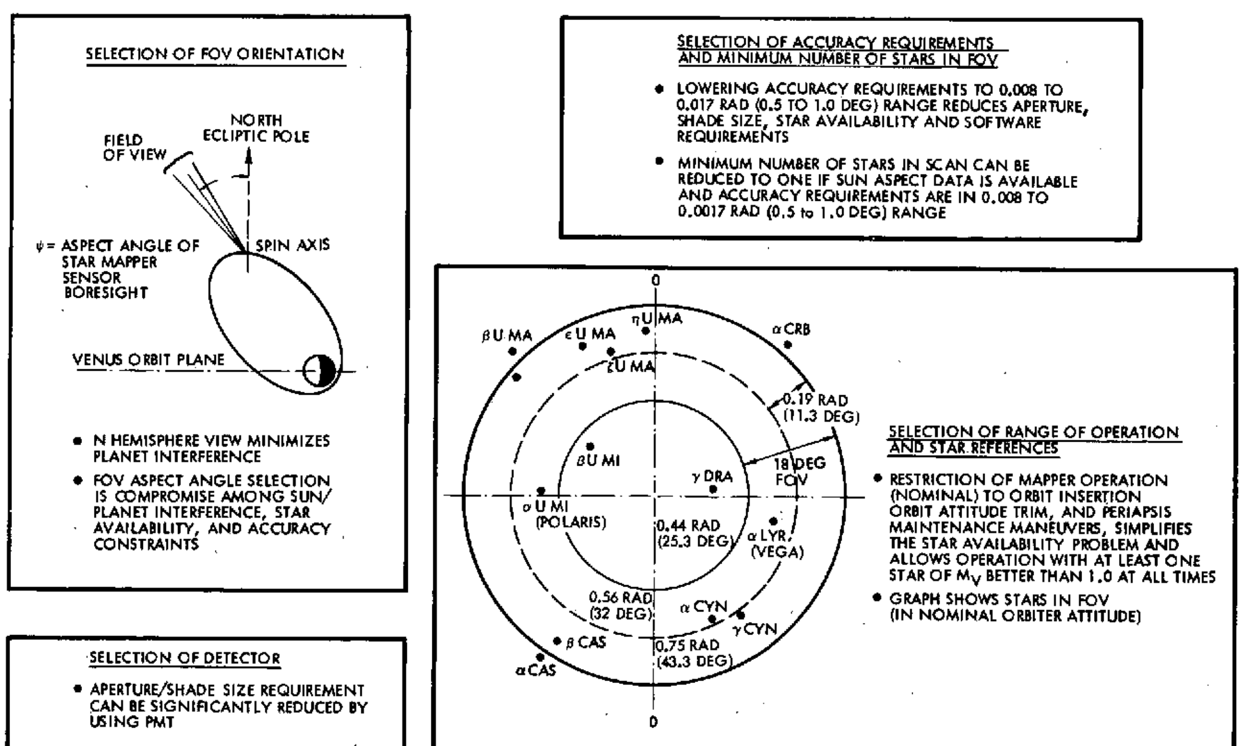

Figure 8.5C-1. Star Mapper Sensor Tradeoffs

A survey of existing and proposed designs revealed there is no instrument applicable to the Pioneer Venus mission that does not require extensive modifications or impose significant cost and weight penalties.

On the assumption that developing a light and simple new design may be more cost effective than modifying an existing one, various configurations have been examined in order to assess the impact of FOV and detector changes on shade size and weight, star availability, and sensor performance.

Table 8.5C-1 presents a summary of a preliminary survey of existing and proposed star mappers aimed at determining their applicability to the Pioneer Venus mission. The conclusion is that none of the designs listed is directly applicable. In most cases, the modifications required are so extensive that they practically imply complete redesigns of the units considered. Fields of view (FOV), apertures, and shade sizes are in general much larger than the ones required by the minimum requirements assumed for the Pioneer Venus application. The lightest sensors shown in the table either have never been built or do not provide star aspect information.

The sensor developed by Johns Hopkins' APL for the SAS-B program appears to be a potential candidate design on the basis of published information. Further studies and tradeoffs will be required for defining whether adaptation of this instrument is a cost effective approach.

Four preliminary star mapper designs based on criteria and requirements outlined in Figure 8.5C-1 have been prepared. Two sensor configurations include photomultiplier tubes with S-20 spectral response and the other two use silicon detectors.

Table 8.5C-2 shows stars available for two fields of view in the normal mode orbiter orientation and the attitudes required for periapsis maintenance maneuvers. A field of view of 1.8 degrees has been tentatively selected to include one star brighter than $M_V = +1$ during each spin revolution, thus allowing operation with small optical apertures. A high threshold level is used in order to reject dimmer stars and reduce background noise. The sun sensor is assumed to provide an additional reference for attitude determination.

Table 8.5C-1. Star Mapper Survey

MANUFACTURER PROGRAM	DETECTOR	OPTICS AND APERTURE	FIELD OF VIEW (DEGREES)	SENSITIVITY (MAGNITUDE)	SPIN RATE (RPM)	ACCURACY (ARC MINUTES)	SUN ANGLE	SIZE (CM)	WEIGHT (KG)	POWER (WATTS)	APPLICATION TO TRW PIONEER VENUS
AS&E SAS-A, B	PMT		10 x 5 N-TYPE SLITS	+5	0.1-1	1.0	40	25.4 x 12.7		0.65	LARGE OPTICS NECESSITATES LARGE SHADE. ELECTRONICS INADEQUATE. BANDWIDTH NARROW. WEIGHT HIGH. REQUIRES EXTENSIVE MODIFICATION.
BBRC OSO-7	PMT	REFRACTIVE	10 V-TYPE	+4.5	30	1.8	NIGHT ONLY	33 x 10.2		1.25	LARGE OPTICS. LARGE SHADE NEEDED. EXTENSIVE MODIFICATION.
CDC ATS-3	PMT		12	+2.5	100	1.5	28	15.24 x 30.5 x 45.7		0.75	VERY LARGE AND VERY HEAVY. NEEDS LARGE SUNSHADE. EXTENSIVE MODIFICATION.
CDC SPARS	CADMIUM SULFIDE SELENIDE	CONCENTRIC 2.25 IN.	4	N/A	N/A	N/A	N/A	N/A	N/A	N/A	WORKS ONLY AT VERY LOW SPIN RATES. CLASSIFIED. FIELD OF VIEW SMALL.
CDC PIONEER VENUS (PROPOSED)	SILICON PIN PHOTODIODE	2.1 IN. EFFECTIVE CASSEGRAIN		0 (SILICON)	75	3	N/A	8.38 x 14	0.73	0.8	NEVER BUILT. FIELD OF VIEW TOO BIG. WORKS ONLY ON BRIGHT STARS.
GSFC S^3	PMT	REFRACTIVE 1.25 IN.		+3.5	4-7	6 (3σ)	90	20.3 x 3.8	1.36	1	DOES NOT GIVE ASPECT. EMI SUSCEPTIBLE. NO SHADE DESIGN. EXTENSIVE MODIFICATION.
HRC SCANNER	PMT		6 x 6	+3	60-120		45	54.6 x 20.3 x 40.6		1	VERY HEAVY AND LARGE. EXTENSIVE MODIFICATION.
JOHNS HOPKINS APL SAS-B	PMT	REFRACTIVE 2 IN.	10 x 5 PARALLEL SLITS	+5	0.1-3	1	60	2.13 DM^3	2.16	0.4	NEEDS BANDWIDTH WIDENED. POTENTIAL PROCUREMENT PROGRAM.
KOLLSMAN PIONEER VENUS (PROPOSED)	SILICON	REFRACTIVE	45	0 (SILICON)	75	18 (1σ)	30	19.3 x 11.4	2.45	1.0	NEVER BUILT. FIELD OF VIEW TOO BIG. WORKS ONLY ON BRIGHT STARS.
TRW PIONEERS 10 AND 11	SILICON	REFRACTIVE CASSEGRAIN BOUWERS 2.5 IN.		CANOPUS	2-5.8	10 (1σ)	50	15.9 x 11.4 x 15.24	1.14	0.5	WORKS ONLY ON BRIGHT STARS. FIELD OF VIEW TOO BIG. DOES NOT GIVE ASPECT.

Table 8.5C-2. Star Availability (Arrow Indicates Preferred Alternative)

CONDITION	STAR				DETECTOR RESPONSE (AMP/CM^2)		18 DEGREES FOV		11.3 DEGREES FOV	
							HIGH THRESHOLD		LOW THRESHOLD	
	YALE B.S. CAT. NO.	NAME	M_V	COLOR	S-20 $\times 10^{13}$	SI $\times 10^{12}$	S-20 (PMT)	SI	S-20 (PMT)	SI
NORMAL	7001	α Lyr VEGA	0.03	A0	0.803	0.438	X	X		
MODE	5191	η UMa ALCAID	1.96	B3	0.197	0.090			X	
ATTITUDE	4301	α UMa DUBHE	1.79	K0	0.090	0.133				X
PM1*	2326	α Car CANOPUS	-0.7	F0	1.5	1.07	X	X	X	X
	188	β Cet DIPHDA	2.08	K1	0.698	0.100			X	
PM2	8727	α PsA FOMALHAUT	1.16	A3	0.267	0.17			X	X
	188	β Cet DEPHDA	2.08	K1	0.698	0.100			X	
	2326	α Car CANOPUS	-0.7	F0	1.5	1.07	X	X	X	
PM3	7924	α Cyg DENEB	1.26	A2	0.254	0.163			X	X
	7796	γ Cyg SADIR	2.2	F8	0.071	0.075			X	X
	7557	α Aql ALTAIR	0.77	A7	0.369	0.263	X	X		
PM4	4301	α UMa DUBHE	1.79	K0	0.090	0.133				X
	7001	α Lyr VEGA	0.03	A0	0.803	0.483	X	X	X	X
	1708	α Aur ARCTURUS	0.09	K2	0.514	0.606	X	X		

*PM1: FIRST PERIAPSIS MAINTENANCE MANEUVER ATTITUDE.

Planet interference is expected in the orientations selected for the third and fourth periapsis maintenance maneuvers. However, the corresponding effects can be easily recognized and removed from the sensor output data.

Sun shade size is determined primarily by field of view, minimum angle between sun and sensor optical axis, and aperture size.

Photomultiplier tubes (with S-20 photocathode spectral response) are more sensitive than silicon detectors due to the essentially noise-free gain of secondary emission multipliers. Thus, PMT's require smaller optical apertures and, consequently, smaller shade sizes than silicon detectors.

Table 8.5C-3 shows shade sizes and weights as functions of detector type and FOV. For an 18-degree FOV, the shade required with a silicon detector is about five times heavier than the one needed with a PMT.

Preliminary design characteristics of the four star mapper configurations considered are shown in Table 8.5C-4. All four designs are based on the same accuracy requirements.

Table 8.5C-3. Sun Shade Tradeoffs (Arrow Indicates Preferred Alternative)

DETECTOR	FOV (DEG)	DIMMEST STAR, MV	APERTURE DIA (CM)	W (CM)	LT (CM)	L1 (CM)	B (CM)	SUN ANGLE (DEG)	WEIGHT (CM)
SI	18	ALTAIR +0.77	4.26	22.96	21.56	17.89	9.93	45	830
	11.3	DUBHE +1.79	5.99	22.17	45.11	28.15	11.56	45	1630
S-20	18	ALTAIR +0.77	1.86	10.01	14.98	7.80	4.33	45	160
	11.3	ALCAID	2.40	8.88	18.07	11.28	4.63	45	265

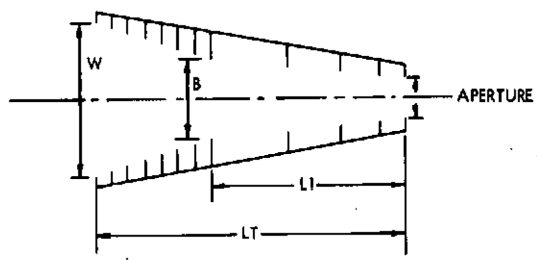

Table 8.5C-4. Star Mapper Design Characteristics

	SI		S-20 (PMT)	
FOV (DEGREES)	18	11.3	18	11.3
SENSITIVITY	+0.77	+1.79	+0.77	+1.96
APERTURE (CM)	4.26	7.98	1.86	3.98
SPIN RATE (RPM)	4.8	4.8	4.8	4.8
BANDWIDTH (Hz)	30	30	30	30
ASPECT ANGLE (DEGREES)	34.3	37.65	34.3	37.65
MINIMUM SUN ANGLE (DEG)	45.0	45.0	45.0	45.0
SIZE* (CM)	8 X 8 X 16	10 X 10 X 20	6 X 6 X 16	8 X 8 X 20
WEIGHT (GRAMS) (SHADE INCLUDED)	2430	4030	1360	2265
POWER (WATTS)	0.9	0.9	1.5	1.5
ACCURACY (DEGREES) (NO PROCESSING ASSUMED)	0.6 TO 1 (3σ)	0.6 TO 1 (3σ)	0.6 TO 1 (3σ)	0.6 TO 1 (3σ)

*DOES NOT INCLUDE SUN SHADE, SEE SUN SHADE TRADEOFF CHART.

The PMT version with a FOV of 18 degrees is the preferred choice (in terms of size and weight) at the present time.

Configuration size estimates are based on experience derived from past designs. Improvements are possible since, for the purposes of the present tradeoff studies, no optimizations have been attempted because relative sizes are essentially correct.

In the solid state detector cases, most of the weight is due to the larger optics. In the PMT designs, the heaviest items are the PMT, the high-voltage power supply and the magnetic shield.

APPENDIX 8.5D

ANTENNA DESPIN CONTROL SYSTEM DESIGN AND PERFORMANCE

APPENDIX 8.5D

ANTENNA DESPIN CONTROL SYSTEM DESIGN AND PERFORMANCE

1. INTRODUCTION

One of the Pioneer Venus orbiter configurations considered is a spin-stabilized spacecraft with its spin axis normal to the Venus orbit plane. For data transmission to the earth, it is required that the spot beam of a despun high gain antenna reflector be pointed at the earth with an accuracy of 0.017 radian (±0.75 degree) throughout the mission. Sun sensors provide an inertial reference line which is used to determine the earth's location relative to the spacecraft. Since the sun's position is measured once per spacecraft revolution, the antenna pointing error is sampled at the same frequency. A brushless DC motor supplies the necessary control torque.

2. CONCEPTUAL DESIGN APPROACH

A functional block diagram of the antenna control loop is shown in Figure 8.5D-1. For the initial despin maneuver, antenna rate control is required. When this inertial antenna rate is small, the position loop and the rate loop are both used. The rate loop is needed as part of the position loop in order to provide satisfactory control of the antenna pointing error during the relatively long position sampling period (12.5 seconds). This implies that the antenna rate has to be sampled much more frequently than the antenna position.

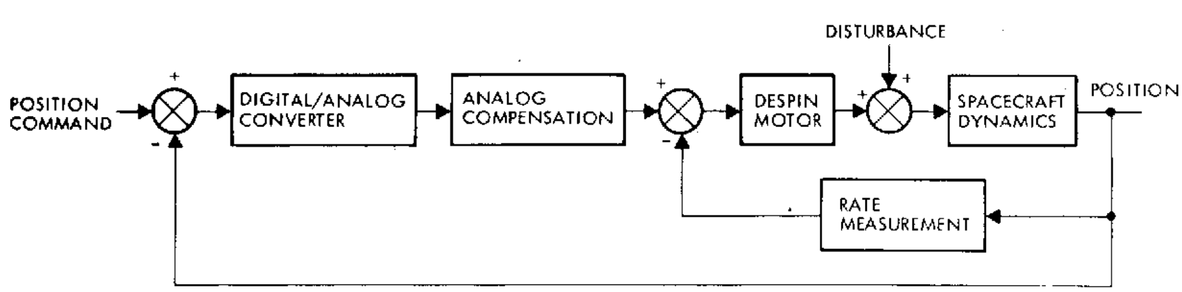

Figure 8.5D-1. Antenna Despin Control System

The antenna pointing error is measured in the following manner. A position pulse indicates the location of the antenna relative to the spinning spacecraft once per revolution. By means of a phase detector, the phase angle between the position pulse and the sun pulse is determined. The difference between this phase angle and the known sun-spacecraft-earth angle determines the antenna pointing error.

The selected analog compensation is a proportional-plus-integral control circuit. The control torque is proportional to the compensated antenna pointing error. Integral control is needed to offset any constant disturbance such as friction in the ball bearing assembly.

Two methods of rate measurement have been considered. For both cases about the same number of rate pulses per spacecraft revolution are required. However, the processing of these rate pulses differs considerably. The first method employs digital circuitry while the alternative design requires only analog circuitry. These two rate loop designs are discussed in more detail in the following sections.

3. DIGITAL RATE LOOP

A digital method for measuring antenna rate, the stability of the rate loop and some characteristics of rate loop performance are investigated in this section.

3.1 Rate Measurement

Consider the rate pulse train and counter shown in Figure 8.5D-2. The residual count, R, is given by

$$R = R_o - (f_c/n)\,T \tag{1}$$

where

R_o — the initial count

f_c — the counter frequency

n — number of rate pulses per spacecraft revolution

T — antenna spin period relative to rotor.

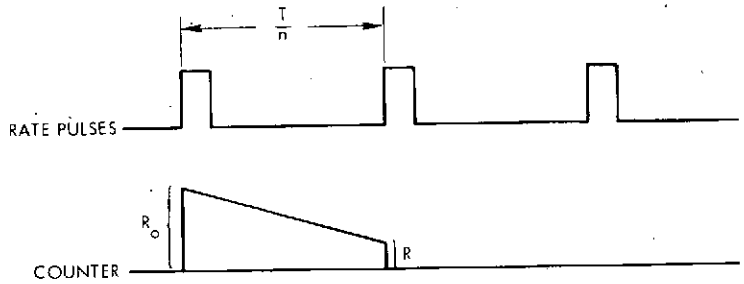

Figure 8.5D-2. Rate Pulse Train and Counter

Set the initial count equal to the count accumulated in (1/n)th of a spacecraft spin period, T_s.

$$R_o = (f_c/n)\, T_s \tag{2}$$

In other words, R_o is the spacecraft spin rate bias. The residual count now becomes

$$R = (f_c/n)\,(T_s - T) \tag{3}$$

The antenna rate in inertial space is given by

$$\omega_a = \omega_s - \omega \tag{4}$$

Substituting $T = 2\pi/\omega$ and Equation (4) into Equation (3), we get

$$R = \frac{2\pi f_c}{n}\left(\frac{-\omega_a}{\omega_s \omega}\right) \tag{5}$$

Thus, the residual count is proportional to the inertial antenna rate.

When the inertial antenna rate is near zero, we have $\omega \cong \omega_s$ and Equation (6) may be written as

$$R = \frac{f_c T_s^{\,2}}{2\pi n}\,(-\omega_a) \tag{6}$$

Equation (6) shows that the rate measurement gain is proportional to the square of the spacecraft spin period.

3.2 Rate Loop Stability

Figure 8.5D-3 shows a linear model of the digital rate loop. The open-loop transfer function in the z-plane is given by

$$G(z) = \frac{K_m K_\omega}{I_a T_r} \left(\frac{z-1}{z}\right)^2 \left(\frac{1}{s^3}\right)^* \tag{7}$$

where * denotes a z-transformation. After carrying out the z-transformation, we get

$$G(z) = K \frac{z+1}{z(z-1)} \tag{8}$$

where

$$K = K_o T_r / 2$$

$$K_o = K_m K_\omega / I_a$$

Note that K and K_o are the root locus gains in the z-plane and s-plane respectively.

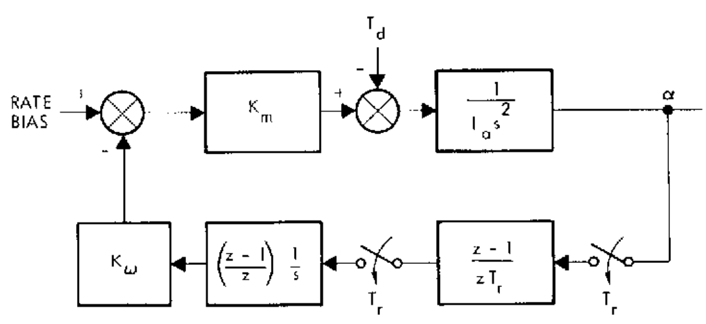

Figure 8.5D-3. Linear Model of Digital Rate Loop

The root locus diagram in Figure 8.5D-4 indicates that the rate loop becomes unstable for $K>1$. Choosing $K = 0.3$ as the nominal operating gain, leaves a gain margin of 10.4 dB. The damping ratio associated with the critical closed-loop poles at $K = 0.3$ is 0.53.

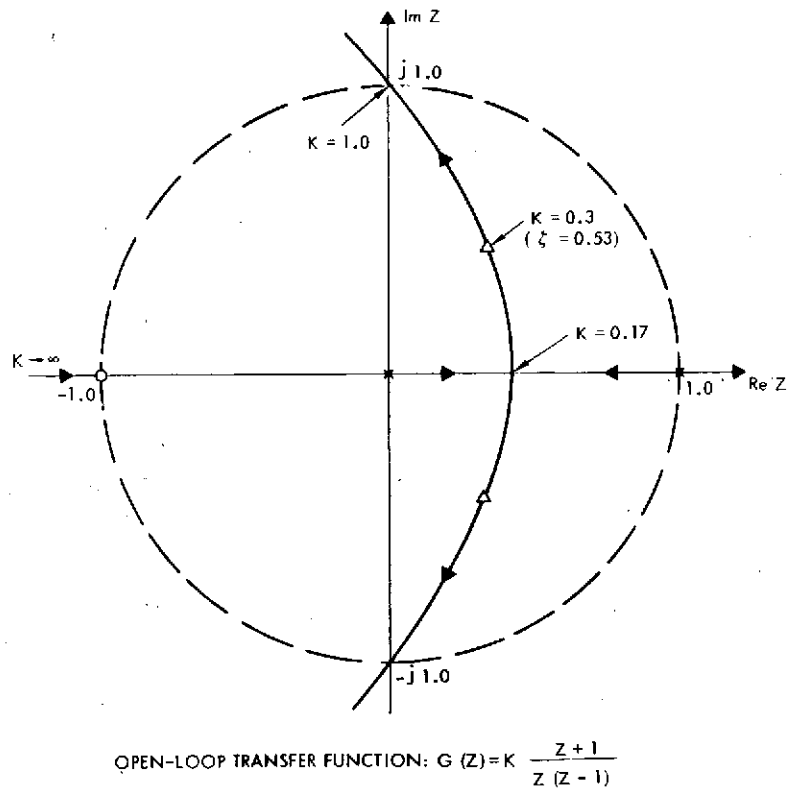

Figure 8.5D-4. Root Locus of Digital Rate Loop

3.3 Effect of Disturbance Torque

In order to determine the required rate sampling frequency, it is necessary to analyze the effect of expected disturbance torques. One of the major disturbances arises from friction fluctuations of the ball bearing assembly. If these torque fluctuations occur at the spacecraft spin frequency or higher frequencies, they have to be primarily controlled by the rate loop. The sampling frequency of the position loop is too low to effectively handle these disturbances.

For the sake of simplifying the analysis, let us approximate the rate loop by a continuous system as shown in Figure 8.5D-5. If T_d = M sin ωt, the magnitude of the resulting antenna pointing error is given by

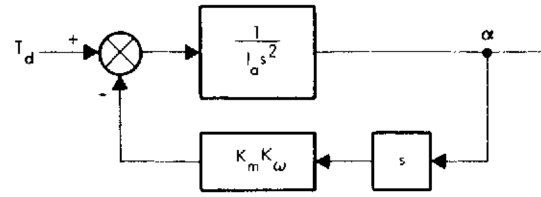

Figure 8.5D-5. Continuous Rate Loop Model

$$|\alpha(\omega)| = \frac{M}{I_a \omega^2 \sqrt{1 + (K_o/\omega)^2}} \tag{9}$$

Figure 8.5D-6 shows a plot of the peak pointing error per inch-ounce of disturbance torque as a function of the rate loop gain (K_o) or bandwidth for $\omega = 0.5$ rad/s (4.8 rpm) and $I_a = 0.24$ kg-meter^2 (0.177 slug-ft^2) which is the Helios antenna spin inertia. Assuming a maximum torque variation of 144.016 gram-centimeters (2 in.-oz), the rate loop gain cannot be lower than 9 rad/s without violating the antenna pointing requirement.

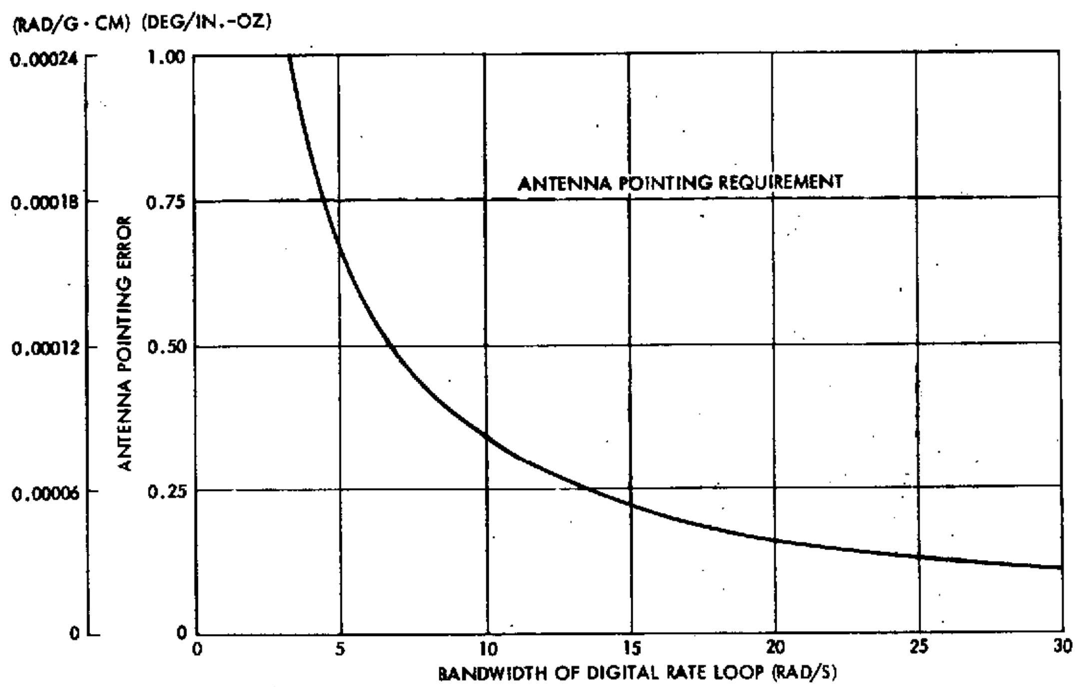

Figure 8.5D-6. Antenna Pointing Error Due to Sinusoidal Disturbance

The above result establishes a criteria for selecting the rate sampling frequency. An expression for the number of rate pulses per revolution (n) can be derived from Equation (8).

$$n = \frac{K_o T_s}{2K} \tag{10}$$

Stability considerations require that K = 0.3 and expected disturbance torque fluctuations require that $K_o > 9$ rad/s. Consequently, at the nominal spin speed ($T_s = 12.5$ seconds) the minimum value of n is 188 ppr.

The foregoing analysis may be repeated by using the more accurate sampled-data model of the rate loop. This is done in the attachment to this appendix since it involves lengthy algebraic manipulations. The steady-state solution of the antenna pointing error due to a sinusoidal disturbance torque is given by

$$\alpha(kT_r) = \frac{M}{\omega I_a K_o}(1 - \cos \omega k T_r) \tag{11}$$

where k is an integer. Except for the constant term, this antenna pointing error agrees well with the result from the continuous rate loop model when $K_o >> \omega$.

The constant offset of the antenna pointing error in Equation (11) initially posed a problem. For a linear system the response has to be sinusoidal if the forcing function is sinusoidal. As the rate sampling frequency is increased, the continuous, linear model of the rate loop becomes a more accurate representation of the actual system. However, Equation (11) indicates that the constant term is independent of the rate sampling frequency. In other words, the solution from the sampled-data model does not converge to the solution of the continuous model as expected when the sampling frequency is increased. Assuming that the derivations of Equations (9) and (11) are correct, it can only be concluded that the two models are not completely equivalent.

In order to check the validity of Equation (11), a short timeshare simulation (see the attachment at the end of this appendix) of the digital rate loop was developed. The simulation plots in Figure 8.5D-7 show the antenna rate and position errors in response to a disturbance torque of 72 g-cm (1 in.-oz). Initially the antenna rate and position are zero and the disturbance torque is modeled as $T_d = \sin(t/2)$ in.-oz. Note that the antenna position error in Figure 8.5D-7 is in perfect agreement with Equation (11).

From the simulation results it becomes apparent that the antenna pointing offset is due to the particular choice of initial conditions. In

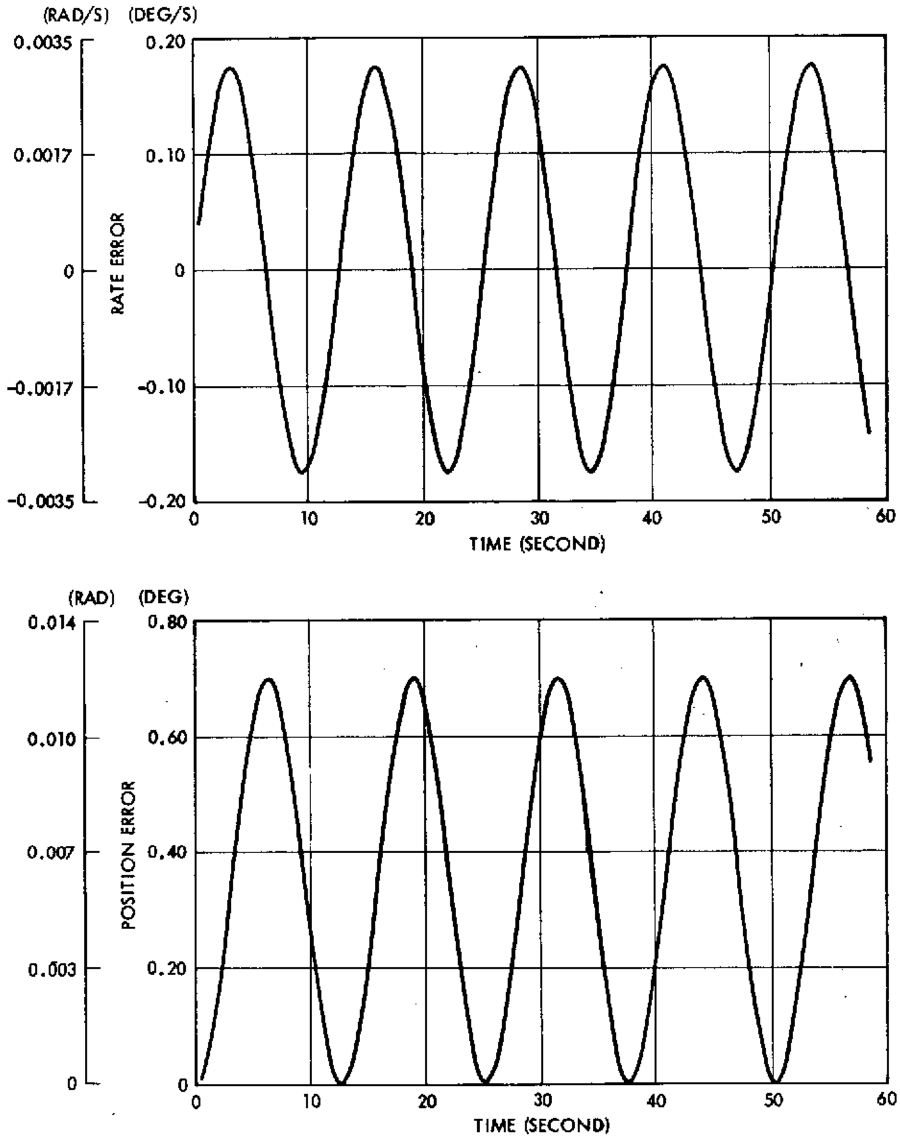

Figure 8.5D-7. Antenna Response to Sinusoidal Disturbance of 72.01 g·cm (1 in.-oz) Rate Sampling Frequency: 200 PPR

deriving Equation (1), zero initial conditions for both antenna rate and position have been assumed. This gives rise to a constant position offset because rate and position have a phase difference of 1.57 radian (90 degrees). When the rate is zero, the position is at a peak value and vice versa. In using the continuous model, the effect of initial conditions is excluded because only sinusoidal terms are considered.

The rate loop does not control a constant position error; this error has to be corrected by the position loop. But it is conceivable for the case shown by Figure 8.5D-7 that the position error is zero whenever it is sampled once per spacecraft revolution. Thus, as a worst case the antenna pointing error may be as large as 0.00017 rad/g-cm (0.7 deg/in.-oz) when the rate sampling frequency is 200 ppr.

To improve this situation, the rate sampling frequency has to be increased. A recommended value is 512 ppr. Figure 8.5D-8 shows the antenna rate and position errors for this rate sampling frequency. The peak antenna pointing error is 0.005 radian (0.26 degree) for a 72.01 g•cm (1 in.-oz) fluctuation of the disturbance torque. If the maximum torque fluctuation is 144.02 g•cm (2 in.-oz), the worst-case pointing error is about 0.009 radian (0.5 degree). Since the antenna pointing requirement is 0.013 radian (0.75 degree), this performance is acceptable.

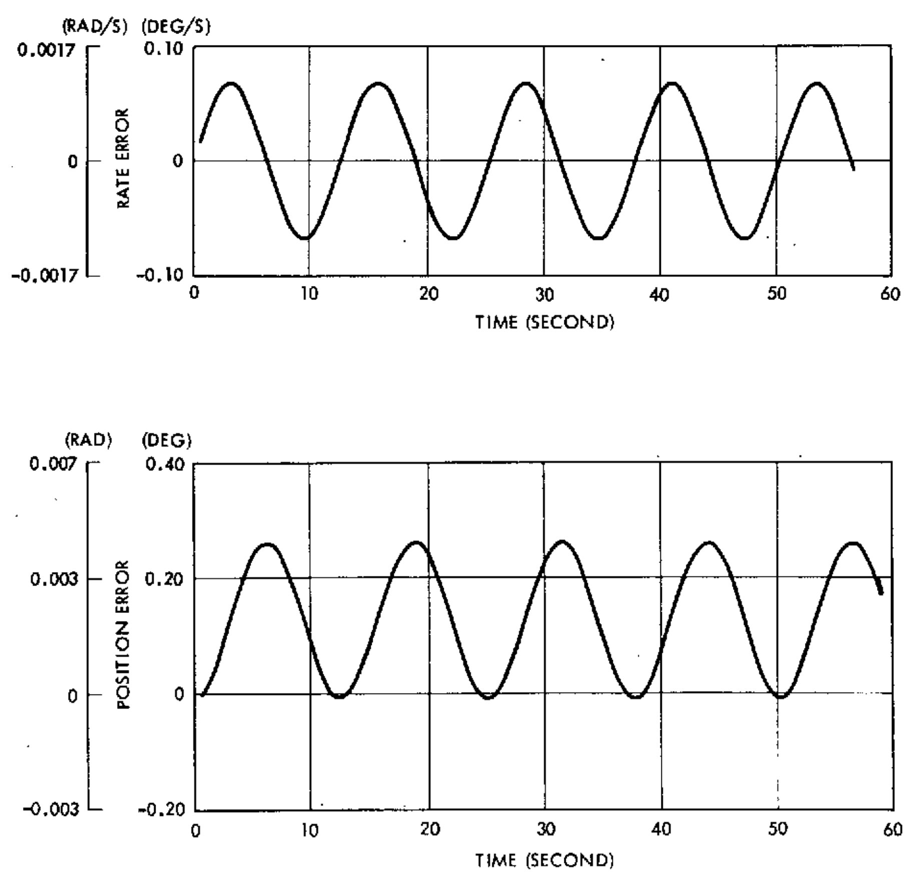

Figure 8.5D-8. Antenna Response to Sinusoidal Disturbance of 72.01 g·cm (1 in.-oz) Rate Sampling Frequency: 512 PPR

4. ANALOG RATE LOOP

The distinguishing feature of this rate loop design is the analog processing of the rate pulses. Unfortunately, an undesirable ripple voltage accompanies the analog rate signal and a low-pass filter is required to clean up the rate signal. The following discussion deals with the rate measurement process, the rate loop stability and several performance characteristics of the analog rate loop.

4.1 Rate Measurement

Antenna rate measurement is accomplished by the following process. The rate pulses trigger a one-shot multivibrator and thus produce a train of equal-duration pulses at a varying frequency. The average value of this pulse train is directly proportional to the relative rate between the antenna and the rotor. By including a bias for the known spacecraft spin rate, a measurement of the inertial antenna rate is obtained.

Figure 8.5D-9 illustrates an implementation of this process. When the rate error is zero, the average value of the pulse train f(t) in Figure 8.5D-9 is equal to the spin rate bias and the unfiltered rate signal r(t) contains only a ripple voltage. The average value of f(t) is given by Ad/T where A is the rate pulse amplitude, d is the pulse duration and T is the period of the pulse train.

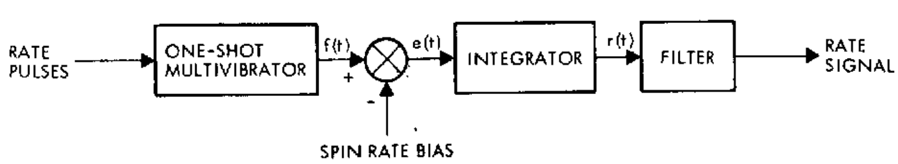

Figure 8.5D-9. Rate Measurement Process

Figure 8.5D-10 shows the waveforms of the integrator and filter input signals when the rate error is zero. Note that the fundamental ripple frequency is equal to the rate sampling frequency. The peak ripple voltage is defined by

$$p = \frac{Ad}{2T}(T - d) \qquad (12)$$

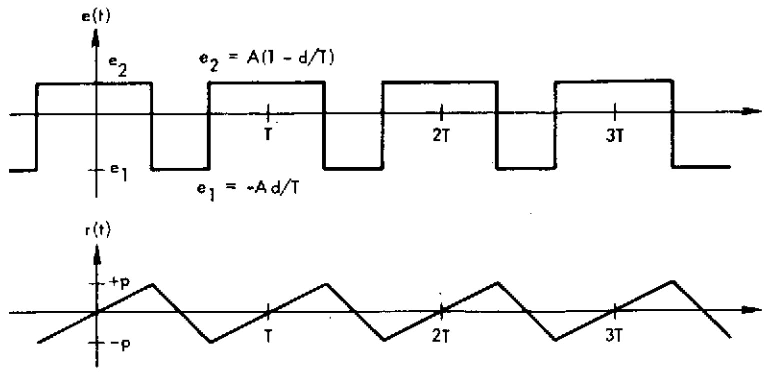

Figure 8.5D-10. Integrator Input and Ripple Voltage

Since d/T is the rate pulse duty cycle and $T \cong T_s/n$, Equation (12) may be rewritten as

$$p = \frac{kA}{n} \tag{13}$$

where

$$k = \frac{T_s d}{2T} \left(1 - \frac{d}{T}\right)$$

The factor k is referred to as the ripple amplitude factor.

The ripple amplitude factor varies as a function of the rate pulse duty cycle. Figure 8.5D-11 indicates that this variation is symmetrical about the duty cycle value of 50 percent and the ripple amplitude factor has its maximum value at that point. For better resolution of the rate signal, a pulse duty cycle larger than 50 percent should be used. For example, when $A = 10$ volts, d/T is 0.8 and $n = 500$ ppr, the peak ripple voltage is 20 mV, while the bias signal for the spin rate of 0.5 radian (4.8 rpm) is 8 volts. Thus, the 20 mV ripple corresponds to a maximum antenna rate variation of about 0.0012 rad/s (0.07 deg/s). If a 20 percent duty cycle is chosen, the peak ripple voltage is still 20 mV. But the spin rate bias is now only 2 volts and consequently the 20 mV ripple corresponds to a maximum rate variation of about 0.0049 rad/s (0.28 deg/s).

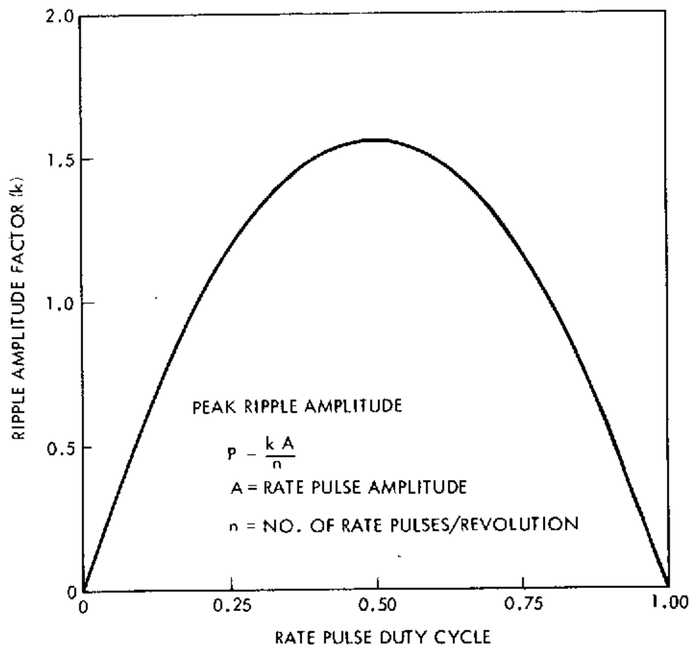

Figure 8.5D-11. Ripple Amplitude Factor Versus Rate Pulse Duty Cycle

4.2 Filter Design

The filter has to be designed in such a way that it sufficiently attenuates the lowest frequency component of the ripple voltage, but on the other hand, does not reduce the required rate loop bandwidth. As mentioned earlier, the lowest ripple frequency is equal to the rate sampling frequency. The required rate loop bandwidth is determined by the system response to friction torque fluctuations. In order to best satisfy these two counteractive performance requirements, the filter should be a low-pass filter with a sharp cutoff characteristic. A filter with such properties is the Chebyshev filter.

The magnitude of the Chebyshev filter is given by

$$|F(j\omega_p)| = \frac{1}{\sqrt{1 + \epsilon C_n^{\,2}(\omega_p)}} \tag{14}$$

where ϵ is a scale factor which determines the amount of ripple in the filter magnitude and C_n is a polynominal of ω_p. The frequency ω_p

is normalized by the filter cutoff frequency ω_c. Choosing a four-pole filter (n = 4) and a 1 dB magnitude ripple, we get $\epsilon = 0.26$ and

$$C_4 = 8\,\omega_p^{\,4} - 8\,\omega_p^{\,2} + 1 \qquad (15)$$

The filter pole locations are determined from

$$C_4^{\,2}(p/j) = (8p^4 + 8p^2 + 1)^2 = -1/\epsilon \qquad (16)$$

Retaining only the poles in the left-half plane, the filter becomes

$$F(p) = \frac{0.245}{(p^2 + 0.278\,p + 0.987)(p^2 + 0.670\,p + 0.278)} \qquad (17)$$

The magnitude of $F(j\omega_p)$ for $0 \le \omega_p \le 1$ varies between 1 and $1/\sqrt{1+\epsilon}$ or 0 and -1 dB.

The cutoff frequency for the filter given by Equation (17) is 1 rad/s. The filter expression for a different cutoff frequency is obtained by substituting $p = s/\omega_c$. Figure 8.5D-12 presents the filter attenuation curve for $\omega_c = 100$ rad/s. Since the nominal spacecraft spin rate is 0.5 rad/s, the lowest ripple frequency in rad/s is equal to one-half the number of rate pulses per revolution. For a ripple attenuation of 20 dB, at least 300 ppr are required.

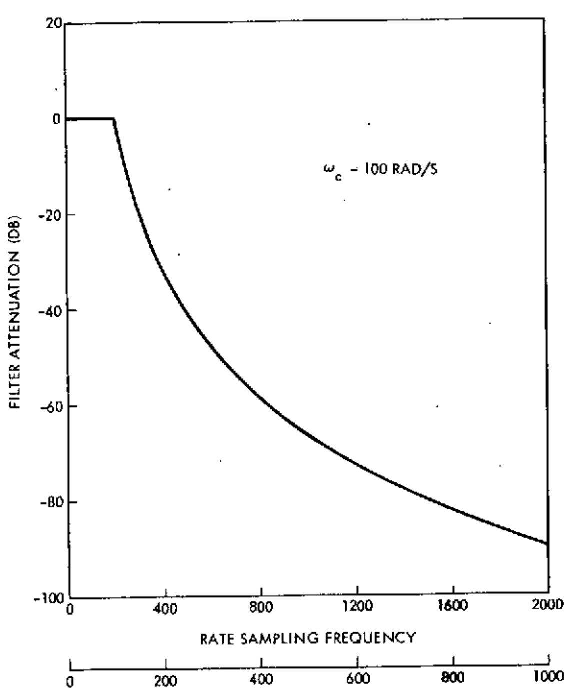

Figure 8.5D-12. Ripple Attenuation by Chebyshev Filter

If the filter cutoff frequency is increased, the attenuation for a given ripple frequency will decrease proportionately. This may be compensated for by increasing the rate sampling frequency. For example, using a filter cutoff frequency of 200 rad/s will require at least 600 ppr for a 20 dB attenuation of the fundamental ripple frequency.

4.3 Rate Loop Stability

Except for the generation of the rate pulses, the analog rate loop is basically a continuous system. In the following stability analysis, the rate loop is modeled as a linear, continuous system, as shown in Figure 8.5D-13. The first task is to determine what type of compensation C(s), if any, is needed to stabilize the control loop.

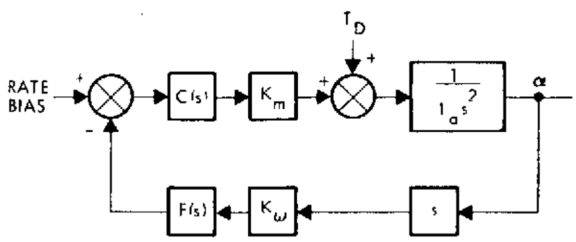

Figure 8.5D-13. Linear Model of Analog Rate Loop

The stability of the uncompensated rate loop is described by the root locus plot in Figure 8.5D-14. Note that a lightly damped pole from the Chebyshev filter dominates the rate loop response. The second complex pole moves towards the right-half plane with increasing loop gain. It is clear that compensation is needed for the highly oscillatory pole. The compensation design approach is to effectively cancel this pole and instead introduce two poles on the real axis.

A bridged-T network, as illustrated in Figure 8.5D-15, provides the type of transfer function required for the compensation filter. With the assumption of zero input source impedance and infinite output load impedance, the transfer function of the bridged-T network can be expressed as

$$\frac{E_2(s)}{E_1(s)} = \frac{s^2 + 2\delta_z \omega_n s + \omega_n^2}{s^2 + 2\delta_p \omega_n s + \omega_n^2} \tag{18}$$

where

$$\omega_n = \frac{1}{R\sqrt{C_1 C_2}} \qquad \delta_p = \frac{1 + 2\delta_z^2}{2\delta_z}$$

$$\delta_z = \sqrt{\frac{C_2}{C_1}}$$

C-3

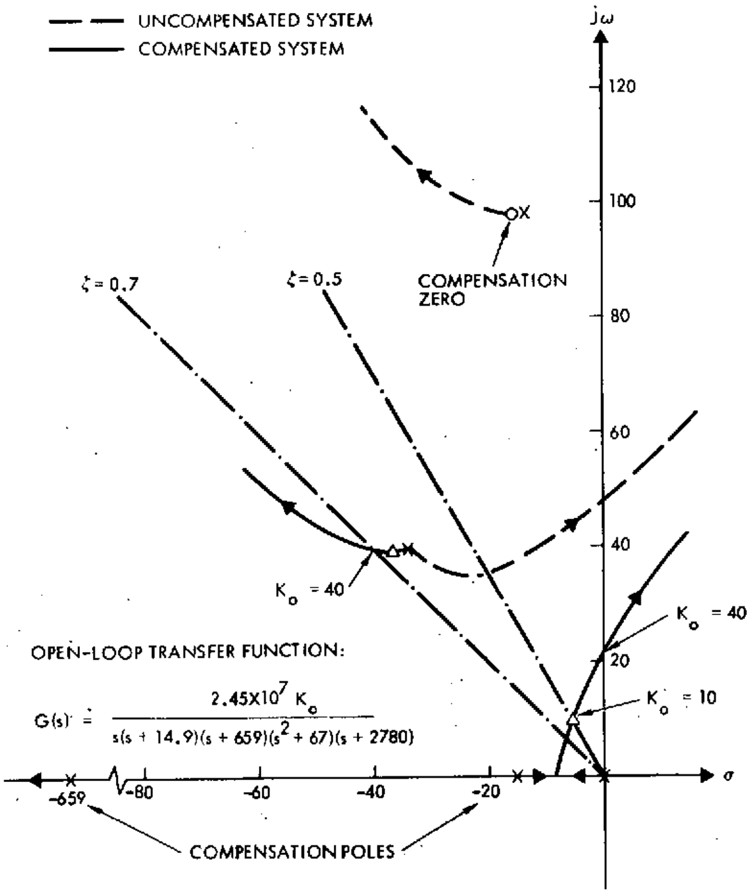

Figure 8.5D-14. Root Locus of Analog Rate Loop

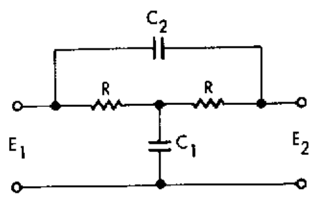

Figure 8.5D-15. Bridged-T Network

Thus, selecting the zeros of the transfer function automatically fixes the pole locations.

For the design under consideration, let the compensation zeros be located at $-15.3 \pm j98$ which is slightly to the left of the undesirable complex poles of the Chebyshev filter (see Figure 8.5D-14). The resulting compensation filter is given by

$$C(s) = \frac{s^2 + 30.6\, s + 9840}{(s + 14.9)(s + 659)} \tag{19}$$

Note that the two compensation poles are located on the real axis.

The open-loop transfer function of the rate loop is given by

$$
\begin{aligned}
G(s) &= \frac{K_o\, C(s)\, F(s)}{s} \\
&\cong \frac{2.45 \times 10^7\, K_o}{s(s + 14.9)(s + 659)(s^2 + 67\, s + 2780)}
\end{aligned}
\tag{20}
$$

In the approximate expression for G(s), it has been assumed that the compensation zeros exactly cancel two of the Chebyshev poles. Figure 8.5D-14 shows the root locus plot of this transfer functions.

The compensated rate loop is stable for a gain as high as 40 rad/s. Choosing a loop gain of 10 rad/s assures a minimum damping ratio of 0.5 for the critical closed-loop poles. The gain stability margin is 12 dB. Thus, the analog rate loop has been satisfactorily stabilized, but the question remains whether this rate loop can adequately handle the expected disturbance torques.

4.4 Effect of Disturbance Torque

The antenna pointing error due to a sinusoidal disturbance torque is given by

$$
|\alpha(j\omega)| = \frac{M}{\omega^2 I_a} \left| \frac{1}{1 + G(j\omega)} \right| \tag{21}
$$

where $G(j\omega)$ is the open-loop transfer function of the rate loop. Assuming that the disturbance torque varies at the spacecraft spin rate (0.5 rad/s) and has an amplitude of 72.01 g·cm (1 in.-oz), Figure 8.5D-16 gives the resulting antenna pointing error as a function of the rate loop gain.

For the selected rate loop gain of 10 rad/s, the antenna pointing error is about 0.00010 rad/g·cm (0.4 deg/in.-oz). If the maximum friction torque variation is 144.02 g·cm (2 in.-oz), then the rate loop gain has to be at least 12 rad/s in order to satisfy the antenna pointing requirement. It was pointed out earlier that the nominal operating gain may be increased without reducing the stability margins if the cutoff frequency of the Chebyshev filter is increased. However, a penalty is paid in terms of a higher ripple voltage.

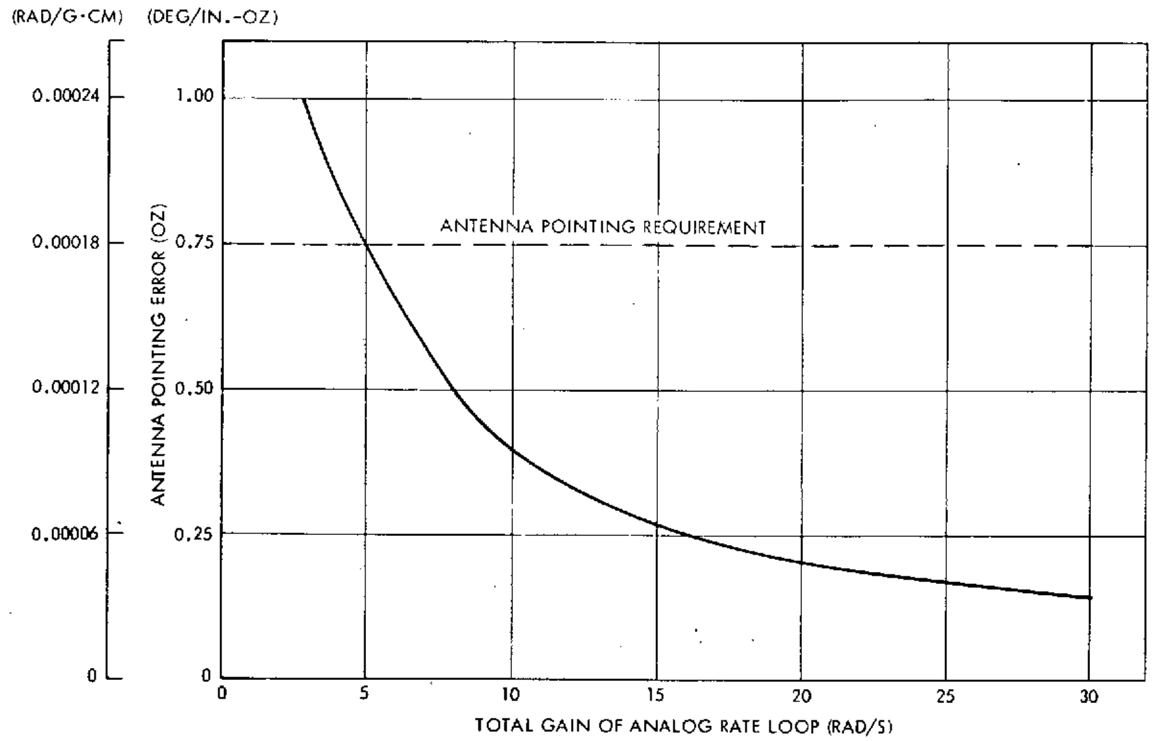

Figure 8.5D-16. Antenna Pointing Error Due to Sinusoidal Disturbance

5. DESPIN CONTROL SYSTEM WITH DIGITAL RATE LOOP

Figure 8.5D-17 shows a linear model of the despin control system with a digital rate loop. Antenna position is sampled once per spacecraft revolution. The analog compensation consists of a proportional-plus-integral control circuit and the rate loop has been described previously. This section considers the position loop stability and identifies several parameters which affect the transient system response. Finally, the effects of an additional rate feedback path (as an input to the proportional-plus-integral control circuit) are investigated.

5.1 Position Loop Stability

For the purpose of this stability analysis, the rate loop is treated as a continuous system. Thus, the rate loop transfer function can be expressed as

$$R(s) = \frac{K_m/I_a}{s(s + K_o)} \tag{22}$$

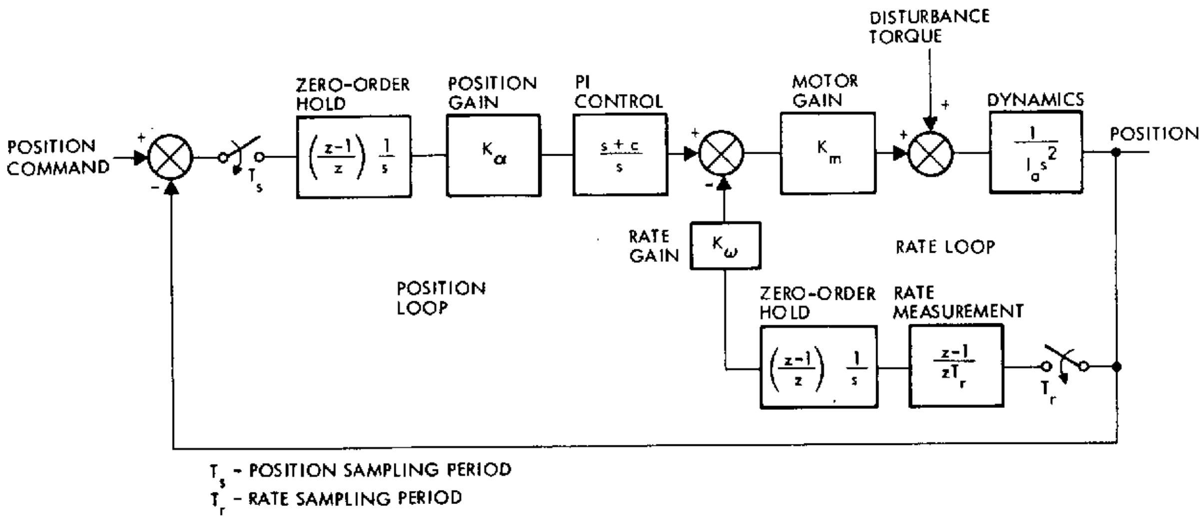

Figure 8.5D-17. Linear Model of Despin Control System With Digital Rate Loop

The total open-loop transfer function is given by

$$G(z) = \frac{K_\alpha K_m}{I_a}\left(\frac{z-1}{z}\right)\left[\frac{s+c}{s^3(s+K_o)}\right]^* \tag{23}$$

Expanding the partial fractions, we get

$$\frac{s+c}{s^3(s+K_o)} = \frac{K_1}{s+K_o} + \frac{K_2}{s^3} + \frac{K_3}{s^2} + \frac{K_4}{s} \tag{24}$$

where

$$K_1 = (K_o - c)/K_o^3$$

$$K_2 = c/K_o$$

$$K_3 = K_o K_1$$

$$K_4 = -K_1$$

Taking the z-transform of the expanded terms, yields the results

$$\left[\frac{s+c}{s^3(s+K_o)}\right]^* = \frac{K_1 z}{z-b} + \frac{K_2 T_s^2 z(z+1)}{2\,(z-1)^3} + \frac{K_3 T_s z}{(z-1)^2} + \frac{K_4 z}{z-1} \tag{25}$$

where

$$b = e^{-K_o T_s}$$

After combining all terms over a common demoninator, the final expression for the open-loop transfer function becomes

$$G(z) = K\frac{(z^2 + a_1 z + a_o)}{(z - 1)^2 (z - b)} \tag{26}$$

where

$$m_o = 2K_o K_1 (1 - b) - cT_s^{\,2} b + 2K_o^{\,2} K_1 T_s b$$

$$m_1 = 4K_o K_1 (1 - b) + cT_s^{\,2} (1 - b) - 2K_o^{\,2} K_1 T_s (1 + b)$$

$$m_2 = 2K_o K_1 (1 - b) + cT_s^{\,2} + 2K_o^{\,2} K_1 T_s$$

$$a_o = m_o/m_2$$

$$a_1 = m_1/m_2$$

$$K = K_a K_m m_2/2I_a K_o$$

The expression for the root locus gain (K) can be simplified by making the following assumptions: $K_o >> c$ and $b \cong 0$.

$$K \cong \frac{K_\alpha}{K_\omega}\left(\frac{cT_s^{\,2}}{2} + T_s + \frac{1}{K_o}\right) \tag{27}$$

Equation (27) indicates how the root locus gain varies as a function of the position sampling period or spacecraft spin period. Recall, however, that the rate measurement gain K_ω is also directly proportional to the square of the spin period.

A typical root locus plot of the position loop is presented in Figure 8.5D-18. For this plot the integrator gain (c) is 0.02 rad/s, the rate loop gain (K_o) is 10 rad/s and the position sampling period (T_s) is 12.5 seconds. Choosing K = 0.6 as the nominal operating point provides a gain stability margin of 11.7 dB and a damping ratio of

0.65 for the critical closed-loop poles. If the rate loop gain is increased, the system response becomes slightly more damped. When K_o = 25 rad/s (512 ppr), the damping ratio of the critical poles is 0.70.

RATE LOOP GAIN: K_o = 10 RAD/S
INTEGRATOR GAIN: c = 0.02 RAD/S

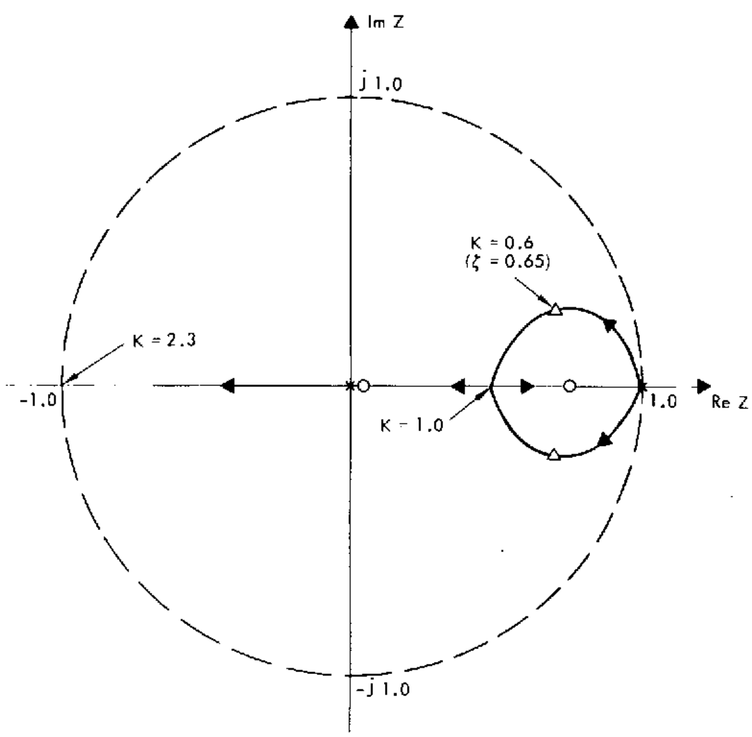

OPEN-LOOP TRANSFER FUNCTION: $G(z) = K \frac{(z - 0.01)(z - 0.75)}{z(z - 1)^2}$

Figure 8.5D-18. Root Locus of Position Loop with Digital Rate Feedback

5.2 Transient Response of Position Loop

The transient response of the position loop is characterized by the damping ratio of the dominant complex pole of the system. It has already been pointed out that variations of the rate loop gain slightly affect the transient response of the position loop. Two other parameters, which need to be considered in this respect, are the integrator gain and the spacecraft spin speed.

First, let us review how the damping ratio ζ is related to a complex root in the z-plane. In the s-plane the damping ratio can be expressed as $\zeta = \sin\beta$ where β is the angle between the imaginary axis and a line drawn from the origin to the location of the complex root. This angle β is related to the real (z_r) and imaginary (z_i) parts of a z-plane root as follows

$$\tan\beta = \frac{-\log|z|}{\tan^{-1}(z_i/z_r)} \tag{28}$$

where

$$|z| = \sqrt{z_r^2 + z_i^2}$$

The z-plane locus for a constant damping ratio is a logarithmic spiral except when β = 0 radian or β = 1.57 radian (90 degrees).

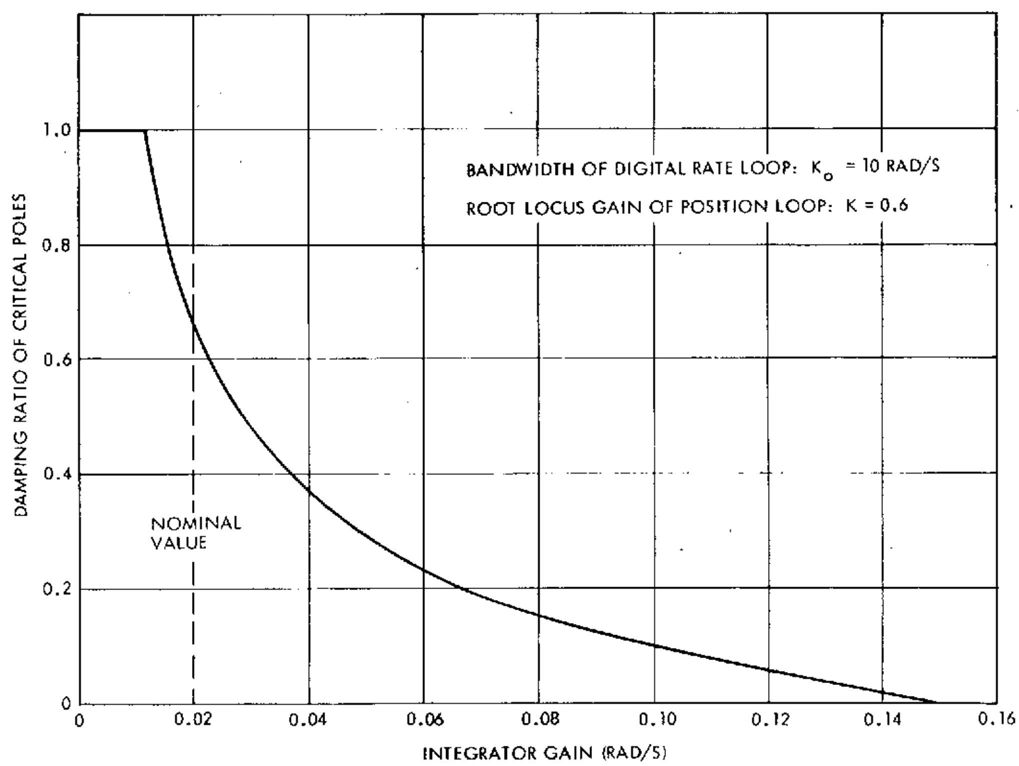

Figure 8.5D-19. Damping of Critical Closed-Loop Poles Versus Integrator Gain

Figure 8.5D-19 illustrates the effect of the integrator gain on the system's transient response. The damping ratio of the critical closed-loop poles is plotted as a function of the integrator gain. While the integrator gain is varied, the root locus gain is held constant at K = 0.6. The transient response of the position loop becomes more and more oscillatory and eventually goes unstable as the integrator gain is increased. For the selected value (0.02 rad/s) of the integrator gain, the damping ratio is 0.65.

Integral control is needed to counteract any constant disturbance in the control loop. It is desirable to use the highest acceptable value of the integrator gain because it improves the system's transient response to sudden shifts in disturbance levels, such as friction step changes in the ball bearing assembly. However, Figure 8.5D-19 indicates that the integrator gain may not be increased arbitrarily because it strongly affects the control loop response. This aspect of control system performance should be further evaluated by means of a simulation.

Spacecraft spin speed variations primarily affect the root locus gain and to a lesser extent, the shape of the root locus plot. Equation (27) describes the dependence of the root locus gain on the spacecraft spin period. Taking into account that the rate measurement gain (K_ω) is proportional to the square of the spin period (see Equation (6)), the root locus gain is almost directly proportional to the spacecraft spin speed. Figure 8.5D-20 shows that the damping ratio of the critical closed-loop poles also varies almost linearly with spin speed. For the spin speed range of 0.42 to 0.63 rad/s (4 to 6 rpm) the lowest damping ratio is about 0.5.

5.3 Two Rate Feedback Paths

An interesting modification of the basic control loop as shown in Figure 8.5D-17 has been made in the despin control system for the Helios spacecraft. Two rate feedback paths are used; they enter the forward path before and after the proportional-plus-integral control circuit. Figure 8.5D-21 locates the additional rate feedback path.

The output to input transfer function of this modified rate loop is given by

$$R(s) = \frac{(K_c K_m / I_a)(s + c)}{s\left[s^2 + (a + b)\,s + bc\right]} \tag{29}$$

where

$$a = K_a K_m / I_a$$

$$b = K_b K_c K_m / I_a$$

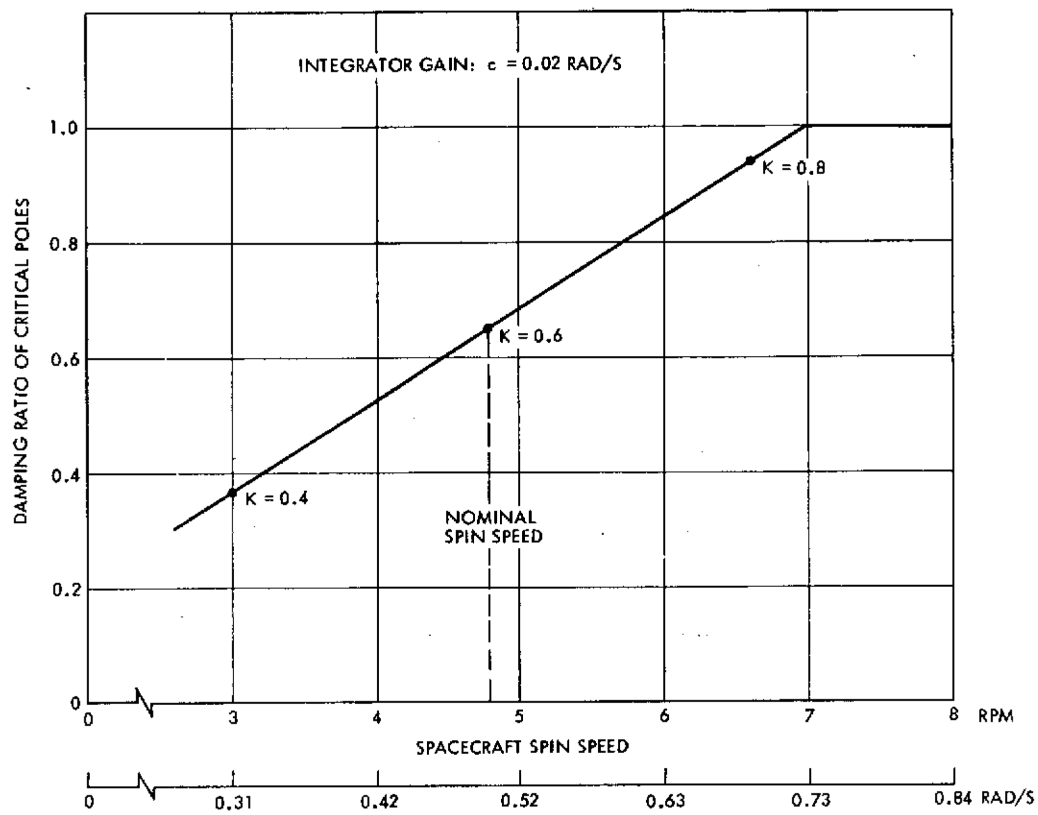

Figure 8.5D-20. Damping of Critical Closed-Loop Poles Versus Spin Speed

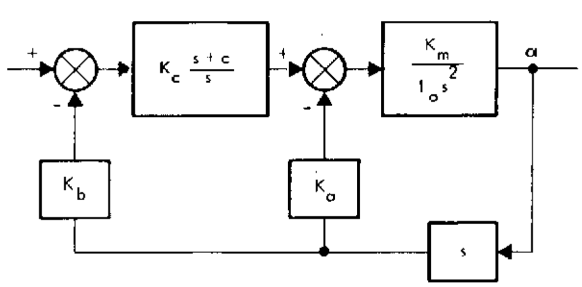

Figure 8.5D-21. Modified Rate Loop

If the control gains are chosen such that b>>a>>c, one can make the following approximation.

$$s^2 + (a + b)s + bc \cong (s + a + b)(s + c) \tag{30}$$

The rate loop transfer function can now be approximated by

$$R(s) \cong \frac{K_c K_m / I_a}{s(s + b)} \tag{31}$$

Note that the zero due to the integral control circuit has been effectively cancelled. This is a significant result because it removes the destabilizing effect of the integrator gain from the position loop response. Previously, stability considerations dictated the maximum acceptable value of the integrator gain. With the modified rate loop, it is possible to use a higher integrator gain which improves the convergence characteristics of the control system.

The open-loop transfer function of the position loop has the form

$$G(z) = \frac{K_\alpha K_c K_m}{I_a} \left(\frac{z - 1}{z}\right) \left[\frac{1}{s^2(s + b)}\right]^* \tag{32}$$

Expanding by partial fractions, we get

$$\frac{1}{s^2(s + b)} = \frac{1}{b^2}\left(\frac{b}{s^2} - \frac{1}{s} + \frac{1}{s + b}\right) \tag{33}$$

Taking the z-transform of the expanded terms yields the result

$$\left[\frac{1}{s^2(s + b)}\right]^* = \frac{1}{b^2}\left[\frac{b\, T_s z}{(z - 1)^2} - \frac{z}{z - 1} + \frac{z}{z - h}\right] \tag{34}$$

where

$$h = e^{-bT_s}$$

After combining all terms over a common denominator and simplifying, the final expression becomes

$$G(z) = K \frac{z + g}{(z - h)(z - 1)} \tag{35}$$

where

$$K = \frac{K_\alpha K_c K_m}{I_a b^2}(bT_s - 1 + h)$$

$$g = \frac{1 - bhT_s - h}{bT_s - 1 + h}$$

The parameter b represents the loop gain of the outer rate loop. Using $b = 10$ rad/s and $T_s = 12.5$ seconds, we get

$$G(z) \cong K\frac{z + 0.008}{z(z - 1)} \tag{36}$$

where

$$K \cong \frac{K_\alpha T_s}{K_b}$$

Figure 8.5D-22 shows a typical root locus plot of the position loop with the two rate feedback paths. The system goes unstable for $K > 2.0$. However, the system's transient response is well damped over this entire gain range. Since the root locus gain is directly proportional to the spacecraft spin speed, this allows stable operation over a wide spin speed range, especially at low spin speeds.

It is easily shown that the antenna pointing error due to a sinusoidal disturbance torque is approximately given by

$$|\alpha(\omega)| = \frac{M}{I_a\omega^2}\ \frac{1}{\sqrt{\left[1 + (b/\omega)^2\right]\left[1 + (c/\omega)^2\right]}} \tag{37}$$

This expression is valid for frequencies equal to or larger than the position sampling frequency. Unless the integrator gain (c) is as large as the excitation frequency, the pointing error is similar to that shown in Figure 8.5D-6. In Equation (37) b is the effective rate loop gain.

RATE LOOP GAIN: b = 10 RAD/S

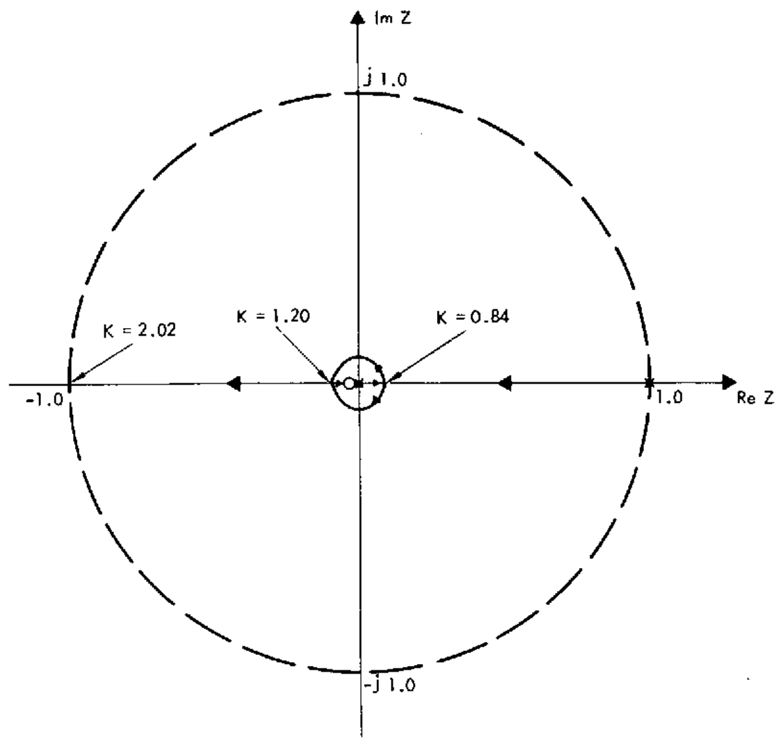

OPEN-LOOP TRANSFER FUNCTION: $G(z) = K \frac{z + 0.008}{z(z-1)}$

Figure 8.5D-22. Root Locus of Position Loop with Two Rate Feedback Paths

6. DESPIN CONTROL SYSTEM WITH ANALOG RATE LOOP

Figure 8.5D-23 shows a linear model of the despin control system with an analog rate loop. The rate loop design is discussed in Section 4. This section examines the position loop stability and briefly considers the transient response of the system.

6.1 Position Loop Stability

The closed-loop transfer function of the rate loop can be approximated by

$$R(s) = \frac{K_m}{I_a}\left[\frac{s + a}{s\,(s^2 + b_1 s + b_o)}\right] \tag{38}$$

where a = 14.9 from the compensation filter and the complex pole depends on the selected root locus gain. (For K = 10 in Figure 8.5D-14,

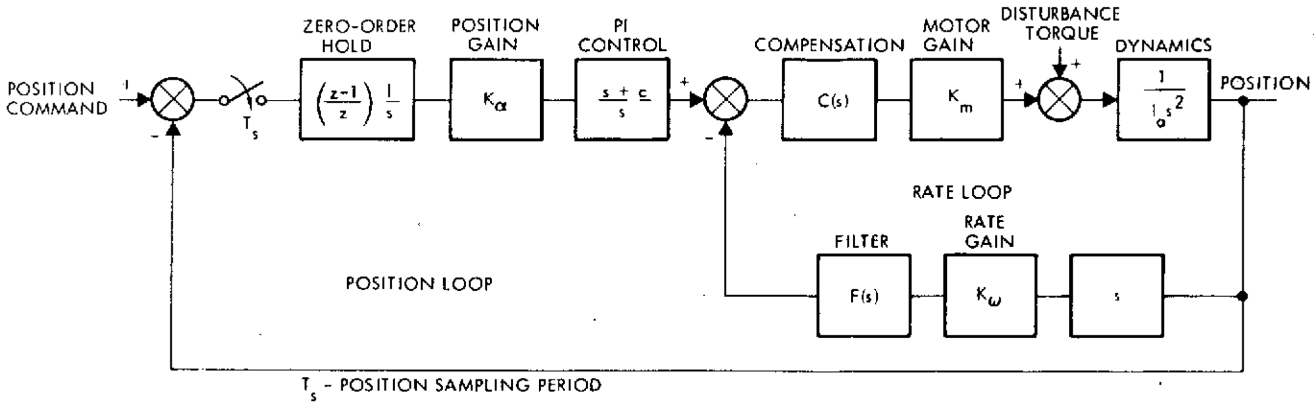

Figure 8.5D 23. Linear Model of Despin Control System with Analog Rate Loop

$b_1 = 11.1$ and $b_o = 130$). The total open-loop transfer function of the despin control system is given by

$$G(z) = \frac{K_\alpha K_m}{I_a}\left(\frac{z-1}{z}\right)\left[\frac{(s+a)(s+c)}{s^3\,(s^2+b_1\,s+b_o)}\right]^* \tag{39}$$

Expanding by partial fraction, we get

$$\frac{(s+a)(s+c)}{s^3(s^2+b_1 s+b_o)} = \frac{K_1}{s^3}+\frac{K_2}{s^2}+\frac{K_3}{s}+\frac{K_4+K_5\,s}{s^2+b_1 s+b_o} \tag{40}$$

where

$K_1 = ac/b_o$ $\qquad$ $K_4 = -K_2 - b_1K_3$

$K_2 = (a + c - b_1K_1)/b_o$ $\qquad$ $K_5 = -K_3$

$K_3 = (1 - K_1 - b_1K_2)/b_o$

In order to simplify the notation, let

$T = T_s$ $\qquad$ $e = \exp(-\alpha T)\cos\omega T$

$\alpha = b_1/2$ $\qquad$ $f = \exp(-2\alpha T)$

$\omega^2 = b_o - \alpha^2$

With this notation, the z-transform of Equation (40) is given by

$$\left[\frac{(s+a)(s+c)}{s^3\,(s^2+b_1 s+b_o)}\right]^* = \frac{A_1\,z\,(z+1)}{(z-1)^3} + \frac{A_2\,z}{(z-1)^2} + \frac{A_3\,z}{z-1} + \frac{A_4\,z + A_5\,z\,(z-e)}{z^2 - 2\,ez + f} \tag{42}$$

where

$$A_1 = K_1 T^2/2 \qquad A_4 = (K_4/\omega - \alpha\, K_5/\omega \exp(-\alpha T) \sin \omega T$$

$$A_2 = K_2 T \qquad A_5 = K_5$$

$$A_3 = K_3$$

After combining all terms over a common denominator, the final expression for the open-loop transfer function becomes

$$G(z) = K\frac{z^3 + a_2 z^2 + a_1 z + a_o}{(z-1)^2\,(z^2 - 2ez + f)} \tag{43}$$

where

$$m_o = (A_1 + A_2 + A_3)\,f + A_4 + e\,A_5$$

$$m_1 = (f - 2e)\,A_1 + (f + 2e)\,A_2 - 2\,(f + e)\,A_3 + 3A_4 -)1 + 3e)\,A_5$$

$$m_2 = (1 - 2e)\,A_1 - (1 + 2e)\,A_2 + (1 + f + 4e)\,A_3 - 3A_4 + 3\,(1 + 3)\,A_5$$

$$m_3 = A_1 + A_2 - 2\,(1 + e)\,A_3 + A_4 - (3 + e)\,A_5$$

$$a_o = m_o/m_3$$

$$a_1 = m_1/m_3$$

$$a_2 = m_2/m_3$$

$$K = K_\alpha K_m m_3/I_a$$

A typical root locus plot of the position loop is presented in Figure 8.5D-24. For this plot the integrator gain (c) is 0.02 rad/s, the rate loop gain (K_o) is 10 rad/s and the position sampling period (T_s) is 12.5 seconds. Since the exponential terms are very small, the open-loop transfer function reduces to the form shown in Figure 8.5D-24. Choosing K = 0.6 as the nominal operating point provides a gain stability margin of 11.7 dB and a damping ratio of 0.74 for the critical closed-loop poles. These stability characteristics are very similar to those of the position loop with a digital rate loop. Apparently the two different rate loop designs have relatively little effect on the total system stability.

RATE LOOP GAIN: K_o = 10 RAD/S
INTEGRATOR GAIN: C = 0.02 RAD/S

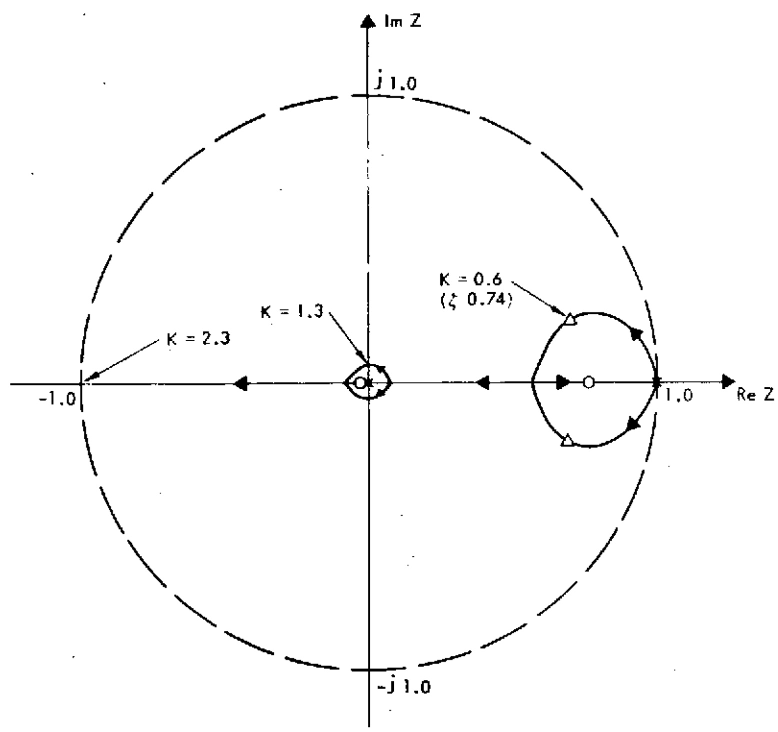

OPEN-LOOP TRANSFER FUNCTION: $G(z) = K \frac{(z + 0.002)(z - 0.78)}{z(z-1)^2}$

Figure 8.5D-24. Root Locus of Position Loop with Analog Rate Feedback

6.2 Transient Response of Position Loop

Figure 8.5D-25 describes the effect of the integrator gain on the system's transient response. As the integrator is increased, the response becomes more and more oscillatory and eventually goes unstable. This result is very similar to that shown in Figure 8.5D-19 for the despin control system with the digital rate loop.

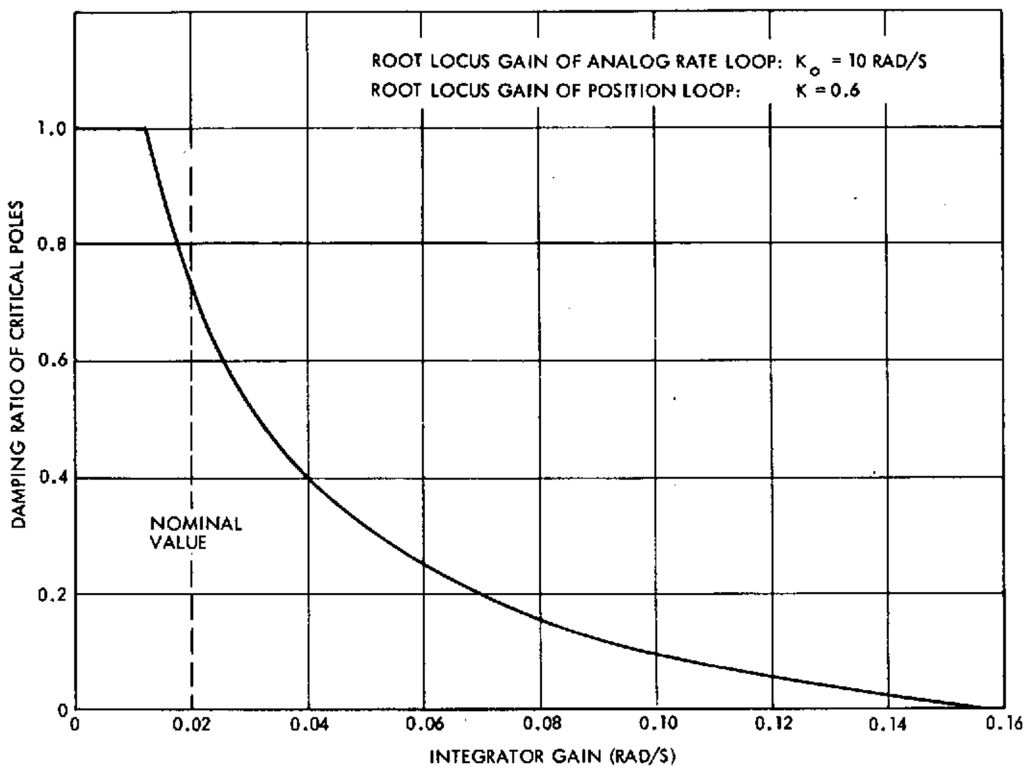

Figure 8.5D-25. Damping of Critical Closed-Loop Poles Versus Integrator Gain

Two rate feedback paths as illustrated by Figure 8.5D-21 may be used to improve the position loop's stability for higher integrator gains. The analysis of such a system is complicated by the filters in the analog rate loop. Assuming that the ripple voltage causes no problems, the effect of the two feedback paths in the analog rate loop is expected to be similar to that previously discussed for the digital rate loop. The major benefit of this design approach is less sensitivity of the system to integrator gain variations. By increasing the integrator gain, the control system response to disturbances, such as bearing friction, will be improved.

7. CONCLUSIONS AND RECOMMENDATIONS

The following two characteristics of the proposed Pioneer Venus orbiter strongly affect the despin control system design for the high gain antenna: 1) the low sampling frequency of the antenna position error (once every 12.5 seconds) and 2) the extremely low antenna spin inertia $[0.24\ \mathrm{kg{\cdot}m^2}\ (0.177\ \mathrm{slug\text{-}ft^2})]$. In order to meet the antenna pointing requirement of 0.013 radian (±0.75 degree) in the presence of the worst expected disturbances, it is essential that error information is available more frequently than once per spacecraft revolution. This is done by introducing a rate feedback loop with a relatively high sampling frequency.

Two implementations of the rate loop have been considered. The basic difference of these two rate loop designs lies in the processing of the rate pulses; one employs a digital tachometer while the other one uses only analog circuitry. The analog rate loop is easier to implement but it has less design flexibility than the digital rate loop. Assuming that the ripple voltage from the analog process is adequately filtered out, the performance characteristics of the two different rate loops are quite similar. For either case the recommended number of rate pulses per spacecraft revolution is 512.

It has been shown that the transient response of the despin control system is highly sensitive to variations of the integrator gain in the proportional-plus-integral control circuit. If it becomes necessary to increase the integrator gain for better system convergence, a second rate feedback path may be used to assure stable operation. With two rate feedback paths (as illustrated by Figure 8.5D-21) the control system response is well damped for relatively high integrator gains.

Past experience indicates that one of the major disturbances of the antenna despin system will be the friction in the bearing assembly. The response to sinusoidal friction fluctuations has been briefly analyzed and found to be satisfactory. However, a further study is needed to evaluate the system response to bearing noise and step changes in the friction level. This is most easily done by means of a simulation.

There are two important nonlinear effects of the despin control system which also need to be investigated. The output of the proportional-plus-integral control circuit has to be voltage limited and the motor torque becomes saturated for large error signals. The linear analysis determines the nominal loop gain necessary for stable operation. However, the nonlinear effects (i.e., hardware considerations) dictate how this total loop gain has to be distributed throughout the control loop for satisfactory system performance.

The performance analysis in this report assumes the use of the Helios despin mechanical assembly for driving the Pioneer Venus antenna. Thus, the disturbance model is based on test data of the Helios despin mechanical assembly. For equivalent or even slightly more severe disturbances, the proposed despin control system is capable of pointing the high-gain antenna of the Pioneer Venus orbiter at the earth with the required accuracy.

ATTACHMENT A

This attachment presents the derivation of Equation (11) which is the steady-state antenna pointing error due to a sinusoidal disturbance torque. It is assumed that the excitation frequency is equal to the spacecraft spin rate and consequently, the rate loop has to control this disturbance. Using the linear model of the digital rate loop as shown in Figure 8.5D-3, the antenna pointing error can be expressed as

$$\alpha(z) = \frac{\left[T_d(s)/(I_a\, s^2)\right]^*}{1 + K\,\frac{z+1}{z(z-1)}} \tag{A-1}$$

where K is the root-locus gain of the rate loop.

Let $T_d = M \sin \omega t$ or

$$T_d\,(s) = \frac{M\omega}{s^2 + \omega^2} \tag{A-2}$$

The z-transform of the numerator in Equation (A-1) becomes

$$\begin{aligned}\left[T_d\,(s)/(I_a\, s^2)\right]^* &= \left[\frac{M\omega}{I_a s^2 (s^2 + \omega^2)}\right] \\ &= \frac{M}{I_a \omega}\left[\frac{Tz}{(z-1)^2} - \frac{z \sin \omega T}{\omega(z^2 - 2z\cos \omega T + 1)}\right]\end{aligned} \tag{A-3}$$

where $T = T_r$ which is the rate sampling period. After substituting Equation (A-3) into (A-1) and simplifying, we get

$$\begin{aligned}\alpha(z) = \frac{M}{I_a \omega^2}\Bigg\{&\frac{\omega T\, z^2}{(z-1)\left[z^2 - (1-K)z + K\right]} \\ &- \frac{z^2 (z-1) \sin \omega T}{(z^2 - 2z\cos\omega T + 1)\left[z^2 - (1-K)\,z + K\right]}\Bigg\}\end{aligned} \tag{A-4}$$

The inverse z-transform of $\alpha(z)$ represents the antenna pointing error at the sampling instants.

Expanding Equation (A-4) by partial fractions yields the result

$$\alpha(z) = \frac{M}{I_a \omega^2}\left[\frac{M}{z-1} + \frac{k_2 + k_3 z}{z^2 - 2z \cos \omega T + 1} + \frac{(k_4 + k_6) + (k_5 + k_7) z}{z^2 - (1-K) z + K}\right] \tag{A-5}$$

For the steady-state solution only the constants k_1, k_2 and k_3 need to be determined since the third expression in Equation (A-5) introduces exponentially decaying terms. The first constant is given by

$$k_1 = \left.\frac{\omega T z^2}{z^2 - (1-K) z + K}\right|_{z=1} = \frac{\omega T}{2K} \tag{A-6}$$

The constants k_2 and k_3 can be determined from

$$\begin{aligned} &\frac{-z^2(z-1) \sin \omega T}{(z^2 - 2z \cos \omega T + 1)\left[z^2 - (1-K)z + K\right]} \\ &= \frac{k_2 + k_3 z}{z^2 - 2z \cos \omega T + 1} + \frac{k_4 + k_5 z}{z^2 - (1-K)z + K} \end{aligned} \tag{A-7}$$

Equating coefficients yields the following four equations.

$$\begin{aligned} k_3 + k_5 &= - \sin \omega T \\ k_2 - (1-K)k_3 + k_4 - 2k_5 \cos \omega T &= \sin \omega T \\ - (1-K)k_2 + k_3 K - 2k_4 \cos \omega T + k_5 &= 0 \\ k_2 K + k_4 &= 0 \end{aligned} \tag{A-8}$$

By solving Equations (A-9) for k_2 and k_3 we get

$$k_2 = \frac{ad + b}{a^2 + bc} \sin \omega T$$
$$k_3 = \frac{cd - a}{a^2 + bc} \sin \omega T \tag{A-9}$$

where

$$a = 1-K$$
$$b = K-1 + 2 \cos \omega T$$
$$c = K-1 + 2K \cos \omega T$$
$$d = 1 - 2 \cos \omega T$$

If it is valid to use the small angle approximations $\sin \omega T \cong \omega T$ and $\cos \omega T \cong 1$, Equations (A-9) reduce to

$$k_2 = \frac{1}{2K} \sin \omega T$$
$$k_3 = \frac{-1}{2K} \sin \omega T \tag{A-10}$$

The steady-state solution of the antenna pointing error from Equation (A-5) is given by

$$\alpha(kT) = \frac{M}{I_a \omega^2} \left\{ k_1 + \frac{k_2}{\sin \omega T} \sin [\omega(k-1)T] + \frac{k_3}{\sin \omega T} \sin \omega kT \right\} \tag{A-11}$$

where k is an integer. This solution is only valid at the sampling instants. By using the small angle approximations for k_2 and k_3, this expression reduces to

$$\alpha(kT) = \frac{M}{I_a \omega K_o} (1 - \cos \omega kT) \tag{A-12}$$

where $K_o = 2K/T$ which is the total rate loop gain.

DIGITAL RATE LØØP SIMULATIØN

```
$

 LIST
10 REM       DIGITAL RATE LØØP SIMULATIØN
100 PRINT "TIME(SEC)","RATE(DEG/SEC)","PØSITIØN(DEG)"
105 I=.177
110 K=9.6*I
115 N=10,S=200
120 R=12.5/S
130 D=R/N
135 X=0,Y=0,F=0
140 Q=57.3
145 T=0
150 A=1/192
160 W=0,M=0
200 FØR P=1 TØ  1/R
205 E=-K*W                RATE
215 X2=X
220 GØSUB 500          SAMPLING
230 W=(X-X2)/R
245 NEXT P                LOOP
250 PRINT T, Q*Y, Q*X
300 GØ TØ 200
500 FØR C=1 TØ N+.5
505 T=T+D
510 X1=X,Y1=Y,F1=F                INTEGRATION
515 M=A*SIN(T/2)
517 F=(E+M)/I                         LOOP
520 Y=Y1+(F+F1)*D/2
530 X=X1+Y1*D+(F+F1)*D↑2/4
550 NEXT C
600 RETURN
$ RUN
```

TIME(SEC)	RATE(DEG/SEC)	PØSITIØN(DEG)
1	.8142739E-01	.39675269E-01
2	.14611106E+00	.15572639E+00
3	.1750211E+00	.31965296E+00
4	.16107987E+00	.49131997E+00
5	.10770067E+00	.62869737E+00
6	.27952591E-01	.69815038E+00
7	-.58639258E-01	.68267446E+00
8	-.13087417E+00	.58605868E+00
9	-.17106652E+00	.43195794E+00
10	-.16937583E+00	.25810148E+00
11		

APPENDIX 8.6A

PREFERRED SOLID PROPELLANT MOTOR FOR ORBIT INSERTION, ATLAS/CENTAUR

APPENDIX 8.6A

PREFERRED SOLID PROPELLANT MOTOR FOR ORBIT INSERTION, ATLAS/CENTAUR

1. MAJOR COMPONENTS

The design of the preferred Aerojet SVM-2 solid propellant orbit insertion motor is shown in Figure 8.6A-1. Major components include the safe and arm device, igniter assembly, propellant grain, motor case, and nozzle assembly. A weather seal is used in the nozzle to protect the grain from humidity. Aluminum electrical grounding straps, connecting the forward boss and the safe and arm device to the mounting skirt, are bonded to the glass filament-wound motor case.

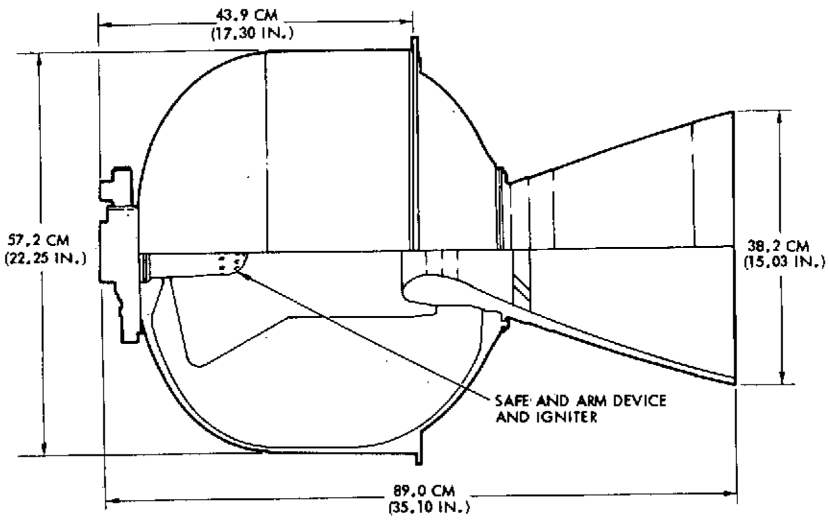

Figure 8.6A-1. Intelsat III Motor for Atlas/Centaur Requires Off-Loading of 7.2 kg (15.8 lb) of Propellant (4.5%)

1.1 Safe and Arm Device

The Aerojet SVM-2 comes equipped with the Bulova KR80000 safe and arm device described in Appendix 8.6B.

1.2 Igniter Assembly

The igniter, manufactured at Aerojet General Corporation, Sacramento, consists of a primary charge and a main charge contained in a 181 glass cloth/Epon 851 epoxy-resin pressure vessel with blowout ports. The 8-gram primary charge of 2A boron potassium nitrate (BPN) pellets is contained in a cavity between the 7075-T6 aluminum adapter and the glass chamber and in line with the safe and arm squibs.

The 136-gram main charge of 2L BPN pellets is contained in an annulus formed by the ineer-wire flame screen and the ID of the glass chamber. A perforated disk at the forward end of the chamber retains the pellets.

Ignition firing current is received by two ES-003 squibs installed in a KR80000-09 safe and arm device. The output from one ES-003 squib is sufficient to ignite the BPN booster charge under hard vacuum conditions.

The BPN booster charge output exhausts into the 210-gram 2L-size BPN pellet main charge.

1.3 Propellant

The propellant is an 88 percent total solid (which includes 15 percent aluminum), carboxy terminated, polybutadiene formulation. The grain configuration has eight fins in the forward end and a cylinder in the aft and is designed for a ±10 percent maximum propellant loading variation.

The propellant grain is cast with a small bore diameter and machined to the final diameter. Balance trim is then made from the forward and aft sections of the grain and will amount to no more than 0.34 kg (0.75 lb) forward and 0.57 kg (1.25 lb) aft.

1.4 Chamber Assembly

The SVM-2 chamber assembly is an epoxy-impregnated, glass filament-wound case with two integral 7075-T73 aluminum bosses for igniter and nozzle installation. A cylindrical attachment skirt (with a thrust ring for attachment to the spacecraft) is integrally wrapped with epoxy-impregnated glass filament on the external cylindrical section of the chamber. The chamber is hydrostatically proof-tested to 3.68×10^6 N/m^2 (534 psig) [1.05 times the SVM-2 maximum expected operations pressure (MEOP)], and is designed for a minimum ultimate burst pressure of 5.07×10^6 N/m^2 (735 psig) or 1.45 times the SVM-2 MEOP of 3.51×10^6 N/m^2 (509 psig). The cylindrical section of the chamber wall is 0.13 cm (0.051 in.) thick. The chamber is internally insulated with a silica-filled Buna-N rubber material. The die-molded insulator is 0.15 cm (0.060 in.) thick in the cylindrical chamber section; the thickness increases to 0.51 cm (0.200 in.) in the forward end and to 0.94 cm (0.370 in.) in the aft end to withstand the longer exposure to flame during firing.

1.5 Insulation

The internal chamber insulation is compression-molded from Gen-Gard V-45. The two-piece insulation system is joined by applying a dispersion of MEK/Gen-Gard V-45 to the 6.35 cm (2.5 in.) overlap area of the forward and aft insulators. The joined surfaces are cured with the chamber. The minimum thickness of the insulator at the aft tangent area is 0.15 cm (0.06 in.).

1.6 Nozzle Assembly

The partially submerged nozzle has a contoured exit cone with a 28:1 expansion ratio. The complete nozzle assembly consists of six major components: entrance cap, throat insert, throat insulator, nozzle shell, nozzle shell insulator, and exit cone. A polyurethane-foam seal is attached to the exit cone.

The entrance cap is made of a composite wrap of laminates of carbon-cloth-reinforced phenolic resin, and the submerged portion of the nozzle shell is insulated with molded V-44 rubber.

The throat insert is machined from silver-infiltrated tungsten to minimize erosion and is retained by a throat insulator made of compression-molded phenolic resin reinforced by carbon cloth.

The nozzle shell is machined from 6061-T6 aluminum and an integral flange with bolt holes to provide attachments to the chamber. The exit cone is fabricated of parallel-wrapped layers of silica-phenolic resin and attached to the shell with layers of glass cloth impregnated with Epon 815 adhesive.

2. PERFORMANCE AND OPERATION

The performance and operational capabilities of the SVM-2 motor are based on 20 static firings and five flights on Intelsat III. The on-loaded performance and operational parameters are shown in Table 8A-1.

Table 8.6A-1. On-Loaded SVM-2 Performance and Operational Parameters

PERFORMANCE	
TOTAL IMPULSE, NOMINAL [N · S (LB-S)]	405 368 (91 137)
TOTAL IMPULSE REPRODUCIBILITY	$3\sigma < 1$ PERCENT
TOTAL DURATION (SECONDS)	23
THRUST LEVEL [N (LBF)]	
NOMINAL	14 990 (3370)
MAXIMUM	21 528 (4840)
MEOP [N/M^2 (PSIA)]	3.54×10^6 (514)
SPECIFIC IMPULSE (SECONDS)	283.6
IGNITION DELAY TIME (SECONDS)	<0.100
SERVICE LIMITS	
OPERATING TEMPERATURE [°C (°F)]	-4 TO +43 (+20 TO +110)
STORAGE TEMPERATURE [°C (°F)]	-13 TO +60 (+10 TO +140)
IMPOSED AXIAL ACCELERATION (G)	14
IMPOSED LATERAL ACCELERATION (G)	2
HUMIDITY (PERCENT)	98 AT 49°C (+120°F)
TEMPERATURE CYCLING LIMITS [°C (°F)]	-4 TO +43 (+20 TO +110)
SPIN RATE [RAD/S (RPM)]	0 TO 11.4 (90 TO 110)
WEIGHT	
LOADED WEIGHT [KG (LB)]	166.2 (366.1) (WITH SAFE AND ARM)
PROPELLANT WEIGHT [KG (LB)]	145.9 (321.4)
THRUST PARALLELISM, MAX [CM/CM (IN./IN.)]	<0.006 (<0.0025)
OFFSET [CM (IN.)]	0.050 (<0.020)
STORAGE LIFE RELIABILITY (YEARS)	>0.98
STORAGE LIFE RELIABILITY (YEARS)	>3

3. POWER REQUIREMENTS

The only electrical power required for the orbit insertion motor is 4.4 ± 0.1 amp, 24 ± 5 VDC to fire the motor for orbit insertion.

APPENDIX 8.6B

PREFERRED SOLID PROPELLANT MOTOR FOR ORBIT INSERTION, THOR/DELTA

APPENDIX 8.6B

PREFERRED SOLID PROPELLANT MOTOR FOR ORBIT INSERTION, THOR/DELTA

1. MAJOR COMPONENTS

The design of the preferred Hercules BE-3-A solid propellant orbit insertion motor is shown in Figure 8.6B-1. Major components include the safe and arm device, igniter assembly, propellant grain, motor case, and nozzle assembly. A weather seal is used in the nozzle to protect the grain from humidity. Aluminum electrical grounding straps connect the forward adapter and the safe and arm device to the mounting skirt and are bonded to the glass filament-wound motor case. The major components are described below.

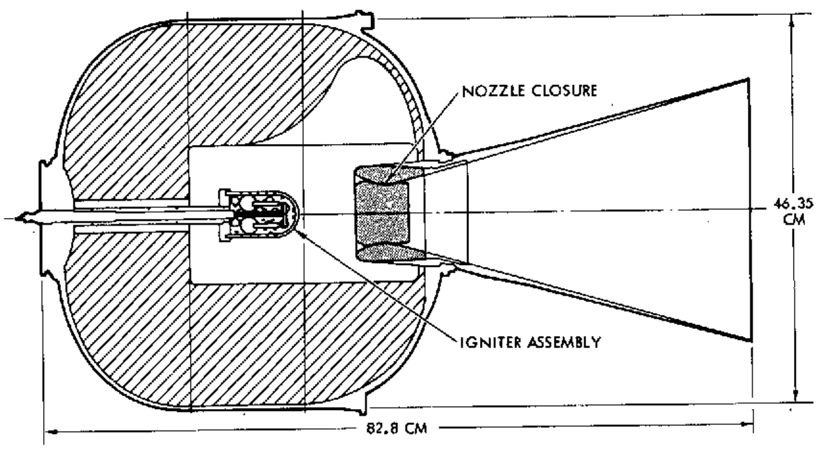

Figure 8.6B-1. Vela Motor for Thor/Delta Orbiter Requires Off-Loading of 3.6 kg (7.9 lb) of Propellant (4.1%)

1.1 Safe and Arm Device

The Hercules BE-3-A motor requires addition of a safe and arm device to satisfy range safety requirements that have been implemented since the motor was last flown.

The KR80000-09 safe and arm device (Figure 8.6B-2), with two integral ES-003 squibs, is a proven, available unit that is fully qualified to Specification S-133-1001-1-5, MAU-904 (Minuteman) Guided Missile Safety-and-Arming device. In operation, the two ES-003 squibs contained in the KR-80000 are rotated out of alignment with the mechanical barrier

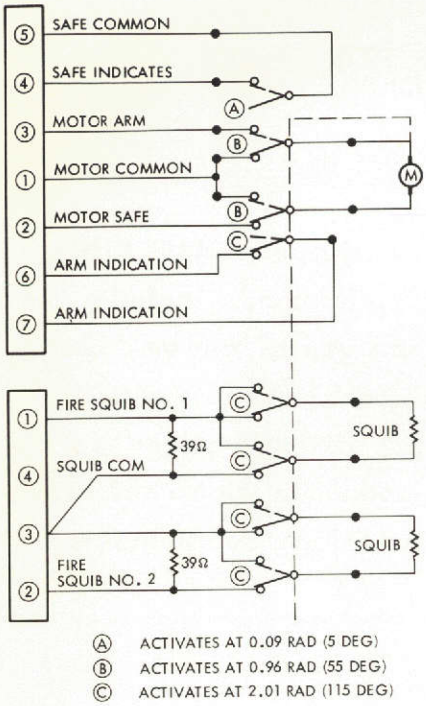

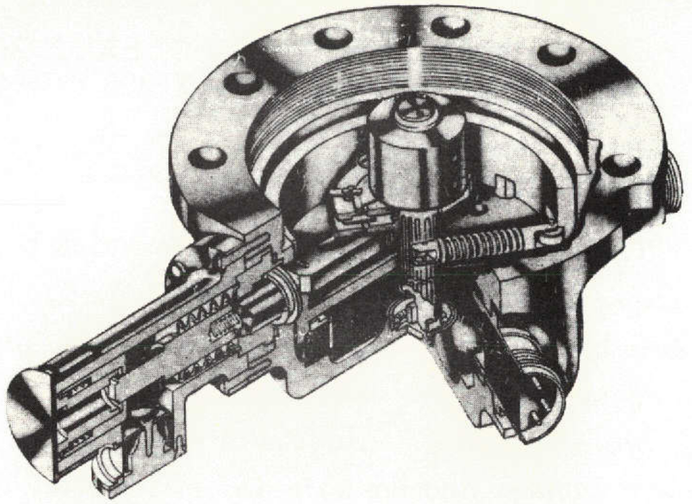

Figure 8. 6B-2. Standardized Ignition Safe and Arm

when the device is in the safe position. In the armed condition, the squibs are aligned with the barrier ports of the device and with mating barrier ports on the booster charge. A mechanical safing pin prevents movement of the device from the safe to the armed position. If the arming circuit is energized, the safing pin cannot be removed. Also, when the device is in the armed condition, insertion of the pin returns the unit to a safe condition. Mechanical and electrical safing is possible. Both visual and remote electrical indication of device condition is provided. The KR-80000-09 safe and arm device meets the ordnance and safety requirements of AEFTRM 127-1, AFM 127-1000.

Pertinent data are listed below.

- Power requirements: 3.5 amp minimum, all fire
  5.0 amp recommended
  Voltage source: 18 to 30 VDC

- The safe and arm contains two ES-003 squibs. The squib reliability is 0.995 at 95 percent confidence

- The safe and arm has two connections:
  - Squib firing circuit* connector, four-pin, Amphenol 200X-23-275(112)
  - Arming and monitoring circuit** connector, seven-pin, NAS1643PR14T7SN
- The safe and arm meets AFETRM127-1 requirements except for the 1 amp, 1 watt, 5-minute no-fire requirement.

1.2 Igniter Assembly

The igniter has two S-11A2 squibs surrounded by crushed and whole BKN pellets. The squibs and pellets are encased in a perforated, filament-wound basket and a phenolic base plate, which is attached to a phenolic igniter shaft extending through the cellulose acetate grain inhibitor. The igniter shaft protrudes from the forward end of the motor with ignition wires extending 6 inches from the end of the igniter shaft and terminating in an electrical connector. The ignition wires are enclosed in a stainless steel wiring harness which is bonded inside the igniter shaft. A glass seal in the wiring harness prevents chamber pressure from escaping out the forward end of the motor.

1.3 Propellant Grain

Propellant is Hercules DDP-80 formulation containing 21 percent aluminum; it is bonded directly to the case insulator. This is a modified double-base propellant. The grain is in a slotted-core configuration, which exhibits the desirable characteristics of near-neutrality and has rapid tail-off. No propellant slivers remain after burnout. A cellulose acetate inhibitor is incased by the grain and supports the igniter.

1.4 Chamber Assembly and Insulation

The BE-3-A chamber is a fiberglass structure with a Buna-N rubber insulator and aluminum pole pieces and skirts. The Buna-N insulator is fitted onto a mandrel and the forward and aft aluminum pole pieces are then attached to the mandrel. S901 fiberglass, wetted with Epon 828

*Redundant electrical firing circuit, redundant squibs.

**Indication of safe or arm position accomplished by switch deck within safe and arm device which indicates position of mechanical barrier between squibs and igniter booster charge.

epoxy resin, is wound over the mandrel assembly in alternating circumferential and helical layers. During the winding and curing process the fiberglass becomes bonded to the insulator and mechanically fastened to the pole pieces. A fiberglass skirt is also integrally wound on the chamber to provide a means to attach the motor to its payload. After the epoxy resin cures, an aluminum skirt is bonded in place and machined to configuration.

The chamber is approximately 48.3 cm (19 in.) long and 46.4 cm (18.25 in.) in diameter with a cylindrical section of 13.5 cm (5.25 in.); it has ovaloid domes.

1.5 Nozzle Assembly

The BE-3-A nozzle is conical with a 0.28 rad (16 deg) half-angle, and an initial expansion ratio of 18.6:1.

The nozzle has a graphite throat, a graphite cloth-phenolic aft throat insert, a chopped fiberglass-phenolic exit cone, an external fiberglass epoxy reinforcement, and an aluminum retaining ring which attaches the nozzle to the chamber. To prevent contaminants from entering the motor grain cavity, a vented styrofoam closure is inserted into the nozzle throat.

2. PERFORMANCE AND OPERATION

The performance and operational capabilities of the BE-3-A motor are based on over 200 firings, 161 of which have been flights. The performance and operational parameters for Pioneer Venus are shown in Table 8.6B-1.

3. POWER REQUIREMENTS

The only electrical power required for the orbit insertion motor is 4.5 ± 0.1 amp, 24 ± 5 VDC to fire the rocket for orbit insertion.

Table 8.6B-1. Off-Loaded BE-3-A Performance and Operational Parameters

PERFORMANCE	
TOTAL IMPULSE, NOMINAL [N · S (LB-S)]	224 838 (50 548)
TOTAL IMPULSE REPRODUCIBILITY (PERCENT)	< 0.5
TOTAL DURATION (SECONDS)	9.1
THRUST LEVEL [N (LBF)]	
NOMINAL	26 243 (5900)
MAXIMUM	28 467 (6400)
MEOP [N/M² (PSIA)]	3.79 x 10⁶ (550)
SPECIFIC IMPULSE (SECONDS)	276.0
IGNITION DELAY TIME (SECONDS)	< 0.1
SERVICE LIMITS	
OPERATING TEMPERATURE [°C (°F)]	-1 TO +38 (+30 TO +100)
STORAGE TEMPERATURE [°C (°F)]	-1 TO +38 (+30 TO +100)
IMPOSED AXIAL ACCELERATION (G)	40
IMPOSED LATERAL ACCELERATION (G)	5
HUMIDITY (PERCENT)	98
TEMPERATURE CYCLING LIMITS [°C (°F)]	-1 TO +38 (+30 TO +100)
SPIN RATE [RAD/S (RPM)]	62.4 (600)
WEIGHT	
LOADED WEIGHT [KG (LB)]	93.6 (206.1)
PROPELLANT WEIGHT [KG (LB)]	83.3 (183.1)
THRUST PARALLELISM, MAX [CM/CM (IN./IN.)]	< 0.005 (< 0.002)
OFFSET [CM (IN.)]	< 0.005 (< 0.002)
STORAGE LIFE (YEARS)	> 3
RELIABILITY (DEMONSTRATED)	0.972 AT 90 PERCENT CONFIDENCE

APPENDIX 8. 6C

CONTAMINATION BY ORBIT INSERTION MOTOR

APPENDIX 8.6C

CONTAMINATION BY ORBIT INSERTION MOTOR

1. ORBIT INSERTION MOTOR EXHAUST PLUME ANALYSIS

For these calculations, it was conservatively assumed that the motor was fired in a hard vacuum. The following assumptions were used in the plume analysis:

- Isentropic continuum flow
- Gas exhibits a constant gamma (γ) aft of nozzle exit, i.e., frozen flow
- Prandtl-Meyer turning angle applies
- Exhaust continues to flow in the direction indicated by maximum Prandtl-Meyer turning angle.

The first three assumptions are standard assumptions used in plume analyses. The last assumption may be conservative, since the plume boundary will tend to curve away from the spacecraft due to the forward acceleration of the spacecraft with respect to the gas molecules in the plume. However, when boundary layer effects are taken into account, the plume expands to larger angles than the corresponding inviscid plume.

Exhaust products consist of solid particles, gases, and condensables. Table 8.6C-1 represents the theoretical ballistic properties of ANB 3066 propellant at the nozzle exit plane. The only solid particles generated are Al_2O_3.

Table 8.6C-1. Exhaust Products

CONSTITUENT	MOLE FRACTION
HCl (G)	0.15553
CO (G)	0.22655
CO_2 (G)	0.03357
H_2 (G)	0.32642
H_2O (G)	0.10174
N_2 (G)	0.07866
P_4O_6 (G)	0.00011
Al_2O_3 (S)	0.07740
MOLECULAR WEIGHT GAS	19.74091
MOLECULAR WEIGHT CONDENSATE	101.96098
WEIGHT FRACTION GAS	0.69768
WEIGHT FRACTION CONDENSATE	0.30232

The characteristics of the existing contoured nozzle design and propellant are:

Expansion ratio, A_e/A_t	=	28
Mach number (at exit), M	=	4.0
Gamma (at exit), γ	=	1.20
Exit half angle, θ_E	=	15.0

The maximum turning angle of the exhaust gases was found by evaluating the Prandtl-Meyer function for ambient conditions and existing conditions at nozzle exit as given in Equation 1.

$$\theta_{MAX} = \nu_{MAX} - \nu_{EXIT} + \theta_E \text{ (measured from nozzle center line)} \quad (1)$$

The Prandtl-Meyer function is:

$$\nu = \sqrt{\frac{\gamma + 1}{\gamma - 1}} - \tan^{-1} \sqrt{\frac{\gamma - 1}{\gamma + 1}(M^2 - 1)} - \tan^{-1} \sqrt{M^2 - 1} \quad (2)$$

Evaluation of Equation 2 yields:

$$\nu_{MAX} = 3.76 \text{ rad } (215.5 \text{ deg})$$

$$\nu_{EXIT} = 1.71 \text{ rad } (98.1 \text{ deg})$$

Therefore, the maximum turning angle is:

$$\theta_{MAX} = 2.31 \text{ rad } (132.4 \text{ deg})$$

2. EXHAUST PARTICLE IMPINGEMENT

A qualitative description of the gas-particle flow in a nozzle throat can be obtained by considering the near-equilibrium case. Using the nomenclature of Table 8.6C-2, in this case the gas properties in the throat region can be approximated by

$$U_g/U_g^* \simeq 1 + \alpha(z/r^*) + (\gamma_e + 1)/8)\alpha^2(r^2/r^{*2})$$

$$V_g/U_g^* \simeq (\gamma_e + 1/4)\alpha^2(zr/r^{*2}) + [(\gamma_e + 1)^2/16]\alpha^3(r^3/r^{*3})$$

Table 8.6C-2. Nomenclature for Impingement Calculations

Nomenclature	
d_p	Particle diameter
f_p	Ratio $C_D Re/24$
K	Constant defining particle velocity lag
m_p	Particle density
R	Gas constant
R*	Nozzle wall radius of curvature at nozzle throat
r_p	Particle radius
r*	Nozzle throat radius
U_g	Axial gas velocity
V_g	Radial gas velocity
W_p	Particle mass flow
z	Axial coordinate
γ	Gas adiabatic expansion coefficient
$\bar{\gamma}$	Expansion coefficient for gas-particle system
μ_g	Gas velocity coefficient
Subscripts	
e	Refers to equilibrium or exit conditions
Superscripts	
*	Refers to throat conditions

where

$$\alpha = \left[\left(\frac{2}{r_e + 1}\right)\left(\frac{r*}{R*}\right)\right]^{1/2}$$

and the nozzle throat location is given by $z*/r* = [(\gamma_e + 1)\alpha]/8$. To Sauer's order of approximation, it is found that

$$\frac{U_p}{U_g^*} = K*\left(1 + \alpha\frac{z}{r^*} + \frac{\gamma_e + 1}{8}\alpha^2\frac{r^2}{r^{*2}}\right) = K*\frac{U_g}{U_g^*}$$

$$\frac{V_p}{U_g^*} \simeq \frac{\gamma_e + 1}{4}\alpha^2\left(\frac{z}{r^*} - \frac{1-K}{K\alpha}\right)\frac{r}{r^*} + \frac{(\gamma_e + 1)^2}{16}\alpha^3\frac{r^3}{r^{*3}}$$

where K* is given by

$$K^* = \frac{9}{4}\,\frac{\mu_g^* f_p^* r^*}{m_p r^2 U_g^*}\left[\frac{\bar{\gamma}+1}{2}\;\frac{R^*}{r^*}\right]^{1/2}$$

$$\times \left\{\left[1+\frac{8}{9}\,\frac{m_p r_p^2 U_g^*}{\mu_g^* f_p^* r^*}\left(\frac{\bar{\gamma}+1}{2}\;\frac{R^*}{r^*}\right)^{1/2}\right]^{1/2} - 1\right\}$$

Particle samples taken from the exhaust of various aluminized propellants have been found to follow a logarithmic normal particle size distribution.

$$W_p(d_p)/W_p = \left[(2\pi)^{1/2} d_p \ln \sigma_g\right]^{-1} \times \exp\left[-\frac{(\ln d_p - \ln \bar{d}_p)^2}{2 \ln^2 \sigma_g}\right]$$

where $\bar{d}_p = 3.5 \pm 1.0\ \mu$, $\sigma_g = 1.9 \pm 1.0\ \mu$.

Figure 8.6C-1 is a plot of this size distribution, which was found to be independent of engine size and geometry, propellant composition, and chamber conditions for rather large engines.

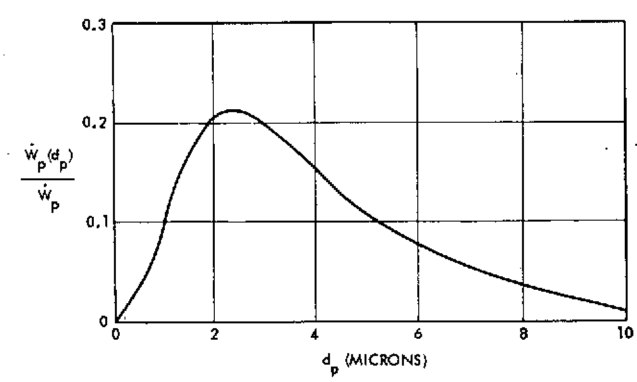

Figure 8.6C-1. Measured Particle Size Distribution for Aluminized Propellants

Figure 8.6C-2 is a plot showing the limiting particle streamlines in the nozzle, which originate at the wall in the nozzle inlet section. All particles of a given size will be located between the axis and its limiting streamline. Only the smallest particles follow the gas and the largest particles are concentrated near the axis, filling about a third of the nozzle area at the exit plane.

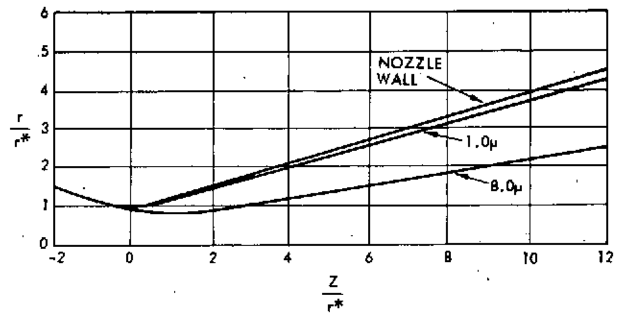

Figure 8.6C-2. Limiting Particle Streamline in Nozzle

Figure 8.6C-3 is a plot of the limiting particle streamlines in the vacuum expansion plume outside the nozzle. Only the smallest particles are turned, and even they are not greatly affected by the expansion outside the nozzle. All particle trajectories become straight lines, tow or three nozzle exit diameters, outside the nozzle, and the particles have little effect on gas expansion because particle drag coefficients go to zero (owing to rarefaction effects) as the gas density drops outside the nozzle. The particle flow field outside the nozzle is conical and appears to originate from a source near the nozzle throat.

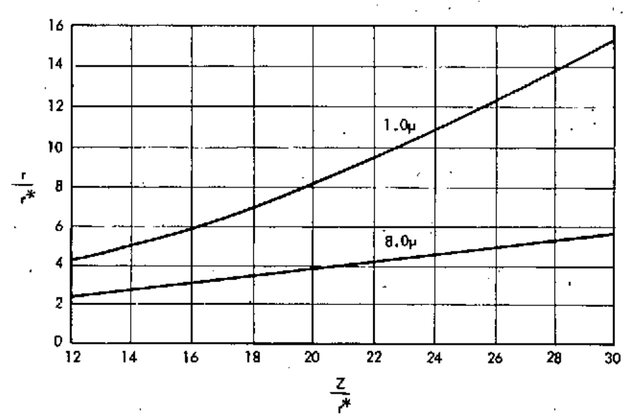

Figure 8.6C-3. Limiting Particle Streamlines in Vacuum Expansion Plume Outside Nozzle

3. OUTGASSING

Outgassing of fugacious materials has been suspected of causing problems in certain instruments sensitive to optical degradations. Outgassed constituents from the solid rocket propellant before motor firing are precluded from exiting the central cylinder by the thermal insulation that is already present and completely encases the motor. Any outgassed products from the motor case materials are likewise controlled. In addition to the thermal insulation protection, propellant outgassing is inhibited by a weather seal located in the motor nozzle.

After the orbit insertion burn of the solid rocket motor, outgassing of the motor case insulation will occur. This outgassing, however, will be directed out the nozzle, most likely in the free-molecular flow regime. Few, if any, of these molecules will reverse their translational velocities and impinge on the spacecraft. Even if outgassing does occur, therefore, it is controlled and no adverse effects are anticipated.

4. CONCLUSIONS

From the foregoing analyses it is apparent that:

- Exhaust gases during the orbit insertion burn may impinge on parts of the spacecraft.
- Solid particles are nearly all contained within a 0.35 rad (20-deg) cone downstream of the nozzle exit plane and will not impinge on the spacecraft.
- Outgassing is controlled and no adverse effects on the spacecraft are foreseen.

5. RECOMMENDATIONS

It is recommended that instruments and probes that are sensitive to degradation by the accumulation of particulate matter be covered by protective shades or that they not be deployed during the time the orbit insertion motor is burning.

SECTION 10 APPENDICES

APPENDIX 10A

DESCRIPTION OF RHUMB LINE PRECESSION MANEUVERS

APPENDIX 10A

DESCRIPTION OF RHUMB LINE PRECESSION MANEUVERS

Open-loop precession of the spacecraft is used for ΔV midcourse corrections and other reorientation maneuvers. The precession is effected by firing the velocity-precession thrusters (VPT's) once every spacecraft revolution at a constant preselected angle from the sun-spin axis plane. During this maneuver the vehicle's angular momentum vector inscribes a path on an imaginary sphere surrounding the spacecraft called the precession path. For each precession step the precession path follows a great circle; however, the total precession path, which consists of a sequence of great circle segments, approximates a loxodromic curve. A segment of the loxodrome is known as a rhumb line. The ideal rhumb line path is at a constant angle to the local meridian line at every point on the sphere. The geometry for the precession path is shown in Figure 10A-1.

The rhumb line path is always longer than or equal to the great circle path connecting the initial and final angular momentum vectors. The angular length of the rhumb line path depends on the precession angle and the sun-spacecraft-earth geometry at the time of the precession maneuver. As part of a ΔV maneuver the spacecraft might have to be precessed through an angle as large as 1.57 radian (90 degrees). Errors in path execution occur in the length of the path and in its direction. Error in the length of the maneuver is caused primarily by thruster impulse uncertainty, while direction error is caused by sensor error and differences between the rhumb line and the sequence of great circles. For the longest precession maneuver the actual precession path deviates in direction from the rhumb line by about 0.008 radian (0.47 degree). The actual path taken by Pioneer must be corrected for this deviation in what is called the "great circle program."

Figure 10A-2 illustrates the rhumb line path geometry. Let us define the following quantities:

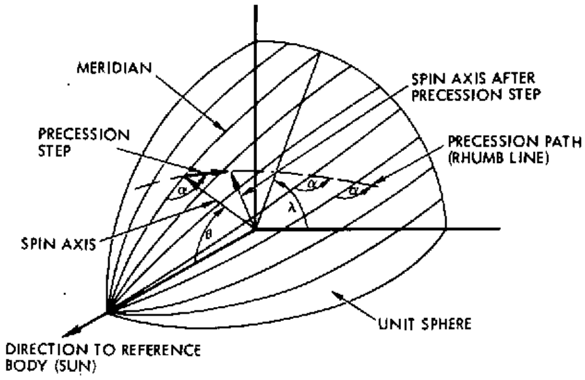

Figure 10A-1. Geometry and Coordinates of Open-Loop Precession

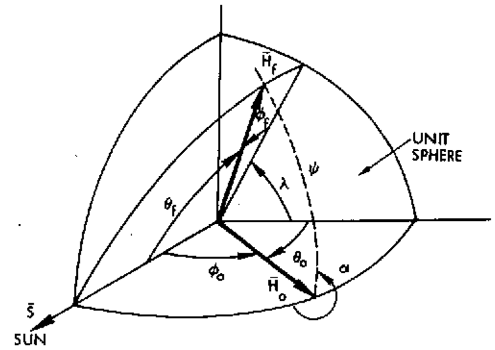

Figure 10A-2. Rhumb Line Geometry

Symbol	Definition
$\bar{S}$	Vector pointing from the spacecraft to the sun or other reference body
$\bar{H}_o$	Initial angular momentum vector of the spacecraft
$\bar{H}_f$	Final angular momentum vector of the spacecraft
φ_o	Complement of angle between $\bar{S}$ and $\bar{H}_o$ $(90 - \theta_o)$
φ_f	Complement of angle between $\bar{S}$ and $\bar{H}_f$ $(90 - \theta_f)$
φ_p	Angle between $\bar{H}_o$ and $\bar{H}_f$ (precession angle)
λ	Angle between the planes formed by the vectors $\bar{S}$ and $\bar{H}_o$ and the vectors $\bar{S}$ and $\bar{H}_f$
α	Angle between meridian line and rhumb line path
ψ	Angular distance of rhumb line path
Δ_ψ	Angular step size of precession
θ_v	Angle between the ΔV thrust vector and the initial spacecraft spin [0 radian (0 degree) $\leq \theta_v \leq 1.57$ radian (90 degrees) to cover entire sphere for ΔV]

To obtain the values for storage in the ACS stored program registers to achieve an open loop precession, a number of steps must be taken. First, the magnitude and direction of the desired ΔV (or final pointing direction) must be determined in the coordinate system indicated in Figure 10A-2. The ΔV (or pointing) direction will then be given in terms of λ and φ_f).

This information must be converted into the rhumb line parameters α and ψ and the time required for ΔV. An example flow chart is given in Figure 10A-3. The precession direction (α) and magnitude (ψ) must be corrected for the quantization in the PSE, for thruster impulse and centroid performance data, for spin rate error, and for path distortion from a true rhumb line caused by execution in the form of a sequence of great circles. The maneuver should also be modified to avoid regions of large error sensitivity — regions near the ± sun-spacecraft line. Sensitivities should be checked using system software prior to maneuver execution. Examples of sensitivity are shown in Figure 10A-4.

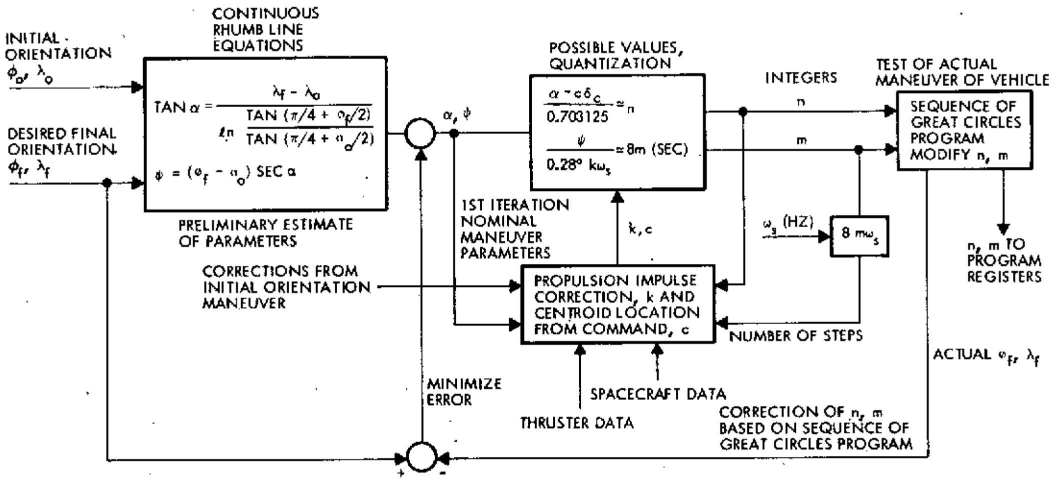

Figure 10A-3. Flow Diagram to Derive Open-Loop Precession Program Data for ACS

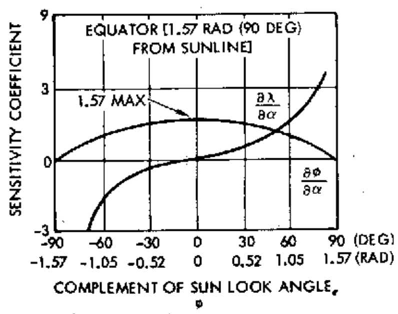

Figure 10A-4. Nominal Sensitivity to Precession Errors (Worst Case Path Length)

Sensitivity equation:

$$\frac{\partial \varphi_f}{\partial \alpha} = -\psi \sin \alpha$$

$$\frac{\partial \lambda}{\partial \alpha} = \frac{1}{\cos^2 \alpha} \ell n \frac{\tan(\pi/4 + \varphi_f/2)}{\tan(\pi/4 + \varphi_o/2)}$$

$$- \psi \frac{\sin \alpha \tan \alpha}{\cos}$$

The regions near the sun or the anti-sun are highly sensitive to error in execution of α. These regions should be avoided by breaking ΔV into vector components. The sun look angle θ is constrained 0.17 radian (±10 degrees) by this requirement.

Once the final desired orientation is determined by DSN tracking for the first 5 days, the system software will transcribe this into the values to be entered into the attitude control system CEA-PSE. A flow chart for the operations to be performed by this software is shown in Figure 10A-3. The required software has already been completely developed for all functions described in this section and has been extensively employed for Pioneers 10 and 11. The operations shown by this figure are as follows:

- The values of longitude (λ_o, λ_f) and latitude (φ_o, φ_f), which describe the initial and final orientation, are used to obtain a preliminary estimate of the rhumb line parameters, α and ψ. These describe the angle to the sun, and the length of the ideal rhumb line.

- Given the nominal rhumb line parameters and the propulsion performance characteristics (impulse correction (k)), preliminary estimates of the number of angle bits (n) and the number of time increments (m) to be used in the ACS stored program for precession can be made. The estimate of α is next corrected for impulse centroid location (δ_c and its correction factor c) and for quantization in α that can be stored in the PSE registers. Since the impulse torque vector which produces the precession either leads or trails the roll index pulse ($\alpha = 0$) then the α used in the registers must be corrected depending on the thrusters and index pulse used:

  $$\alpha_R = \alpha - c\delta_c \pm 90^\circ$$

  Note that α is measured from the sun spin axis plane (plane defined by $\overline{S}$ and $\overline{H}_o$) to the plane of precession and is described by the righthand rule.

- A system test of the estimate of n and m are made via the sequence of great circles program which steps through the actual maneuver and produces error estimates from the desired orientation.

- The information obtained from the sequence of great circles program is used to improve the estimates of n and m and obtain minimum error in the final orientation.

APPENDIX 10B

PROBE ENTRY DSN SUPPORT
(VERSION III SCIENCE)

APPENDIX 10B

PROBE ENTRY DSN SUPPORT (VERSION III SCIENCE)

The 1977 multiprobe mission imposes some new and different requirements on the Deep Space Network (DSN) for support. One of the more unusual is to receive data simultaneously from five vehicles: the bus, the large probe, and three small probes. Part of this requirement is based on the DLBI experiment, which wants to have all four probes enter at the same time and to use the bus, which has been delayed, as a common reference. The selection of PCM/PSK/PM modulation is compatible with the DSN, and the use of two-way tracking for the bus and the large probe also appears to be compatible. However, both hardware and personnel are limited at the DSN sites, and therefore the impact of the five simultaneous downlinks must be minimized.

A method of achieving minimum impact is shown in Figure 10B-1. This shows a configuration for the 1977 launch and the possible use of Arecibo and/or Haystack to support the DLBI experiment and to back up the DSN stations.

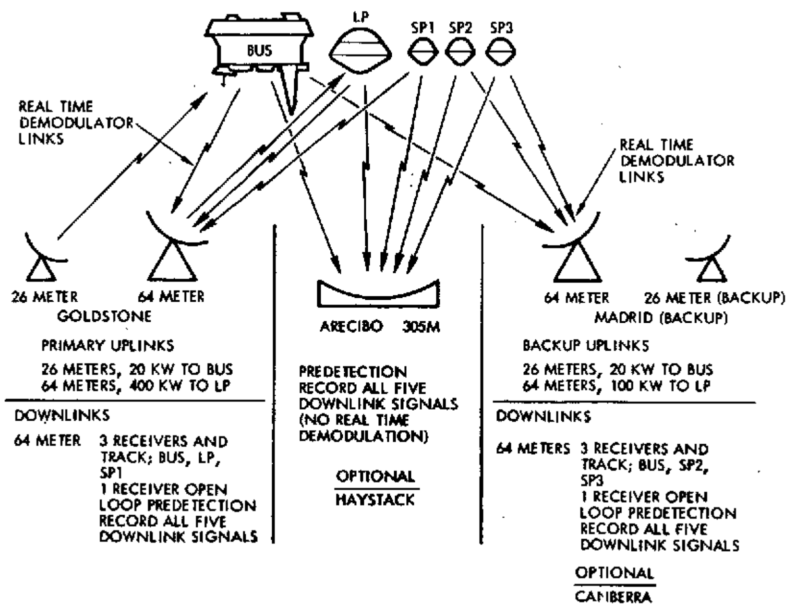

Figure 10B-1. Probe Entry DSN Configuration

From the DSN/Flight Project Interface Design Handbook 810-5, Revision C and material supplied at the DSN Interface meeting held at JPL on 22 November 1972, each of the three 64-meter stations will have four receivers and three doppler trackers available, while the 26-meter stations will have two receivers and one doppler tracker. For the 1977 opportunity, Goldstone and Madrid would be the preferred DSN stations for it would then be possible for Arecibo and Haystack to also observe the probe entry. Goldstone would be the preferred primary station and would transmit all uplink signals, Madrid would provide backup and could transmit if a problem developed at Goldstone.

To minimize acquisition time and maximize downlink performance, it is recommended that the Goldstone 400 kW transmitter at the 64-meter site be used for the large probe uplink. A 20 kW transmitter at one of the Goldstone 26-meter stations can be used for the uplink signal to the bus. All five downlink signals will be received by the 64-meter antennas. Since there are only three doppler trackers at the 64-meter station, it is suggested that three receivers be used with them to track and recover real time data from the bus, the large probe, and one small probe. Thus, both two-way links and one one-way link would be received and processed at Goldstone. The fourth receiver at Goldstone's 64-meter station would be operated open loop to receive all five downlink signals for predetection recording, described in Appendix 10C.

The Madrid 64-meter station could operate in a "listen only" mode, unless a problem develops at Goldstone, with a slight improvement in performance. Its three doppler trackers and three receivers could track and recover data from the bus and the two small probes, SP2 and SP3, not being tracked by Goldstone. Thus, all five vehicles are being tracked and data recovered in real time. Both stations are receiving and tracking the bus, which provides a common reference for time, DLBI, and any other uses. The fourth receiver at the Madrid 64-meter station could also be used to receive all five downlink signals for predetection recording.

If Arecibo is used for backup (it is probable that Haystack would be of little use for data recovery), it is suggested that a single, open-loop receiver and predetection recording are all that would be required. The added gain available from the Arecibo antenna could make the tapes recorded there, the preferred ones to use for off-line data recovery.

The preceding discussion has not considered any special provisions for collecting DLBI data. However, all amplitude and phase relationships of the five downlink signals are stored on the predetection recorded tapes and offline processing could be used to extract desired information.

It has been shown how the multiprobe mission can be supported by two DSN 64-meter stations without requiring additional RF equipment and how the real time operations load can be distributed between them to minimize personnel loading. At the same time backup recordings can be made in case there are any problems in acquiring and locking to any of the signals in real time.

Some additional alternatives could be considered. For example, the overseas sites have a common control center for both the 64-meter and 26-meter antennas. Thus, it might be possible to patch the signal from the 64-meter antenna into the receivers at the 26-meter site, and thus receive and recover data from all five downlinks as well as doing predetection recording at the 64-meter site. However, there would only be four doppler trackers available so one vehicle would be left out anyway. At Goldstone there is no common control center, but enough equipment might be collected to permit handling all five links in real time.

If the 1978 launch opportunity is chosen, the recommended arrival time would not allow adequate Goldstone-Madrid coverage and thus Canberra and Goldstone would have to be used. The overlap time would be greater, but there would be no backup coverage and the DLBI experiment would be limited to a single base line, as there do not appear to be any additional stations available that could view the probe entry.

APPENDIX 10C

SPECIALIZED DSN HARDWARE AND SOFTWARE

APPENDIX 10C

SPECIALIZED DSN HARDWARE AND SOFTWARE

The Systems Design Study Statement of Work General Task (7) reads: "Define the specialized hardware and software necessary to process the telemetry data to an uncoded PCM data stream." This appendix answers this task for the preferred bus and probe communications links for both real time and nonreal time (predetection recording) data recovery.

1. REAL TIME DATA RECOVERY

The recommended communication modulation scheme for orbiter, bus, and probes (PCM/PSK/PM) is completely compatible with the DSN Block III and IV receivers, subcarrier demodulator assemblies, and symbol synchronizers. For the preferred Atlas/Centaur configuration, the use of Pioneers 10 and 11 convolutional code ($K = 32$, $R = 1/2$) with real time sequential decoding is also completely compatible with the existing DSN data decoder assembly. The recommended uplink and downlink frequency assignments are to use the standard DSN channels. Therefore, no specialized hardware or software will be required to recover the uncoded PCM data stream for the preferred Atlas/Centaur configuration. For the Thor/Delta configuration, the recommendation for the probes of a short constraint length ($K = 6$, $R = 1/3$) error correcting code designed for use with the Viterbi decoding algorithm may represent a requirement for a nonstandard DSN data decoder assembly. It is uncertain at this time if this capability will be implemented for the Mariner-Jupiter-Saturn program. If not, this capability would be required to enable real time recovery of Pioneer Venus probe data if the Viterbi decoding algorithm were chosen.

2. PREDETECTION RECORDING

Regardless of launch vehicle selection, we strongly recommend that predetection recording be used for the probe and bus entry to back up the real time tracking and data recovery and permit later, off-line analysis of the received signals. For this mode of operation, some specialized hardware and possibly software will be required. There are several ways of accomplishing the predetection recording of all probe plus bus downlink signals. A method which has minimal impact on the DSN stations is shown in Figure 10C-1. The antenna, preamplifier, S-band receiver, frequency standard/frequency synthesizer, and magnetic tape recorder are all existing DSN hardware. The only potentially new hardware is the narrowband filter/down-converter/low-pass filter required to translate from the receiver's 10 MHz IF to the less than 1.5 MHz capacity of the FR-1400 or FR-2000 magnetic tape recorder. If this equipment is not available at the DSN stations, standard commercial hardware is available at relatively low cost and no development or modification is required. Typical examples are the Microdyne 1171-PR(A) and the Defense Electronics PC-101 units.

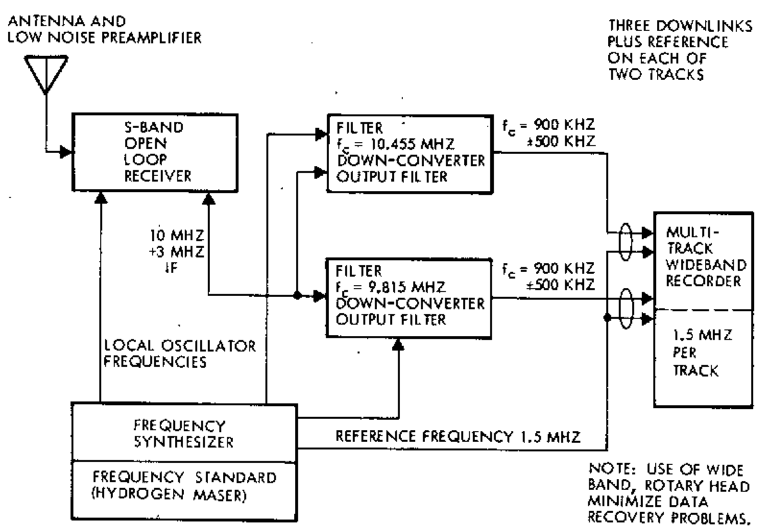

Figure 10C-1. Predetection Recording - Pioneer Venus Standard DSN Frequencies

The recording center frequency and bandwidth is selected in accordance with Table 9, page 53 of the Telemetry Standards, IRIG document 106-71, in order to be compatible with commercially available hardware. Of critical importance is the recording of a stable reference frequency on each track along with the data in order to permit later compensation for effects such as tape skew, differential stretch or pucker in the tape, etc. Figure 10C-2 shows the spectra of the receiver 10 MHz IF passband, the downlink channel spacings and data bandwidths, and the narrowband filters.

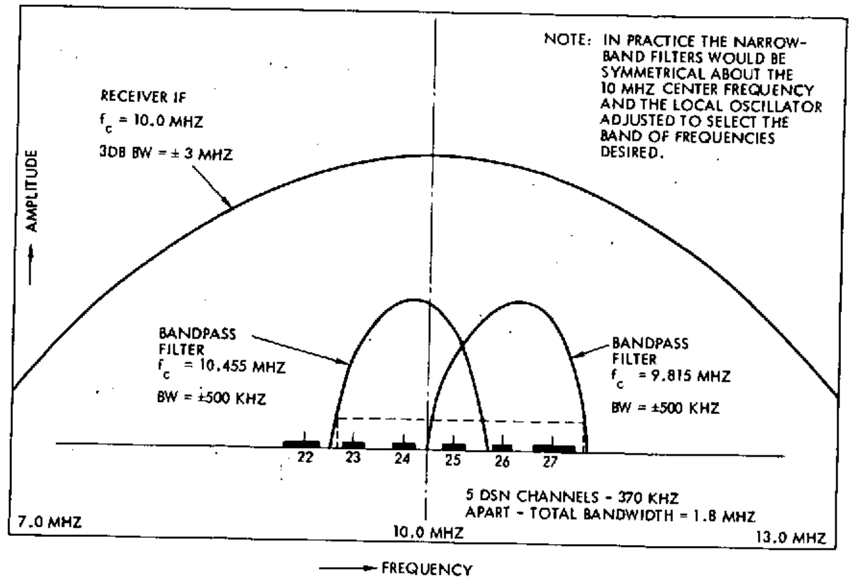

Figure 10C-2. Probe Mission Downlink Channels

(Note: Channels 22 and 27 are bus downlink channels and only one will actually be in use. By placing them at the outer ends of the group, the occupied bandwidth will be the same regardless of which is in use. With this configuration, Channel 25 will be recorded on both tracks and can aid in time correlation between all downlinks. With this recording scheme all time and phase relationships (as well as interfering signals plus noise) are permanently stored on tape.

If the offline processing is to be done elsewhere, such as at JPL or at ARC, this would be the total impact on the DSN stations, although there is a small operational problem that should be noted. To realize the 1.5 MHz capability of the tape recorders, they must run at 120 inches per second, which restricts the recording time to approximately 12 minutes per reel of tape. This means that two recorders must be available at each station and provision made for transferring back and forth without loss of data. For a small probe entry time of 63 minutes, allowing for tolerances and overlap, a minimum of six reels of tape will be required at each recording site and personnel on site to change tape.

The offline processing of the predetection recorded data will require some additional hardware and possibly some software as well. Figure 10C-3 shows a method of recovering the data at a site that has the equivalent of most of the standard DSN equipment. For example, the magnetic

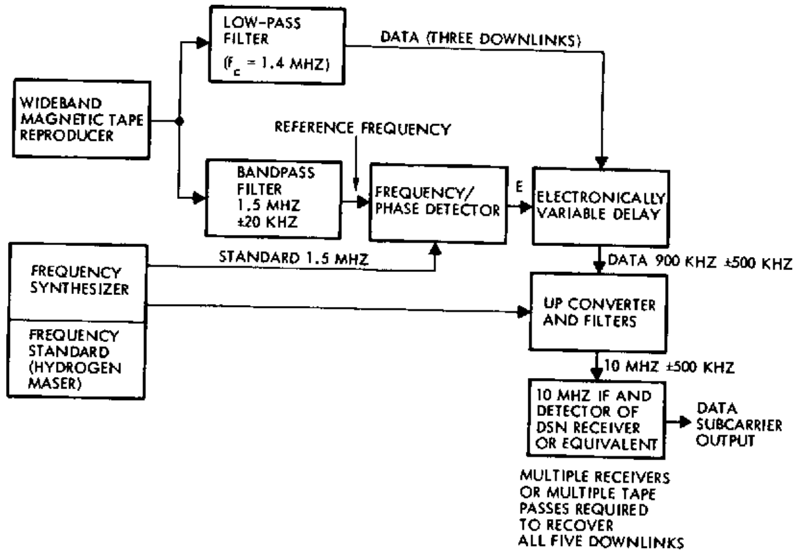

Figure 10C-3.- Recovery of Pioneer Venus Data From Predetection Recorded Tapes

tape reproducer must be an FR-2000 or equivalent with as good a time base stability as is possible to obtain. The frequency standard/frequency synthesizer should be comparable to the DSN equipment, as should be the receiver/detector shown at the bottom right of the figure. Following the receiver/detector could be the usual DSN subcarrier demodulator and data recovery equipment used for recovering the data in real time.

The specialized hardware, which comprises the remaining five blocks of the diagram, up-converts the signal to 10 MHz and reduces the time base instabilities to acceptable levels. The up-conversion function is straightforward and may be accomplished with the same hardware shown for down-conversion in Figure 10C-1, since many of the commercially available units provide both functions. The unique function is the reduction of time base errors or instabilities. Recent specifications for the FR-2000 quote a time base error of ±0.3 microseconds (±300 nanoseconds) at 120 inches per second. When this error is converted to phase error at the high end of the data bandwidth (use the 1.5 MHz reference as an example) this becomes ±2.83 radians (±162 degrees), which is much too great to track with a phase-locked loop (PLL), hence coherent operation is not possible. However, if the time base instability could be reduced by an order of magnitude to around ±0.28 radian (±16 degrees) (±30 nanoseconds), then a PLL could probably track and the data could be recovered. It is the purpose of the narrowband filter to select the 1.5 MHz reference frequency from the tape playback. The signal is then compared with a stable 1.5 MHz signal in the frequency/phase detector and the difference or error signal is used to control an electronically variable delay line to reduce the time base errors to an acceptable error. At the time of this writing, this correction loop has not been demonstrated to work as described. However, the technique is used in the Ampex FR-900A/950 transient-free, time-base stabilized, wideband, rotary head record/reproduce models. The data sheets on these models quote a relative time base stability of ±15 nanoseconds, which would be sufficient. Therefore, it is worth noting that suitable hardware does exist to permit satisfactory predetection recording of all probe and probe bus downlinks, even though such equipment is not available in the DSN. Such equipment lends credence to the belief that the technique shown in Figure 10C-3 will work and demonstrates that a fallback capability truly exists. It should also be noted that the FR-900A can record a full hour on a single reel of tape, which would minimize tape changes.

Other methods of recovering data from predetection recorded magnetic tape can be postulated, but would require development and do not have a demonstrated application. For example, all of the data inherent in the received signal (including doppler) is defined by the frequency and phase variations between the data signal and the stable reference signal. Computer techniques could be developed to recover the data from these relationships, but are not known to be available for this application at this time.

To summarize, for the recommended use of an Atlas/Centaur launch vehicle probe mission, all probe and probe bus downlink data can be received and recovered in real time using existing DSN hardware and software. The modulation is PCM/PSK/PM and the error correcting coding is the Pioneer, K = 32, R = 1/2, code for sequential decoding. To back up the real time recovery mode, predetection recording is recommended, as shown in Figure 10C-1, where the only potentially new hardware is identified by the boxes labeled "filter/down-converter/output filter." This hardware comprises commercially available equipment, although the filters may have to be built to specification for the application. This would be the only hardware impact to the DSN, and there should be no software impact up to the point of recovering the uncoded PCM data stream.

If a Thor/Delta launch vehicle is used, it is recommended that a different error correcting code be used for the probes. The code recommended is a $K = 6$, $R = 1/3$ code for Viterbi decoding. This decoding could possibly be accomplished at the DSN either by a hardware decoder or by software for a mini-computer. However, it would be the only change other than the predetection recording hardware as described for the Atlas/ Centaur launch.

Regardless of launch vehicle, a method of recovering data from the predetection recorded tapes is required. The method shown in Figure 10C-3 is suggested as a minimal impact method using all DSN-type equipment except for the equipment used to improve time base stability. This would be new equipment to be developed for the program, but would be required only at the off-line facility where data recovery and processing would be done. It would not be required at the data acquisition sites.

SECTION 11 APPENDICES

APPENDIX 11A

ALLOCATION OF WEIGHT TO MINIMIZE COST

APPENDIX 11A

ALLOCATION OF WEIGHT TO MINIMIZE COST

A flight vehicle consists of several elements (i). Each element has a weight, W_i, and a cost C_i which is a function of its weight: $C_i = C_i(W_i)$. This function may be continuous, or it may be discrete, being defined at only a limited number of points. In the latter case, connect the points by straight-line segments for the purpose of this analysis, so that we may regard $C_i(W_i)$ as being quasi-continuous and differentiable.

The problem is to allocate weight within some upper limit so as to minimize total cost, i.e.,

Retaining $W_T = \Sigma W_i \leq W_o$

Minimize $C_T = \Sigma C_i$

In the solution, recognize that if total cost C_T is minimized, then it will have no incremental change δC_T for incremental reallocations ∂W_i:

$$\delta C_T = \Sigma \frac{\partial C_T}{\partial W_i} \delta W_i = \Sigma \frac{dC_i}{dW_i} \delta W_i = 0 \tag{1}$$

provided W_T is maintained constant:

$$\delta W_T = \Sigma \delta W_i = 0 \tag{2}$$

Thus, these two equations are to be satisfied:

$$\begin{bmatrix} \frac{dC_1}{dW_1} & \frac{dC_2}{dW_2} & \frac{dC_3}{dW_3} & \cdots \\ 1 & 1 & 1 & \end{bmatrix} \begin{bmatrix} \delta W_1 \\ \delta W_2 \\ \delta W_3 \\ \vdots \end{bmatrix} = \begin{bmatrix} 0 \\ 0 \end{bmatrix} \tag{3}$$

For them to be satisfied for other than the trivial case,

$$\delta W_1 = \delta W_2 = \delta W_3 = \ldots = 0$$

the rank of the matrix

$$[M] = \begin{bmatrix} \frac{dC_1}{dW_1} & \frac{dC_2}{dW_2} & \frac{dC_3}{dW_3} \cdots \\ 1 & 1 & 1 \;\; \cdots \end{bmatrix}$$

must be less than 2. This requires that every 2 x 2 determinant in the matrix must vanish:

$$\begin{vmatrix} \frac{dC_j}{dW_j} & \frac{dC_k}{dW_k} \\ 1 & 1 \end{vmatrix} = 0, \quad \text{any } j, k. \tag{4}$$

Thus all the derivatives are equal

$$\frac{dC_1}{dW_1} = \frac{dC_2}{dW_2} = \frac{dC_3}{dW_3} = \ldots = -K^2 \tag{5}$$

For a given total weight, W_T, K is constant, but it varies with W_T.

Figure 11A-1 shows how the above relations may be satisfied graphically. The flight vehicle, in this example, has three elements, b (bus), e (experiments), and p (probes), whose cost-weight relations are reciprocal functions C_i versus W_i shown in the upper left portion of the figure.

These functions are differentiated to give curves of derivatives dC_i/dW_i versus W_i in the lower left portion.

The relation $W_T = \Sigma W_i$ is generated subject to the restriction of Equation (5) by summing horizontally to the curve dC_i/dW_i versus W_T in the lower right portion, using the same dC_i/dW_i for each element as its weight is summed. In the upper right, we construct $C_T = C_b + C_e + C_p$ versus W_T using, for each W_T, the values of C_b, C_e, and C_p as shown. This gives the minimized C_T for any weight limit W_o.

Once the graph is constructed, if a weight limit W_o is given, the reverse process implied by straight lines labeled $C_T = C_b + C_e + C_p$; dC_i/dW_i; C_b; C_e; C_p immediately gives the minimized total cost C_T, the weight to be allocated to each element, W_b, W_e, and W_p, and the cost of each element C_b, C_e, and C_p.

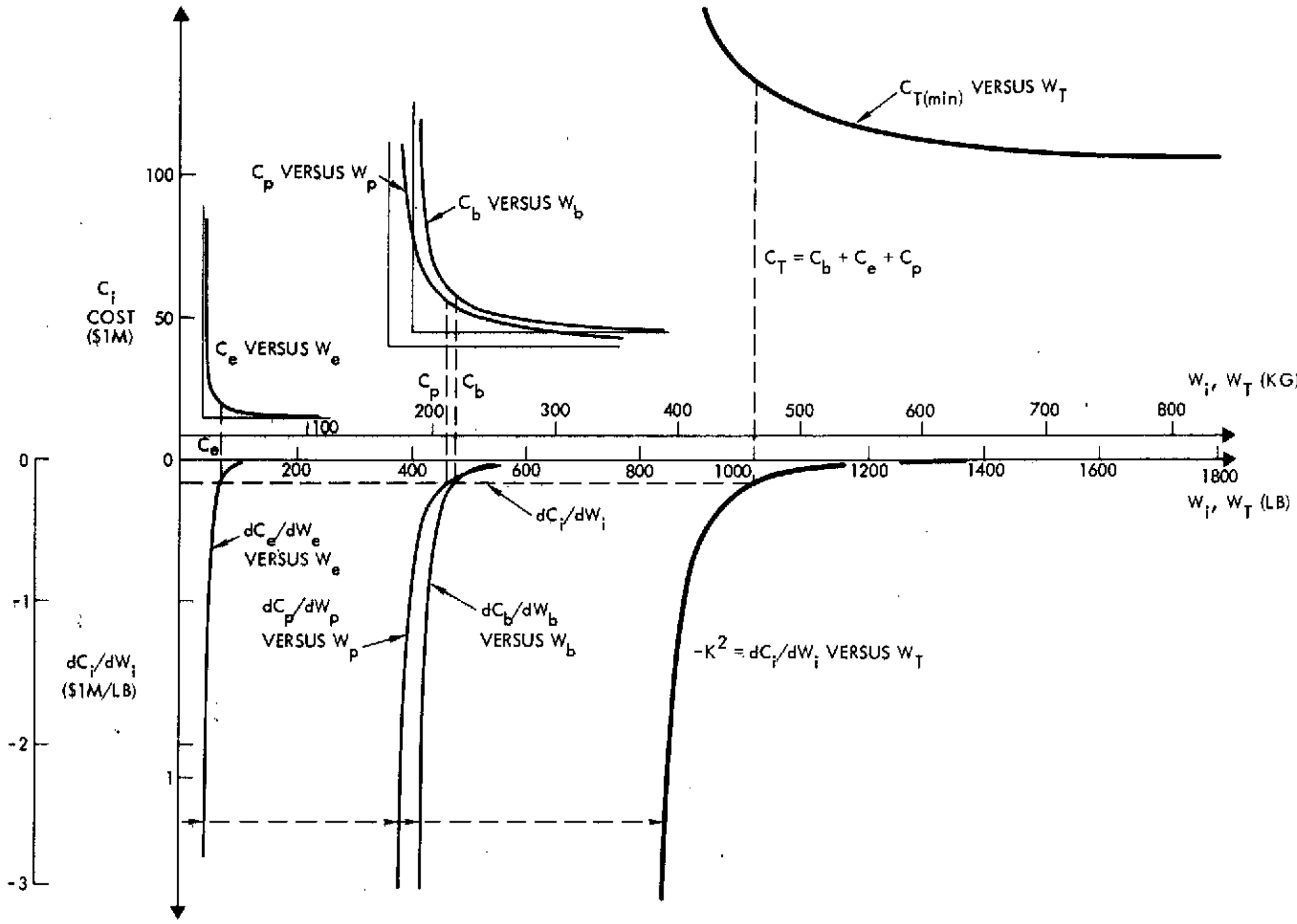

Figure 11A-1. Cost/Weight Curves

The procedure can also be used equally well when the functions are discrete rather than continuous.

APPENDIX 11B

ALLOCATION OF WEIGHT AND RELIABILITY TO MINIMIZE COST

APPENDIX 11B

ALLOCATION OF WEIGHT AND RELIABILITY TO MINIMIZE COST

In Appendix 11A a method is derived mathematically and implemented graphically to allocate weight among various elements of a flight vehicle so as to minimize total cost, where the cost of each element is a function of that element's weight.

In this appendix, the situation is generalized from the allocation of one limited resource (weight) to two resources (weight and reliability). It is assumed that the cost of each element is a function of both the weight and reliability of that element:

$$C_i = C_i(W_i, R_i)$$

Presumably, for this element to fulfill a fixed function, C_i will be a decreasing function of weight W_i, but an increasing function of reliability R_i. The entire flight vehicle (it is assumed) must observe limits on the two resources: a maximum weight and a minimum reliability:

$$W_T = \Sigma W_i \leq W_o$$

$$R_T = \Pi R_i \geq R_o$$

and we are to minimize the total cost,

$$C_T = \Sigma C_i$$

To determine the solution, we recognize that there will be no incremental change in cost, δC_T for incremental reallocations of either weight (δW_i) or reliability (δR_i) provided system weight and reliability are maintained constant. Thus:

$$\delta C_T = \Sigma\left(\frac{\partial C_T}{\partial W_i} \delta W_i + \frac{\partial C_T}{\partial R_i} \delta R_i\right)$$

$$= \Sigma \frac{\partial C_i}{\partial W_i} \delta W_i + \Sigma \frac{\partial C_i}{\partial R_i} \delta R_i = 0$$

$$\delta W_T = \Sigma\, \delta W_i = 0$$

$$\delta R_T = \delta \ln R_T = \Sigma \frac{\partial \ln R_T}{\partial R_i}\, \delta R_i = \Sigma \frac{d \ln R_i}{d R_i}\, \delta R_i = \Sigma \frac{1}{R_i}\, \delta R_i = 0.$$

matrix form:

$$\underbrace{\left[\begin{array}{cccc|cccc} \frac{\partial C_1}{\partial W_1} & \frac{\partial C_2}{\partial W_2} & \frac{\partial C_3}{\partial W_3} & \cdots & \frac{\partial C_1}{\partial R_1} & \frac{\partial C_2}{\partial R_2} & \frac{\partial C_3}{\partial R_3} & \cdots \\ 1 & 1 & 1 & & 0 & 0 & 0 & \cdots \\ 0 & 0 & 0 & & \frac{1}{R_1} & \frac{1}{R_2} & \frac{1}{R_3} & \cdots \end{array}\right]}_{[M]} \begin{bmatrix} \delta W_1 \\ \delta W_2 \\ \delta W_3 \\ \vdots \\ \delta R_1 \\ \delta R_2 \\ \delta R_3 \\ \vdots \end{bmatrix} = \begin{bmatrix} 0 \\ 0 \\ 0 \end{bmatrix}$$

›r this matrix equation to be satisfied for other than the trivial case $W_1 = \delta W_2 = \delta W_3 = \ldots = 0$; $\delta R_1 = \delta R_2 = \delta R_3 = \ldots = 0$) the rank of the ›efficient matrix [M] must be less than 3. This, in turn, requires that ›ery 3 x 3 determinant in the matrix must vanish. For those 3 x 3 ›terminants derived entirely from the left half or entirely from the right ›lf of [M], this vanishing is automatic. Where the 3 x 3 determinants ›corporate columns from both halves of [M], we have:

$$\left|\begin{array}{cc|c} \frac{\partial C_\ell}{\partial W_\ell} & \frac{\partial C_m}{\partial W_m} & \frac{\partial C_n}{\partial R_n} \\ 1 & 1 & 0 \\ 0 & 0 & \frac{1}{R_n} \end{array}\right| = \frac{1}{R_n}\left(\frac{\partial C_\ell}{\partial W_\ell} - \frac{\partial C_m}{\partial W_m}\right) = 0; \text{ any } \ell,\ m,\ n$$

$$\begin{vmatrix} \frac{\partial C_\ell}{\partial W_\ell} & \frac{\partial C_m}{\partial R_m} & \frac{\partial C_n}{\partial R_n} \\ 1 & 0 & 0 \\ 0 & \frac{1}{R_m} & \frac{1}{R_n} \end{vmatrix} = \frac{1}{R_m}\frac{\partial C_n}{\partial R_n} - \frac{1}{R_n}\frac{\partial C_m}{\partial R_m} = 0; \text{ any } \ell, m, n$$

These two sets of equations can be rewritten:

$$\frac{\partial C_1}{\partial W_1} = \frac{\partial C_2}{\partial W_2} = \frac{\partial C_3}{\partial W_3} = \ldots. = -K \tag{1}$$

$$R_1\frac{\partial C_1}{\partial R_1} = R_2\frac{\partial C_2}{\partial R_2} = R_3\frac{\partial C_3}{\partial R_3} = \ldots = L \tag{2}$$

1. GRAPHICAL CONSTRUCTION

The graphical method of Appendix 11A can be extended to two dimensions, Figure 11B-1, to conform to Equations (1) and (2). In the upper part of the figure the functions $C_1(W_1, R_1)$ and $C_2(W_2, R_2)$ are shown by means of contours against the coordinates W and ℓn R. (Only 2 elements are used in this example.)

Differentiation of each of these functions, and the plot of the derivatives with respect to both W_i and R_i is indicated in the central part of the figure. Contours of

$$K = -\frac{\partial C_i}{\partial W_i}$$

$$\text{and} \quad L = R_i\frac{\partial C_i}{\partial R_i} = \frac{\partial C_i}{\partial \ell n\, R_i}$$

are shown. Taking a single value of K and a single value of L to apply to both elements, the intersecting contours will fix the coordinates W_1, $\ell n\, R_1$, W_2, $\ell n\, R_2$ such that Equations (1) and (2) are satisfied. Corresponding to these values of K and L are $W_T = W_1 + W_2$ and $\ell n\, R_T = \ell n\, R_1 + \ell n\, R_2$, giving the system weight and reliability.

System cost can be determined:

$$C_T = C_1 + C_2 = C_1(W_1, R_1) + C_2(W_2, R_2).$$

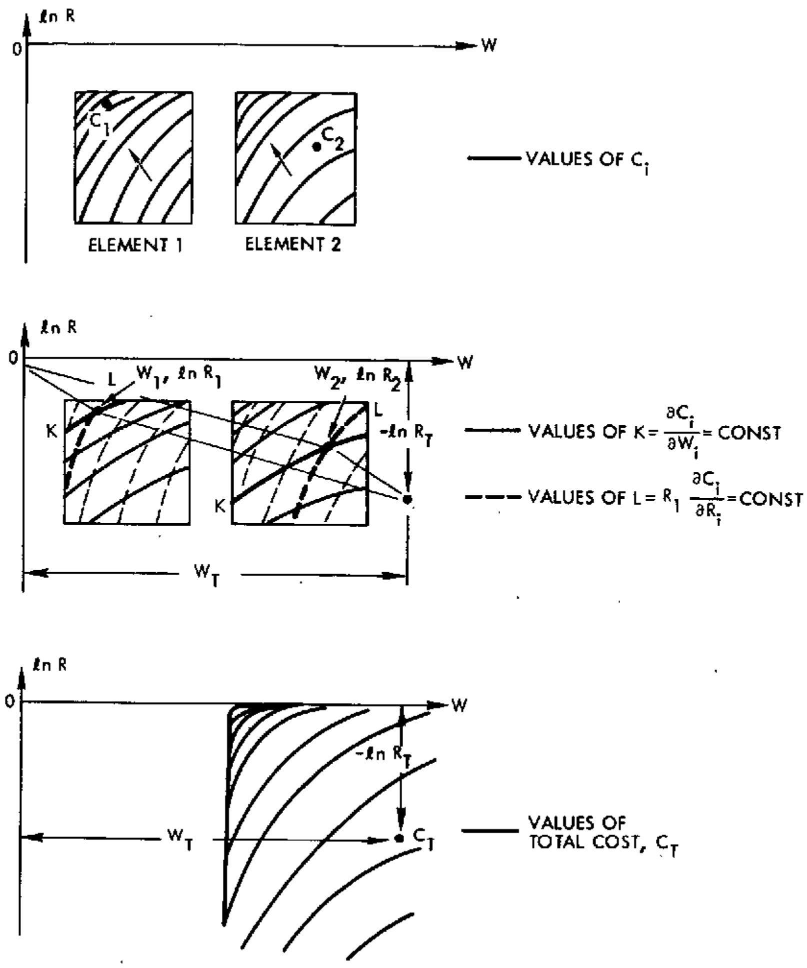

Figure 11B-1. Graphical Method Extended to Two Dimensions

It also results from the selected values of K and L, and is plotted in the lower part of the figure as a function of W_T and $\ell n\ R_T$. The method of construction assures that this value of C_T is the minimum possible for the W_T and R_T indicated.

This construction shows how to go from the derivatives K and L to the system level parameters W_T, R_T, and C_T by way of W_i, R_i, and C_i for each element.

What is necessary is a reversal of this process: Starting with W_T and R_T, determine W_i, R_i, and C_i for each element. This can be done by a process (not shown) on the lower portion of the figure. Since the point at the coordinates (W_T, $\ell n\ R_T$) is derived from a single value of K and a single value of L, by repeating the calculations over a field of variations in K and L, we can determine values of K and L at many such points, (W_T, ℓn R_T). These values of K and L can be indicated by contour plots of them vs W_T and ℓn R_T on the lower portion of the figure. Then, given the weight and reliability limits for the system, we can proceed as follows, determining all necessary quantities:

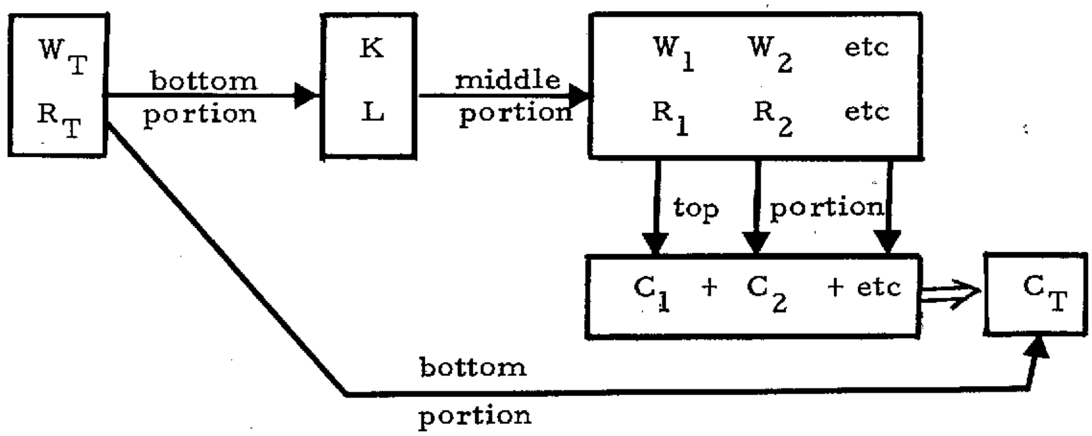

2. ANALYTICAL EXAMPLE

For illustrative purposes, consider this example. Let there be n elements to the flight vehicle. For each element cost assumed to be is related to weight and reliability by the following relation:

$$C_i = \frac{A_i^3}{(W_i - W_{io})(-\ell n\ R_i)} \quad ; \quad i = 1,\ 2,\ \ldots\ n \tag{3}$$

C_i, W_i, and R_i are the variable cost, weight, and reliabilities of the element, and lie within these ranges:

$$0 < C_i$$
$$0 < W_{io} < W_i$$
$$0 < R_i < 1$$

The form of the function is realistic, with cost rising reciprocally as:

(a) the element weight is reduced toward some "unrealizable minimum weight", W_{io}, and

(b) as reliability is increased toward unity.

A_i and W_{io} are constants which distinguish the cost relation of the ith element from that of other elements.

The derivatives, Equations (2) and (3) are determined and equated:

$$\frac{\partial C_i}{\partial W_i} = \frac{C_i}{(W_i - W_{io})} = -K^3 \quad (4)$$

$$R_i \frac{\partial C_i}{\partial R_i} = \frac{C_i}{(-\ell n\, R_i)} = L^3 \quad (5)$$

The constants A_i^3, K^3, and L^3 are used rather than A_i, K, and L merely for later convenience.

Solve Equation (4) for W_i and (5) for $(-\ell n\, R_i)$:

$$W_i = W_{io} + \frac{C_i}{K^3} \quad (6)$$

$$(-\ell n\, R_i) = \frac{C_i}{L^3} \quad (7)$$

Now substitute for these quantities in (3) and solve for C_i:

$$C_i = \frac{A_i^3}{\frac{C_i}{K^3}\ \frac{C_i}{L^3}}$$

$$C_i = KL\, A_i$$

By means of Equations (6) and (7) we may now express all quantities in terms of K and L

$$C_i = KL\, A_i \qquad C_T = \Sigma C_i = KL \Sigma A_i \quad (8)$$

$$W_i = W_{io} + \frac{L}{K^2} A_i \qquad W_T = \Sigma W_i = \Sigma W_{io} + \frac{L}{K^2} \Sigma A_i \quad (9)$$

$$(-\ell n\, R_i) = \frac{K}{L^2} A_i \qquad R_T = \Pi R_i$$

$$(-\ell n\, R_T) = \Sigma (-\ell n\, R_i) = \frac{K}{L^2} \Sigma A_i \quad (10)$$

Reversing the process, we solve (9) and (10) to find derivatives K and L in terms of the weight and reliability limits W_T and R_T:

$$\left.\begin{aligned} \frac{L}{K^2} &= \frac{W_T - \Sigma W_{io}}{\Sigma A_i} \\ \frac{K}{L^2} &= \frac{(-\ell n\, R_T)}{\Sigma A_i} \end{aligned}\right\} \quad \left\{\begin{aligned} K &= \frac{\Sigma A_i}{(W_T - \Sigma W_{io})^{2/3}\,(-\ell n\, R_T)^{1/3}} \qquad (11) \\ L &= \frac{\Sigma A_i}{(W_T - \Sigma W_{io})^{1/3}\,(-\ell n\, R_T)^{2/3}} \qquad (12) \end{aligned}\right.$$

We may now go back to Equations (8), (9), (10), and using the results of (11) and (12) determine all quantities in terms of the weight and reliability limits, W_T and R_T:

$$C_i = \frac{(\Sigma A_i)^2}{(W_T - \Sigma W_{io})\,(-\ell n\, R_T)}\, A_i \qquad (13)$$

$$C_T = \frac{(\Sigma A_i)^3}{(W_T - \Sigma W_{io})\,(-\ell n\, R_T)} \qquad (14)$$

$$W_i = W_{io} + \frac{W_T - \Sigma W_{io}}{\Sigma A_i}\, A_i \qquad (15)$$

$$(-\ell n\, R_i) = \frac{(-\ell n\, R_T)}{\Sigma A_i}\, A_i\,, \quad R_i = e^{-\frac{(-\ell n\, R_T)}{\Sigma A_i} A_i} \qquad (16)$$

These equations provide for <u>explicit</u> allocations of weight W_T and reliability R_T among the n elements so as to minimize system cost, with an assumed dependence of the cost of each element on the weight and reliability of that element as in Equation (3).

The graphical and analytical methods are capable of being adapted to cases where the cost relation of each element is a discrete function defined at only several points, rather than a continuous function of two variables as assumed in this memo. This adaptation would proceed in a manner similar to that indicated for the one-dimensional case in Appendix 11A.